PHOTODESORPTION OF NITRIC OXIDE FROM Au(100) USING 3D SURFACE-VELOCITY MAP IMAGING

A thesis submitted to the University of Manchester
for the degree of Doctor of Philosophy
in the Faculty of Science and Engineering

2023

Saada Abujarada
School of Chemistry

Contents

Word count 27231

List of Tables

List of Figures

The University of Manchester

Saada Abujarada
Doctor of Philosophy
Photodesorption of Nitric Oxide from Au(100) using 3D surface-velocity map imaging

Abstract
Nitric oxide photodesorption by nanosecond lasers on Au(100) single crystal at two desorption energies (3.5 eV and 4.6 eV) has been investigated in order to understand the surface-gas reaction dynamics.
NO/Au is an important system in catalysis, but this thesis focusses on using the NO/Au system to develop a novel 3D-surface velocity map imaging (3D-SVMI) setup.

This was done using a combination of experimental techniques including time-of-flight mass spectroscopy, 3D-surface velocity map imaging, near-ambient pressure X-ray photoelectron spectroscopy, and theoretical calculations based on density functional theory.

Two distinct desorption mechanisms for the photodesorption of NO from gold dependent on the photon wavelength were revealed.The 355 nm desorption is dominated by a direct excitation mechanism leading to a super-thermal and narrow angular velocity distribution. The desorption with 266 nm photons leads to slower average speed and wider angular distribution and it is dominated by a thermally activated mechanism.

The results from the 3D-VMI experiments togather with NAP-XPS and DFT results reveal that NO is molecularly adsorbed on the gold at a high-symmetry (2f) site, which ensures efficient overlap of the NO π^* orbital with the orbitals on the two neighbouring Au atoms, and with the N–O bond axis aligned along the surface normal.

Declaration

No portion of the work referred to in the thesis has been submitted in support of an application for another degree or qualification of this or any other university or other institute of learning.

Copyright Statement

i. The author of this thesis (including any appendices and/or schedules to this thesis) owns certain copyright or related rights in it (the "Copyright") and s/he has given The University of Manchester certain rights to use such Copyright, including for administrative purposes.

ii. Copies of this thesis, either in full or in extracts and whether in hard or electronic copy, may be made **only** in accordance with the Copyright, Designs and Patents Act 1988 (as amended) and regulations issued under it or, where appropriate, in accordance with licensing agreements which the University has from time to time. This page must form part of any such copies made.

iii. The ownership of certain Copyright, patents, designs, trade marks and other intellectual property (the "Intellectual Property") and any reproductions of copyright works in the thesis, for example graphs and tables ("Reproductions"), which may be described in this thesis, may not be owned by the author and may be owned by third parties. Such Intellectual Property and Reproductions cannot and must not be made available for use without the prior written permission of the owner(s) of the relevant Intellectual Property and/or Reproductions.

iv. Further information on the conditions under which disclosure, publication and commercialisation of this thesis, the Copyright and any Intellectual Property and/or Reproductions described in it may take place is available in the University IP Policy (see http://documents.manchester.ac.uk/DocuInfo.aspx?DocID=487), in any relevant Thesis restriction declarations deposited in the University Library, The University Library's regulations (see http://www.manchester.ac.uk/library/aboutus/regulations) and in The University's Policy on Presentation of Theses.

Dedication

To Dad

Ahmed Abujarada

(01/01/1940 - 23/12/2021)

Who taught me that it's never late to chase your passions.

Though you never got to see this

"you are in every page."

Acknowledgements

Undertaking this PhD has been a truly life-changing experience for me and it would not have been possible to do without the support and guidance that I received from many people.

I would like to express my sincere gratitude to my supervisor Dr. Sven Koehler for the continuous support of my PhD study and related research, for his patience, motivation, and immense knowledge. His guidance helped me in all the time of research and writing of this thesis. Thanks a lot Sven for considering, all my difficult conditions along the way and providing me with different kind of support whenever I need it.

Many thanks also to my supervisor Dr Andrew Thomas and Dr Alex Walton for their insightful comments and encouragement.

I would like to thank everyone in my group for their support, I am also thankful of the difficult people I met along the path as well. They have shown me exactly who I do not want to be.

Last but not the least, I would like to thanks my parents and my whole family. Your prayer for me was what sustained me thus far and I would like to thank: my husband and to my son for supporting me spiritually throughout writing this thesis and with my life in general.

Abbreviations

UHV	Ultra-High Vacum
UV	Ultra Violet
TPD	Temperature programmed desorption
ESD	Electron Stimulated Desorption
MGR	Menzel Gomer-Redhead
PES	Potential Energy Surface
FCC	Face Centered Cubic
TWC	Three-Way Catalysts
MO	Molecular Orbital
GNP$_s$	Gold NanoParticles
EARN	Energy and Angular-Resolved Distributions of Neutrals
ESDIAD	Electron-Stimulated Desorption Ion Angular Distributions
DFT	Density Functional Theory
STEM	Scanning Transmission Electron Microscopy
LIF	Laser Induced Fluorescence
REMPI	Resonant Enhanced Mult iphoton Ionisation
MPI	Multi Photon Ionisation
MS	Mass Spectrometry
TOF	Time Of Flight

VMI	Velocity Map Imaging
S-VMI	S-Surface Velocity Map Imaging
PM	Photolysis Mapping
PFI	Photofragment Imaging
NS	Newton Sphere
XPS	X-Ray Photoelectron Spectroscopy
NAP-XPS	Near Ambient Pressure X-Ray Photoelectron Spectroscopy
SAMs	Self-Assembled Monolayers

Chapter 1

Introduction

The investigation of the elementary steps of a chemical reaction and the direction of a rational mechanism for the reaction is the realm of reaction dynamics. Most of the experiments performed in this area have concentrated on the study of molecules in the gas phase to obtain reliable and accurate results.

One approach to investigate the dynamics of a reaction is to probe the internal quantum states and translational or kinetic energies of the reactant and product molecules; hence the choice of the appropriate techniques is of great importance here. Determination of the internal energies of the products has been made possible through the use of high resolution laser spectroscopy, while for kinetic energies of gaseous products, velocity map imaging (VMI) has become the technique of choice since its invention in the late 80s (ion imaging) and mid 90s (VMI). VMI is capable of extracting the velocity distribution of the products of a gas-phase reaction. Most of the studies have been focused on gas phase reactions because of their relative accuracy level of detail obtained, experimental considerations, and for ease of comparing with computational studies (and relevance to atmosphere chemistry in some cases). However, other systems, in particular at the gas-solid interface, although more complex, are equally important, especially for many industrial processes such as heterogeneous catalysis.

Several techniques have been used in the past for studying photon-induced desorption of adsorbed molecules from solid surfaces. Time-of-flight (TOF) technique coupled to a rotatable mass spectrometer has been one technique of choice. [1] This set-up allows angular resolved transitional energy distributions to be recorded. However this set-up suffers from being time-consuming, and additionally cannot probe the internal

energy distributions. These shortcomings have paved the way for the rise in the use of imaging techniques, even for surface reactions. The energy and angular-resolved distributions of neutrals (EARNs) was reported by Winograd *et al.*[2, 3] Desorption of neutrals was induced by ions. Angular distributions of ions desorbed from surfaces were also achieved using the electron-stimulated desorption ion angular distributions (ESDIADs) method.[4] This method has furthermore proven to be successful in some cases in deriving the orientations of molecular bonds at surfaces.[5, 6] State-resolved detection of neutrals typically involves the laser ionisation of neutral fragments, often performed in a resonance-enhanced multi-photon ionisation (REMPI) scheme. Usually a pump/desorption laser is used to start the event at the surface and this is followed by detection of the neutrals by another laser operating a few mm above the surface in which the kinetic energy distribution of the fragment leaving the surface can be optioned. However, this can only be achieved by the use of an elaborate optical detection geometry, otherwise the kinetic energy distributions obtained would lack any of the angular information needed. Menges *et al.* demonstrated the possibility of recording a state-selective two-dimensional velocity distribution by sheet-focussing of the ionisation laser (with the sheet perpendicular to the surface).[7] This was performed for the model system of NO photodesorbed from NiO, for which a bi-modal velocity distribution was obtained, with most of the kinetic energy release being directed along the surface normal.

Velocity map imaging will have an advantage over other techniques by offering a higher resolution, and the ability to record a 3D velocity distribution. This 3D-velocity distribution can be recorded in a single experiment as will be explained in this work. The aim is to use imaging techniques to obtain a level of detail for surface reaction similar to gas-phase reactions, and recently there has been some work and publications in that area.[8, 9] Other surface techniques were applied in this study to confirm the capability of the Surface-velocity-Map-Imaging (S-VMI).

The structure of this thesis is as follows:

Chapter two explains fundamentals of the interaction between the gaseous molecules and metal surfaces, with special emphasis on adsorption and desorption of pre-adsorbed gases. A distinction is made between the different types of adsorption of gaseous molecules onto surfaces. Special attention is paid to the methods of desorption of

gaseous molecules from the surface including thermal desorption, electron stimulated desorption and desorption triggered by photons. A brief description of the structure of the face-centred cubic system is provided, in particular the low-index fcc(100), (110) and (111).

Chapter three, summarises the most important experimental techniques and the stringent requirements placed on the techniques used as spectroscopic probes when studying reaction dynamics.

Chapter four is dedicated to the Surface Velocity Map Imaging technique, the core of this thesis. The development of Velocity Map Imaging and modifications of the spectrometer and the set-up to be suitable for investigating the desorption of gases from a single crystal surface are reported here.

Chapter five reports on the use of surface velocity map imaging to investigate the photodesorption of pre-adsorbed NO from Au(100). Translational energy distributions of the desorbed NO molecules are reported. Rotational energy distributions of the desorbed NO molecules are also reported and discussed, aiming at separating thermal from non-thermal desorption mechanisms. The effect of photon energy on the desorption mechanism is also reported.

Chapter six presents the result obtained on adsorption and desorption of NO from the Au(100) using Near-Ambient Pressure X-ray photoelectron spectroscopy (NAP-XPS). This technique offers information on the type of adsorption (molecular or dissociative), and is capable of providing information on the adsorption site and the orientation of the adsorbed NO molecules on the surface.

Chapter seven is a theoretical study of the adsorption of NO onto the Au(100) surface using Density Functional Theory, which was carried out with the aim of identifying the most energetically favourable adsorption site through calculating the adsorption energies of NO onto the three high symmetry sites.

In chapter eight the results obtained from the three used techniques are summarised and the conclusions of this thesis are given, Future work is mentioned here.

Chapter 2

Background

2.1 Fundamentals of Interactions between Gaseous Molecules and Solid Surfaces

Understanding of chemical reactions occurring at the surface of a solid necessitates unravelling the elementary steps at a molecular level associated with the interactions of gaseous molecules with the solid surface. These interactions may be more diverse than the ones associate with gas phase reactions, as the surface can play an important role in modifying the reactivity as well as the selectivity of the products.[10] Interactions of gaseous molecules with a solid surface include certain processes including collisions, adsorption, surface reactions and desorption of products.

2.1.1 Collision and Energy Transfer

The following processes occur when an atom or a molecule impinges on a surface.[10–14]

1. *Elastic collisions*: In this process, particles are reflected off the surface, and there is no net exchange of energy between the gaseous particles and the solid surface. In this type of collision, the kinetic energy is conserved.

2. *Inelastic collisions*: In this process, energy transfer or exchange between the particle and the surface takes place. The particle might impart energy into the surface or receive energy from the surface. However, if enough energy is transferred then, it may stick to the surface and ends up as an adsorbed species. In

this case, the change in the energy of the particle is not confined to its translational energy since a re-distribution of energy in the internal degrees of freedom might occur which could lead to vibrational and rotational de-excitations.

3. *Reactive collisions*: The outcome of this type of collision is a chemical reaction where bonds are broken and/or bonds are formed. This type of collision typically occurs when the collision energy is high enough to surmount the activation energy barrier of the specific reaction.

4. *Adsorption*: In this case, the impinging particle loses enough of its energy to prevent it from bouncing back from the surface into the gas phase. The particle spends some time (dwell-time) where it will be weakly bound at the surface. However, the particle can escape back to the gas phase if it absorbs energy from the phonon bath of the substrate (lattice vibrations) of the solid, or it might hop to a surface site where it ends up as a chemisorbed species, in which case it is said to be a precursor mediated chemisorption.

5. *Energy transfer*: In principle, two energy transfer mechanisms can be envisaged between the impinging particle and the solid surface. These involve the excitation and de-excitation of the substrate phonons, as well as electron hole pairs of the substrate. An electron hole pair is generated when an electron acquires sufficient energy to move from the valance band to the conduction band. On leaving the valance band the electron is said to have created a hole, hence an electron hole pair is generated. The impinging particles might interact with the electronic system of the metal substrate, as a result of which an electron is excited from an occupied state below the Fermi level (E_f) (which usually refers to the energy difference between the highest occupied states and lower ones in quantum system at absolute zero temperature) to an unoccupied state resulting in an excited state usually blue referred to as an electron-hole pair.

A schematic diagram illustrating electron-hole pair excitation when a gas molecule collides with a metal surface is shown in the Fig. 2.1.

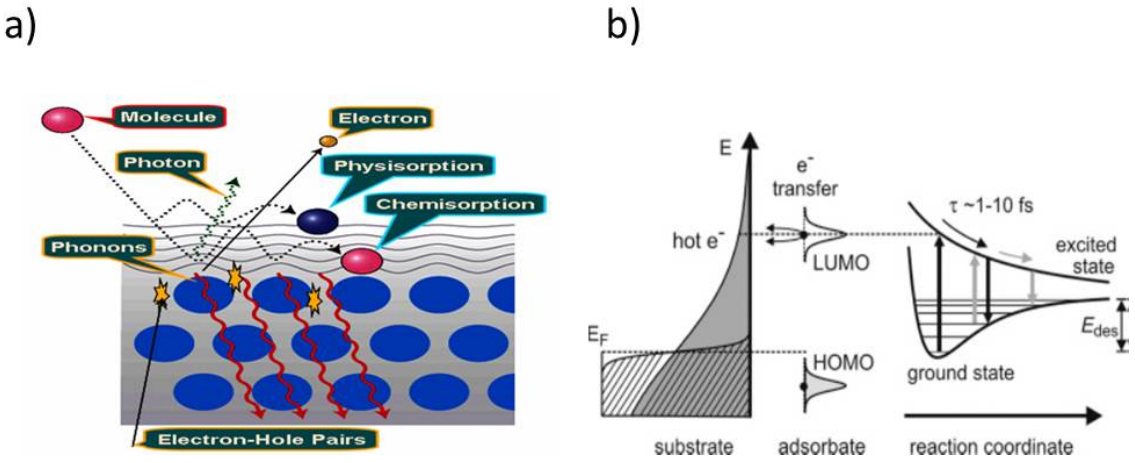

Figure 2.1: a)Primary interactions between a molecule and a solid surface, b) Schematic showing the creation of an electron-pair.[15]

2.1.1.1 Adsorption

When an atom or a molecule approaches the surface, it experiences an attractive potential energy that eventually will bind it to the surface. The process involved in trapping atoms or molecules to the surface is called adsorption.[16]

The probability of adsorption is influenced by many parameters. Some of these parameters are related to the surface of the solid including its composition, orientation (exposed crystal face) and temperature, while others are related to the to the incoming gaseous molecules including its nature, the translational energy and the angles of incidence of the approaching molecules, together with its initial electronic, vibrational and rotational quantum states and its orientation in space during collision.

When the nature of bonding between the molecule (adsorbate) and the solid surface (substrate) is considered, one can distinguish between two types of adsorption, namely physisorption and chemisorption.[17]

2.1.1.1.1 Types of Adsorption

- *Physisorption* is characterized by weak van der Waals interaction between the adsorbate and the surface corresponding to binding energy of about 20 kJ mol^{-1}.

- *Chemisorption* is characterized by strong chemical bonding of the atoms or molecules to the surface, with corresponding binding energies of 80 to 200 kJ mol^{-1}. It involves the establishment of a chemical bond between the adsorbate and the surface (ionic or covalent) resulting from the transfer or sharing of charge between the molecular orbitals and the surface electron bands. Chemisorption can be categorized as *non-dissociative adsorption* if the molecule is adsorbed intact or *dissociative adsorption* if bonds break when molecules are adsorbed.[17] Furthermore, it can be divided into activated and non-activated adsorption as explained by the potential energy curves Fig. 2.2 which are especially advantageous in illustrating energy relations during adsorption. In both cases an energy barrier (E_a) has to be surmounted to proceed from the physisorbed state to the chemisorbed state. For activated adsorption, the barrier lies above the potential energy "zero" (V_p) = 0, hence energy has to be supplied for the chemisorption to occur Fig. 2.2 a), while in the non-activated chemisorption the energy barrier is below the potential energy "zero", and the incoming molecule will always have enough energy to overcome the barrier and chemisorb. Fig. 2.2 b).

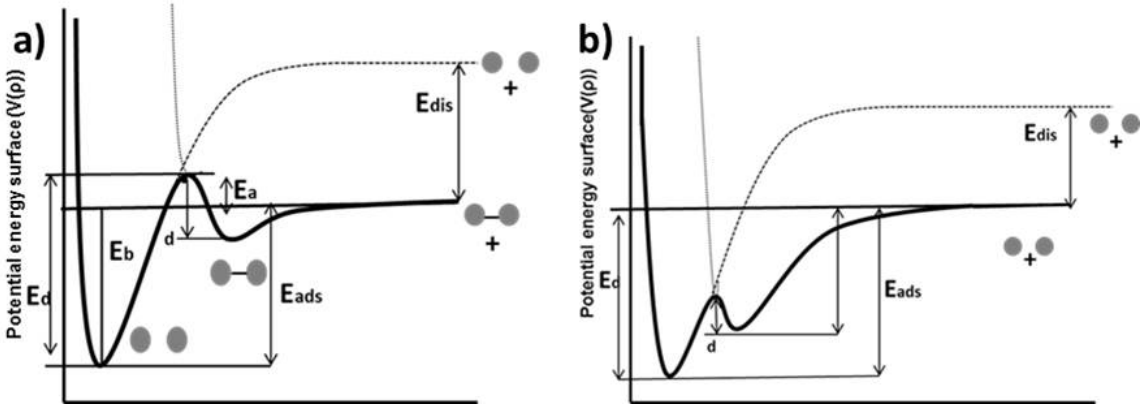

Figure 2.2: a) Potential energy diagram showing activated chemisorption; b) Non-activated barrierless chemisorption.

2.1.1.1.2 Flux of Gaseous Atoms Striking a Solid Surface

Thorough investigation of adsorption of gaseous molecules onto a solid surface requires an atomically clean surface, which has not become saturated by surrounding gas phase molecules for a time period of hours.

The collision rate or flux of gas molecules striking the surface of unit area at ambient pressure P is given by eq 2.1[18]

$$f = \frac{N_A P}{\sqrt{2\pi M R T}} \tag{2.1}$$

where: f is the flux of gas molecules or atoms (atoms) $\mathrm{cm}^{-2}\mathrm{sec}$, N_A is Avogadro's number 6.023×10^{23} mol^{-1}, P is the pressure measured in Pascal, M is the average molar weight of the gaseous species, R is the ideal gas constant and T is the temperature in Kelvin.

$$f = 2.63 \times 10^{20} \frac{P(\mathrm{Pa})}{\sqrt{M(\mathrm{g\ mol}^{-1})T}} \tag{2.2}$$

$$f = 3.52 \times 10^{22} \frac{P(\mathrm{Torr})}{\sqrt{M(\mathrm{g\ mol}^{-1})T}} \tag{2.3}$$

Eq. 2.2 & 2.3 allow us to calculate the number of molecules striking a solid surface per second per unit area. Using the equation 2.3 for calculating the number of water molecules impinging the surface at 3×10^{-6} Torr and using $M = 18$ g mol^{-1} and $T = 300$ K yields a value of about 10^{15} molecules $\mathrm{cm}^{-2}\mathrm{sec}^{-1}$.

Given that a typical metal surface has about 10^{15} surface sites cm^{-2} and assuming that every molecule sticks to the surface when colliding (sticking probability = 1), one can see that at this pressure it takes only one second for the surface to be covered with a monolayer of water molecules. Water vapour is known to be the main residual gas at this pressure. Exposing the surface to a pressure of 10^{-6} Torr for 1 second will cover the surface with a monolayer of the gas molecules used. A Langmuir is defined as 10^{-6} Torr sec.

For studying gas-solid interactions, typically the adsorbed gas coverage should not exceed one monolayer, because we are interested in the gas solid interactions and not interactions between molecules adsorbed in what is called multilayer adsorption Fig. 2.3.[19]

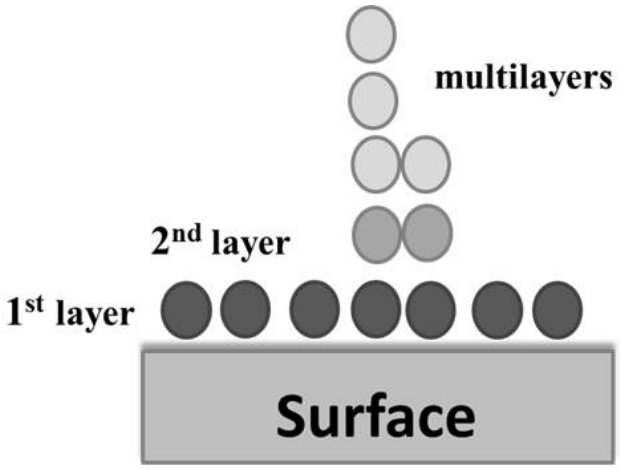

Figure 2.3: Schematic illustration of the first, and second layers of adsorption, and multilayer.

Table 2.1[18] shows the times in seconds required to contaminate a clean surface with adsorbate molecules e.g. water, CO and H_2, with the former being reactive towards many metals. It is clear that a significant reduction in the background pressure is of paramount importance if one is to avoid the interference of contaminated molecules on the investigation. A background pressure in the range of 10^{-10} Torr is usually employed to prepare and maintain an atomically clean surface in a contamination free-state for the duration of a typical experiment of a few hours.

Table 2.1: Surface saturation times at different pressures.

Pressure Torr	**Impingement Rate**	**Time to Saturation**
760	3×10^{26}	3.3×10^{-8}
1	3.9×10^{23}	2.6×10^{-5}
1×10^{-3}	3.9×10^{20}	1.5×10^{-2}
1×10^{-6}	3.9×10^{17}	15
1×10^{-9}	3.9×10^{14}	15.000

2.1.1.1.3 Sticking Probability

The rate of adsorption of a gas onto a solid surface is expressed in terms of a parameter called sticking probability, defined by the rate of adsorption per unit area divided by the number of molecules colliding with the surface per unit area per second or simply the flux.

King and Wells used an ultra-high vacuum system (UHV) and a molecular beam technique to measure the sticking probability of a gas on a crystal surface. The design of the ultra-high vacuum molecular beam system constructed in glass is shown Fig 2.4.

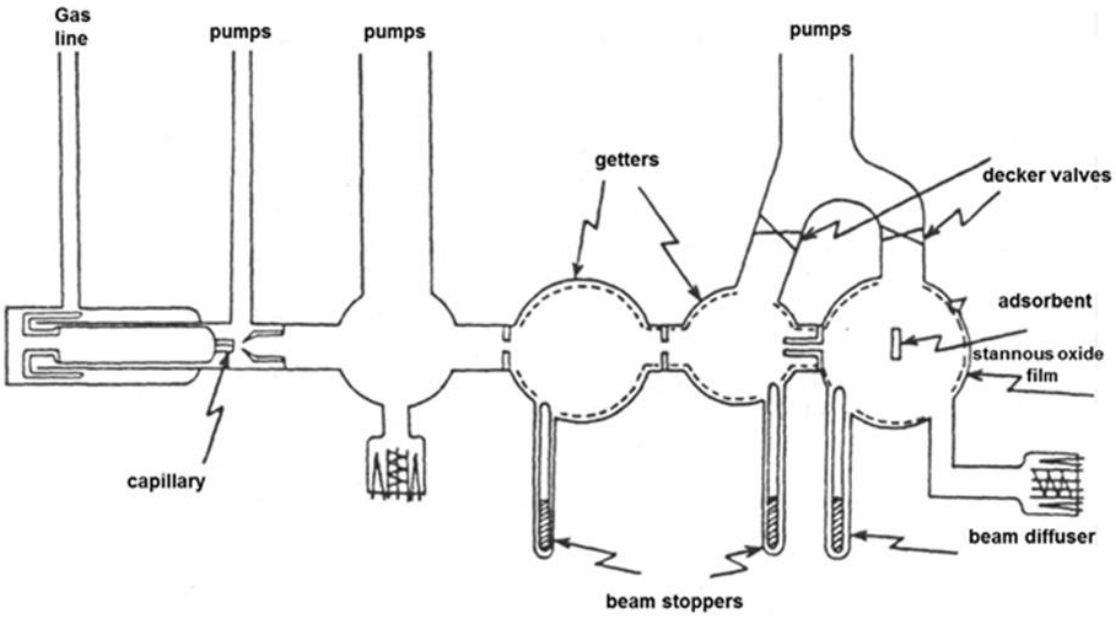

Figure 2.4: A molecular beam apparatus constructed of Pyrex glass for measuring sticking coefficient.[14]

The method involves directing a well-collimated molecular beam, with a flux in the range of $10^{12} - 10^{13}$ molecules $cm^{-2}sec^{-1}$ at a single crystal. The molecular beam with the mentioned characteristics is achieved by using several differentially pumped chambers to achieve ultra-high vacuum conditions in the adsorption chamber.

Two consecutive experiments are performed to determine the sticking coefficient. In the first one, the pressure in the adsorption cell, p_1 was recorded as a function of time after the exposure of the pre-cleaned crystal surface to the molecular beam. In the second experiment, the pressure in the cell, p_2 was recorded as a function of time after moving the crystal out of the path of the molecular beam.

The difference between p_2(t) and p_1(t) is taken as a measure of the amount of molecules trapped on the surface. The sticking coefficient at time t was then calculated by using this eq:[20, 21]

$$S = \frac{p_2(t) - p_1(t)}{p_2(t)} \tag{2.4}$$

2.1.1.2 Desorption

Desorption of an adsorbed chemical species from a solid surface can typically be caused by several methods, namely:

- Thermal Desorption[21, 22]
- Electron-stimulated desorption[23–25]
- Photo-induced desorption[26]

2.1.1.2.1 Thermal Desorption

Thermal excitation initiates desorption of the adsorbed species. The technique temperature programmed desorption (TPD)[21] involves first the adsorption of gaseous molecules onto an initially clean solid surface (usually a single crystal at a low temperature) followed by heating of the crystal preferably with a linear heating rate.

$$T = T_0 + \beta t \tag{2.5}$$

where: T is the temperature at any time, T_0 is the initial temperature and β is the heating rate in degrees per unit time.

The partial pressure of the desorbed species as a function of time is monitored and recorded using an ultra-high vacuum chamber equipped with a mass spectrometer. The temperature at which a species desorbs from the surface can be measured from the heating rate and time. In this method, the area under the peak in the desorption spectrum recorded is directly proportional to the amount of the gas adsorbed on the substrate. When calibration is carried out, one can determine the coverage from the temperature desorption spectrum recorded. Fig. 2.5 a) depicts the TPD spectrum obtained following adsorption of CO onto a Pd(111) surface at 300 K.[27] The temperature at peak maximum is indicative of the enthalpy of adsorption, which is a measure

of the strength of binding of the adsorbed molecule to the surface. If more than one adsorption site is present for the molecule at the surface, multiple peaks may appear in the spectrum reflecting different enthalpies of adsorption. An example is given Fig. 2.5 b) which shows the TPD spectrum following the adsorption of oxygen on Pt(111) at 80 K. The peak appearing at lower temperature corresponds to a weakly adsorbed state of oxygen.

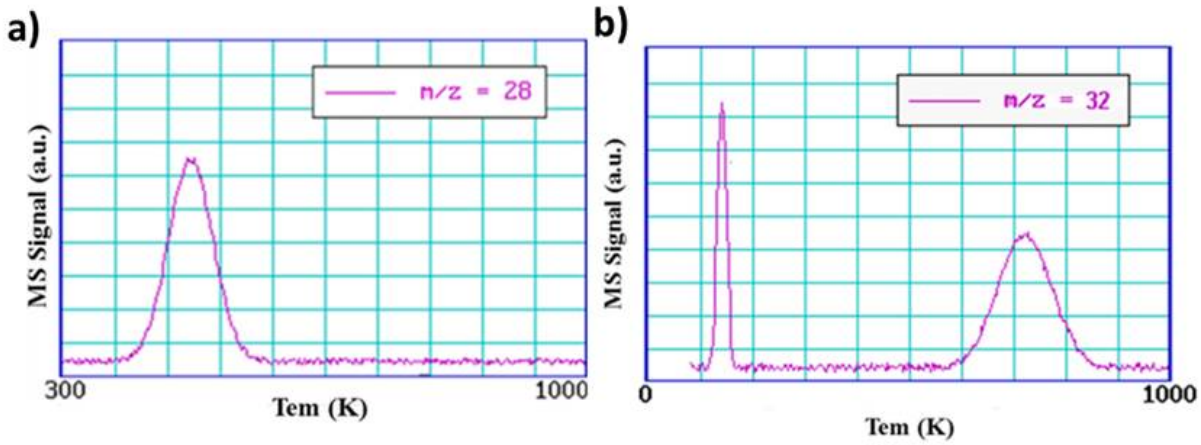

Figure 2.5: a) TPD spectrum following the adsorption of CO on Pt(111) surface at 300 K; b) TPD spectrum following the adsorption of CO on Pt(111) surface at 80 K.[27]

The two examples chosen for adsorption were of the non-dissociative type (molecular), and the molecule desorbed intact from the surface during heating. In some cases when molecular adsorption takes place at low temperature, a surface reaction might occur during heating.[27]

2.1.1.2.2 Electron Stimulated Desorption

The term electron-stimulated desorption (ESD), was first introduced by Madey and Yates [25] to describe the process by which different chemical species are produced when an adsorbate-surface system is bombarded by low energy electron (E $<$ 500 eV). The desorption products as a result of this electron bombardment include ground-state neutrals, and vibrationally and electronically excited as well as ionic fragments, i.e. positive and negative ions.[28] As it is much easier and more efficient to detect ions rather than neutrals, most of published data have been on electron-induced ion desorption.[29]

ESD had been used in surface science to determine the structure and orientation of the adsorbed species. This stems from the fact the desorbed ions do not necessarily exhibit isotropic distribution. The direction of the desorbed ions was found to depend on the orientations of the ruptured bond. [29] It has been reported that the kinetic energy of desorbed positive ions lies in the range of 1 to 10 eV, although energies as high as 15 eV have been reported. These high energies cannot be explained by thermal effects or by direct energy transfer when considering the collisions between a low-energy electrons of mass $m_e \approx \frac{1}{1840}$ a.m.u and an adsorbed atom or molecule. It can be shown that the magnitude of the maximum energy transferred between the colliding electron with energy E_i and mass m_e and atom or molecule of mass M, where m is much less than M, can be approximated to [29, 30]

$$\frac{\Delta E}{E_i} = \frac{2m_e}{M} \tag{2.6}$$

Calculating the fractional energy transfer for electron-atomic hydrogen collision for example, will give a transfer of the order of $\frac{2}{1840} \approx 0.001$. Considering that $E_i = 500$ eV implies that less than 0.5 eV would be partitioned to the hydrogen atom under these conditions. [31] Hence for interpreting the observation of "massive" ions with high kinetic energies in ESD it was suggested that the stimulated desorption is initiated by an electronic excitation of the surface molecular bond. [29]

Two models have been suggested to describe the stimulated desorption, namely Menzel-Gomer-Redhead (MGR) [31, 32] and the Antoniewicz model . [33] In both of these models electronic excitation of the adsorbate-substrate complex leads to a vertical transition from the ground state potential energy surface (PES) to an excited state. On returning to the ground state after a certain residence time in the excited state, the adsorbed molecule might desorb as an ion or a neutral species.

In the **MGR model** Fig. 2.6 a), the excited state surface is of repulsive nature. This is reflected by an increase in the nuclear distance between the adsorbate and the substrate molecule as the adsorbate-substrate complex moves towards the minimum of the excited PES. As the potential energy decreases, the kinetic energy (E_k) of the adsorbate- substrate complex increases. If the energy gained is greater than the energy of adsorption, the adsorbate will desorb, if not it will be recaptured again as it decays to the ground state. In case of an ionic primary excitation and if no electron tunneling

occurs, then the ionised molecule can desorb as a positive or negative ion. If, however, tunneling occurs, the molecule can desorb as a neutral.

Antoniewicz model Fig. 2.6 b), which is a modification of MGR model, proposes that the initial interaction between the adsorbed atom or molecule and the impinging electron leads to the formation of a positively ionised excited particle. In this model the excited state PES is of attractive nature due to attraction of the negative or positive ion to its image charge at the surface. This is reflected by the decrease in the nuclear distance between the adsorbate and the substrate.

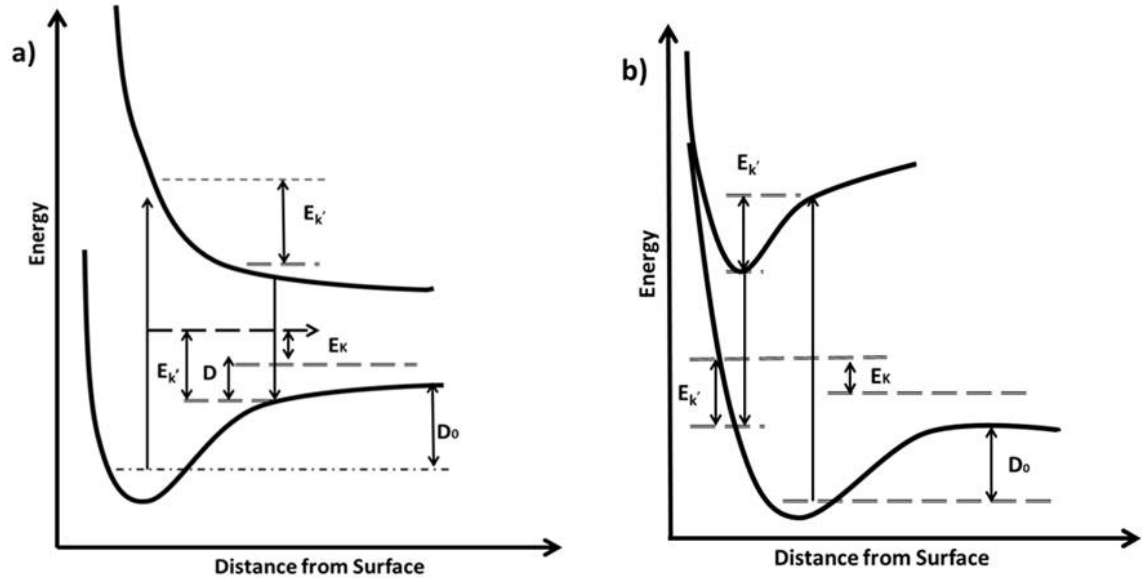

Figure 2.6: Schematic of a) MGR model, b) Antoniewicz model.

As the ion is accelerated towards the surface by the image force it comes very close to the surface which enhances the probability of its neutralisation by resonant tunneling by a substrate electron. the re-neutralised species-now being very close to the surface-is repelled as a result of Pauli repulsion [34] and is scattered away from the substrate and escapes as a desorbing neutral particle, this is illustrated in Fig. 2.7. Desorption of the positive ions was explained by Antoniewicz by adopting a more complex process involving a two-electron process. The initial ground state configuration is raised to the excited ionic curve $(M + A^+)^*$ this is followed by the movement of the excited ion towards the surface where it is neutralized by tunneling of an electron from substrate, placing the system at a higher energy level on the ground-state curve $(M + A)$. This hot neutral species (high energy) is repelled by the substrate as it comes closer to the surface (Pauli repulsion).[34] The hot neutral species might

escape with high kinetic energy away from the surface or it might be reionised by resonant electron tunneling into the substrate during its escape, hence yielding positively charged desorbing species. [35] In both models, the excess energy is distributed into the translational, rotational, and vibrational energies of the desorbed molecule. These models have been formulated in one dimension, but molecular desorption dynamics happen in a multi-dimensional configuration space, in which the internal motions of the molecule are also included.

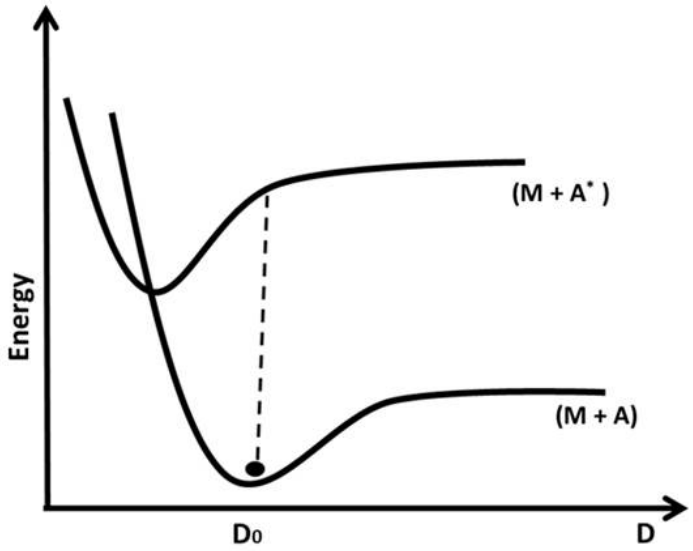

Figure 2.7: Illustrates the proposed sequence leading to neutral particle desorption (The moving point simply shows the changing potential of desorbing particle).

ESD experiments involve measurements including identification of the desorbing species, desorption yield and energy dependence or threshold energies for desorption. An important extension of the ESD technique allows measurement of the angular distribution of the desorbing particles (ESDIAD, electron stimulated desorption ion angular distribution). [4] Considerable improvement in the digital data acquisition and background subtraction and the display of the acquired ESD data has led to digital ESDIAD imaging, which provided information on the symmetry of the adsorption site together with the configuration of the adsorbates on the solid surface and the direction of the adsorbate bond.

2.1.1.2.3 Photo-Induced Desorption

Photons of light having enough energy can cause desorption of chemisorbed or physisorbed species from solid surfaces. The close relationship between the electron-stimulated desorption and photodesorption (PID) has been pointed out by amongst others, Madey. [25, 26] Photons can induce molecular desorption from a solid surface by different processes, namely surface heating, resonant vibrational, or electronic excitation of the adsorbate-substrate system. Surface heating comes about by direct absorption of the incident photon energy by the substrate causing lattice phonon excitation, which raises the temperature of the solid surface. If this thermal energy is sufficient to overcome the potential energy barrier of adsorption, the adsorbate-substrate bond may rupture, leading to desorption of the adsorbed molecule. Another mechanism for solid surface excitation is initiated by substrate electronic excitation via electron hole-pair creation and the transfer of the electron or hole produced into an unoccupied adsorbate state leading to its excitation, which subsequently decays into the heat bath of the substrate (lattice vibrations) before desorption occurs, see Fig. 2.8. This mechanism is usually termed as substrate mediated excitation or indi-

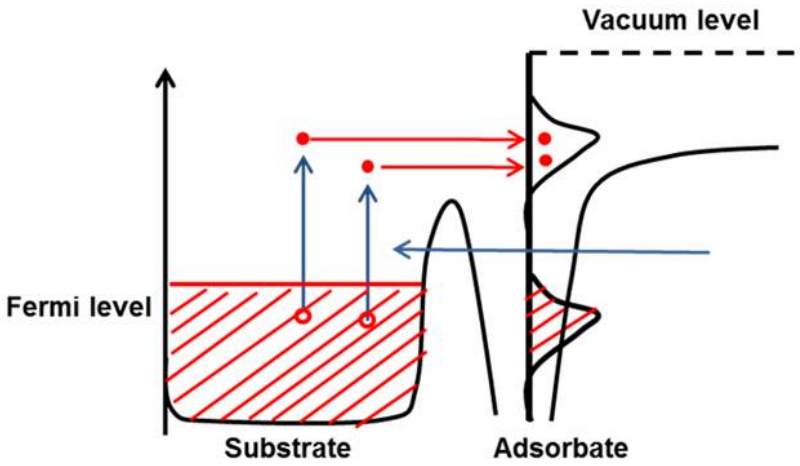

Figure 2.8: Substrate mediated excitation. Photochemistry is mediated by hot carriers at the surface.

rect excitation. The thermal effects of the process are dependent on the thermal and optical properties of the solid surface (e.g. thermal conductivity, thermal diffusion) and the laser beam characteristics such as wavelength, fluence or intensity and pulse width. The advantages of using photon stimulated desorption when compared to thermal desorption is the fast and wide range of heating rates that can be used, allowing

the study of desorption kinetics over a wider dynamic range. The use of short laser pulses provides an efficient tool for desorbing short-lived intermediates that cannot be detected by other methods.[11]

The other mechanism termed as direct excitation involves the absorption of photon energy directly by the adsorbate, leading to vibrational or electronic excitation of the adsorbate, see Fig. 2.9. Generally surface photochemical processes initiated by direct photon absorption of the adsorbate exhibit a wavelength dependence that is qualitatively similar to absorption by the corresponding gas phase molecule. After a short

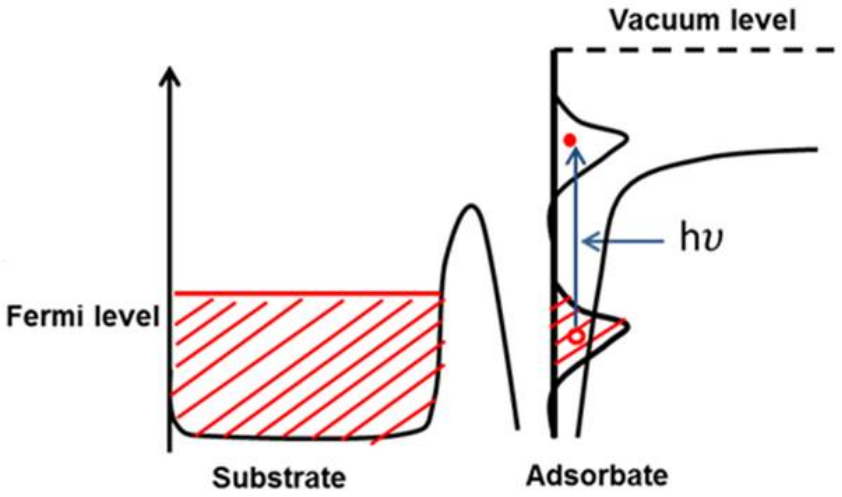

Figure 2.9: Adsorbate localized excitation or direct excitation. Photoexcitation takes place within the adsorbate complex.

time in the excited state, it relaxes and nuclear motion follows accompanied by energy transfer into the adsorbate-substrate bond. In case the amount of energy transferred is large enough to overcome the potential barrier of the adsorbate-substrate bond, the molecule will desorb.

2.2 Surface Structure of Face-Centered Cubic System Metals

The fcc is one of the close packed structures, appropriate for metals, with 12 nearest neighbors to each site (i.e., a coordination number of 12). The Bravais lattice for the fcc structure is shown in Fig. 2.10.

It is composed of parallel planes of nearest neighbors (with six nearest neighbors to each site in the plane). In the face-centered cubic system, an atom is located

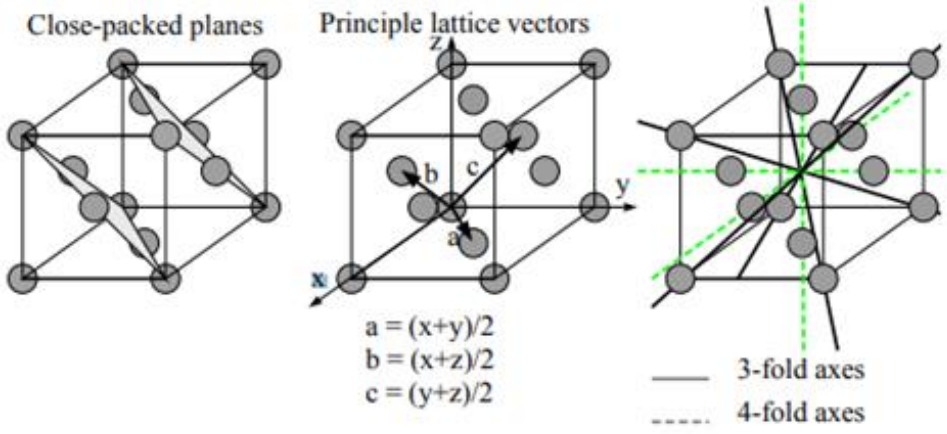

Figure 2.10: The Bravais lattice of a face-centered cubic (FCC) structure.

at the corner of each cube and on the face of each side. Precious metals such as platinum, gold, rhodium and palladium that are catalytically important all exhibit a face-centered cubic crystal structure.

A brief description for the low indexed fcc(100), (110) and (111) will be given here.

1. The *fcc*(100) surface

   One can obtain the fcc(100) surface by cutting an fcc metal parallel to the front of the fcc cubic unit cell and this exposes a surface (dark brown atoms) with an atomic arrangement of 4-fold rotational symmetry Fig. 2.11. The coordination

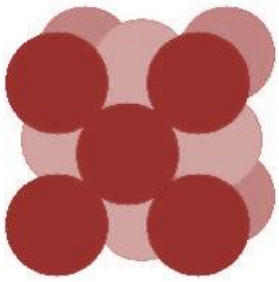

Figure 2.11: An *fcc* unit cell (100) face.

   number of the surface layer atoms is 8. This is because each surface atom is surrounded by four other atoms as nearest neighbours in the first layer and another four in the layer directly below it. It is worth noting here that all the surface atoms are equivalent and that the surface is smooth on an atomic

scale. The surface offers different adsorption sites for the approaching molecules namely, on-top sites above a single metal surface atom, 2-f bridging sites where the molecule is adsorbed and bound to two metal atoms and 4-f hollow sites where the molecule is adsorbed and bonded to four metal atoms Fig. 2.12.

Figure 2.12: The three possible adsorption sites offered by the *fcc*(100) metal surface.

2. The *fcc*(110) surface

   An *fcc(110)* surface is obtained by cutting the *fcc* unit cell in a manner that intersects the x and y axis but not the z-axis. This exposes a surface with an atomic arrangement of 2-fold symmetry Fig. 2.13.

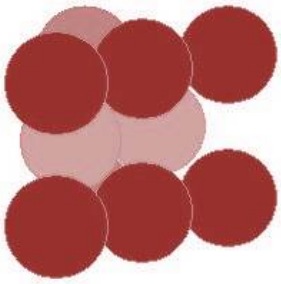

Figure 2.13: An *fcc* unit cell (110) face.

The coordination number of the topmost layer atoms in this case is 7. This can be explained by the fact that each surface atom has two nearest neighbours in the first layer, and another four in the underlying second layer, and one directly below it in the third layer. The lower coordination number for the surface atoms in Au(110) compared to Au(100) is reflected in the different chemical Reactivities of these two surfaces. The adsorption sites offered by this surface includes, on-top sites, 2-f bridging sites between two neighbouring atoms in a single row, and another bridging site between two atoms in adjacent rows. Higher coordination sites in the troughs are also available.

3. The *fcc*(111) surface

   The surface (111) is obtained by cutting the fcc metal in such a manner that the surface plane intersects the x, y and z axes at the same value. This exposes a surface with an atomic arrangement of 3-fold rotational symmetry Fig. 2.14.

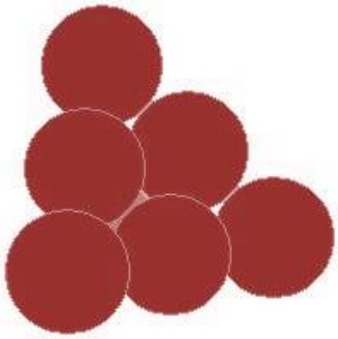

Figure 2.14: An *fcc* unit cell (111) face.

These surfaces are described as "close-packed" because it is the most efficient way of packing atoms within a single layer. The coordination number of the surface layer atoms on the *fcc*(111) surface is 9, since each of the atoms in the first layer has 6 neighbouring atoms and three atoms in the layer directly below it. It offers three adsorption sites namely, on-top sites, 2-f bridging sites between two atoms and 3-f hollow sites between three atoms.

2.3 Nitric Oxide Adsorption on Gold Surfaces

Nitric oxide (NO) is a diatomic radical with one unpaired electron, causing its noticeable reactivity.[36] NO is a major air pollutant and its removal by heterogeneous transition metal catalysts is an important industrial process.

NOx is produced in fuel combustion engines, and its reduction to nitrogen by three-way-catalysts (TWC) is crucial in reducing air pollution,[37] hence the interaction of nitric oxide with metal surfaces is of considerable importance. are three major reduction reactions that take place over TWCs.[38]

$$2\,NO + 2\,CO \longrightarrow N_2 + 2\,CO_2 \tag{2.7}$$

$$2\,NO + 2\,H_2 \longrightarrow N_2 + 2\,H_2O \tag{2.8}$$

$$NO + C_xH_y \longrightarrow CO_2 + H_2O + N_2\ (\textit{not balanced}) \tag{2.9}$$

The complexity of the interaction between NO and metal surfaces is due to the unpaired electron in the antibonding $2\pi^*$ orbital (see Fig. 2.15), and the low dissociation energy (630 kJ mol^{-1}) compared to other gases such as CO (1076 kJ mol^{-1}).[39]

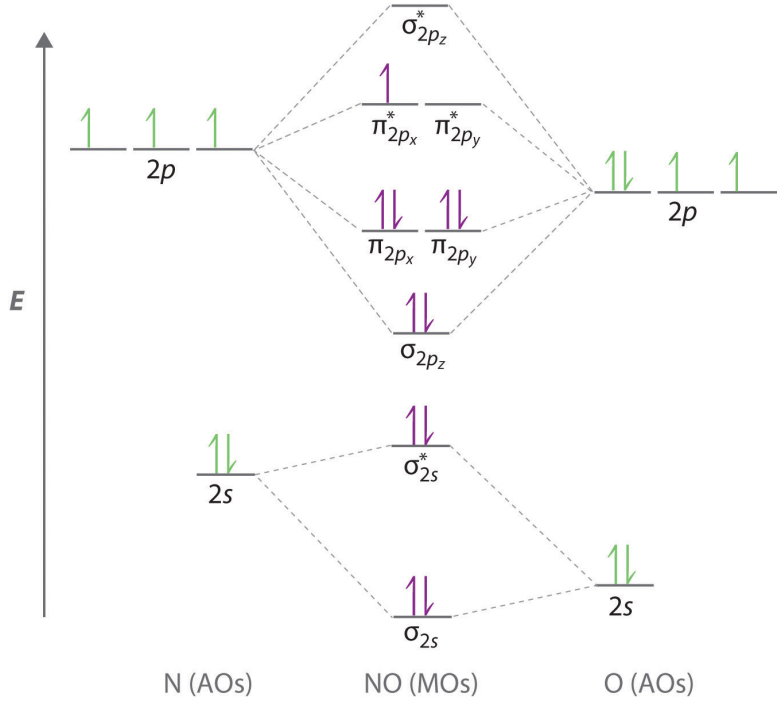

Figure 2.15: Molecular Orbital (MO) diagram of free Nitric oxide (NO) molecule.

The presence of the unpaired electron in its $2\pi^*$ orbital means that NO can either donate its $2\pi^*$ electron to the surface on adsorption, or it can accept an electron from the surface into the half-filled $2\pi^*$ orbital.

NO as a ligand displays a variety of coordination modes in metal complexes as demonstrated in the Fig. 2.16.

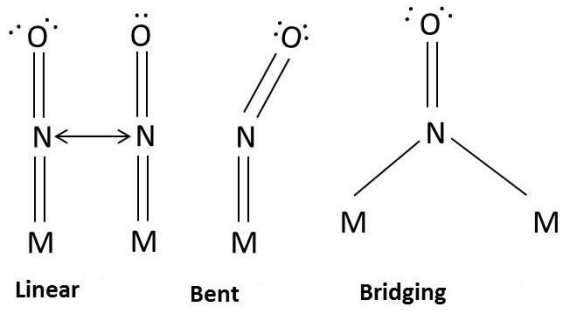

Figure 2.16: Nitric oxide display a wide variety of coordination geometries (linear, bent, bridging).

NO dissociates easier than nitrogen or carbon monoxide, hence the possibility of finding a variety of adsorbates on metal surfaces under the different conditions of pressure and temperature, including NO, N, O, N_2O, $(NO)_2$ and NO_2. These species come about as a result of molecular adsorbate, or dissociative adsorption and recombination of adsorbed species.[40]

2.3.1 Electronic Structure

The dual nature of NO of being an acceptor or donor of an electron makes the electronic structure of the molecule on metal surfaces more complicated than the more widely studied CO. Gados *et al.* adopted the Blyholder model for the electronic structure of CO bonded to metal surfaces;[41] according to this model, NO interaction with a transition metal surface involves the donation from the NO 5σ orbital to the metal substrate, and a back donation from the metal substrate to the NO $2\pi^*$ orbital see Fig. 2.17.

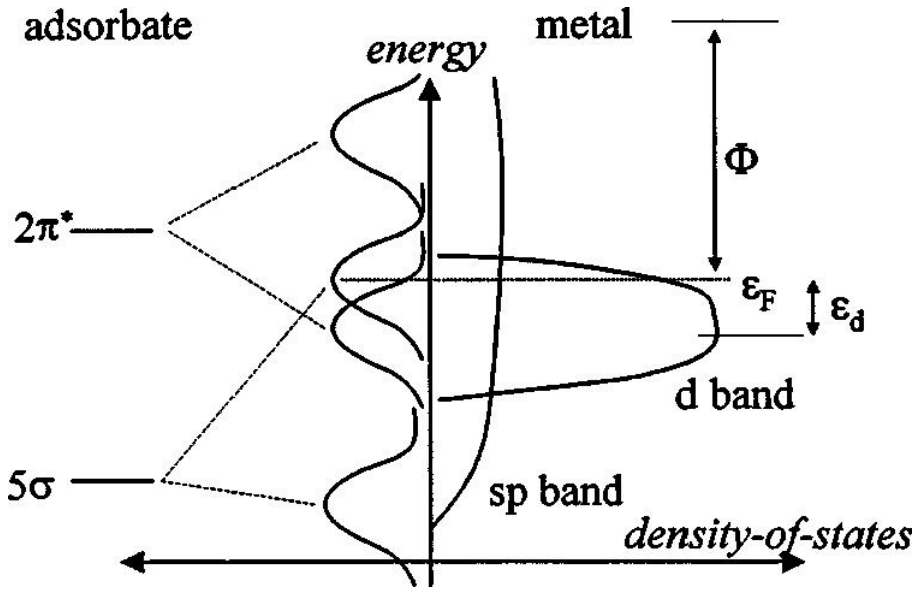

Figure 2.17: An energy diagram of NO on a transition metal substrate based on the Blyholder model.[41]

Both of the NO 5σ and $2\pi^*$ orbitals split up into bonding and antibonding orbitals due to their interaction with the localized d-band states of the substrate.

2.3.2 The Importance of Gold in Catalysis

Little attention has been paid for a long time on using gold in catalysis, which is in contrast to the platinum metal group. This was mainly due to its filled d-band, associated with low activity.[42] The reason behind this inactivity was later realised to be due to the fact that the methods used for the preparation of supported gold catalysts did not always produce nano-size gold particles which proved to be essential for its catalytic activity.[43] Gold-based catalysts found applications in a variety of reactions as can be seen from Table 2.2.

Table 2.2: Use of gold-based catalysts for a variety of reactions.

Type of reaction	**Reactant**	**Temperature** (K)	**Support**	**Ref**
Complete oxidation	CO	200-400	$Be(OH)_2$, $Mg(OH)_2$	[44]
	HCHO	300-450	TiO_2	[45]
	CH_3OH	300-450	TiO_2	[45]
	CH_4,C_3H_8	450-650	Co_3O_4	[46]
Selective oxidation	C_3H_6 + H_2 +O_2	300-500	TiO_2,Ti-SiO2	[47]
	C_3H_8 +O_2 +H_2	300-400	TiO_2(anatase)	[47]
	C_4H_{10} +O_2 + H_2	300-450	TiO2(anatase)	[47]
	glycols	room temp	activated carbon	[48]
Selective hydrogenation	CH = CH	400-500	Al_2O_3	[49]
	CH = CH – CH = CH_2	400-500	Al_2O_3, SiO_2	[50]
	crotonaldehyde	500-550	ZnO	[51]

The number of publications in which Au has been used have witnessed an exponential increase in the last two decades as demonstrated in Fig 2.18.[52–54]

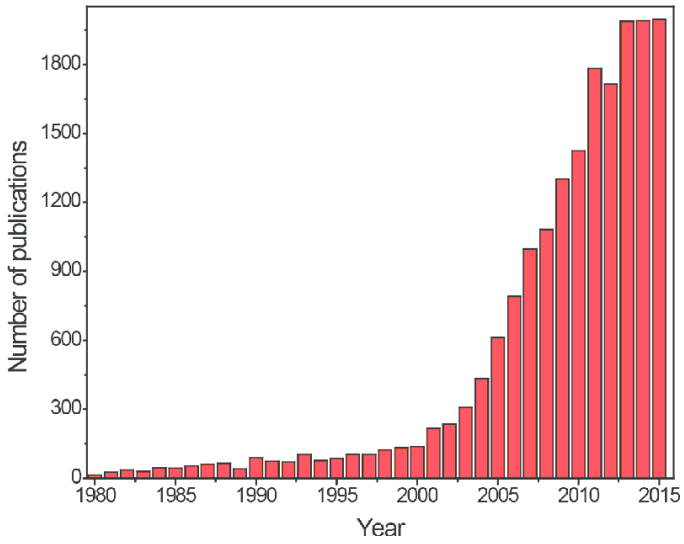

Figure 2.18: Number of Publication on gold catalysis from 1900 to 2016.[55, 56]

2.3.2.1 Carbon Monoxide Oxidation

Huruta and coworkers demonstrated the high activity of gold nanoparticles deposited on a support in the oxidation of carbon monoxide below room temperature. The activity was suggested to be due to the presence of low coordinated gold atoms on corners and edges.[57] This discovery trigged much of research focusing on the oxidation of carbon monoxide on gold supported catalysts.[58, 59] Research in this field, as the majority of publications indicate, deals with the preparation and characterisation of gold supported catalysts,[60] testing these catalysts in various catalytic reactions,[61, 62] role of support and additive,[63–66] elucidation of the nature of the active site,[42, 67–70] and reaction mechanisms.[42, 59, 71, 72] employed the deposition-precipitation method for preparing a series of Au/ TiO_2 catalysts with varying particle sizes through changing pH of the aqueous solution of the gold precursor $HAuCl_4$.[73] Catalysts with high dispersion of gold exhibited a significant enhancement in the catalytic activity for CO oxidation at sub-ambient temperatures. This was attributed to the enhancement of oxygen adsorption at the interface between the metal and the titania support. This seems to be somehow related with the findings of Mirsuhara *et al.* who reported that O_2 adsorbs dissociatively on $TiO_2(111)$, giving an O-rich surface that reacted with CO to yield CO_2. [74] It was postulated that electronic charge transfer from the gold

nano-clusters to the O-rich $TiO_2(110)$ is responsible for the observed enhancement of the catalytic activity in CO oxidation.

There is ample evidence that CO and O_2 can be adsorbed on nano-size gold particles, hence, three different mechanisms have been proposed for the oxidation of CO over gold supported catalysts:

1. The Langmuir-Hinshelwood mechanism in which both CO and O_2 are adsorbed onto the surface and subsequently react.[75]

2. Eley-Rideal mechanism where only one of these molecules are adsorbed onto the surface with the other interacting with it from the gas phase.[76]

3. Mars van Krevelen: For some supported gold catalysts the lattice oxygen of the support reacts with the adsorbed CO and this is replenished by the oxygen in the gaseous stream.[64, 77]

2.3.2.2 Nitric Oxide Reduction over Supported Gold Catalysts

Exhaust gases such as H_2, CO and incompletely burnt hydrocarbons (HCs) are capable of reducing NO. The reactivity of NO with these reducing gases over supported gold catalysts was the focus of a review by Ueda and Haruta with the prospects of using such catalysts to reduce air pollution caused by these harmful gas emissions.[78] Galavango and Parravano investigated the reduction of NO by hydrogen over gold supported catalysts including Au/MgO, Au/Al_2O_3 and Au/SiO_2.[79] A marked difference in the selectivity towards the formation of N_2 was observed over these catalysts. The overall reactions taking place were:

$$2\,NO + 2\,H_2 \longrightarrow 2\,H_2O + N_2 \tag{2.10}$$

$$2\,NO + 5\,H_2 \longrightarrow 2\,H_2O + 2\,NH_3 \tag{2.11}$$

A light selectivity for N_2 production was observed on Au/MgO and Au/Al_2O_3, while on Au/SiO_2, NH_3 is the main reaction product. The authors attributed that major difference in selectivity to an increased electron density on the Au site which in turn increases the electron back donation from the gold site to the adsorbed NO, hence weakening the N-O bond, thereby facilitating its rupture in the case of Au/MgO and Au/Al_2O_3. However, an associative adsorption of NO was proposed on Au/SiO_2 and

its eventual hydrogenation to form NH_3. Modification of the electronic properties of the Au active site by the support has been suggested for the observed difference in the selectivity of gold supported catalysts , which seems to in agreement with Extended X-Ray Absorption Fine Structure (EXAFS) data collected on Au/MgO which indicated highly dispersed gold particles and the simultaneous presence of Au^{+1} and Au(0) species.[80] Gold based catalysts have proven to be more efficient for the reduction of NO by CO compared with those based on the platinum group metals conventionally used in the TWCs. Significant activities were observed even at room temperature with complete conversion of NO to nitrogen at around 150°C. Reduction of NO by CO was studied by Iliva *et al.* over gold supported on CeO_2 and CeO_2-Al_2O_3. The catalysts were found to exhibit 100% selectivity for the formation of nitrogen at 200°C with a remarkable high and stable activity.[81] For the same catalysts, N_2O was formed and above 250°C formation of ammonia was detected. Alumina played a major role in preventing the sintering of both the gold and ceria nano-particles in Au/CeO_2-Al_2O_3.[82] Ueda *et al.* reported the reduction of NO with propene over a series of highly dispersed supported gold catalysts in the presence of oxygen and water vapour.[61] The Au/Al_2O_3 catalyst achieved the highest conversion to nitrogen of nearly 70% at 427°C. Based on the fact that NO_2 reacted with propene at lower temperature, the authors suggested that NO reduction proceeds via oxidation of NO to NO_2 followed by reaction of NO_2 with propene. Catalytic activity of Au/Al_2O_3 was improved by mixing it mechanically with Mn_2O_3, known to oxidize NO to NO_2. The mixture exhibited good activity for the reduction of NO with several HCs including methane, ethane, ethene, propane and propene, in the presence of oxygen and water vapour in a temperature range of 250°C– 500°C.[83] A major problem with supported gold catalysts in the selective catalytic reduction with hydrocarbons is that its maximum efficiency is reached above 300°C.[84–86] Since the most economical way in the elimination of NOx is to reduce to nitrogen by using CO or H_2 or HC in the exhaust gas under the operating conditions of the engine, a lot of research has gone into improving the performance of supported gold nanoparticles.[87]

2.3.3 Nitric Oxide Interaction with Gold Surfaces

The interaction of NO with gold surfaces has been studied with the aim of gaining more insight into the adsorption behavior and mechanism of NO reduction on gold nano particles (GNPs) supported catalysts. A variety of experimental and theoretical methods have been used towards this end. The studies focused on defining the type of adsorption being associative or dissociative under different conditions of pressure and temperature, nature of active sites and its activities, binding geometries and configuration of the adsorbed NO, binding energies and the relevant intermediates in the NO reduction. Hussein *et al.* employed Density Functional Theory (DFT) method to investigate the adsorption of NO and CO adsorption on low indexed gold surfaces Au(100), Au(110) and Au(111) together with stepped surfaces Au(310) and on adatoms on Au(100).[88] Both adsorption energies and vibration frequencies were calculated. The results indicated clearly that the low coordinated gold atoms have high activity towards adsorption of NO, hence supporting the general view assumption that steps, defects and kinks are responsible for the catalytic activity of gold catalysts. The findings of this study seem to agree with those obtained by Wang *et al.* who studied the activities of cationic, anionic and neutral Au(100), Au(111) and Au(310) besides an Au adatom on Au(111) surfaces for NO adsorption.[89] The authors observed that the increase in the activity of gold was accompanied by a decrease in the coordination number of gold atoms on the surface. Cationic surfaces were found to be more active than the anionic and neutral surfaces. It was concluded that the presence of low coordinated gold surface atoms together with a high concentration of positive charges on the surface are essential requirement for the good activity.

On the Au(111) surface, each gold surface atom has 9 nearest neighbours, i.e. a coordination number of 9. This is the highest coordination number of all types of gold single crystal surfaces.[90] No adsorption of NO on Au(111) was observed by Bartram *et al.* under UHV conditions even at temperatures as low as 95 K.[91] Adsorption of NO and its reaction on clean and oxygen precovered Au(111) surface was studied by DFT. The clean Au(111) surface was found to be inert, and NO adsorbs very weakly on the surface bound to an on-top surface site with tilted geometry. In contrast, the oxygen pre-covered surface was found to be very active for NO where NO reacted with the O_{ad} species to form NO_2. The activation energy for this reaction was dependent on the

oxygen surface coverage. Torres *et al.* performed DFT calculations to investigate the reaction between nitric oxide and atomic oxygen on Au(111) at low temperature to form NO_2.[92] The authors reported very low adsorption energies of 19 and 39 kJ mol^{-1} at fcc and defect sites, respectively. Enhancement of adsorption on pre-adsorbed oxygen atoms on gold surfaces seems not to be confined to NO adsorption. In a recent theoretical study on the adsorption of crotonaldehyde on gold nanoclusters, it was reported that the presence of oxygen enhanced the crotonaldehyde adsorption relative to the bare gold clusters and that enhancement was oxygen coverage dependent.[93]
On Au(100) surface the Au surface atom has a coordination number of 8. The Au(100) is known to reconstruct in a similar manner to the other late 5d metals such as Pt and Ir. The more open bulk terminated unreconstructed phase form have different adsorptive properties than the reconstructed form.[94] Rienks *et al.* investigated the effect of exposing reconstructed a Au(100) single crystal to NO, CO and O_2 over a small temperature range. Phase transition to the unreconstructed (the more open, bulk terminated) form of the Au(100) surface was observed by scanning transmission electron microscopy (STEM) upon exposure to 5 x 10^{-6} mbar of NO at a temperature of 170 K for several minutes. It was concluded that a low temperature was essential to ensure a sufficiently high NO coverage and relatively strong chemical adsorption to induce a phase transition from the hex surface to the more open bulk terminated surface. TPD was performed to determine the strength of NO chemisorption on the bulk terminated Au(100). Using the highest temperature maximum (217 K) in the desorption spectrum after saturation at (170 K), the NO chemisorption energy was calculated to be ∼57 kJ mol^{-1}, indicating a rather weak interaction to affect the dissociation of NO molecule on this surface. This is further hampered by the enthalpy change associated with the dissociation step $NO_{ad} \rightarrow N_{ad} + O_{ad}$ (endothermic reaction).
The Au(310) surface is composed of (100) terraces and (110) steps. The terraces atoms have a coordination numbers of 8 and 9, whereas the steps have 6 coordinated atoms. NO adsorbs on Au (310) preferably on a single Au atom adsorption site at the step with an adsorption energy of 0.71 eV (68.4 kJ mol^{-1}), while the second energetically favorable adsorption site is the (100) bridge site at the step with an adsorption energy of 0.65 eV (62.6 kJ mol^{-1}). Vinod *et al.* using X-ray photoelectron spectroscopy (XPS)

and TPD techniques reported that NO and N_2O adsorbs on the Au(310) surface.[95] In contrast to other Au surfaces, NO was found to decompose on Au(310) surfaces at temperatures as low as 80 K with the formation of N_2O_{ads} and O_{ads} on the surface. Bukhtiyariv *et al.* employed XPS to investigate the decomposition of NO on flat Au(111) and stepped Au(310) and (533) surfaces at elevated NO pressures up to 7 Pa and temperature range between 300 and 500 K. NO was found not to chemisorb on Au(111), however, dissociation of NO was observed on both Au(310) and (533) surfaces. The authors concluded that Au step-sites are responsible for adsorption and dissociation of NO.[96] The study revealed that while NO dissociation on Au(310) exclusively forms N_{ads} on the surface whose coverage decreases with increasing surface temperature, NO dissociation on Au(533) initially forms N_2O_{ads} on the surface that is replaced by more stable Nads at increasing NO exposure and/or surface temperature. Fajin *et al.* used DFT to conclude that the presence of hydrogen was necessary for the dissociation of NO on the stepped Au(321) surface. The authors found that the hydrogen adatoms on the surface reacts with NO giving way to a series of alternative path ways for the dissociation of the N-O bond with lower activation barriers.[97] This seems to be in agreement with studies carried out on gold supported catalysts where it was found that the reduction of NO commenced at moderate temperatures only in the presence of hydrogen gas. A common theme amongst many of these studies is the importance of low coordinated Au atoms acting as active sites for adsorption.[76, 98, 99]

Wu *et al.* investigated the low-temperature adsorption and decomposition of NO on low-coordinated Au(997) and Au(110)-1x2 surfaces employing Thermal desorption spectroscopy (TDS) and XPS measurements as well as DFT calculations.[100] Although the lowest coordinated Au atoms on both surfaces are 7-coordinated, their surface chemistry towards NO adsorption and decomposition was found to be different. On both surfaces, $(NO)_2$ dimer species and not NO_{ads} were found to be the active surface species for the NO decomposition into O adatoms and N_2O. However, different types of $(NO)_2$ dimers were found to form depending on the Au surface structure. $(NO)_2$ dimer species adsorbed on the 7-coordinated ridge Au atoms on both surfaces decompose into O adatoms and N_2O upon heating. This type of dimer dominates on Au(997).

Chapter 3

Experimental Techniques

In probing molecular reaction mechanisms, whether in the gas-phase or reactions at surfaces, it is rather essential to be able to monitor the progress and every step that takes the reactants to products. This probing is rather difficult, mainly because of the fast timescales of these elementary steps, in case of which bond breaking and forming reaction is in the range of femtoseconds.[101] An alternative strategy is to study the energy partitioning in the products after the reaction has taken place, this is often done typically using nano-second lasers. In both cases, a high resolution (temporal or spectral) is essential requirement. Many fundamental questions and issues arise when dealing with molecular reaction dynamics such as[102]

1. How do the initial conditions of the reacting molecules impact the outcome of a chemical reaction?

2. How is the excess of the initial imparted energy in the reacting molecules partitioned among internal degrees of freedom or quantum states of the products?

3. The evolution of the system from reactants to products.

These fundamental issues pose serious challenges to the experimental studies which aim to study the kinetics of chemical reactions by using powerful, high-resolution lasers. However, the development has made it possible to monitor individual elementary reactions as they occur as well as to probe internal energies of the chemical species including the electronic, vibration and rotational energies and the partitioning of the energy imparted in the product molecule(s).[103, 104] Defining the initial conditions of

molecules in terms of velocity and internal energies is important in order to compare with that of the product(s) if any energy balance is needed to be carried forward. Many methods and measurement techniques have been adopted to address the questions and issues in molecular reaction dynamics. Spectroscopic probes used in the study of reaction dynamics have to meet some stringent requirements including:

1. High sensitivity: in particular where molecular beams are involved, as the densities are low and product concentrations even lower.

2. Specificity: the technique must have the ability to isolate signals from chemical species of interest.

3. Quantum state resolution of the chemical species in the reaction medium since these carry the finger prints of the elementary steps that produced the product.

4. High time resolution in the range of nanosecond to femtoseconds as most of the dynamic processes occur within these short times, otherwise one loses to track the flow of the excess energy of a reaction into the specific internal degrees of freedom.

The methods and spectroscopic techniques applied in this study will be discussed in the following sections.

3.1 Techniques

A combination of various experimental and theoretical techniques have been applied in this study. A brief description of the main experimental techniques will be presented here.

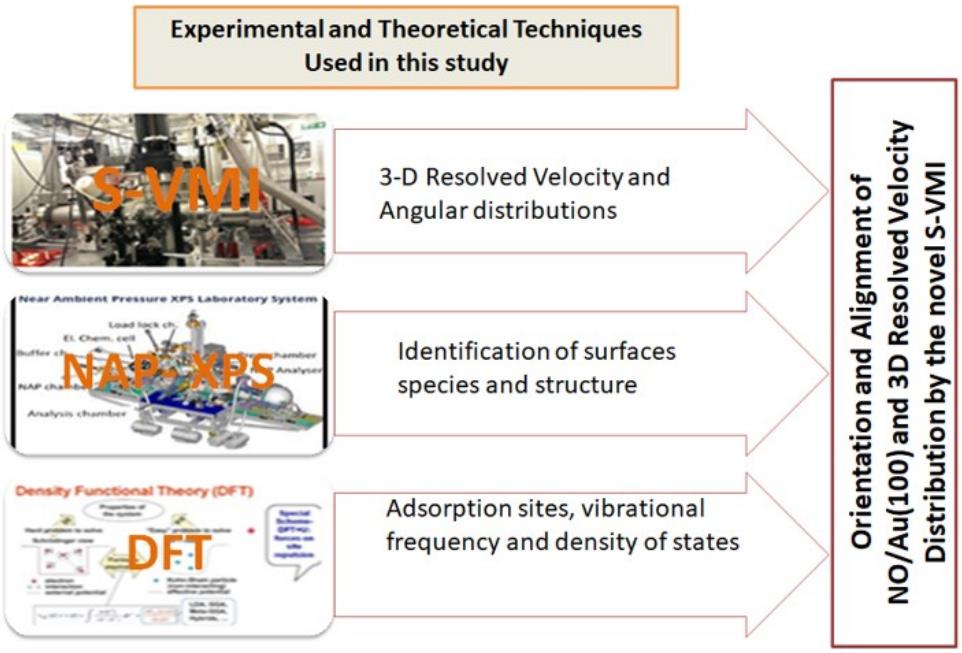

Figure 3.1: The main three techniques used in this study: 3D Surface Velocity Map Imaging (S-VMI), Near-ambient pressure X-ray photo-electron spectroscopy (NAP-XPS) and the Density Functional Theory (DFT).

3.1.1 Pump-Probe Spectroscopy

Pump-probe spectroscopy is an important technique that has been widely used since demonstrated by Porter and Norrish in the 1960. [105, 106] The principle of pump-probe experiments is simple (shown in Fig. 3.2).

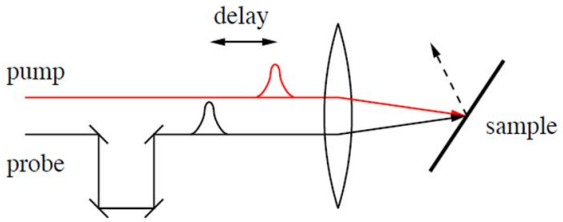

Figure 3.2: Sketch of the pump-probe principle of two lasers. One is used as the pump beam, which excites the sample. Another beam is used to probe the change.

The sample under investigation is excited or perturbed by interaction with the pump which is often a short laser pulse nowadays. The probe is timed to arrive at the sample after a known delay from the pump in order to probe the change that has occurred as a result of the interaction of the pump laser's action. The pump should be more intense than the probe, because it produces the changes in molecules, whereas the probe merely interrogates them.
Time-resolved spectroscopic systems have been able to achieve a time delay control in the range of femtoseconds.[106]

In this study here, the pump and probe were two nanosecond lasers, the first "pump" laser is used to initiate the reaction, i.e. desorption of the adsorbed chemical species through bond rupturing, and the second 'probe' laser pulse time-delayed from the first one, is used to detect and characterise the products. The delay time is chosen to prevent thermal equilibration of the system as this results in the loss of information of the rotational and vibrational energy distributions of the nascent product molecule.

3.1.2 Laser Spectroscopic Detection

Out of the many laser spectroscopic, two techniques are widely used to detect products in specific quantum states; Laser Induced Florescence (LIF) and Resonant Enhanced Multiphoton Ionisation (REMPI). Both techniques have advantages and disadvantages but quantum state detection can be achieved with either one.[107] Here, only REMPI will be explained as it is the one applied in this study.

3.1.2.1 Resonance Enhanced Multi-Photon Ionization Spectroscopy

Resonance enhanced multi-photon ionisation is a spectroscopic technique that is characterised by high sensitivity and selectivity. Ionisation of most atoms or molecules cannot be achieved by the absorption of one photon only using typical table-top light sources since that photon energy would have to be in regions of the electromagnetic spectrum (deep UV, soft X-rays), which are difficult to obtain in standard laboratories. Hence, one can choose to use more than one photon simultaneously. The term of multi-photon ionisation (MPI) comes about simply because more than one photon is used to ionise the species under investigation. In MPI experiments (Fig. 3.3), the first photon excites the atom or molecule to a "virtual state", i.e. to an imaginary

energy level, which is not a solution of Schrodinger equation or a real energy level. A second photon (or third) might take the system either to a virtual or a real energy level intermediate state before one last photon will ionise the excited state. The ionization efficiency of the chemical species will be much greater if the intermediate state reached by absorption of one or more photon corresponds to a real energy level. In this case, we will have what is termed as resonance-enhanced multi-photon ionisation (REMPI).[107] The process is resonantly enhanced when the energy of n photons nhυ (typically $n = 1$ to 4), where υ is the laser frequency, is resonant with that of an electronically excited state. The molecule is further ionized by absorbing m photons and the total process is often referred as an $(n + m)$ photon ionization. This can be achieved experimentally by the use of tunable dye lasers. Labelling the REMPI scheme is linked to the number of photons needed to reach the resonant state and the number of photons needed to achieve ionisation from the resonant state. Thus a (1+1) REMPI abbreviation is used to describe a REMPI process in which one photon is absorbed to take the molecule of interest from its ground state to an intermediate resonant state, and the second photon to ionise the molecule from this state (Fig. 3.3). The excess energy is distributed between the kinetic energy of the ejected electron and the ion.

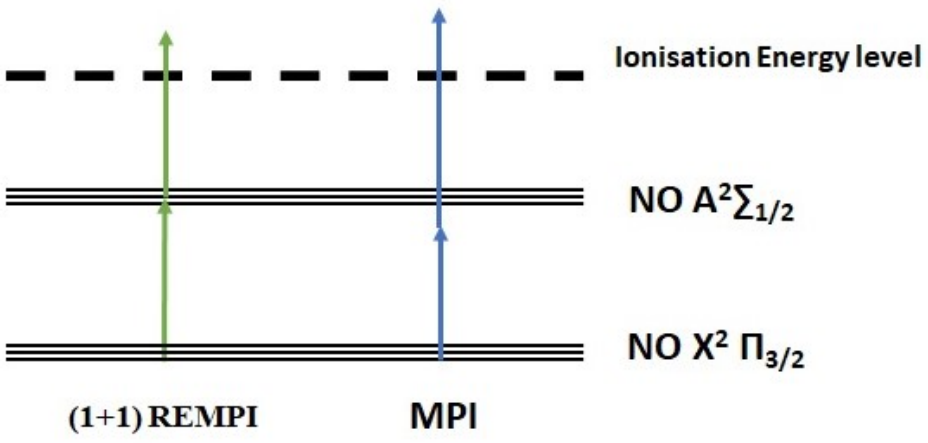

Figure 3.3: Comparison of (1+1) REMPI scheme and MPI for the electronic ground state NO. The horizontal lines present vibrational states. Note that REMPI is a state selective method, while the MPI is not.

Additionally, different wavelengths can be used for each stage (two colour REMPI) yielding schemes such as $1 + \acute{1}$, $2 + \acute{1}$ etc. By selecting specific excitation wavelengths (laser tuning), it is possible to excite intermediate energy levels that are characteristic for a particular molecule, hence one is able to ionise a specific quantum state of the molecule investigated. By scanning the laser wavelength, REMPI absorption spectra can be recorded from which the quantum state distribution can be determined.
A REMPI spectrum displays the parent ion signal as a function of laser wavelength from which information about the rotational and vibrational distributions of the nascent product can be obtained. REMPI spectroscopy is a widely used technique as it can be employed to a wide range of molecules. REMPI is frequently combined with time-of-flight mass spectrometry (TOF) or velocity-map imaging (VMI),both of which will be discussed below.

3.1.2.2 State - resolved detection of NO via (1+1) REMPI

Spectroscopy of NO.
To understand REMPI spectroscopy of NO molecules, one needs to understand the quantum states of nitric oxide. The electronic structure of diatomic molecules and their energies can be found in the book by Herzberg. [108] The electronic state of a molecule is noted by $\Lambda_{(2S+1)_\Omega}$, with S the electronic spin, Λ the electronic orbital and Ω the angular momentum quantum number, resulting in the spin-orbit coupling. The coupling of the angular momenta is taken into consideration when an unpaired electronic spin and non-zero orbital momentum are present. The rotational structure's order and spacing are determined by the interaction between the nuclear angular momentum R and the electronic motion of angular momentum L and spin S as well as their coupling to the inter-nuclear axis. Hund formulated 1926 a system of five cases called Hund's cases (a to e). [109] These cover the possible combinations of couplings between these components. Most molecules can be well described by one of these Hund's cases. This work will focus on Hund's case (a) and (b) because they work best to describe the properties of NO in its lower electronic states. Figure 3.4 left side shows the diagram for Hund's case (a). In this case both the electronic orbital angular momentum L and the total electronic spin S are strongly coupled to the inter-nuclear axis and very weakly coupled to the nuclear angular momentum R which results in

a precession around the molecular bond. L interacts strongly with the axial field of the molecule and hence precesses about the molecular axis, so that its projection into the molecular axis is constant. Similarly, S precesses with constant projection Σ, so that the total angular momentum along the molecular axis is $\Omega = \lambda + \Sigma$ with λ and Σ the projection of L and S into the molecular axis respectively. Ω takes on the values $\Omega = \lambda + \Sigma, \Lambda + \Sigma, \Lambda$ - Σ, where $\Sigma = S, S$ - 1,..., - S. $\lambda + \Sigma$ takes adds vectorially to the orbital angular momentum due to nuclear motion R to form the total angular momentum J. In Hund's case (b) Figure 3.4 right side, the electronic orbital angular momentum L is strongly coupled to the internuclear axis but the spin S is not. Typically, this occurs when electronic motion is zero and there is no inner-molecular magnetic field. In consequence the spin is not coupled to the inner-nuclear axis. It is still well defined but Σ is not and neither is Λ. Therefore J cannot be constructed from the nuclear rotation R and Ω. Instead, the total angular momentum vector without spin K is generated by adding R to Λ. Thus, J and S are always both integral or half-integral depending on whether the number of electrons is even or odd.

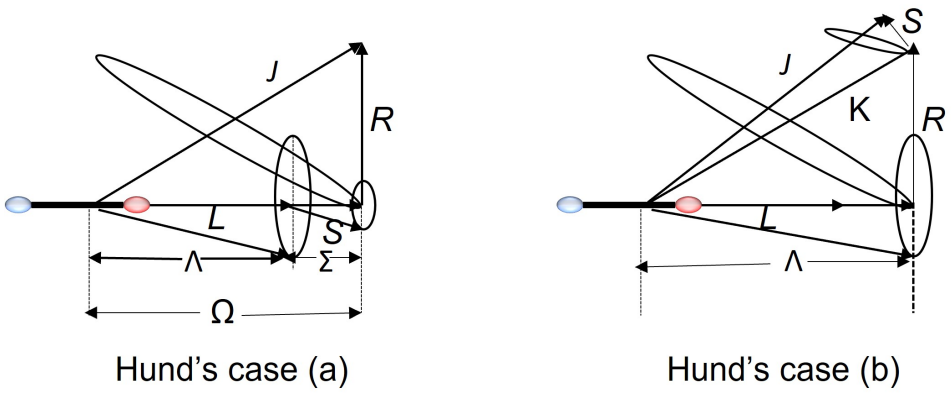

Figure 3.4: a) In Hund's case (a) the coupling of L and S to the internuclear axis is very strong while the coupling between the nuclear rotation R and the electronic motion is negligible. As a result its components along the inter-nuclear axis Λ and Σ are constant and well defined. L and S combine with the nuclear angular momentum R to the total angular momentum of the molecule J with it inter-nuclear axis component. b) In Hund's case (b) S is no longer coupled or bound to the inter-nuclear axis. This makes Σ and Ω no longer applicable. Λ and R combine to the total angular momentum apart from spin K.[108]

The (1+1) REMPI scheme was implemented in this work for the quantum state resolved detection of photodesorbed NO (Fig.3.3). This was achieved as follows:
The first photon promotes NO from its ground state, $X^2\Pi$, to the first excited state,

$A^2\Sigma$. [110] Nitric oxide has an unpaired electron in its $2\pi^*$ orbital. Spin-orbit interaction splits the $X^2\Pi$ state into two spin levels $X^2\Pi_{1/2}$ and $X^2\Pi_{3/2}$ which are mixed by the rotation of the nuclei resulting in a partial lifting of the fourfold degeneracy of the ground state into two doubly degenerate states, F_1 and F_2.

The coupling of the angular momentum present in NO is described by Hund's case a) or b). [108]. At low J, Hund's case (a) applies: the orbital and angular momentum are coupled with the internuclear axis and for a regular $2\pi^*$ state, the lower spin state is $^2\Pi_{1/2}$ and the upper $^2\Pi_{3/2}$. In this case will have a value of $\Omega = 3/2$ or $1/2$ depending on the orientation of the spin and orbital angular momenta. Each spin orbital are further split into two symmetry adapted parity states *e* and *f*, full details can be found Ref. [111] In the high J limit, Hund's case (b) is more appropriate in the excited state $A^2\Sigma$ which also split into F_1 and F_2 components, corresponding to the e and f states. The selection rules for electronic transition such as $A^2\Sigma(\nu,R) \leftarrow X^2\Pi(\nu,J)$ are given by Hollas' book as [107]

$$\Delta J = 0, \pm 1 \tag{3.1}$$

$$\Delta S = 0 \tag{3.2}$$

$$\Delta \Lambda = 0, \pm 1 \tag{3.3}$$

The $A^2\Sigma \leftarrow X^2\Pi$ transition of NO has twelve rotational branches for each vibrational state as showes in Fig 3.5 . The individual transitions are labeled as P, Q or R depending on whether ΔJ is -1, 0 or +1. For the hund's case (a) the spin label is assigned regarding the Σ quantum number. F_1 if $\Sigma = 1/2$ and F_2 if $\Sigma = -1/2$. For Hund's case (b), Σ is undefined, so the spin label depends on the direction of the total spin S in relation to the total angular momentum of the molecule without spin R. For every two rotational states of the same R, the state with the larger J has the spin label F_1 and the one with the lower J has the spin label F_2.

In this thesis work, we characterized the internal population of NO photodesorbed from adsorbed NO from Au(100) to obtain insight into the desorption mechanism.

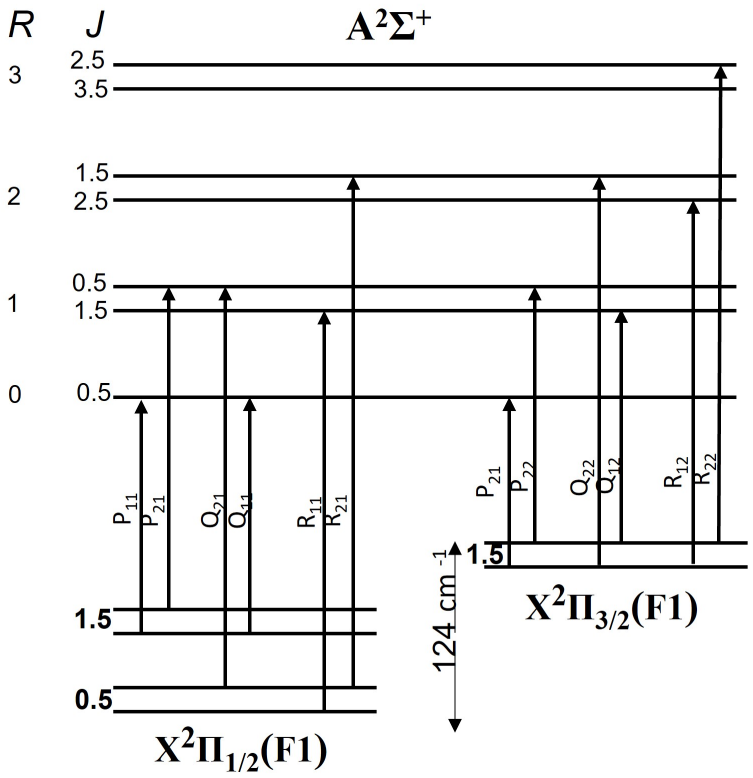

Figure 3.5: Rotational branches of the allowed transitions for a generic vibrational band of the γ band system. Adopted from Ref [111]

3.1.3 Time of Flight Mass Spectrometry

The principal of time-of-flight mass spectrometry (TOF) first published by Stephens in 1946 involves the production of ions by ionising atoms or molecules. It is followed by accelerating these ions through a fixed potential after which ions are allowed to transverse along a field free path of known length, after which they are detected.[112] The time of flight t is given by the simple eq. 3.4:

$$t = L\sqrt{\frac{m}{2VQ}} \tag{3.4}$$

Where is L the length of the drift tube in cm, V is the accelerating voltage, m is the mass of the ion, Q is the ion charge.

Different ions travelling down the time-of-flight tube at different velocities are separated according to their mass/charge ratio, hence reaching the detector at different times, with lighter ones arriving earlier than heavier ones.

Ions can be created in many different ways including:

1. Electron bombardment in which an energetic beam of electrons is allowed to collide with gaseous molecules causing them to lose electrons, hence forming positive ions.

2. Exposing the gaseous molecules to a high intensity laser beam, whereby the molecules will absorb energy and may become ionised.

Analysis of ions, flight time is useful only when they leave the ion source at the same time. This is easier to achieve when a pulsed laser is used. As a result of this, a group or packet of ions are ejected and determined by the ionizing laser pulse duration. Hence an ionizing pulse of e.g. 5 ns will yield ion packets which are initially at least 5 ns wide. The width of the ion packet is known as temporal distribution. Another parameter on which the width of ion packet depends on the position at which the ions were created or accelerated. The variation related to this position is referred to as initial spatial distribution. This variation in the velocity of the ions within the ion packets is called energy distribution.
A basic time-of-flight mass spectrometer design shown in Fig 3.6 and comprises of three different regions.

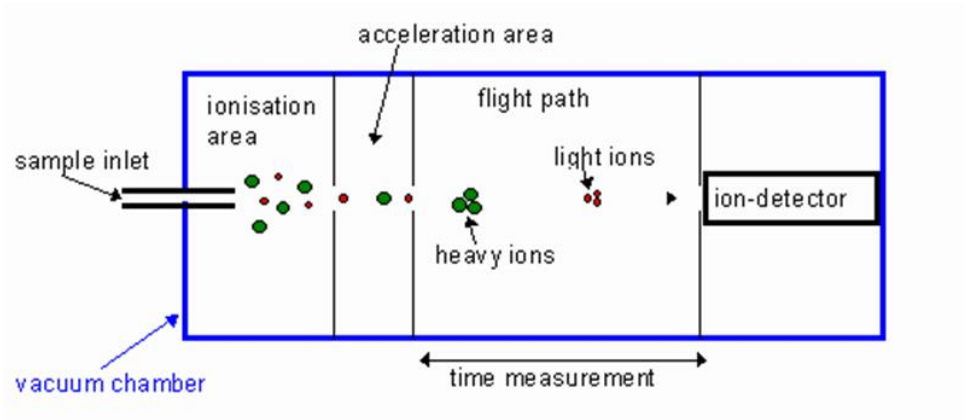

Figure 3.6: Schematic showing the different sections of a TOF spectrometer.

The ion source region, a very small and short compartment where ions are created consists of the sample to be analysed with a repeller and an extractor plates. A relatively long drift region that is field-free, which is bounded by the extraction grid and another grid positioned just before the detector. The non-magnetic TOF spectrometer have many advantages including the speed by which a whole spectrum can be obtained (microseconds or less), the ability to record the entire mass spectrum for each accelerating

pulse, hence one can still measure the relative intensities with high accuracy even if the conditions of the source vary unexpectedly. [113–115] Furthermore, a mass range of up to 500 000 Da is possible making it suitable for analysing large biomolecules. However, a main disadvantage is the limited resolution. This is because during the ionization process ions will be formed at different times (instant of ion formation) and at different locations at the time of acceleration (space) with different kinetic energies (velocities) as was explained before. These three parameters collectively limit the resolution in a TOF instrument. TOF was used here for measuring the velocity distribution of the flying NO molecules from the surface upon desorption followed by ionization in z direction as shown in Fig. 3.7

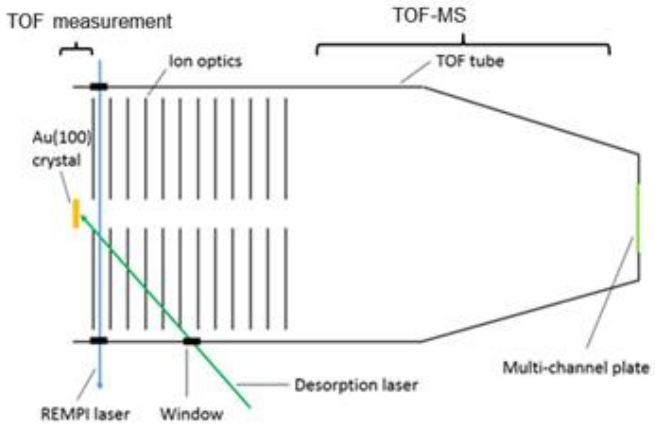

Figure 3.7: Diagram showing two different sections of a TOF spectrometer. First, TOF measurement which were used for the Velocity distribution measurements. Second, a TOF-MS which directed the flying NO to be detected.

3.1.4 Molecular Beam

A molecular Beam is a beam of atoms or molecules that are formed when a gas at a higher pressure is allowed to expand through a small orifice into a chamber at a lower pressure. These particles are then travelling at roughly the same velocities (speed and direction) but with very few collisions.

Molecular beams can steer in into the surface, at a certain angle relative to the surface. A Molecular Beam is characterised by parameters including beam intensity, beam kinetic energy, velocity distribution and spread.

The molecules in the beam can be excited using laser beams affecting their internal quantum state distribution. If these measurements for the molecules in the incident

beam can be carried out before impinging on the surface together with similar characteristics for the scattered beam, detailed information on the energy transfer during the chemical surface reaction can be obtained, leading to a better understanding of the dynamics of surface reactions on an atomic scale.

Two main beam sources are known, namely effusion sources and supersonic sources, each with different properties. In both cases, gas is allowed to expand from a high pressure cell into vacuum through a small orifice or hole, see Fig. 3.8.

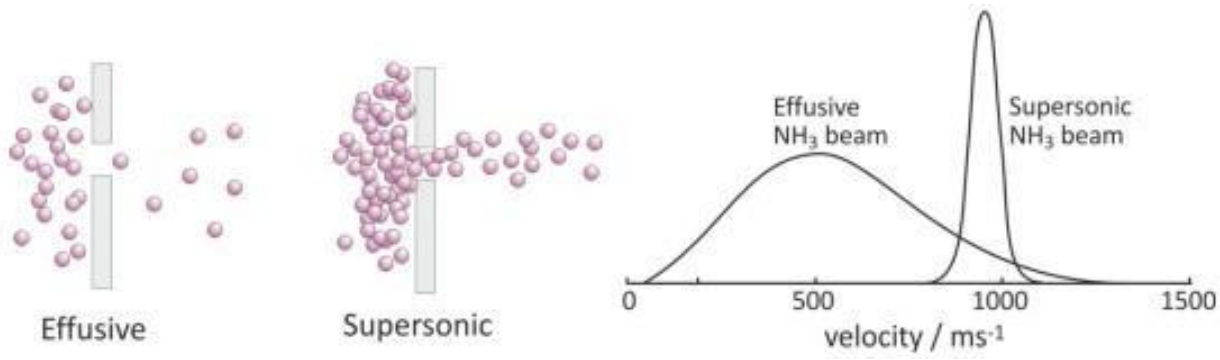

Figure 3.8: Diagrams showing effusive and supersonic molecular beams, and typical velocity distributions for ammonia beam prepared in effusion and supersonic beam cells.

In an effusion source, the diameter of the hole *(d)* is less than the mean free path (λ) of the gas. The mean free path is defined as the average distance travelled by a molecule between two successive collisions. Under these conditions, a molecule suffers no significant collisions as it leaves the cell. A collimated beam can be formed by pumping the gas through one or more orifices connected in series. The generated effusive beam have a Maxwell-Boltzmann molecular velocity distribution characteristic of the temperature of the effusion cell and a cosine angular distribution, where θ is the angle between the molecular velocity vector and the axis normal to the effusion cell wall with the orifice. The limitation imposed on the pressure in the effusion cell to satisfy the effusion condition ($\lambda > d$) results in low beam intensity typically 10^{13}-10^{15} particles cm^{-2} s^{-1}.

In a supersonic beam source, the diameter of the hole is bigger than the mean free path in the gas. In such sources, many collisions take place as the molecules exit the hole as well as in the region immediately beyond it. This source has a very narrow speed distribution, see Fig. 3.8 and narrower angular distribution about the beam

axis when compared to that of the effusion source. With proper collimation of such a beam, intensities of 10^{18}-10^{19} particles cm^{-2} s^{-1} have been achieved.

Supersonic molecular beams are very cold and velocity distributions corresponding to rotational temperatures as low as 4 K have been reported. Under these conditions, beam molecules have little internal energy with only very low rotational quantum states being occupied. Although supersonic beams offer many advantages over effusive sources, the main disadvantage is that these require very high pumping speeds in order to handle the large gas flows associated with it. This can be countered by using pulsed beams.

3.1.5 An Introduction to Velocity Map Imaging (VMI)

The first inspiration towards velocity map imaging was Photolysis mapping (PM) invented in 1967. This ion imaging technique was pioneered by Solomon, who described a method that has the ability to determine the orientation of the transition moment of photo-dissociated species in gas phase reactions.[116] A full 3-D angular distribution of the photo-fragments was recorded during the etching of the inside of a coated glass sphere using a laser.[117] The significance of photolysis mapping (PM) as introduced by Solomon was not really realised until twenty years later.

Photofragment imaging (PFI)

Photofragment imaging (PFI) was presented in 1987 by Chandler and Houston, who introduced a combination of a position sensitive detector with a Charged-Coupled Device (CCD) for the detection of photo-fragmented species.[118] The authors were able for the first time to demonstrate the ability to obtain a two dimensional image from a three dimensional spatial distribution for the produced CH_3 photofragment originating from photo-dissociation of CH_3I, using the combination mentioned earlier in their system i.e. REMPI and TOF. The technique has many advantages over ion imaging reported by Solomon, including mass specificity, higher sensitivity and spatial resolution. In their experiment, Chandler and Houston used a Nd:YAG laser beam (266 nm pump beam) to intersect a molecular beam of CH_3I seeded in He at right angle to photolyse CH_3I. The produced methyl fragment was then state selectively ionised using a tunable dye laser 10 ns after its production using a (2+1) REMPI scheme.The state-selected methyl ions were created between a repeller and an extractor region of

the electrodes. Crossing a molecular beam with a laser beam resulted in the evolution of an expanding cloud of fragments in three dimensions (spherical distribution of velocities), known as a **Newton Sphere (NS)**, the radius of which is directly proportional to the fragment's speed. The Newton sphere of the newly formed ionised fragment expanded and was allowed to fly in a field-free tube in a TOF-MS [114] towards a detector consisting of 2D micro channel plate (MCP), phosphor screen and a charged couple device (CCD) camera. When the incident ions hit the MCPs, pulses of electrons are formed which in turn hit the phosphor screen converting each hit into a flash of light which can be imaged by a CCD camera placed behind the screen for processing and analysis in a PC. The produced image is 2D projection of the complete 3D velocity distribution of the nascent reaction products. As a result of crushing the Newton spheres onto the 2D detector plane, circular images are formed. The image of the methyl fragment from CH_3I dissociation is shown in Fig. 3.9.

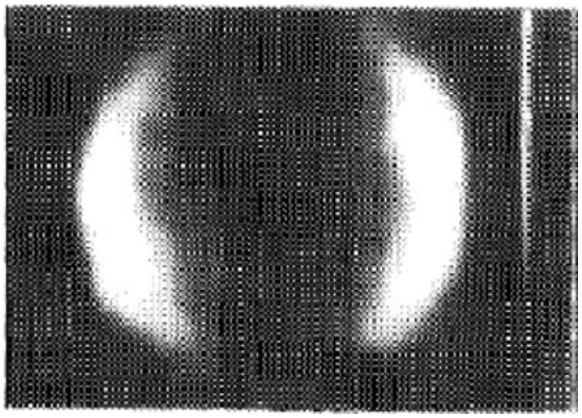

Figure 3.9: Image produced by projecting onto two dimensions the three-dimensional spatial distribution of CH_3 fragments produced from photolysis of CH_3I with 266 nm laser light.[118]

Velocity Map Imaging (VMI)

Velocity Map Imaging (VMI) was a further development in 1997 by Eppink and Parker [119] who carried out modifications and improvements of the PFI technique by the use of an electrostatic system. This modified technique has been coined as velocity map imaging (VMI) ever since and has been regarded as an excellent and indispensable technique for reaction dynamics, see Fig. 3.10.

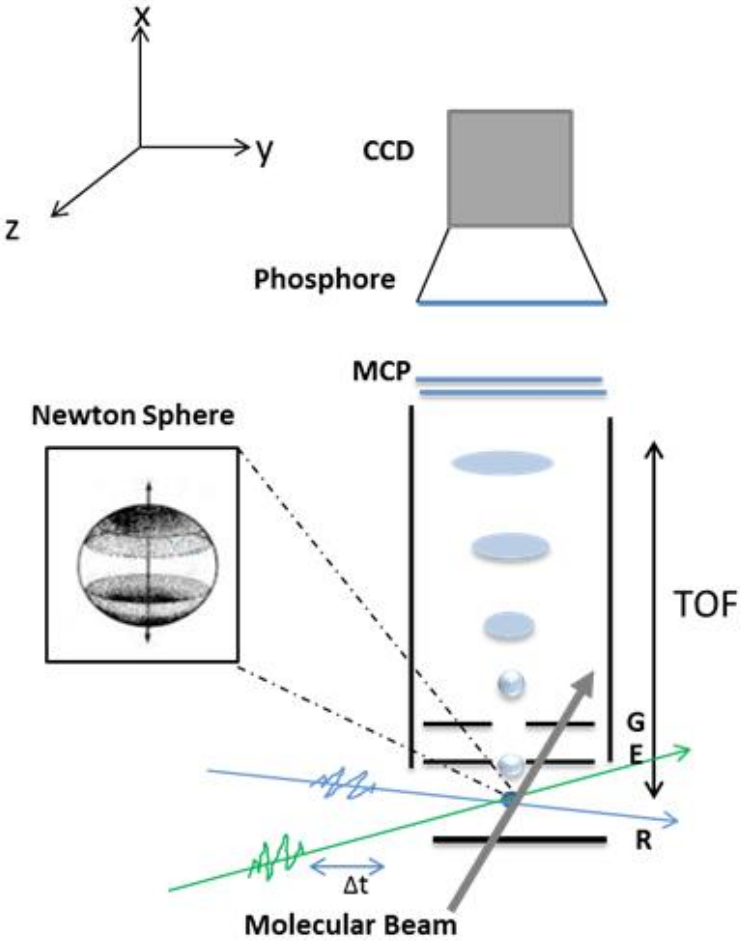

Figure 3.10: a) Schematic pump-probe VMI setup. It shows the electrode system with repeller (R), extrator (E) and ground (G) to accelerate the photo-products towards the detector which consists of a microchannel plate (MCP), a phosphor screen and a charged-coupled device CCD to image the phosphor and to send a digitised picture to the PC. Two laser pulses with a variable delay are overlapped in the molecular beam between the repeller end extractor electrodes. The time-of-flight (TOF) gives enough time to separate the fragments in mass and to stretch the Newton spheres in the yz-plane

.

The modification introduced by Eppink and Parker included the removal of the grids from the electrodes, hence removing the grid distortions in the image formed. More importantly, the new design provided an opportunity for exploiting the electrostatic lenses system in such a way that ions produced with the same initial velocity are mapped onto the same point on the detector, regardless of their initial spatial position, hence the name "velocity mapping", see Fig. 3.11.

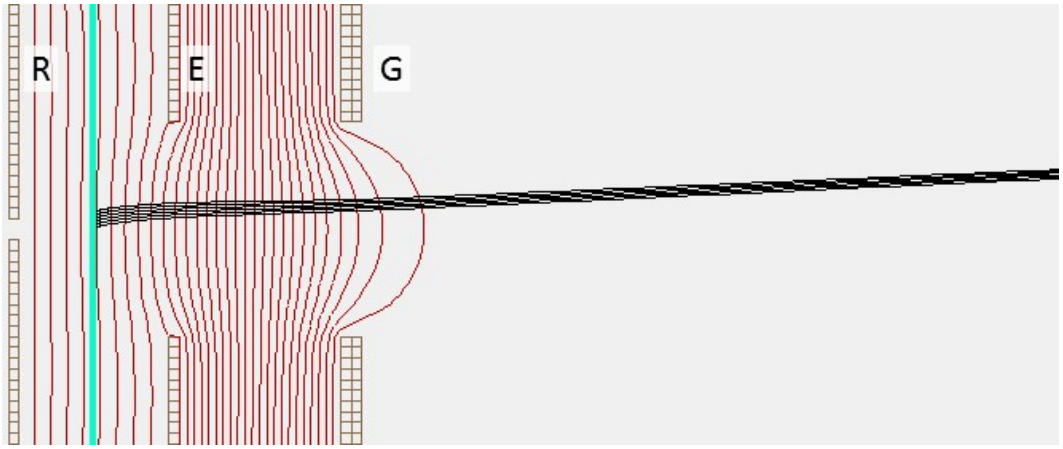

Figure 3.11: SIMION simulation of the electric fields in Eppink and Parkers VMI design. The repeller (R), extractor (E) and ground (R) electrodes are shown. Some of the representative inhomogeneous electric field contours are shown as red lines. A beam of molecules enters the ionisation region through a small aperture in the repeller plate. Ions are generated by REMPI using a laser. The subsequent trajectories of the ions are shown as black lines, showing that the ions with the same velocity are being focused onto the same spot on the detector.

An electric field is maintained within the electrostatic lens region. The established electric field has three functions to perform simultaneously:

1. Acceleration of the produced ions along the TOF flight tube to the detector. The TOF tube is potential free and the ions drift freely in this field-free region after being accelerated.

2. Mapping all the ions having the same velocity component onto the same point on the detector.

3. Compression or crushing of Newton sphere for a given ion mass into the detector resulting in the formation of a 2D circular image.

It must be noticed that the electric field applied will accelerate all ions to the same kinetic energy given by:

$$E_{Kin} = \frac{1}{2}mv^2 \tag{3.5}$$

where m is the mass of the ion and v is the velocity of the ion, since the force on these ions is the same for all the ions, and hence the kinetic energy is the same.

$$F = qE \tag{3.6}$$

where F is the force experienced by the charge at the point, and the field is E. Accordingly, ions of different masses will be flying to the detector with different velocities and hence separate in time when reaching the detector. Although VMI is analogous to time-of-flight mass spectrometry, the difference between these two techniques is that with the appropriate choice of the electric fields in the ion source compartment, ions with the same mass and initial velocity can be directed to the same position on the detector where their positions can be used to extract their velocities. In VMI experiments, the ions investigated can be mass selected. This will allow the ion of interest to reach the detector while at the same time rejecting others.

3.1.6 X-ray Photoelectron Spectroscopy

3.1.6.1 Principles of X-ray Photoelectron Spectroscopy

X-ray photoelectron spectroscopy (XPS) is a surface sensitive spectroscopic technique that has been widely used for investigating the chemical composition of surfaces of materials (and the nature of the chemical bonds that exist between the atoms on the surface).The wide use of XPS for probing surfaces of various materials lie it its operational simplicity. XPS is based on the photoelectric effect originally observed by Hertz,[120] and later explained by Einstein in 1905 using the quantum nature of light.[121] Einstein realised that when light is incident on a sample, a photon may be absorbed and causing an electron to be ejected from the material. The ejected electron is called photoelectron. It took scientists more than fifty years after Einsteins discovery to develop an analytical spectroscopic technique using the photoelectric effect. In the XPS process, a primary beam of soft X-rays, usually Mg K_α or Al K_α with photon energy of 1253.6 eV and 1486.6 eV, respectively, is allowed to interact with the specimen leading to excitation and subsequent ejection of low-energy electrons resulting

from the photo-inonization of the atoms molecules or ions of the specimen. Fig. 3.12 depicts the XPS photoelectric emission process, where an electron is ejected from a 2p orbital.

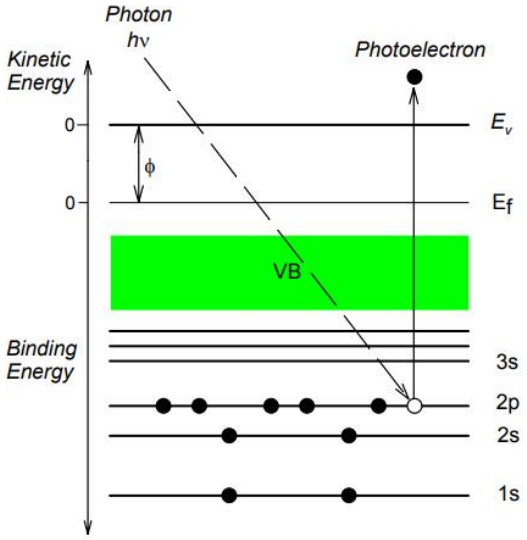

Figure 3.12: XPS Photoelectron emission process.

where: $h\upsilon$ is the energy of the incident photon beam, E_f is the Fermi level Φ is the work function of the sample, defined as the energy difference between the Fermi level and the vacuum or free energy level (E_v).

Taking advantage of the law of conservation of energy, one can relate the kinetic energy of the photoelectron to its binding energy in the solid by the following equation:

$$E_k = h\upsilon - E_b - \phi_{sample} \tag{3.7}$$

where: E_k and E_b, are the kinetic energy and binding energy of the ejected photoelectron relative to the Fermi level, ϕ_{sample} is the work function, which is the energy barrier required to remove the photoelectron from the Fermi level of the material to the vacuum level, as shown in Fig 3.12. E_b has a specific value for each element and core level from which the electron has been ejected. The binding energy depends on the atomic number of the element Z, and is related to the ionisation energy.

Fig. 3.13 shows the variation of the core level binding energies of the photoelectrons as a function of the atomic number of the element and the core level from which it is ejected. Each element produces a characteristic set of XPS peaks at characteristic binding energies values that directly identify each element that exists on the surface of the specimen being analysed.

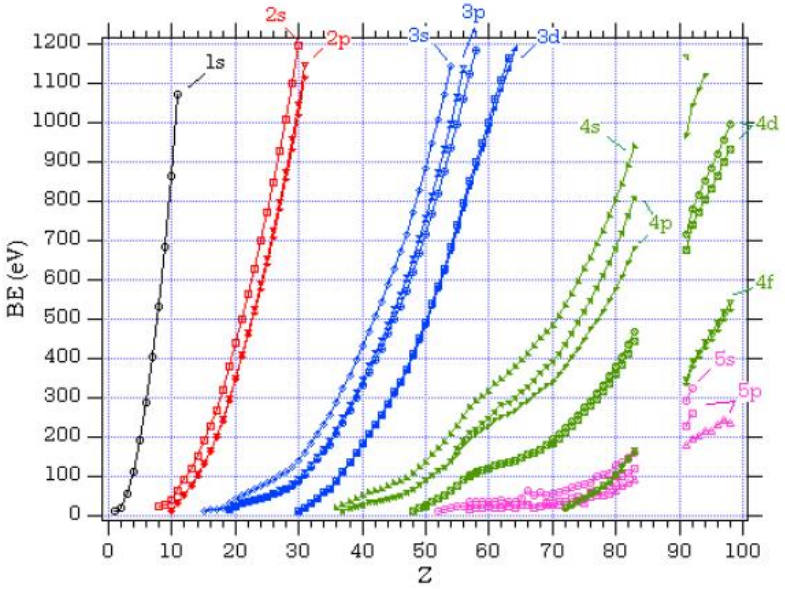

Figure 3.13: Core level binding energies of the ejected photoelectrons as a function of the atomic number of the element and the orbital from which it is ejected. [122]

An XPS spectrum is a plot of the intensities of the ejected photoelectrons against their kinetic energies or binding energies. Different orbitals give different photoelectron peaks in the spectrum. Fig 3.14 demonstrates a wide scan XPS spectrum for gold.

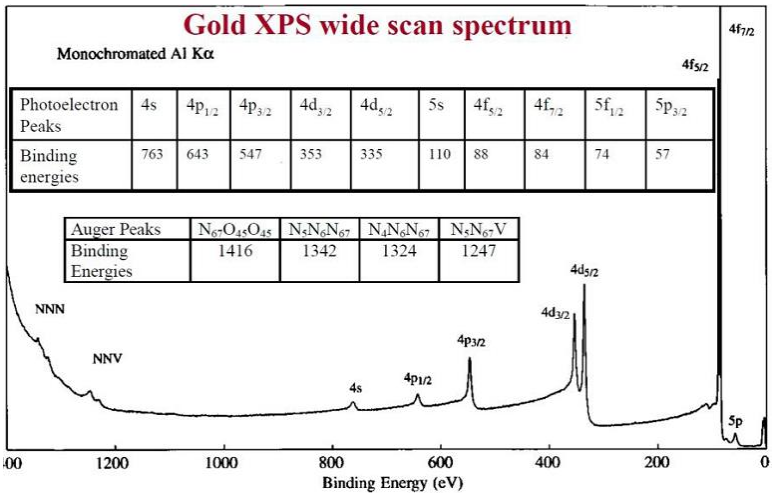

Figure 3.14: XPS wide scan spectrum for gold metal.

The extra emission peaks NNN and NNV in Fig 3.14 are Auger peaks. The core hole created by the XPS photoemission process leaves the atom in an excited state. An electron falls from a higher energy level to fill the core hole created and the energy released in the process can eject a further electron from the atom, this is called Auger electron and the process is called Auger emission. The process is depicted in Fig. 3.15 beside the photoelectron emission process in contrast to the photoelectron emission process the kinetic energy of Auger electrons is independent of the incident photon energy.

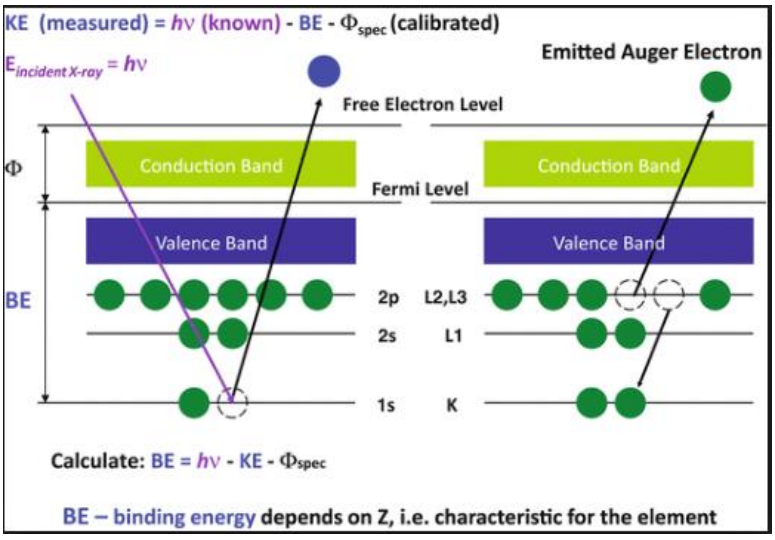

Figure 3.15: Auger emission process.[123]

Binding energies (BEs) of core electrons of an element are determined by the electrostatic interaction between the electron and the nucleus. These BEs of a particular orbital of a particular element depend on the chemical environment of the atoms of that element. Core level binding energy shifts are due to a change in the chemical bonding of the atoms of the element under investigation. Withdrawal of valence electron charge increases the binding energy of that element, while addition of valence electron charge decreases its binding energy.

Fig 3.16 is an illustration of how the binding energy of C 1s changes depending on its chemical environment, while Fig 3.17 shows how the binding energy of the Mo(0) changes as its changes to Mo^{4+} and Mo^{6+}. The higher the oxidation state of the metal, the higher is the Binding energy (BE) shift compared to the pure metal Mo(0).

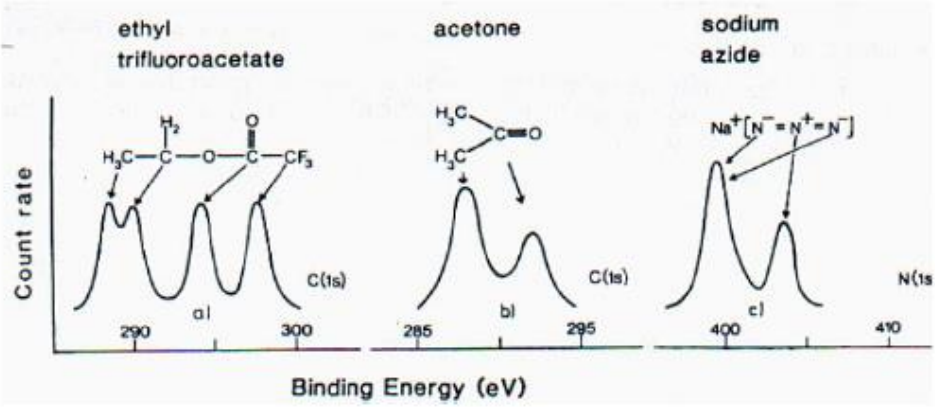

Figure 3.16: Binding energies of core levels of C 1s and N 1s in different chemical environments. [122]

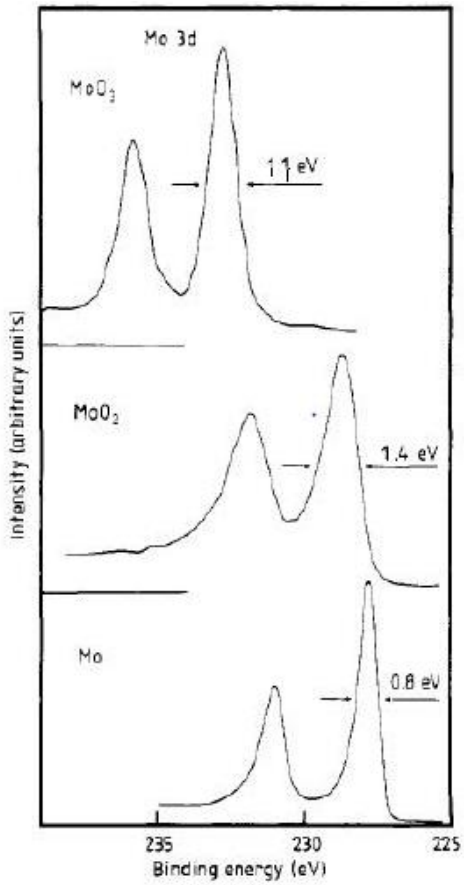

Figure 3.17: The XPS spectra of 3d core level spectra of metallic Mo, MoO_2 and MoO_3. [122]

3.1.6.2 Instrumentation

An XPS instrument system is comprises mainly of an X-ray source, a sample vacuum chamber, an electron energy analyzer and electron detector (channel electron multiplier or channel plate), see Fig. 3.18. XPS requires a monochromatic source of soft X-ray usually from an anode or from a synchrotron, and in both modern instruments cases a X-ray monochromator is used. This is essential to improve the resolution of the photoelectron peaks in the XPS spectrum.

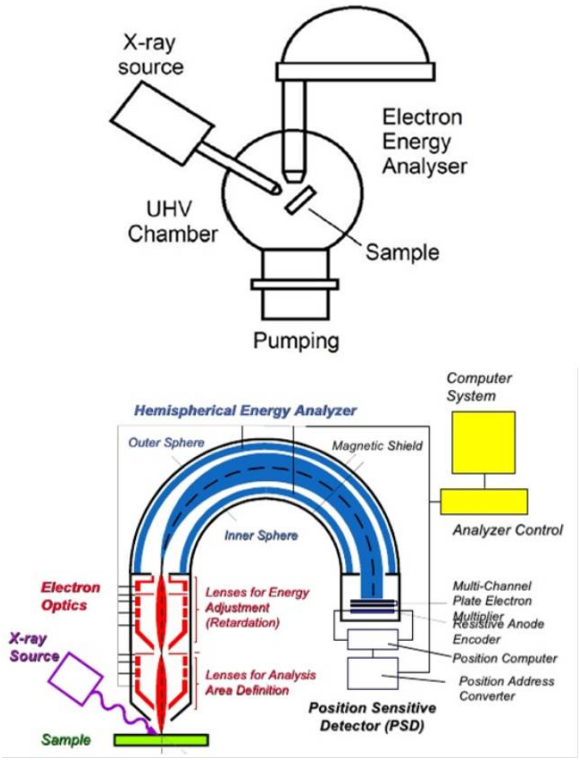

Figure 3.18: Basic components of XPS system (above) and X-ray photoelectron spectrometer (below).

XPS is typically used in ultrahigh vacuum. This is required for maintaining sample surface integrity, maximizing the mean free path of the ejected photoelectrons and minimizing the scattering of photoelectrons in gases. However, XPS systems have been built witch operate in the mbar pressure range, as described below.

3.1.6.3 Near-Ambient Pressure X-ray Photoelectron Spectroscopy

The Near-Ambient Pressure XPS (NAP-XPS) method is designed to partially overcome the so-called pressure gap in surface science. The pressure gap refers to the fact

that whereas many technological processes, including heterogeneous catalysis, take place in pressure ranges 1-200 bars, most the surface science experiments are performed in ultrahigh vacuum (UHV) conditions. In NAP-XPS systems, the sample is exposed to pressures in the order of millibars, while it is placed very close to a massively pumped nozzle (with an entrance aperture of a few hundred microns in diameter) which brings photoelectrons quickly to UHV environment, where they are separated and detected by a differentially pumped electrostatic lens system attached to a standard hemispherical electron energy analyser, as shown in Fig. 3.19

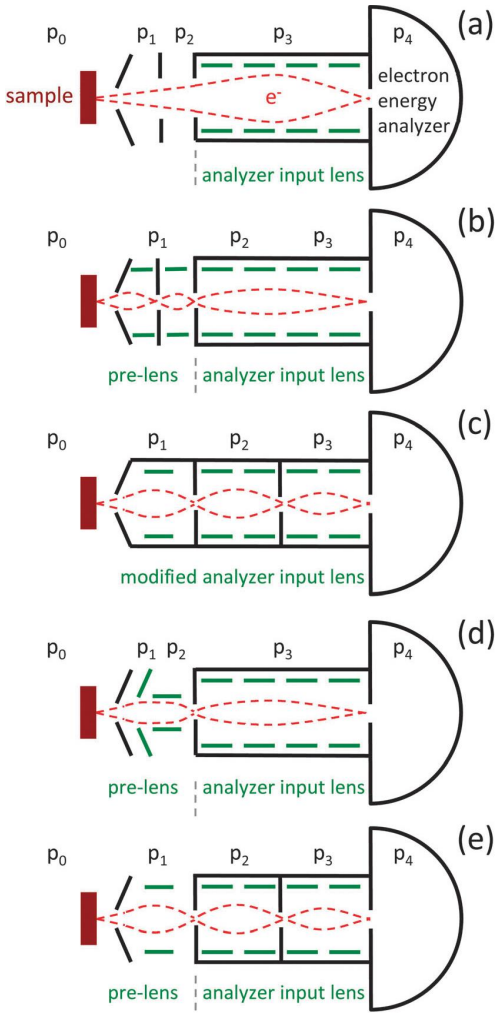

Figure 3.19: Principle layouts of differential pumping schemes (P_0-P_4) for ambient pressure XPS. Schemes (b–e) use a variation of a differentially-pumped lens system generations, while scheme (a) the most basic differential pumping system inserts two or more differential pumping stages between the sample location and the entrance to a standard electron energy analyzer input lens. [124]

In NAP-XPS spectra, it is possible to observe new peaks emerging from the gas-phase. Moreover, it allows observing the catalysts *in vivo* conditions (during the chemical reactions) by XPS, which is by its nature chemically sensitive. So, unlike ordinary XPS, NAP-XPS allows study the dynamics of catalytic reactions. Here we have used the NAP-XPS to study the adsorption of NO/Au(100) at near ambient pressure and to combined the results with the S-VMI results.

Chapter 4

Surface-Velocity Map Imaging Methodology

The purpose of this chapter is to provide full details of the surface VMI concept as a new approach for studying surface reaction dynamics. The VMI set-up is one of the handful of surface VMI spectroscopy world wide. Information on the experiments apparatus used in this study and also an understanding of how the experiments were preformed and analysed provided in this chapter.

4.1 Surface-Velocity Map Imaging Background

Since its introduction in 1997,[119] most of the velocity map imaging applications were focused on studying gas-phase reaction dynamics (see chapter 2). In a typical VMI experiment, one can extract the 3-D velocity and angular distribution from the two dimensions (2D) parallel to the detector. Although the region in space in which the fragments can be detected under VMI conditions is rather small (< 3 mm), it is still large enough to reliably detect gaseous photodissociation. [Exploitation of this technique in surface studies requires special modifications of the setup and taking certain precautions into consideration, as will be explained later on]. The first application was pioneered by Wodtke and co-workers (2009). [8] The authors applied the VMI technique to surface desorption processes by combining VMI with TOF measurements. In the laser induced desorption of neutral Br atoms from a KBr single crystal, the surface of the crystal was oriented parallel to the ion optics and the detector, and the surface

normal to the crystal was aligned along the TOF tube. TOF information and hence velocity distributions along the surface normal was obtained by varying the delay time between the desorption and the ionisation lasers, while VMI was used to derive the velocity distributions in the two dimensions parallel to the KBr surface. The surface was placed outside the electrodes, i.e. behind the repeller plate. In 2017, the Wodtke group used the S-VMI combined with fs-MPI to study water scattering from Pt(100) and surface desorption kinetics. The work was carried out to demonstrate the capabilities of their new ion imaging instrument.[125]

White and co-workers employed the surface-VMI technique to shed light onto the photodesorption of O_2 and photofragmentation of butanone adsorbed on TiO_2(110).[9, 126] Nesbitt and co-workers also employed surface-VMI which combines REMPI to study the molecular beam scattering of HCl from Au(100) single crystal and to yield the quantum state and 2D velocity distribution. The surface was mounted onto one of the electrodes and the scattering plane was perpendicular to the detector.[127] Most recently, they have combined REMPI with (DC) slicing VMI to obtain 3D velocity information for HCl scattered from self-assembled monolayers and achieved velocity resolution along the surface normal of around 11%. Only grazing angles of incidence are possible in this arrangement, as gas molecules have to pass between the electrodes to strike the surface.[128] In all of the above experiments, the surface normal was aligned along the TOF axis of the VMI spectrometer.

In contrast, Harding *et al.* have recently demonstrated measurements of speed and angular distributions of N_2 scattered from a Au(111) single crystal whose surface normal lies in a plane parallel to the ion optics and detection plates. Velocity distributions in this case were measured under spatial imaging conditions by varying the delay between the ionization laser pulse and extraction pulse to follow the movement of the scattered molecules away from the surface but parallel to the imaging detector.[129]

A new application of velocity-map imaging (VMI) was demonstrated, whereby the momentum distribution of photoelectrons ejected from a tungsten nanoscale metal tip by Bryan group.[130] They have adapted the multi-electrode design of Suzuki and co-workers, which makes use of a larger stack of multiple focusing electrodes to achieve higher resolution, hence eight electrodes were used. Hong Ye and co-workers have presented the VMI in electron emission surfaces studies as well; velocity-map-imaging

spectrometer was used to characterize the normalized emittance (root mean- square, rms) of photoemitted electron bunches with energy resolution of 0.2 meV. This application opens up opportunities for studying correlated electron emission from surfaces and vacuum nanoelectronic devices. [131] Three ion optics VMI was used, with the sample mounted on the top of the sample holder which is in contact with the repeller plate.

In summary, so far S-VMI has been used in three different applications namely the desorption, scattering and electron emission.

4.1.1 Area and Conditions

As has been mentioned earlier, the aim in this study is to obtain the 3D velocity distribution of NO molecules adsorbed from Au(100) in a single experiment. All three velocity components must be measured individually as illustrated in the Fig. 4.1.

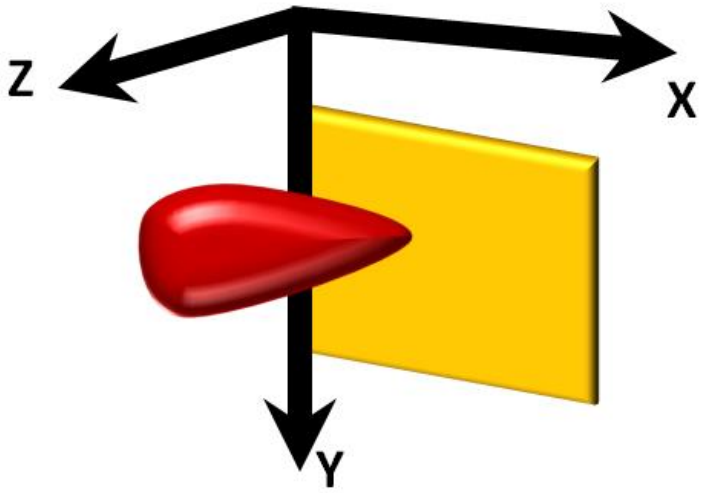

Figure 4.1: Molecules desorbed from the surface and fly in all directions above the surface (in red) and possess three distinct velocity components, all of which must be determined separately, in order to obtain the full three-dimensional velocity distribution.

The VMI image will record the velocity component in two dimensions parallel to the surface (along X and Y direction). The third velocity component along the surface normal (Z-axis) cannot be obtained from a single VMI image. In this study, the velocity component in the Z direction was obtained by using time-of-flight measurements. The time taken for the fragments to fly from the surface to the focus of the ionisation laser is measured by recording the intensity of the signal produced by the fragments at

different time delays between desorption and ionisation laser. By combining the VMI images two velocity components v_x and v_y, with the TOF velocity component v_z, the 3D velocity distribution can be obtained.

For surface desorption processes which are studied here, where the direction of travel of the desorbed particles can be described by a spherical coordinate system. Here, the polar angle (θ) is the angle at which the fragments travel relative to the surface normal (Z axis), and the azimuthal angle (ϕ) is the angle at which they travel relative to the vertical (Y) axis. particular attention has to be paid to the optical detection geometry. This is due to the fact that the laser pulse causes desorption of NO molecules which can potentially fly in all directions in the hemisphere above the surface. Since we are interested in the 3D velocity distribution, we have to ensure the capture of all NO molecules desorbing under all possible angles and that the fragments travelling at a particular angle are not preferentially detected over others .

Two options are available for the surface studies here, see Fig. 4.2. If the fragments are produced at one small spot on the surface and detected within a small volume above the surface (which is not ideal for the surfaces studied studies), then some fragments may be missed, and hence the angular distribution measured is determined by this optical geometry, and may not reflect the dynamics of the process.

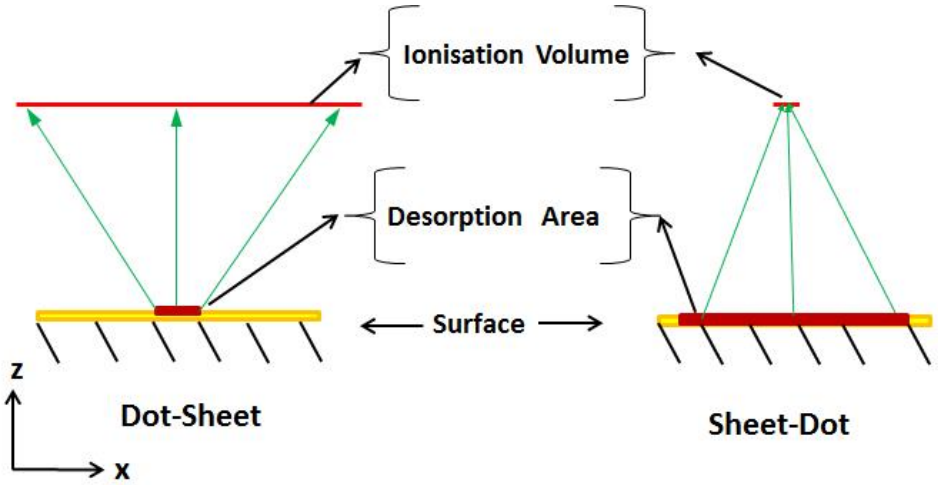

Figure 4.2: 2-D diagram of a dot-sheet and a sheet-sot geometry, the green arrows indicate the desorbed particles.

Wodtke and co-workers overcame this problem by desorbing fragments from a relatively large spot on the surface, and ionising the neutral fragments within a small volume above the surface about 1.5 mm (referred to as sheet-dot), such that fragments

from a relatively large polar angle of 60° symmetric around the surface normal could be recorded, Fig. 4.2.[8] The more intuitive 'dot-sheet' laser geometry configuration was employed in this work here to record fully resolved three-dimensional velocity distributions over almost the full solid angle (2π sr), Fig. 4.2.[132]

A small non-focused desorption laser spot illuminated the surface (< 1 mm). A cylindrical lens with a focal length of 28 cm, yielding a Rayleigh length of 20 mm for 1+1 REMPI, hence effectively creating an $\sim$ 20 x 8 mm^2 "curtain" above the surface through which the NO molecules have to fly. The solid angle of the cone that is reliably covered by a REMPI laser sheet is given by :

$$2\,\mathrm{x}\tan^{-1}(\frac{\mathrm{d}}{2}\,\mathrm{x}\,\mathrm{z}) \tag{4.1}$$

Where: d is the diameter of the laser sheet and z is the surface-laser distance. The probe laser was focused parallel to the surface with a distance varying in all surface studied between 1.5 and 4 mm.[8] A typical surface-to-laser distance of 3 mm, allowing the detection of all those NO molecules leaving the surface with a solid angle of 6.5 sr (53° symmetrically around the surface normal).

The dot sheet laser geometry is not realistic with the typical VMI. As mentioned previously, the elegance of the VMI technique is that all fragments with same velocity will be mapped to the same position on the detector regardless to their creations, and this is only true with small area of $\sim$3 x 3 mm^2. The dot-sheet laser geometry will create a large ionisation area. Simulations were carried out previously,[133] and found that the $\sim$10 x 10 mm^2 area of VMI (where the ionisation will occur) is required for the planned surface desorption studies here which is commensurate with the desired dimensions of the probe laser sheet.[134] A design consisting of twelve electrodes, resulting in a shallow electric field gradient and weak extraction conditions of 50 V cm^{-1}, was applied to produce a VMI area of $\sim$ 12 x 12 mm^2. Hence that all NO molecules crossing the laser sheet are ionised and accelerated under true VMI conditions.[134]

4.2 Experimental Apparatus

The S-VMI apparatus used in this study have been originally designed to carry VMI gas-phase experiments. In this study, it was adapted for VMI surface studies. The system comprises of many parts, namely the VMI vacuum system, the molecular beam, the surface mount, the electrodes, the detection system and the controls. Each of these parts will be described here briefly; more details can be found elsewhere.[134] The surface mount part however, will be described in detail.

4.2.1 Vacuum System

Fig. 4.3 depicts the vacuum system used in the study, which is ∼1.5 m in length.

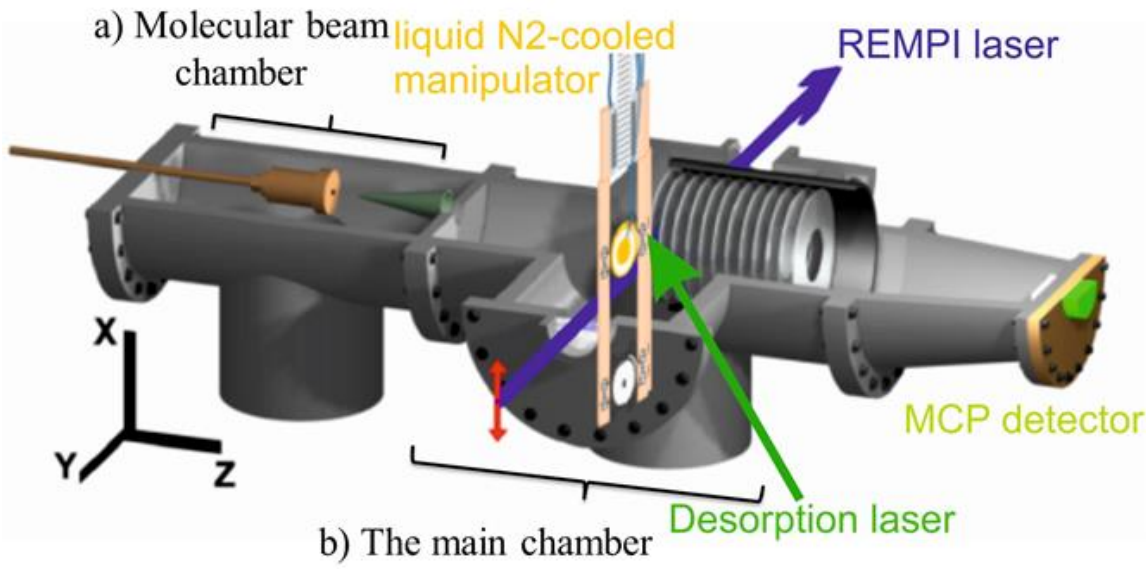

Figure 4.3: The stainless steel vacuum chamber a) molecular beam chamber containing the skimmer and the valve, b) the main chamber containing the ion optics and the manipulator to introduce the surface to the chamber. The desorption laser intersects the surface at 45° and the REMPI Laser is parallel to the surface between the first two plates. Adopted from[134]

The system consists of two chambers:

Molecular beam chamber: containing the valve for introducing the target molecule and the seeding gas together into the main chamber through a skimmer.

Reaction chamber: containing the VMI ion optics (twelve electrodes stacked together), with TOF tube (0.45 m in length measured from the point of laser interaction (i.e. the ionization region) to the MCP detector. The gold single crystal is mounted directly

behind the repeller plate which is the first plate of the stack by using a manipulator that is introduced vertically into the chamber. The molecular beam and the reaction chamber are separated by a ∼1 cm thick plate with ∼2 cm hole in its center, onto which the molecular beam skimmer is mounted.

The experiment were typically performed under UHV conditions in order to ensure that the surface studied is kept clean during the time of the experiment, hence preventing the interference of contaminants. Very low pressure is also an essential requirement since it increases the mean free path of the molecules, hence lengthening the time between successive collisions, allowing detection of the nascent product fragment before it collides with other molecules. Secondary collisions are likely to change the nascent product fragment energy and directions of travel apart from shifting the population torwards thermal equilibrium. The mean free path can be calculated by using

$$\lambda = \frac{RT}{\sqrt{2}\sigma p} \tag{4.2}$$

where: R is Gas law constant, T is Temperature (K), p is Pressure (Torr), σ is the collisional section (m^2). UHV was achieved by using a combination of turbo pumps (the molecular beam chamber is evacuated by a refurbished Edwards STP-1000 C turbomolecular pump, and the main chamber is evacuated with an Edwards STP-1003 turbo pump) backed up by an Edwards E2M28 rotary pump. A pressure of 10^{-9} torr was routinely achieved. The system can be baked up to 200°C in order to reduce the background pressure to allow a pressure in the region of 10^{-10}torr. Isolation gate valves are used to isolate the MCP detector from the TOF if needed. Gate valves enable the rotary pumps to be isolated from the turbo molecular pumps during evacuation. To monitor the pressure, four pressure gauges are mounted on the apparatus.

The molecular beam chamber and reaction chamber are each monitored by a SRS-NW-F-UHV and an Edwards AIM-X-DN40CF ion gauge respectively (used for measuring ultra high vacuum). The forelines of the turbomolecular pumps are monitored by SRS-PG105 Pirani gauges.

4.2.2 Molecular Beam

Reaction dynamic studies require target molecules that are spread over as few quantum states as possible. This can be achieved by use of a molecular beam, since supersonic

expansion results in the production of a molecular beam with extremely low internal temperature. Under standard conditions, many rotational states are populated and a broad velocity distribution of molecules is observed, usually Maxwell-Boltzmann distribution. Supersonic expansions lead to narrower and well- defined kinetic energy and well defined internal energies of target molecules within the molecular beam, which is useful for crossed-beam and beam-surface interaction experiments. Supersonic molecular beams offer target molecules that are translationally and rotationally cold. In this study, a gas sample composed of 2-5% of the target NO molecule seeded in helium as a carrier gas is used in the gas phase experiments, which are used here as a calibration guide for surface experiments. The mixture was held behind the molecular beam valve (a General Valve with 500 µm diameter orifice) at a stagnation pressure of 2.5 bar. The valve is pulsed using an Iota One pulse driver from Parker. The molecular beam was extracted from the supersonic expansion using a Beam Dynamics skimmer (Model 2, 1.2 mm orifice) placed ∼15 mm from the valve's orifice. The opening time of the molecular beam is controlled relative to the laser energy and the NO partial pressure. It was varied between 500-800 µs in these experiments. A manual leak value attached to the main chamber was used to introduce the adsorbate NO to the chamber for background surface coverage.

4.2.3 The Electrodes

A standard set of VMI ion optics consists of three electrodes, namely repeller, extractor and ground plate. However, the VMI set up used in this study is composed of 12 electrodes. ***The use of such a design has the benefit of increasing the volume in which the VMI condition prevails, i.e. all the fragments with the same velocities arriving at the detector at the same time***. It has further advantages:

- Much tighter focussing of the NS in the x and y directions.
- Good conditions for dc slicing.
- Improving temporal resolution.

Each of the electrodes used was 10 cm in diameter; 1 mm thick with a hole at the centre through which the molecular beam path and TOF axis is directed. The hole

in the repeller was increased to ∼12 mm to allow a gold crystal to be introduced to the stack assembly and be flush with the repeller plate and maintain electrical contact. Because of the physical contact between the liquid nitrogen-cooled crystal and the room-temperature repeller plate, the crystal heated up too quickly; hence it was set-back by 0.5 mm away from the repeller plate. Both the crystal and repeller are connected to separate power supplies held at the same voltage (1000 V) such that the electric field experienced by the fragments in vacuum at the point is homogenous, as proven by gas-phase calibration experiments and simulation. The electrodes are separated from each other by 9.5 mm thick ceramic spacers. A diagram showing the mounting of the twelve electrodes assembly is shown in the Fig. 4.4.

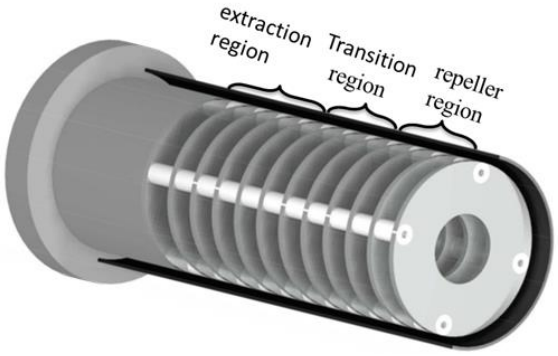

Figure 4.4: The electrodes are mounted over four insulated rods onto a metal cylinder and separated by insulating spacers. The repeller region spreads over the first four electrodes, the extraction region spreads over electrodes seven to twelve and the transition region spreads from electrode fourth to seven.

In a standard set of VMI optics, there are two field regions: the region between the repeller and the extractor plates (acceleration field), and the region between the extractor and the ground plates (extraction field). The gradient of the field between these two regions plays a pivotal role in achieving VMI focussing conditions. However, when many electrodes are used, the situation is more complicated, and three field regions can be envisaged here namely acceleration, transition and extraction. The transition field is located between the other two regions. In the VMI set-up used here, the repeller region spreads over the first four electrodes, while the extraction region spreads over electrodes seven to twelve. The transition region on the other hand spreads from electrode 4 to 7, see Fig. 4.4. The voltages of the electrodes can be varied (except for electrode 12 which is always kept at 0 V) by a resistor chain and are optimised depending on the gradient ratio required. The optimum extraction:repeller

gradient ratio is usually around 2.4, but for this experiment was was 2.1.

Table 4.1 shows the voltages applied on these plates.

Table 4.1: The voltages applied on the ion optics.

Plate	1	2	3	4	5	6	7	8	9	10	11	12
Voltage	982	945	890	835	751	671	576	483	371	257	129	0

4.2.4 Manipulator

The manipulator (MCD Vacuum products corporation, Hayward, CA 94545 USA, 4 1/2 flange, throw 1 m) is designed in such a manner to allow moving, cooling and heating of the surface in a sealed main chamber maintained under ultra high vacuum. A schematic illustrating the manipulator mounted on top of a translation stage on top of the reaction chamber is depicted in Fig. 4.5.

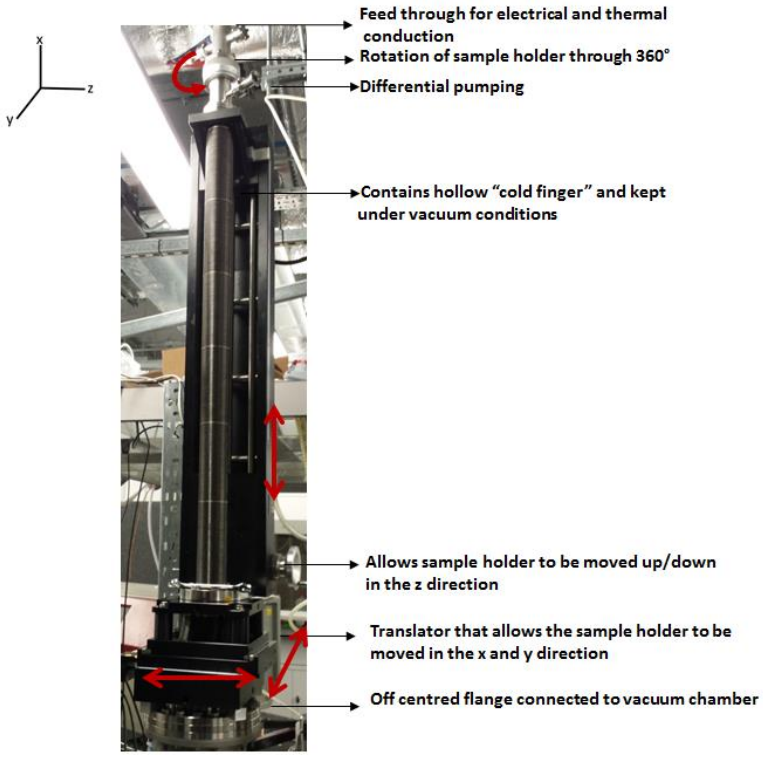

Figure 4.5: Schematic showing manipulator allowing movement of surface within the reaction chamber. The red indicates the movement of the crystal in all directions.

The design allows the sample to be moved upward and downward, left and right as well as backward and forward with respect to the direction of the TOF. Rotation of the sample about the vertical axis of the manipulator is also possible. The crystal

manipulator was placed vertically along the chambers central axis. The manipulator consisted of a UHV x-y-z stage. The sample could be moved by + 25 mm of translation in the x and y directions, 600 mm in the z direction and by 360° around the z axis.

4.2.5 Surface Mount

A schematic illustrating the mounting of the gold single crystal is shown in Fig. 4.6.

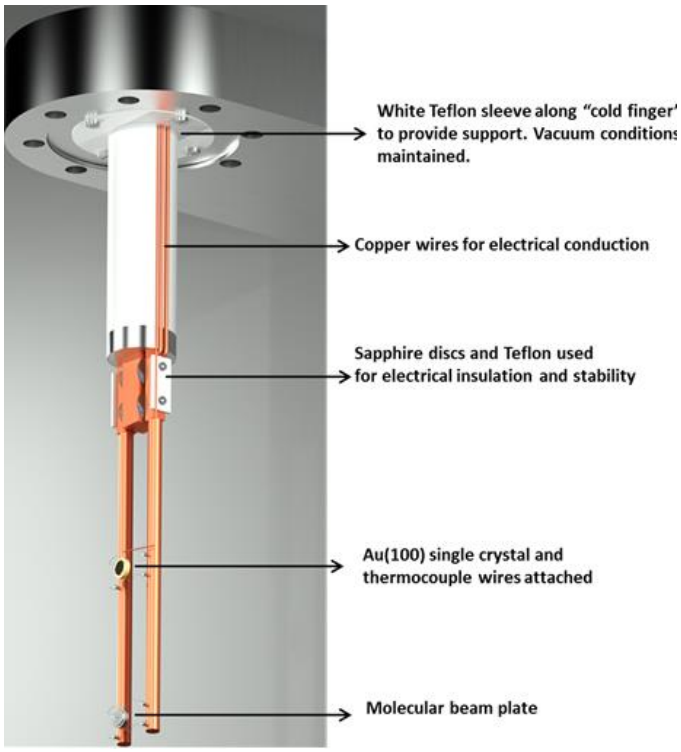

Figure 4.6: Schematic of surface mount incorporating resistive heating, cooling and monitoring of the surface temperature.

This mount allows resistive heating and cooling of the surface. Two copper arms hold the crystal by the use of tungsten wires that are electrically conductive and able to retain their mechanical strength at high temperatures. The wires are shaped as U loops that fit into slots on both sides of the single crystal, kept it in place during heating and cooling. Tungsten wires were heated by passing a current (∼18 A) through the copper arms and that in turn heated the gold crystal. The copper arms were connected to the manipulator tube via sapphire disks which are thermally conductive but electrically insulating. This was necessary to prevent any electricity to flow from the copper arms to the manipulator tube when applying current to the copper arms via the copper wires

during the heating process. Cooling of the gold crystal is achieved by feeding liquid nitrogen into the hollow metal tube of the surface mount system. The temperature of the surface is monitored during the experiment using a thermocouple embedded in the gold crystal. The manipulator also holds a 12 mm diameter stainless-steel disc with a central 2 mm hole; this disc can be placed in position instead of the gold crystal and allows to run gas-phase calibration experiments using the molecular beam under otherwise identical conditions without having to break the vacuum.

4.2.5.1 Surface Preparation and Gas Handling and Exposure

The purity of NO gas used in this study was 99.9%. The Au(100) (10 mm diameter, 1.5 mm thick, from Surface Preparation Laboratory) was cleaned from impurities prior to adsorption of NO. This was achieved by heating it resistively to a temperature of ∼700 K by applying a current of 18 A through 0.5 mm tungsten wires, see Fig. 4.7. This was followed by cooling it with liquid nitrogen to a temperature of ∼178 K, after which NO was allowed to adsorb onto the surface, see Fig. 4.6

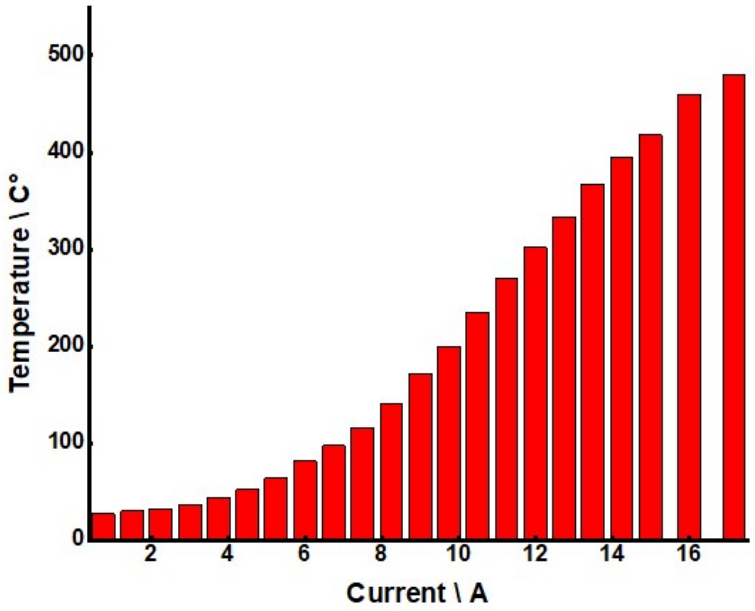

Figure 4.7: Chart showing the gradual increase in the temperature with the current while cleaning the surface by applying 18 A through the copper arms attached to the surface.

Desorption was carried out after adsorption by nearly an hour to ensure that all background NO has been pumped out of the system. The crystal surface was dosed

with NO molecules by one of the following methods. The first method was using molecular beam opening for 4 minutes. Higher coverage can be achieved by using this method. The second method was by backfilling the chamber to a static pressure using a manual leak valve or through a connection on the rotary pumps using the gas manifold which is filled from standard compressed gas cylinders.

4.2.6 Laser System

A pump-probe set-up (mentioned in chapter 2) was employed in this study. Photo-desorption of the target molecules NO was carried out using a pump laser, and the desorbed molecules were subsequently ionised using the probe laser, which enabled the detection of products in specific quantum states. Desorption of NO from the surface was caused by laser irradiation at 355 nm and 266 nm using the output of a Quanta Ray- YAG laser. The laser beam is characterized by a maximum pulse energy of 1.5- 2 mJ and and a pulse length ∼9 ns. After desorption ∼ 226 nm probe laser with pulse energy of 150 µJ was used to ionise the photo-NO using a (1+1) REMPI Scheme. This laser system allows for the possible use where the distance between dissociation (desorption in our case) and ionisation are known.

4.2.6.1 The Pump Laser (Quanta Ray laser (DCR-11))

The laser active medium of a Nd:YAG are $Nd3^+$ ions which is optically pumped by a flash lamp. The time delay between Q switch and the flash lamb was controlled and it was 250 µs. The laser was either frequency tripled (3.5 eV) or quadrupled (4.7 eV) with a pulse duration of 7 ns at a repetition rate of 20 Hz and a pulse energy of ∼1.2 mJ. The beam was directed by dichroic mirror impinge upon the Au surface at an angle of 45°.

4.2.6.2 The Probe Laser (YAG Dye laser)

The probe laser used in this work to ionised desorbed NO molecules is a Radiant Dyes Narrowscan, dye laser pumped by a Continuum Powerlite Nd:YAG Laser.

Nd:YAG Lasers

Continuum Powerlite Nd:YAG which emits at a wavelength of 1064 nm from $Nd3^+$ ions which are doped in an Yttrium Aluminium Garnet.

This wavelength is converted through double and harmonics to produce a wavelength of 532 and 355 nm. The "Q switch" defines the "time zero" in this experiment. The timing between the Q switch and the flash lamps is controlled to yield high energy, and was (320 µs). The laser has an important feature of the dye laser is that it is tuneable, and different dyes can be used in order to obtain a range of different wavelengths. The beam from the Nd:YAG is split into various fractions using mirrors and beam splitters to send the laser through to the oscillator and amplifier cell, see Fig. 4.8.

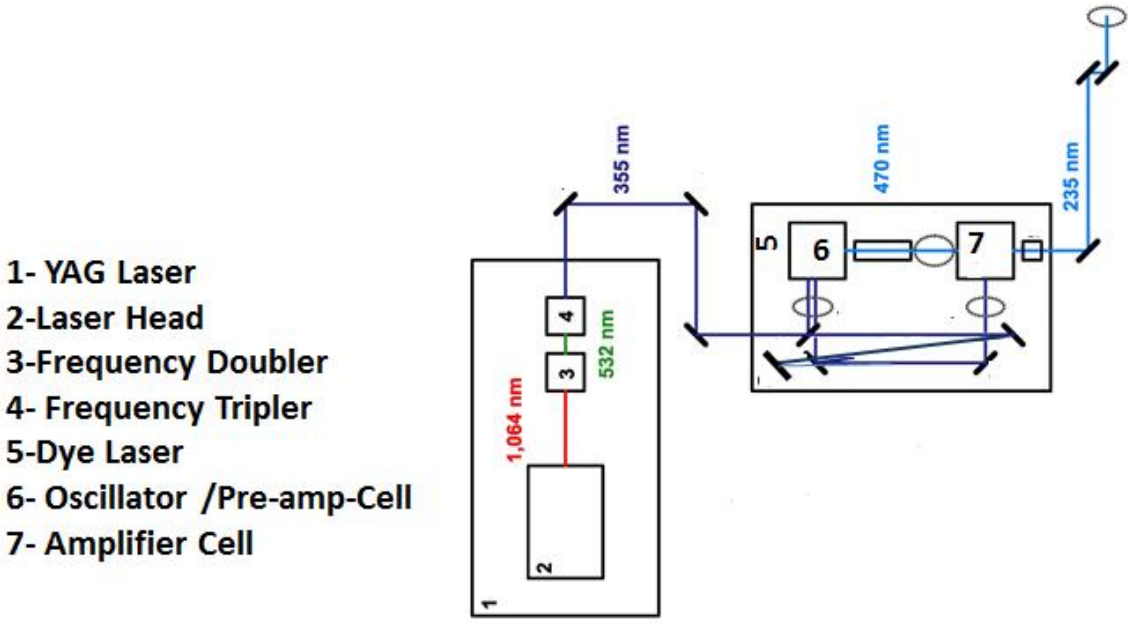

Figure 4.8: The probe laser beam path in the lab. 1,064 nm light is converted to 355 nm. This is directed via mirrors into the dye laser to yield 470 nm. In the dye laser a beam-splitter sends a small portion (10%) into the oscillator cell. The remainder of the 355 nm light is then divided using mirrors and one more beam splitter such that a second beam (the pre-amp) containing (25%) of the light enters the oscillator cell and the remaining 355 nm enters the amplifier cell. The wavelength light from the oscillator beam is tuned using a diffraction grating to 470 nm. The beam passes through a spatial filter telescope, and then through an amplifier cell were the rest of the 355 nm light overlaps to amplify the 470 nm beam. After leaving the amplifier cell, the 470 nm is frequency doubled to 235 nm, before being reflected by several dichroic mirrors, through a focussing lens and into the chamber.

Dye Lasers

Dye lasers belong to the family of liquid lasers. The active material is a dye dissolved in a liquid solvent which is circulated through the laser. Dye lasers may produce a wide range of wavelengths by varying the pump radiation's wavelength and

using the appropriate dyes. The approximate working ranges of various laser dyes are shown schematically in the figure below, 4.9.

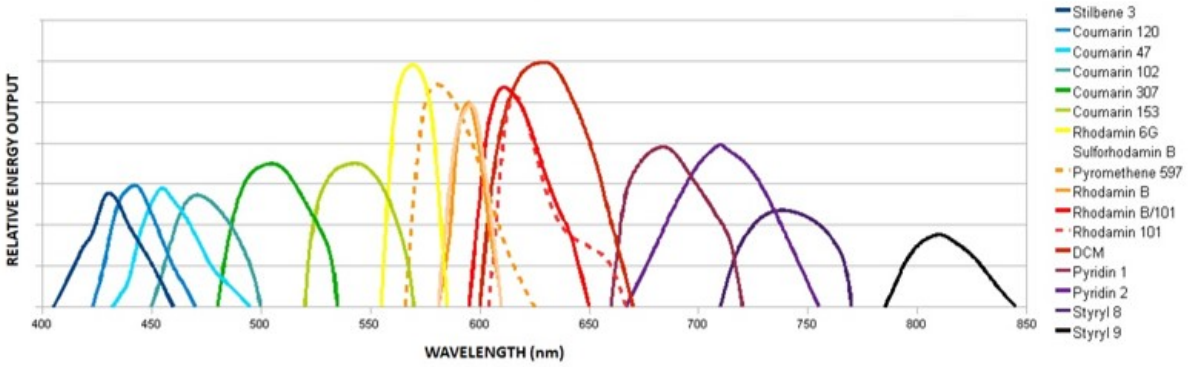

Figure 4.9: Dye spectral emission characteristics.

The efficiency of the dye laser is determined by the dye, and is usually between 10% and 20% with respect to the energy of the pump beam. For the experiments reported here the dye Courmarin 47 was used to achieve the desired wavelength between 445 - 470 nm, see Fig. **??**. This was prepared with ethanol at an optimum concentration of 0.3 g/l. The dye laser beam is frequency doubled using a BBO crystal, producing horizontally polarised output with 0.5 to 1 mJ pulse energy. This beam is then directed through the chamber and focused in one dimension using a cylindrical convex lens to form the laser sheet.

4.3 Ion Detection and Data Acquisition

Following the NO desorption, the NO fragment drift into the ionisation area by (1+1) REMPI as mentioned earlier which is 3 mm from the surface and between the first and second plate. Once the NO molecules are state-selectively ionised, they are repelled down the TOF tube and under the VMI focussing conditions provided by the electrodes, they arrive at the detector. The position sensitive detector used in this study is a BurlePhotonis 40 mm MCP coupled to a P43 phosphor screen. The MCP consists of an array of pores, each acting as a single electron multiplier. A potential difference of about 1.8 kV is applied across the detector, and the pores eject electrons when a particle hits the MCP (referred as to continuous mode). The first ejected electron creates a cascade of secondary electrons upon hitting the interior wall of the

pores leading to an amplification of the signal. Up to 10^6 electrons are formed and exit the MCP when one charged particle impacts on the detector at the start. The exiting electrons collide with a phosphor screen causing it to emit fluorescence. The fluorescence is detected using a Foculus L-SV-FO614 CCD camera that is pulsed at the same frequency as the experiment, i. e. 20 Hz. The exposure time can be set to any value; this was in the region of 100 - 400 µs in the measurements carried here (referred as to imaging mode). The recorded image is sent to a lab computer where it is processed to produce the final image that is a composite of ∼20,000 single images. Pulsing and synchronisation of the various parts of the apparatus are very important for the performance of the experiment.

During the experiment, various parameters might be changed to optimise performance and the system has to provide such changes. For example, the time delay between the opening of the molecular beam and the firing of the laser beam may be varied, as well as the time between the pump and probe laser pulses. This is provided by two Standard Research Systems DG-645 digital delay generators and custom-written LabVIEW programs.[134]

4.3.1 Choice of the Probe Laser Wavelength using Gas-Phase Nitric Oxide

Before starting the surface studies on the NO-Au(100), the modified VMI setup, was run in gas-phase mode i.e. when the molecular beam plate is in place instead of the surface to obtain REMPI spectra of NO gas. This was necessary in order to determine the most appropriate probe laser wavelength to be used to ionise and detect the photodesorbed NO from the gold surface. The most appropriate laser wavelength in this case is chosen to be the one corresponding to the highest intensity line.

NO for this gas-phase study was obtained by dissociation of NO_2 using a ∼2% of NO_2 and ∼2% of O_2 seeded in He (∼95%) molecular beam at ∼226 nm. The NO produced was probed using (1+1) REMPI scheme via the A ←X (0,0) transtion. A wavelength scan was carried out to record the REMPI spectrum. The spectrum and the wavelength ∼225 nm corresponding to the highest intensity that was selected (indicated by the arrow) for the probe laser is shown in Fig. 4.10.

The probe laser for the surface studies was set to this wavelength, for both TOF and imaging experiments.

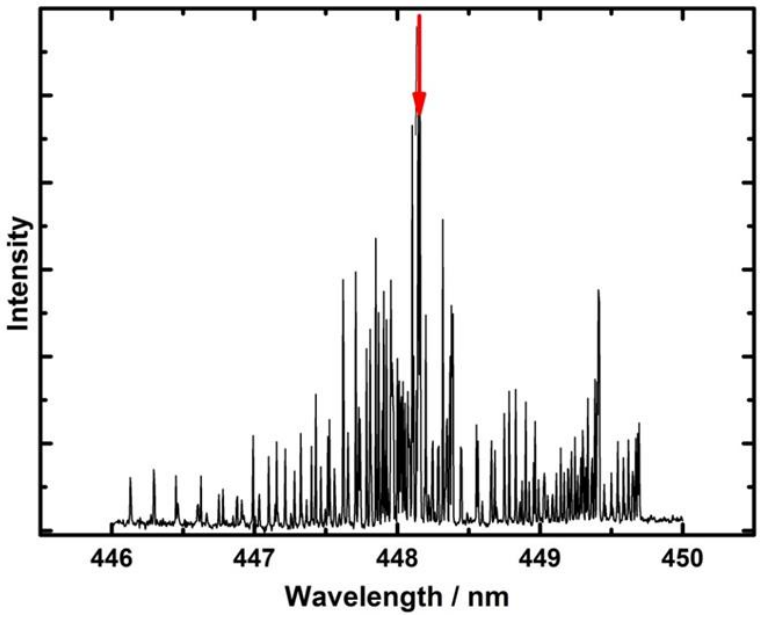

Figure 4.10: Nitric Oxide REMPI spectrum showing the dye laser wavelength at which the experiments were conducted.

An image of NO is recorded; the raw data can be constructed by extracting a distribution of intensity against radius in pixel using BASEX.[135] In order to convert the radius to velocity, our raw data was calibrated using the results by Whitaker and co-worker [136] and a conversion factor of $\sim$11 ms^{-1}/pixel was obtained, see Fig. 4.11.[133].

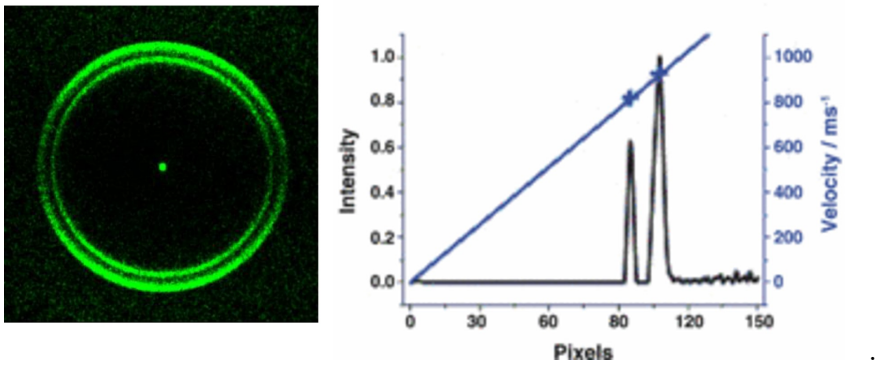

Figure 4.11: Raw image of the dissociation of NO_2 at 226 nm and calibration measurement for surface studies.[133]

4.3.2 Substrate Heating

The gold surface is irradiated with a nanosecond laser pulse. The light is absorbed in the substrate uppermost layer at the surface (optical penetration depth), where the photon energy is transferred to metal electrons, which rapidly lose their energy through electron-electron and electron-phonon collisions, transferring the energy to the lattice vibrations (phonons), and then transfer sufficient vibrational energy to the adsorbates on the surface for desorption. The time for the decay into heat is for most metals in the order of a few picoseconds at room temperature. The Quanta laser used in the experiments carried here has a pulse length of $\sim$7 ns pulse energy of a few mJ for both wavelengths (355 and 266 nm). The laser fluence was kept extremely low. First to ensure signal on scope, and avoid damage to the surface. In the case of 266 nm irradiation the diameter of the laser spot was bigger than the one used in the 355 nm. More energy was required to obtain the signal when using the 266 nm desorption. However, the fluence was kept at a minimum to minimise the temperature rise of the surface and therefore the thermal desorption signal that could have obscured the observation of the non-thermal desorption. A temperature rise of (27 K and 20 K) were obtained for wavelengths of 355 nm, and 266 nm respectively.[137, 138] In both cases the temperature rise were quiet small.

Chapter 5

Photodesorption dynamics of NO from Au(100) using S-VMI

This (main) chapter of the thesis is concerned with the dynamics of nanosecond (ns) laser-induced desorption of NO from Au(100) using S-VMI, TOF and (1+1) REMPI techniques to get detailed insights into the 3D velocity and angular distribution and the desorption dynamics at various wavelengths.
Photodesorption of pre-adsorbed NO on Au(100) was investigated using two separate laser beams of 3.5 and 4.7 eV aiming at investigating the translational and internal energy distributions of the photodesorbed species. It was expected that the results obtained will shed some light into the desorption mechanism.

5.1 Introduction

Monitoring of elementary processes on surfaces is essential in the field of photochemistry of molecules adsorbed on surfaces for both fundamental and practical purposes since these are somehow related to the field of catalysis. Surface reaction or desorption of adsorbed molecules involve processes such as excitation and relaxation of substrate electrons and adsorbates, together with energy transfer and partition among the various degrees of freedom of the system. Hence, accurate description of photo-induced processes requires good understanding of these fundamental issues. Photoinduced processes involving NO adsorbed on different well-defined metal single crystal surfaces have been widely studied by various research groups employing different experimental

and theoretical methods, see chapter 2. NO has been extensively used in such studies because of its association with many catalytic reactions and the fact that NO molecules in the gas phase can be easily detected state-selectively by resonance-enhanced multiphoton ionization (REMPI), see chapter 3.

Two different mechanisms can be envisaged for the desorption of molecules from metal surfaces when a laser beam of specific wavelength hits the surface, namely a non-thermal and a thermal mechanism. The energy of the photon causing electronic excitation of the system is partitioned into translational and internal (vibrational and rotational) energy, as well as dissipation into the substrate. This partitioning is determined by the potential energy surface and the lifetime of the intermediate excited state as described by the Menzel-Gomer-Redhead theory.[25, 32] Therefore, measurements of the translational and internal energy distribution of the desorbed molecules can shed some light onto the desorption mechanism and the energy flow pathways during photodesorption. Although non-thermal desorption is important in this study, thermal desorption due to partial thermal equilibration with the substrate cannot be avoided. The dynamics of thermal desorption of molecules with the surface have been investigated in great detail by the combination of molecular beam and laser spectroscopic techniques.[139–141] Distinction between these two forms of desorption mechanisms is not as straightforward and both forms might be occurring simultaneously.

Fukutani *et al.* concluded that substrate valence excitation was responsible for the laser-induced non-thermal NO desorption from Pt(001) at 80 K for photon energies of 6.4 and 3.5 eV.[142, 143] Evidence supporting this conclusion came from the observations that 1) translational and internal energy distributions were independent of the pump laser wavelength, and 2) the desorption was induced by a single photon process. Buntin group has studied the photodesorption of NO from Pt(111) at different wavelength (1907, 1064, 532 and 355 nm) and two desorption channels were observed.[144, 145] A thermal and non-thermal chanel, the latter of which is driven by adsorbate interactions with hot carries (holes or electrons) initiated due to excitation of the substrate at photon energies in the range from 1.17 to 3.5 eV, resulting in desorbed NO molecules exhibiting a non-Boltzmann rotational energy distribution.

The photon-stimulated desorption of NO from a Pt(111) surface at 80 K was investigated by Chuang and co-workers using REMPI spectroscopy.[146] Two distinctive

desorption channels were identified on a non-annealed surface and a surface annealed to 220 K after NO adsorption at 80 K. The rotational energy distribution was found to follow a Boltzmann distribution for as-adsorbed Pt(111) and was non-Boltzmann on the annealed Pt(111) surface, with an inverted population of spin−orbit states, in agreement with the results reported by Buntin *et al.* [145] In an electron-stimulated desorption study of NO from Pt(111), Burns *et al.* reported that direct excitation of adsorbates induces the desorption, which was supported by the experimental result of a 6 eV threshold for desorption and also by theoretical calculations. [147]

Mulugetaet *et al.* reported on the internal energy distributions of desorbed NO obtained by REMPI spectroscopy for Ag(111) and for Ag nanoparticles by laser light (2.3, 3.5 and 4.7 eV); NO molecules were detected with hyperthermal velocities and with vibrational and rotational temperatures significantly higher than the sample temperature. [148]

Richter *et al.* studied the laser-induced desorption of NO from Si(111) at a surface temperature of 100 K and found the desorption dynamics to be sensitive to the initial coverage with NO.[149] The energy partitioning in the desorbed NO and its dependence on the desorption laser wavelength suggested that different photoreaction channels are in operation at low and high coverage; for low coverage, the resultant energy partitioning in the desorbed NO is such that translation and vibration carry most of the photon energy. The kinetic energy distributions were found to be non-Maxwellian, while the rotational state populations were adequately described by a Boltzmann distribution.

Freund and his co-worker analysed fully state-resolved NO molecules desorbed from an oxygen-covered Ni(100) surface by 193 nm radiation. [150] The authors reported two desorption channels, thermal and non-thermal, via electronic excitation. The non-thermal part exhibits very strong spin-orbit selectivity at low rotational quantum numbers. Ho and his group studied laser induced desorption of NO/GaAs(110) at 90 K over a wide range of wavelengths from 457 to 900 nm and found the desorption and dissociation are induced by a non-thermal mechanism. [151]

Here, it was reported the use of a combination of time-of-flight (TOF) and VMI techniques for resolving 3-dimensional velocity distributions of NO photodesorbed from a gold single crystal using 355 nm and 266 nm photons.

The rotational state distribution for both excitation wavelengths were calculated to compare and analyse results to identify any differences in the mechanism of the photodesorption of NO from Au(100).

5.2 Experimental

The velocity map imaging (VMI) technique has been successfully applied to many gas-phases photodissociation experiments. A new approach to the study of reaction dynamics on surfaces focused on the idea of adapting the VMI only one of many spectrometer utilised in gas-phase studies for surface studies. The setup was designed to obtain the 3D velocity distribution of desorbed molecules from the surface (see chapter 3). Briefly, a typical VMI gas-phase experiment involves a molecular beam that is directed along the TOF axis, through holes in the centre of a series of electrodes. Desorption of chemisorbed NO from the Au(100) crystal was initiated by a Nd:YAG laser (Quanta Ray DCR-11), which was either frequency tripled (3.5 eV) or quadrupled (4.7 eV) with a pulse duration of 7 ns and a pulse energy of ∼1.2 mJ for both wavelength. The beam was directed at the NO/Au(100) surface at an angle of 45°, see Fig. 5.1.

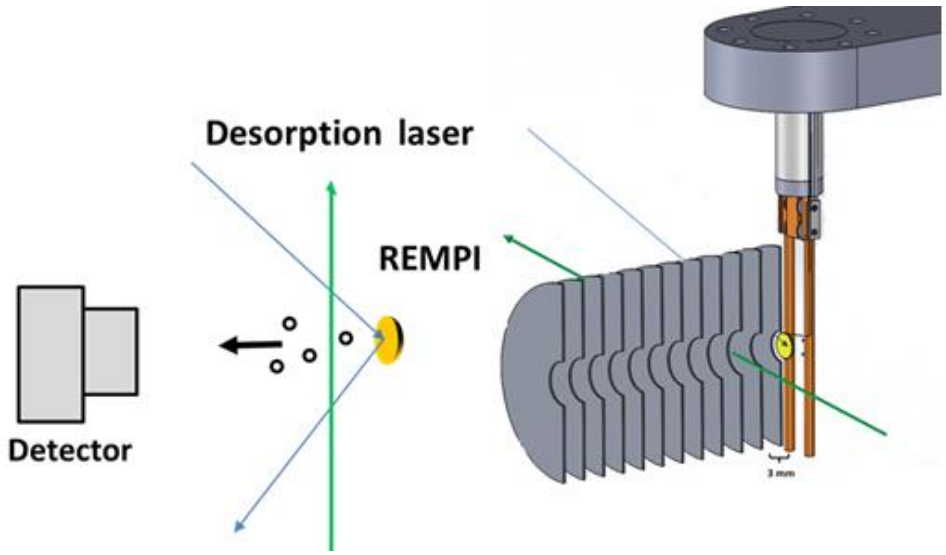

Figure 5.1: Schematic of the S-VMI showing the parallel alignment of the gold surface, in relation of the ion optics (right), and schematic of the experiment and molecules desorption direction.

The desorbed molecules ionised by ∼226 nm REMPI laser and repelled down the TOF tube and under the VMI focussing conditions provided by the electrodes, they arrive at the detector and measured either as a current as a function of flight time recorded on an oscilloscope (TOF-MS experiment) or via the generation of an image using a position sensitive detector, see (Ion Detection and Data Acquisition) 4.3. We recorded TOF profiles by varying the time delay between the desorption and the probe laser; these profiles were converted into velocity distributions that deliver the velocity component along the surface normal (v_z) exclusively, i.e. not the overall speed of the desorbed molecules. Since the gold surface and the detector are parallel to each other but perpendicular to the TOF axis of the spectrometer, the velocity distributions extracted from the VMI images correspond to the remaining two velocity components v_x and v_y parallel to the gold surface, where y is along the propagation direction of the REMPI laser, i.e. horizontal in the laboratory frame, and x is the vertical axis, for specific values of v_z. Hence, it was possible to record velocity distributions along z (v_z) by varying the time delay between the desorption and the probe laser in discrete steps, and for each time delay, i.e. v_z, we obtain the velocity distributions along x and y from the velocity map images. In order to record rotational state distributions, the delay time between the pump and the probe laser was fixed to correspond to specific velocities of the v_z distribution for both 355 and 266 nm desorption laser wavelengths. The probe laser was scanned over an appropriate wavelength range in steps of 0.005 nm to obtain REMPI spectra for NO for a given v_z. To extract rotational state distributions of the desorbed NO molecules only, rotational spectra in the absence of the desorption laser were recorded, and background subtraction was carried out. A relative calibration scheme was applied to avoid any factors that influence the sensitivity of different rotational lines to a different degree. This was done by recording thermal NO spectra which yield a well known Boltzmann distribution; the intensities of each rotational line of these thermal spectra were compared to the Boltzmann population of NO at 298 K to extract calibration factors which were used to convert the line intensities of the photo-desorbed NO to rotational populations.

5.3 Results

5.3.1 Translational Energy Distributions

The main purpose of the TOF measurements was to investigate the translational energy of photodesorbed molecules. TOF measurements were taken following the 355 nm desorption laser at 2 mm and 3 mm surface-to-REMPI distance. In order to record all desorbed NO molecules (rather than selectively only a small fraction that happens to be intersected by REMPI the laser), a large laser sheet (focused by a cylindrical lens) was used parallel to the surface. The probe laser wavelength was tuned to be resonant with $Q_1(1)$ line of the (0,0) transition. The signal-to-noise (S/N) ratio at 2 mm was comparable to that at 3 mm, indicating that we detect all NO molecules in both cases, however the velocity resolution along z at 2 mm is slightly worse such that all results reported here are for a 3 mm surface-to-REMPI laser distance, see Fig. 5.2

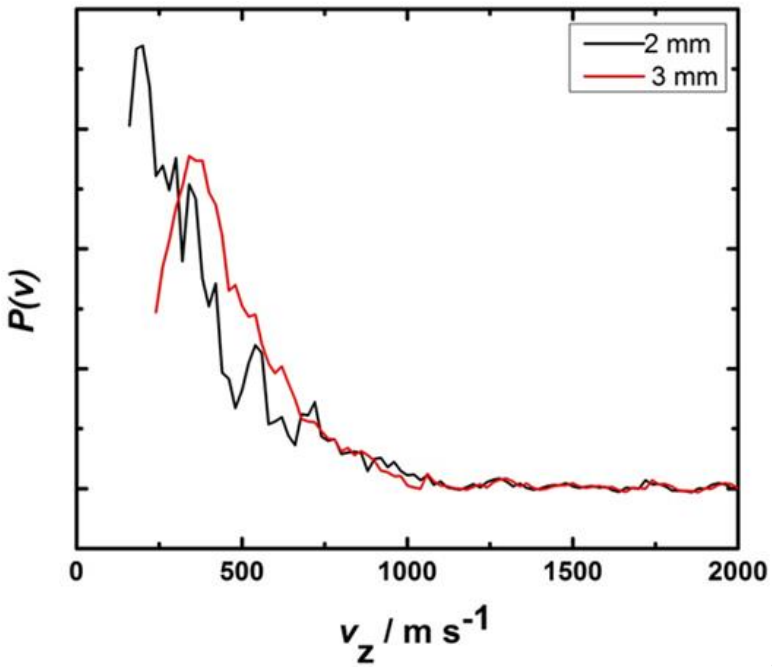

Figure 5.2: Normalized v_z velocity distribution of photodesorbed NO after density-to-flux conversion of the raw data at 355 nm at 2 mm REMPI distance (black line) and 3 mm REMPI distance (the red line).

The error in the velocity distribution along the z axis is given by $\Delta l/l$, where Δl is the uncertainty of determining the exact distance between the surface and the probe laser; assuming we can adjust the position to within 100 µm, we estimate the error to

be around 0.1 mm/3.0 mm = 3%. As only the 3 mm surface-to-REMPI laser distance is considered here, the TOF spectra of NO following 355 and 266 nm photodesorption will be referred to as 355 nm and 266 nm for simplicity. As an average of three runs is shown in Fig. 5.3 (a & b), respectively, as a function of the desorption laser wavelength. All other experimental conditions are the same. These TOF spectra only measure the velocity component of the desorbed NO molecules along the surface normal (z) and were subsequently converted into a v_z distribution; Fig. 5.3 (c & d) shows the velocity distribution v_z of NO molecules; the time delays for both pump wavelengths were chosen to yield equally spaced velocity intervals; a density-to-flux conversion was applied, as was the appropriate Jacobian, see Appendix A.[152]

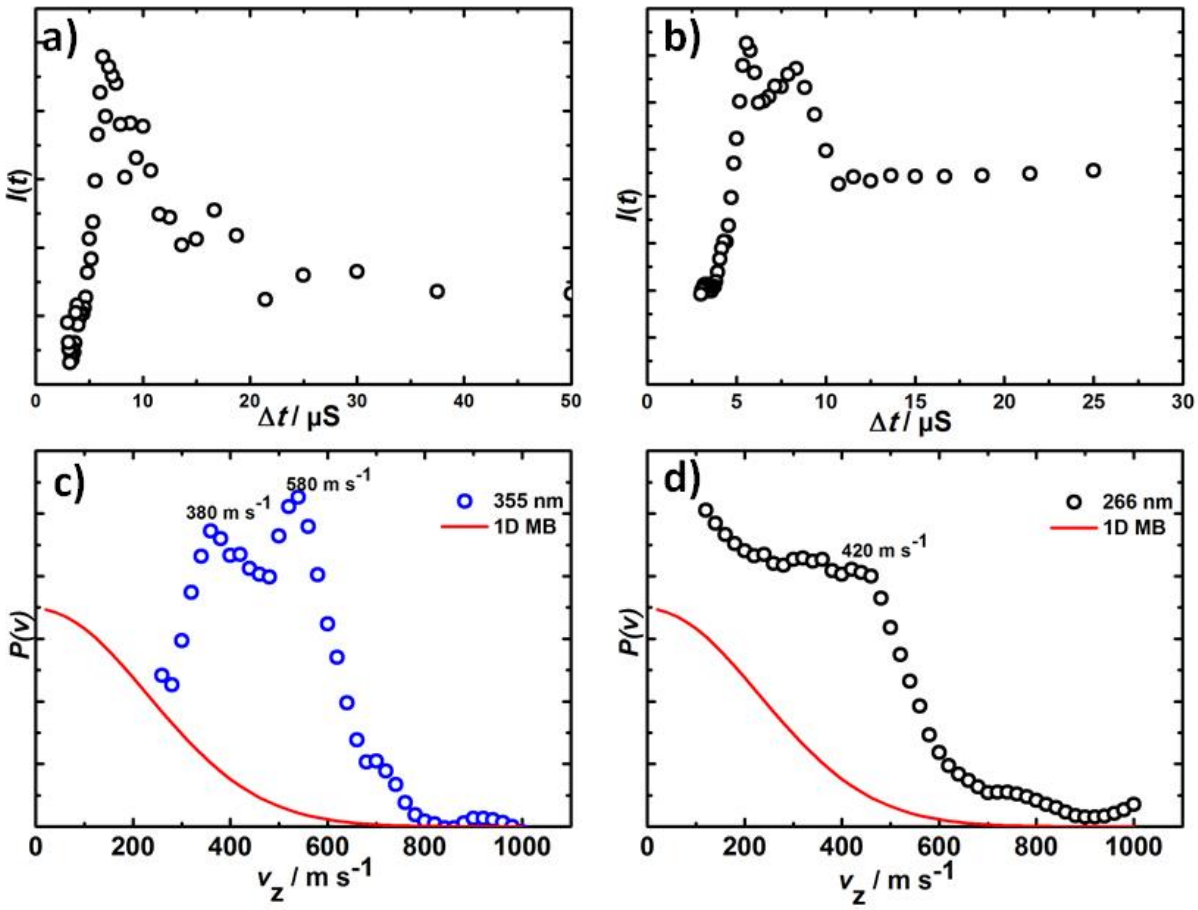

Figure 5.3: Top (a & b) time-of flight data for NO photodesorbed from Au(100) at 355 and 266 nm. Bottom (c & d) normalised velocity distribution of photodesorbed NO after density-to-flux conversion of the raw data at 355 nm (blue circles) and 266 nm (black circles) by using a LabView program. 1D Maxwell Boltzmann at 178 K is provided for comparison in both cases (red line).

Fig. 5.3 shows that for the 1D velocity distribution in case of 355 nm desorption (blue circles), the velocity components are shifted to higher velocities when compared to a 1D Maxwell-Boltzmann distribution at the surface temperature of 178 K. The 355 nm velocity distribution peaks at $380\,\mathrm{m\,s^{-1}}$ and $580\,\mathrm{m\,s^{-1}}$, and the signal ends at velocity of $\sim 800\,\mathrm{m\,s^{-1}}$. It can be described as bi-modal, giving unambiguous evidence for the two different desorption mechanisms, which will be discussed later. These results are in agreement with those obtained by Menges and his group.[7] They have combined a state selective (REMPI) detection with an imaging technique to study the photo-desorption of NO/NiO(111). The obtained 2D velocity distribution was described as bi-modal. Mull *et al.* observed bi−modal velocity distributions that were independent of internal vibrational excitation after UV-laser induced desorption on NO from oxide surfaces and attributed this to the presence of two non−thermal desorption channels.[153] The different velocities observed for the desorbing NO molecules could be caused by different mean lifetimes which provide a natural explanation of the bi-modal velocity flux distributions.

In Fig. 5.3, the 266 nm velocity distribution (black circles) peaks at around $420\,\mathrm{m\,s^{-1}}$ followed by sharp decline and extending to $\sim 900\,\mathrm{m\,s^{-1}}$. Both velocity distributions are indicating a non-thermal desorption mechanism for both wavelengths investigated. However, remarkably the velocity distribution for the lower energy 355 nm desorption is shifted towards higher velocities compared to the 266 nm desorption. This may be indicative of one desorption channel present for the 355 nm that was not available for 266 nm desorption.

The translation temperature for both 226 and 355 nm desorption were calculated using

$$T_{tr} = E_{tr}/2\,k_B \tag{5.1}$$

where: E_{tr} is the transnational energy and k_B is boltzmann constant.

It found to be 116 K and 290 K for the slowest and fastest velocity component for 355 nm, respectively. A temperature higher than the surface temperature i.e. 290 K indicates the velocities in the direction normal to the surface, and the other temperature which is lower than the surface temperature, indicates velocities in the direction parallel to the surface. In the 266 nm desorption, the T_{tr} is about the same as the surface temperature (178 K) which indicates thermal desorption mechanism. Again the sharp decay in the 266 nm velocity distribution might indicate a thermal mechanism due to

the temperature jump (20 K) for 266 nm desorption. Photon-induced thermal desorption would exhibit a relatively slow onset following the beginning of irradiation due to the thermal equilibrium. Another noticeable difference was that the absolute signal intensity is significantly weaker by ∼40% for 266 nm desorption compared to 355 nm desorption for similar laser fluences, hence bigger laser diameter beam was used for 266 nm. The low signal obtained for the 266 nm desorption could be due to the fact that the photon energy is very close to the work function of gold (∼ 4.8 eV) [154], raising the possibility of ionisation of surface gold atoms forming a cationic surface which is more active, as NO donates electrons to Au, hence the adsorbed NO will be more strongly held onto the surface.[89]

It was mentioned earlier that the goal was to obtain the 3D velocity distribution. The recorded images from velocity map imaging provided the remaining two velocity components v_z and v_y, which are parallel to the Au(100) surface. Images were recorded at laser delay times corresponding to velocities v_z in 20 m s^{-1} intervals from 120 to 470 m s^{-1} for both wavelengths, as the signal before and after the indicated range is very week and does not yield images. The images were recorded at different velocities not just at the peak ones, see Fig. 5.4.

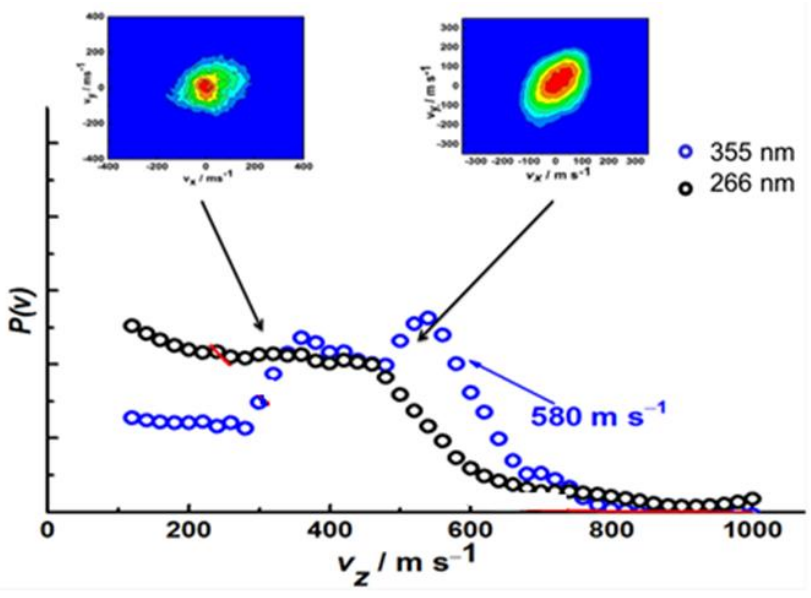

Figure 5.4: Raw 640 x 480 VMI images of NO desorption from Au(100) taken at time delays corresponding to different values of v_z, 240 m s^{-1} and 590 m s^{-1} for 266, and 355 nm, respectively.

The centre of these images corresponds to zero velocity in the x and y dimension, even though this centre is shifted slightly with respect to the centre of the CCD camera, an effect that was also observed in previous gas-phase experiments and was attributed to a slight misalignment of the ion optics.

Fig. 5.5 shows a set of images for 266 and 355 nm desorption at the same velocities.

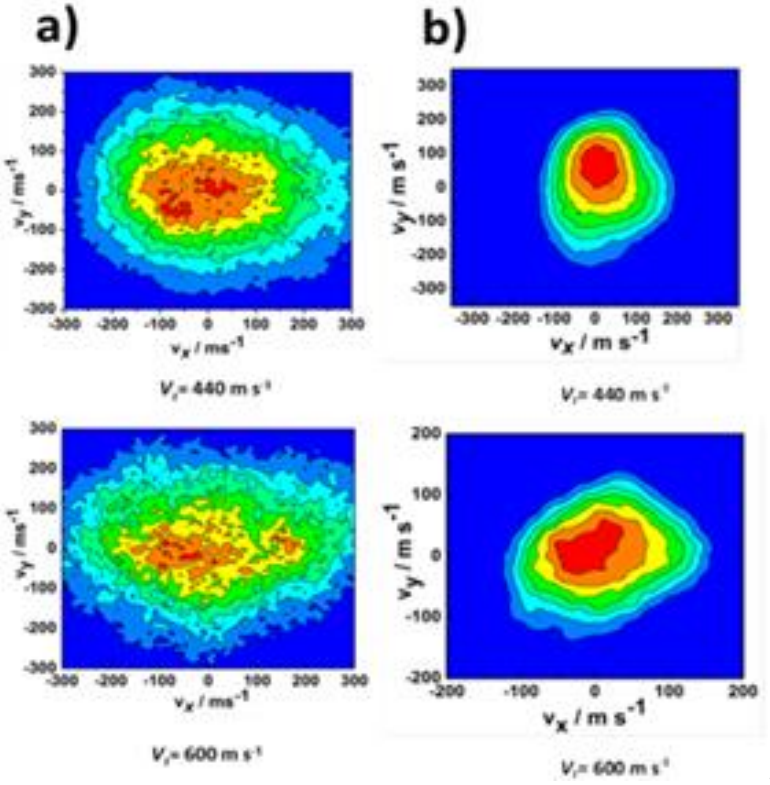

Figure 5.5: Set of images at different values of v_z (440 m s^{-1}, 600 m s^{-1}) a) 266 nm desorption laser and b) 355 nm desorption laser.

The images were of low quality compared with the 355 nm ones due to the weak signal intensity obtained. Other factors, however, could be contributing the this image asymmetry such as the illumination of an ellipsoidal area on the surface by the desorption laser due to its 45° angle of incidence and the probe laser which is being focussed using a cylindrical lens and having a Gaussian intensity profile in one direction not subjected to focussing. The latter favours ionising molecules desorbing along the surface normal over those flying up or down in the laboratory frame, the flying desorbed molecules seem to intersect the central part of the laser beam, keeping distortions at a modest level.

As the VM images appear roughly circular, i.e. there does not seem to be a preference for the NO molecules to fly along the [001] over the [010] direction, we azimuthally averaged the two velocity distributions parallel to the Au(100) surface to yield $v_{x/y}$. Fig. 5.6 explains how it is done by using a custom-written LabVIEW program.

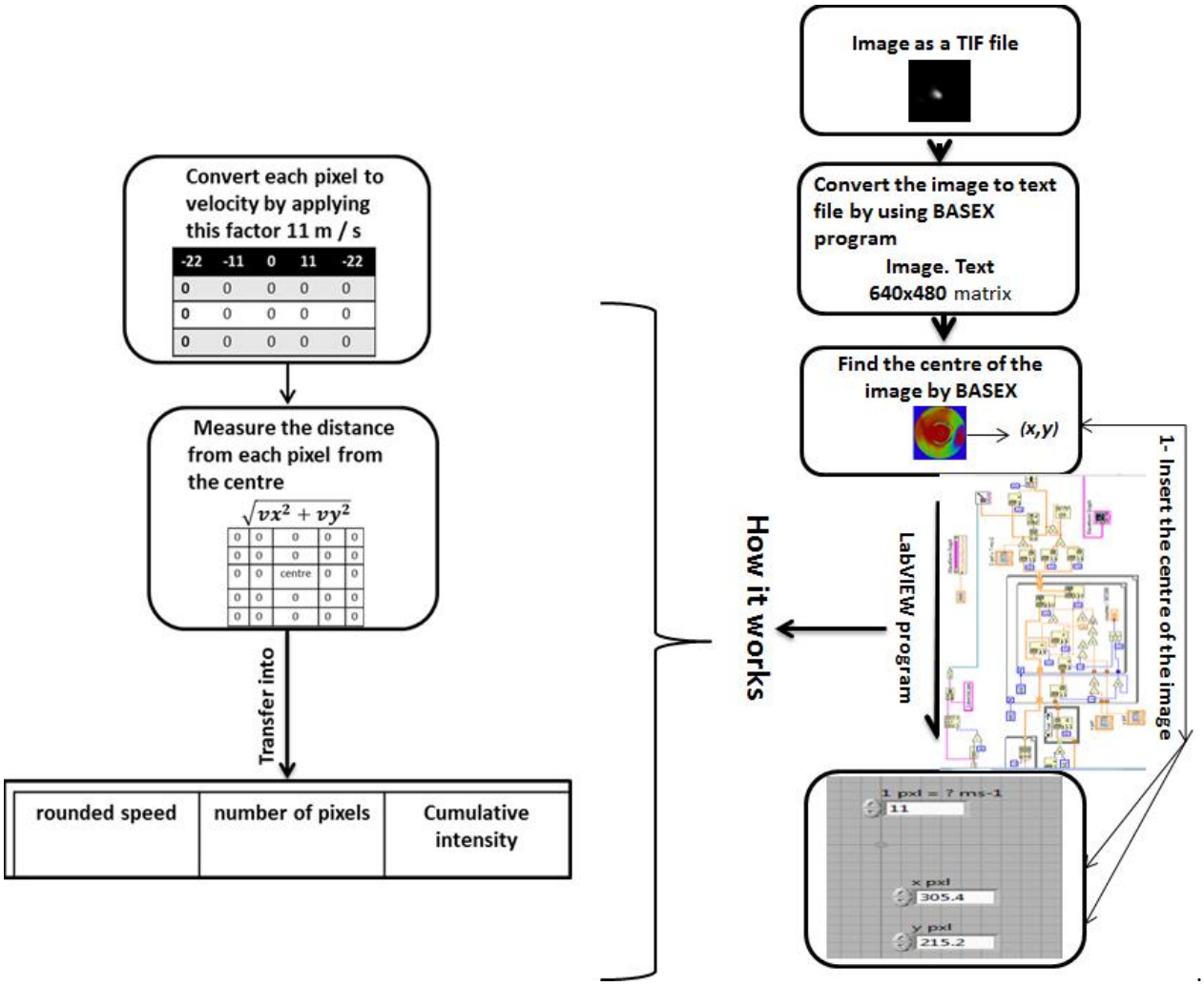

Figure 5.6: Flow diagram showing how to extract v_{xy} from VMI image, for each pixel in the matrix, the distance from that pixel to the centre of the image (i.e. the normal) is calculated. The centre is taken as $v_{x/y} = 0$ and pixels furthest from the centre correspond to the largest values of $v_{x/y}$. Each pixel corresponds to a step in speed of $11\,\mathrm{m\,s^{-1}}$. The newly calculated speeds at each pixel are rounded to the nearest whole number, and transferred into a three column array. Pixels corresponding to the same speed are binned together. The first column of the array contains the rounded speed, the second column contains the number of pixels corresponding to that speed, and the third column contains the cumulative intensity.

Fig. 5.7 shows the smoothed NO intensity as a function of $v_{x/y}$ and v_z as a surface plot for a) 355 and b) 266 nm desorption. For the 355 nm potons, i.e. energy is below the substrate's work function, the velocity in z direction peaks at 380 and 580 $\mathrm{m\,s^{-1}}$ but extends up to $\sim$800 $\mathrm{m\,s^{-1}}$ with $v_{x/y}$ almost completely vanishing at velocities $\sim$200 $\mathrm{m\,s^{-1}}$, hence a narrow angular distribution is obtained along the surface normal in this case. When using 266 nm photons, i.e. energies just below the substrate's work function, the v_z velocity distribution seems to plateau between 120 and 420 $\mathrm{m\,s^{-1}}$ followed by a sharp decline with v_z vanishing at around 900 $\mathrm{m\,s^{-1}}$, as seen in Fig. 5.7 b), while $v_{x/y}$ extends all the way to below 400 $\mathrm{m\,s^{-1}}$.

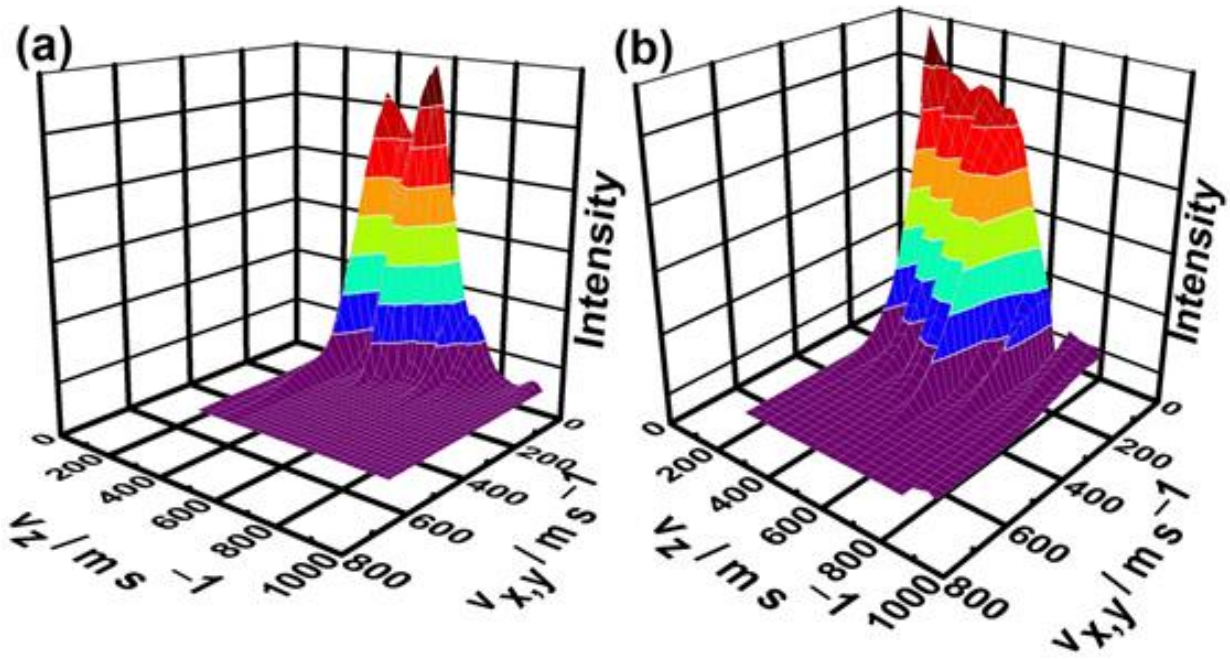

Figure 5.7: Smoothed surface plot of the NO flux desorbed using (a) 355 and (b) 266 nm photons as a function of v_z (from TOF measurements), and averaged parallel (to the gold surface) $v_{x/y}$ velocity components (from the VM images).

The faster and narrower distributions in the 355 nm and the slower and wider distributions in the 266 nm desorption is another indication that two different desorption mechanism are in operation.

The angular distribution as a function of the overall speed has also been calculated. Fig. 5.8 a) shows that the angular distribution at 355 nm is rather narrow ($< \pm 20°$), i.e. the NO molecules preferentially desorb along the surface normal. The geometry of our 3D surface VMI setup as mentioned earlier allows much wider angular distribution to be detected than those measured here, up to $\pm$ 53°.

Fig. 5.8 b) shows fits of these distributions to $\cos^n \theta$ functions. A fitting parameter of

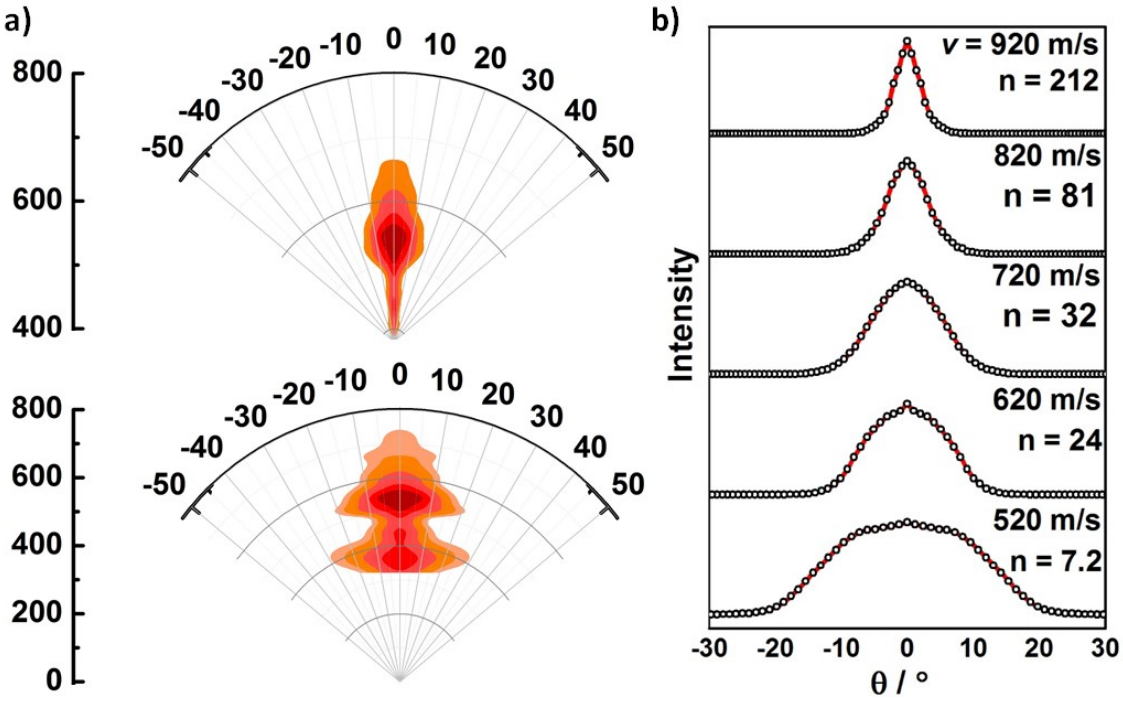

Figure 5.8: a) Nitric oxide flux as a function of overall speed and angle after 355 nm photodesorption. Color scheme from red (most intense) to orange (zero intensity). b) Angular distributions for selected speeds of desorbed NO molecules after 355 nm photodesorption together with fits to a $\cos\theta$ function.

n i.e. a $\cos\theta$ distribution processes. For 355 nm desorption, the angular distributions for even the slowest NO molecules can only be fitted with n > 1, and it can be seen that the angular distributions become narrower with increasing overall speed. This strongly peaked distribution of the fast channel means that the molecules have a fast velocity component pointing along the surface normal and only slow velocity components parallel to the surface (i.e. the x and y direction).

Fig. 5.9 a) shows the angular distributions of 266 nm desorption as a function of overall speed. The angular distribution is much wider than the 355 nm (± 35°), however, NO is still preferentially flying along the surface normal. For 266 nm des-

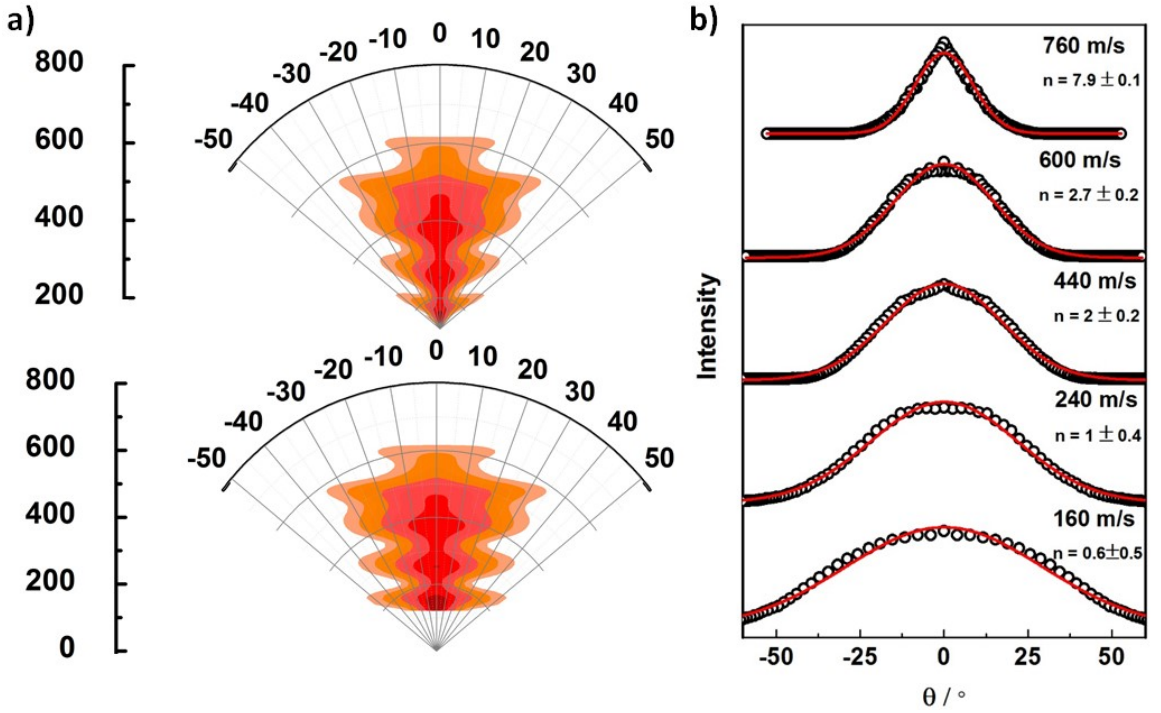

Figure 5.9: a) Nitric oxide flux as a function of overall speed and angle after 266 nm photodesorption. Color scheme from red (most intense) to orange (zero intensity). b) Angular distributions for selected speeds of desorbed NO molecules after 266 nm photodesorption together with fits to a $\cos\theta$ function.

orption, Fig. 5.9 b), at overall speeds of $240\,\mathrm{m\,s^{-1}}$ or lower, the angular distribution can be fitted to $\cos^n\theta$ resulting in n $<$ or $=$ 1 suggesting that a thermal desorption mechanism may be operating. However, for the higher speeds shown here, n $>$ 1, indicating a non-thermal desorption process. At both wavelengths investigated, the NO molecules is flying roughly symmetrically along the surface normal. The strong peaking along the surface normal has also been observed in laser desorption experiments of NO/Pt(111),[144, 145, 150] and electron-stimulated desorption experiments of NO from NO_2/Pt(111).[155]

For 266 nm desorption, all of the above results indicate that thermal and non-thermal desorption mechanisms are operating. This has also been suggested in the case of laser-induced desorption of NO from Ni(100)−O,[150] and from condensed films.[156] The authors reported that ultraviolet laser of ($4.6-5.5\,\mathrm{eV}$) induced desorption from

the surface of a thin nitric oxide film proceeds via two mechanisms which are present simultaneously. One mechanism is attributed to laser induced thermal desorption while the other is due to a non-thermal process. This seems to be in agreement with the angular distributions, where a thermal desorption mechanism seems to be responsible for the slower NO molecules after 266 nm photodesorption.

5.3.2 Internal Energy Distributions

To obtain a better understanding of the underlying mechanism of NO photodesorption from Au(100), we have extended the above translational energy measurements to internal state (rotational) distribution measurements.

5.3.2.1 Rotational Energy Distribution

The rotational state distributions of NO photodesorbed from Au(100) were extracted from the intensity distributions of the (1+1) REMPI spectra recorded on the transition $A^2\Sigma_{1/2} \leftarrow X^2\Pi_{3/2}(0,0)$ at a fixed time delay (i.e. for a fixed velocity) of 7.1 µs corresponding to the peak in the velocity distribution $v_z = 420\,\mathrm{m\,s^{-1}}$ in case of 266 nm, and 7.8 µs and 5.1 µs corresponding to peaks in the velocity distribution $v_z = 350\,\mathrm{m\,s^{-1}}$, $580\,\mathrm{m\,s^{-1}}$, respectively as mentioned above in the Experimental (5.2). No vibrationally excited NO molecules were detected. Fig. 5.10 shows a REMPI spectrum for 355 nm desorption at $350\,\mathrm{m\,s^{-1}}$.

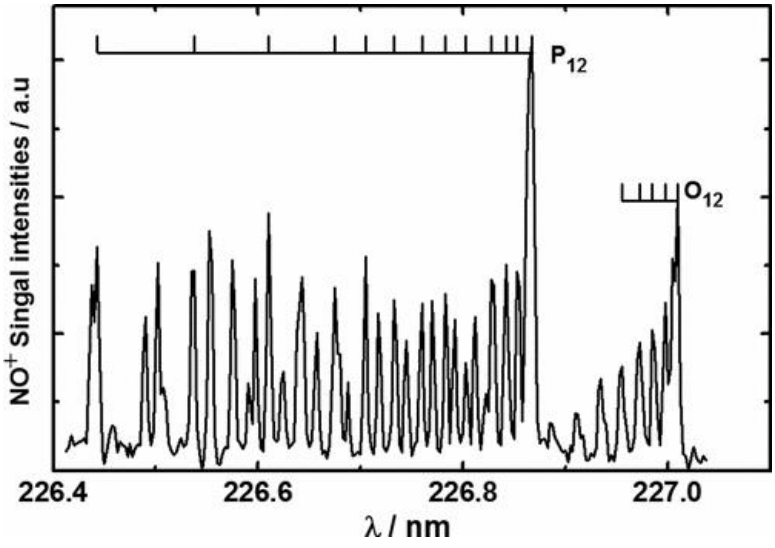

Figure 5.10: Typical (1+1) REMPI spectrum of NO desorbed from gold using 355 nm photons at a time delay corresponding to NO molecules with $v_z = 380\,\mathrm{m\,s^{-1}}$

As described in the Experimental, spectra of thermal NO were recorded to perform background subtraction and to apply a relative calibration scheme to extract the rotational state distribution of the photodesorbed NO. To obtain the rotational population distributions for the $v = 0$, first we assigned the observed transitions in the measured REMPI spectrum based on a simulated spectrum carried out with the software LIFBASE, see Appendix C. In the course of fitting, attention was only paid to lines and branches which did not overlap with any other lines. To determine the energy of the rotational levels, the experimental findings of Gillette and Eyster were used,[157] deploying the formula suggested by Herzberg. The rotational temperature was calculated then by dividing each transition peak intensity by the Honl−London factors and the degeneracy of the initial state $(2J + 1)$, see eq 5.2.

$$T = (121.1)\,\mathrm{cm}^{-1} + \omega_e(v + 0.5) - \omega_e x_e(v + 0.5)^2 + BvJ(J + 1) \tag{5.2}$$

where is: $\omega = 1903.68$, $\omega_e x_e = 13.97$ cm^{-1}, $B_e = 1.7046$ cm^{-1}

To simplify population analysis, isolated lines from single branches were observed, hence avoiding overlap, to obtain reliable rotational populations. Transitions originating from N = 4-7 and N = 7-16 of the O_{12} and P_{12} rotational branches of NO were chosen, respectively. After weighing the populations by the degeneracy of the lower level, the energies of the rotational levels were calculated to yield Boltzmann plots for selected velocities. Fig. 5.11 shows the Boltzmann plot of photodesorbed NO corresponding to a velocities of 580 and 350 m s^{-1} for the 355 nm, respectively, and 420 m s^{-1} for 266 nm desorption, characterized by a single straight line yielding a rotational temperatures.

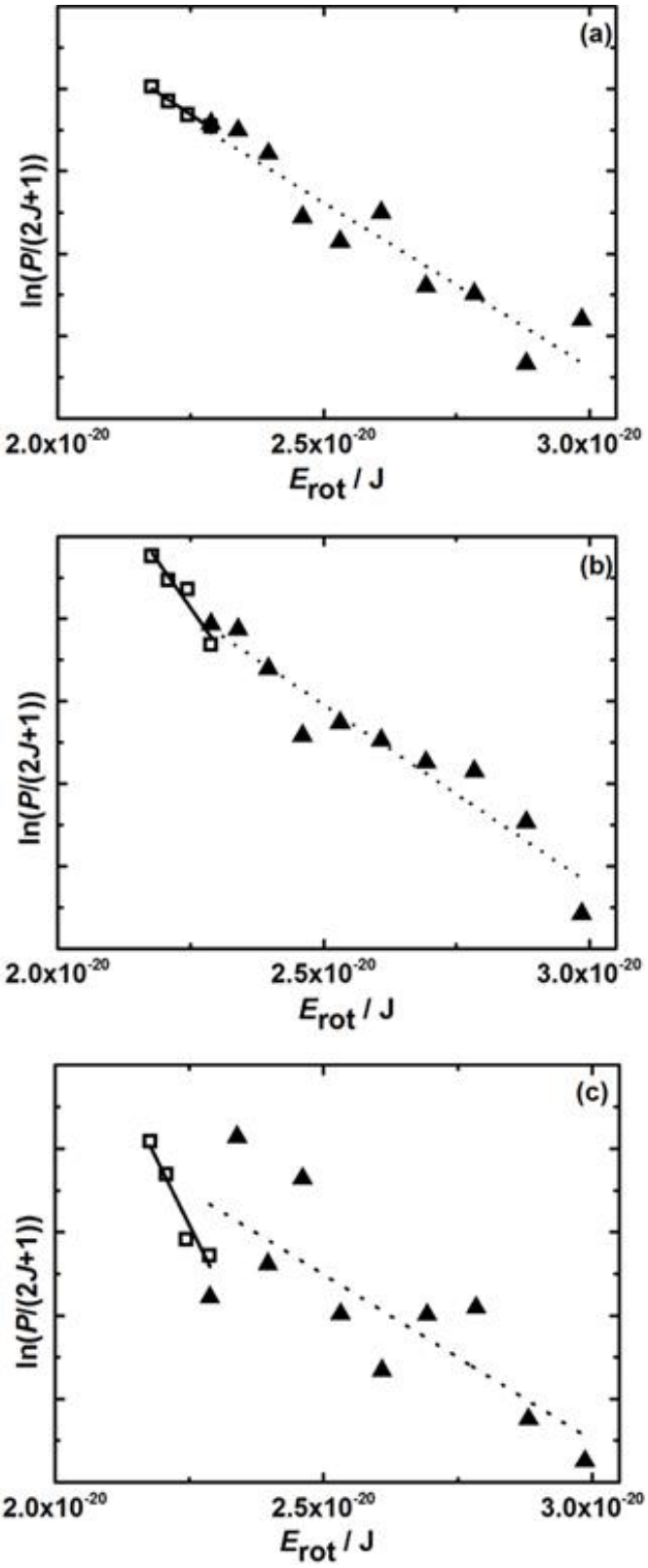

Figure 5.11: Rotational populations of NO molecules in v = 0 desorbed at 178 K extracted from the O_{12} (open squares) and P_{12} (closed triangles) branches; solid and dotted lines are linear best fits to evaluate the rotational temperature a,b) for 355 nm at 380 m s^{-1} and 580 m s^{-1} respectively c) for 266 nm at 420 m s^{-1}.

The contributions from the two spin−orbit states $X^2\Pi_{1/2}$ and $X^2\Pi_{3/2}$, which are energetically separated by about 124 cm^{-1}, fall along the same line in the Boltzmann plots. When the rotational populations in the two spin−orbit states are fitted separately, they give almost the same rotational temperature, which suggests the spin−orbit excitation is in thermal equilibrium. In such cases, the abscissa in the Boltzmann plot can be represented by the sum of the rotational and the spin-orbit energy. Since spin−orbit states are related to the axis around which rotation occurs, the results indicate that there is no preference for tumbling of the NO around a particular axis; this is expected for NO adsorbed along the surface normal on a symmetric Au(100) substrate. While there is no a priori reason for these nascent rotational state distributions of photodesorbed NO to be thermal, we nonetheless fitted the distributions to obtain rotational temperatures, thus simplifying comparison between different experimental conditions, the results are summarised in Table. 5.1 below:

Table 5.1: Rotational temperatures T_{rot} of nascent NO photodesorbed from an Au(100) surface using 355 and 266 nm photons.

	Desorption laser wavelength		
	355 nm		**266 nm**
Rotational Branch	$v_z = 380\,\mathrm{m\,s^{-1}}$	$v_z = 580\,\mathrm{m\,s^{-1}}$	$v_z = 420\,\mathrm{m\,s^{-1}}$
O_{12}	(337 ± 12) K	(206 ± 5) K	(102 K ± 1) K
P_{12}	(363 ± 4) K	(334 ± 4) K	(226 K ± 5) K

Inspection of the above table, shows that the rotational temperatures for 355 nm desorption at the two investigated velocities above the surface temperature for both branches O_{12} and P_{12}, indicating a non-thermal desorption mechanism, in agreement with our previous results from the transnational and angular distributions. The average rotational temperature in both O_{12} and P_{12} branches after 355 nm desorption is lower for the faster component, this indicates a positive correlation, i.e. the translational and rotational energy are coupled and energy is partitioned during a common single step of the desorption process which confirms the non-thermal desorption mechanism. A correlation between rotational and translational excitations has been observed in many system.[153, 158] A striking feature is that with increasing temperature, the intensity of the slow channel increases compared with the fast one, and this is in agreement with work by Hasselbrink *et al.* who used Ultraviolet irradiation of

NO_2 adsorbed on top of a NO saturated Pd(111) surface, by using excitation energies between 3.5 and 6.4 eV caused the photodissociation of NO_2/N_2O_4 and results in the desorption of NO molecules. [159] For the higher energy wavelength of 266 nm, the temperature at the investigated velocity is less than the average rotational temperatures at 355 nm for the two investigated velocities. This was also the case for the translational temperatures as the average translational energy after 266 nm desorption is also lower compared to 355 nm desorption. The temperature for the O_{12} branch is less than the surface temperature which suggests that rotational cooling may have occurred during desorption. This is not unexpected for a thermal process based on the principle of detailed balance; NO molecules are likely to adsorb more readily onto a metal surface when they are rotationally cold (as rapidly rotating molecules would not spend sufficient time in the favorable head-on orientation for adsorption to occur), hence the fraction of NO molecules thermally desorbing from the Au(100) surface after the laser-induced temperature jump may also be rotationally cold. This is in agreement with Burgess *et al.* who studied desorption of CO from Cu substrates heated with UV lasers. They measured Maxwellian TOF distributions below the predicted surface temperature, with no evidence of collisions, although desorbed fluxes were high. [160] Similar results were obtained by Cavanagh and King on NO-Ru(100) by using a combination of TPD and LIF to study the rotational distribution, where the surface temperature was 455 $\pm$ 20 K.[161] The rotational temperatures obtained were found to correspond to nearly half of the surface temperature which is an evidence for rotational cooling. Mantell and his group studied the thermal desorption of NO on Pt(111) and established that NO is essentially fully rotationally accommodated. [162] Tully and Cardillo reported on rotational cooling of NO desorbed from an Ag(111) surface. [163] The authors argued that some of NO molecules would desorb by transforming rotational energy to translational energy, hence these molecules will have less that the average rotational energy corresponding to the surface temperature The rotational cooling phenomenon in the desorption process of molecular adsorption system has been observed experimentally and explained theoretically. For the P_{12} branch the obtained rotational temperature is above the surface temperature which again points towards a non-thermal mechanism. This seems to agree with conclusions from the previous section, i.e. the presence of potentially two different mechanisms, or at

least the contribution of a thermal mechanism to the 266 nm desorption. Theoretical calculations for very rapid laser-induced desorption (LID) processes have indicated a propensity toward near full translational accommodation in the desorbing molecules but less than full rotational accommodation, similar to what we observe here.[164]

5.3.3 Effect of Photon Density

Examination of the power dependence of the desorption laser can shed light on the mechanism of the desorption process. An energy dependence scan was recorded by varying the energy of the desorption laser and recording the signal intensity. The desorption of NO induced by nanosecond laser pulses (355 nm in this case) from Au surface was found to be linear with the laser energy. 5.12 displays a logarithmic plot of the neutral NO signal vs laser energy which was probed by REMPI through the (0.0) transition.

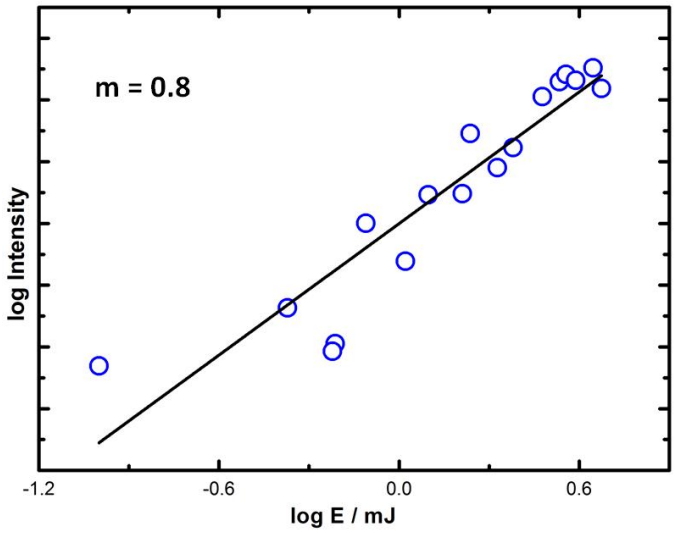

Figure 5.12: Logarithmic plot of neutral NO intensities after 355 nm desorption laser as a function of laser intensity.

The slope of the line is ∼0.8, suggesting that single photon absorption leads to photodesorption of NO from the Au surface. This is similar to the observation for the ion current produced in electron stimulated desorption (ESD).[165, 166] A linear power dependence with a slope of 1 of the NO photodesorption yield contradicts the expected exponential power dependence for thermally induced desorption.[167]

5.3.4 Summary

In this chapter, Photodesorption of NO molecules pre-adsorbed on an Au(100) surface was investigated at 355 and 266 nm desorption laser. The transnational and rational distributions for each wavelength were recorded, analysed and interrupted. Two desorption mechanism are available for both investigated wavelengths. For the 355 nm desorption, it seems to predominantly occur through a non-thermal channel, likely involving an electronic excitation. However the thermal mechanism cannot be excluded. However for the 266 nm desorption a thermal mechanism is operating. Results obtained also suggest the photodesorption mechanism of NO is wavelength dependent.

Chapter 6

Near-Ambient Pressure X-ray Photoelectron Spectroscopy

In this chapter the NAP-XPS used to investigate NO adsorption on Au surface at high pressure and different surface temperatures.
In this study adsorption was "performed" on a sputtered gold surface Au(100) as no adsorption was observed on the sputtered annealed smooth surface at the lowest temperature achieved in the system.

6.1 Introduction

The adsorption structures of NO on metal surfaces have been studied by various surface techniques, most of which require ultrahigh vacuum (UHV) conditions. However, the behavior of adsorbates on model systems in UHV can differ significantly from real catalysts under ambient conditions. To overcome the gap between model and the real surfaces, it is important to know the NO adsorption behavior under ambient pressure. A high-frequency of collisions of gaseous species occur at elevated pressures, this can cause some surface processes, for example bond breaking, chemisorptions, and lateral shifts of adsorption sites. No previous study have been conducted on NO/Au(100). The NAP-XPS technique was developed in the early 2000s, but is still in its infancy. Therefore the established literature is limited, especially with respect to the study of adsorption on metal surfaces by a NAP-XPS system. However, there are a few studies relevant to the work presented here, but on different metal surfaces.

Bukhtiyarov *et al.* investigated the adsorption of NO on gold particles deposited on an alumina film in the temperature range 300 - 500 K using in situ X-ray photoelectron spectroscopy (XPS). [168] Two nitrogen-containing adsorbed species were found to exist on the surface of gold particles. The first was identified as adsorbed nitrogen atoms characterised by a N 1s binding energy (BE) of 399.4 eV. The second species was identified as a surface complex with N_2O stoichiometry characterised by a BE of 402.7 eV and found to be thermally stable only in a narrow temperature range of 325-425 K. Identification of these species was aided by a separate experiment in which NO was adsorbed onto a stepped Au(533) crystal.

Bukhtiyarov *et al.* employed in-situ-XPS to investigate the decomposition of NO on flat Au(111) and stepped Au(310) and (533) surfaces at elevated NO pressures up to 7 Pa and in a temperature range between 300 and 500 K. [96] NO was found not to chemisorb on Au(111) under the conditions used. However, dissociation of NO was observed on both Au(310) and (533) surfaces. The authors concluded that Au step-sites are responsible for adsorption and dissociation of NO. The study revealed that while NO dissociation on Au(310) exclusively forms N_{ads} on the surface whose coverage decreases with increasing surface temperature, NO dissociation on Au(533) initially forms N_2O_{ads} on the surface that is replaced by more stable N_{ads} at increasing NO exposure and/or surface temperature.

Shimada and his group have used the (NAP-XPS) to investigate NO adsorption on Pt(111) under various pressures of NO up to 1 Torr at room temperature. [169] They found that NO molecularly adsorbed below 10^{-7} Torr and occupied the most stable fcc-hollow sites and partially the more energetical atop sites. At higher pressure of 10^{-6} Torr, irreversible adsorption of atomic oxygen takes place via NO dissociation, leading to the formation of NO+O domains.

Toyoshima *at el.* reported the molecular CO and NO adsorption structures on Pd(100) single crystal surfaces by using a combination of ambient pressure X-ray photoelectron spectroscopy and density functional theory under sub-Torr pressure conditions at room temperature. [170] In the case of NO adsorption at 10^{-7} Torr, a $(2\sqrt{2} \times \sqrt{2})$R45° structure with occupying bridge sites is formed, additional site occupation of on-top sites caused after subsequent gas introduction up to 0.5 Torr is also observed. The authors found that NO partially dissociates into atomic N and O species, but these

disappear from the surface due to further reaction with NO under ambient conditions. Ueda *et al.* studied the adsorption of CO and NO on the Ir(111) surface at room temperature under UHV and NAP conditions. They found NO under NAP conditions only molecularly adsorbed on the surface, while under UHV, could dissociated species and molecular NO are co-adsorbed in a (2 x 2) structure.

In this thesis work, NAP-XPS has been used at different substrate temperatures and pressure of 1 mbar in order to obtain some insight in to the alignment of NO on gold and how it is adsorbs on the surface.

6.2 Experimental Apparatus

The Near-Ambient Pressure X-ray Photoelectron Spectroscopy (NAP-XPS) instrument is a recent acquisition in the Photon Science Institute at the University of Manchester. The system is a custom-built design developed by SPECS-GmbH. The instrument is equipped with a SPECS focus 500 monochromated Al Kα source (photon energy 1486.6 eV), which can be focused to a spot size of 300 μm. The instrument can be operated in conventional XPS mode, i.e. under ultra-high vacuum conditions ($< 10^{-9}$ mbar) or under near-ambient pressures (1 mbar in the experiments carried out here). The instrument is equipped with an Ar^+ ion source and e-beam capable of heating the surface to 1000 K. Samples can be cooled to ~100 K using liquid nitrogen under UHV conditions. For the NAP-XPS measurements, the sample is placed in a high-pressure chamber separated from the X-ray source by a SiN window, which is transparent to X-rays, see Fig. 6.1.

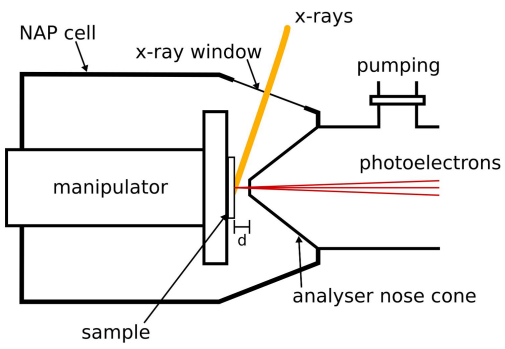

Figure 6.1: Diagram of a NAP cell. Incident X-rays must first pass through a SIN window that is transparent to X-rays. This window is only a few microns thick and can withstand pressures in the NAP cell up to 20 mbar.

Electrons and gas can escape through the differentially-pumped aperture, as shown schematically in Fig. 6.2

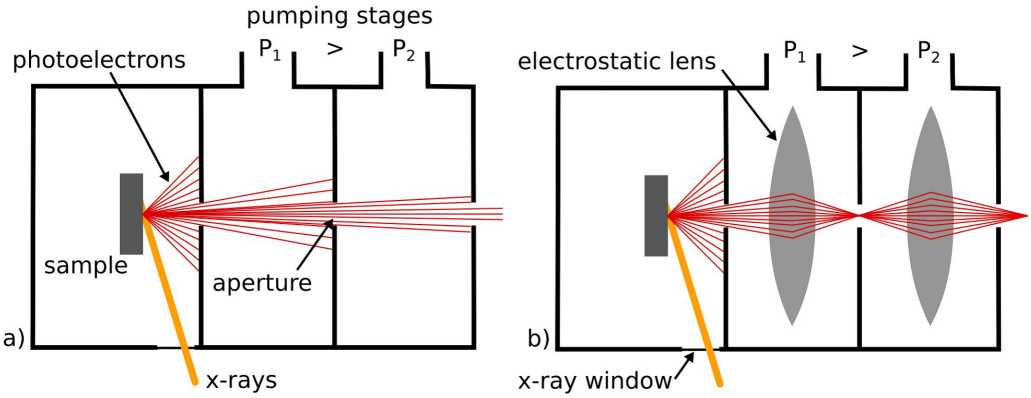

Figure 6.2: Schematic showing how electrostatic lenses can be used to increase electron count rate at the analyser. a) A differential pumping system consisting of individually pumped chambers separated by small apertures to allow photoelectrons to reach the analyser while also maintaining a steep pressure gradient from sample to analyser. b) The same system with the addition of electrostatic lenses between each aperture.[171]

The electron analyser, see Fig. 6.3, is a 150 mm mean radius SPECS Phoibos 150 NAP electron energy analyser with three differential pumping stations.

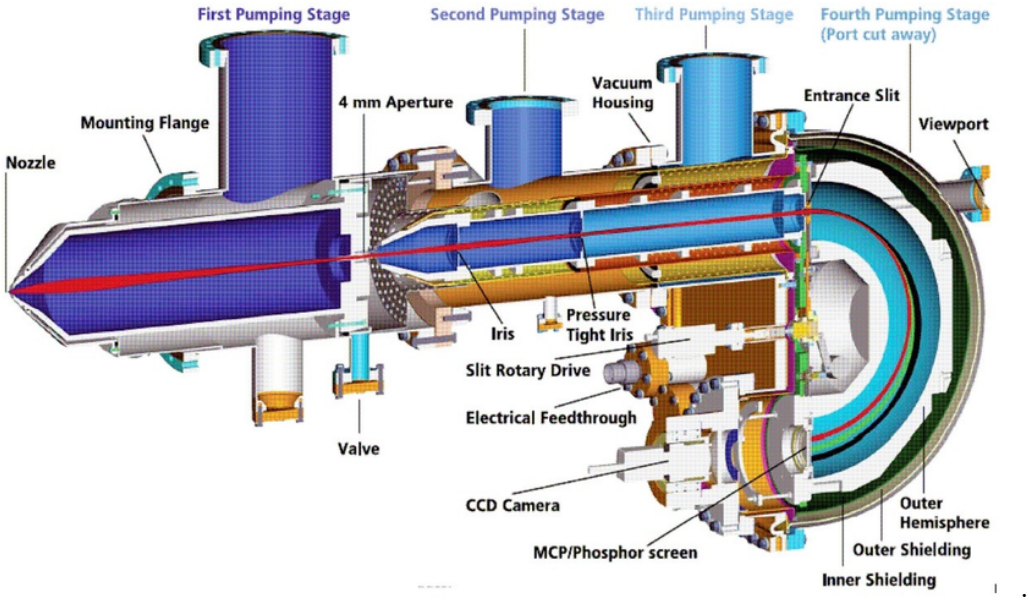

Figure 6.3: Cross-section of PHOIBOS 150 NAP analyser showing the differentially-pumped electron energy analyser. The four differential pumping zones are colored in different blue shades.[172]

The first pumping station (pre-lens) is separated from the analysis chamber by a nozzle with a 0.3 mm hole at the tip. A turbo pump (500 l/s) on the pre-lens stage enables a pressure difference of four orders of magnitude compared to the NAP cell. The first and second sections are separated by a 4 mm aperture. The second section contains the first set of electrostatic lenses. The front and rear components of the electrostatic lenses are separated by an iris aperture and the third pumping stage is placed behind the iris. The fourth and final pumping station services the hemispheres and detector. The near-ambient-pressure cell allows measurements at gas pressures at the sample of up to 20 mbar. NAP-XPS has been developed in order to overcome one of the main drawbacks of XPS, i.e. that UHV does not mimic real-life conditions. While NAP-XPS cannot be carried out at atmospheric pressures, 20 mbar is ∼11 orders of magnitude higher than UHV, and in the case of water adsorption, achieves the sort of pressures found in typical average humidity conditions.

6.3 Sample Preparation and Experimental Producer

The Au(100) crystal, which has been used for the S-VMI work, was mounted on a tantalum sample plate, polished side up, by spot-welding two clips made of tantalum foil over each of the short edges, leaving a visible surface area of approximately 5 × 5 mm between the clip, as shown in Fig. 6.4.

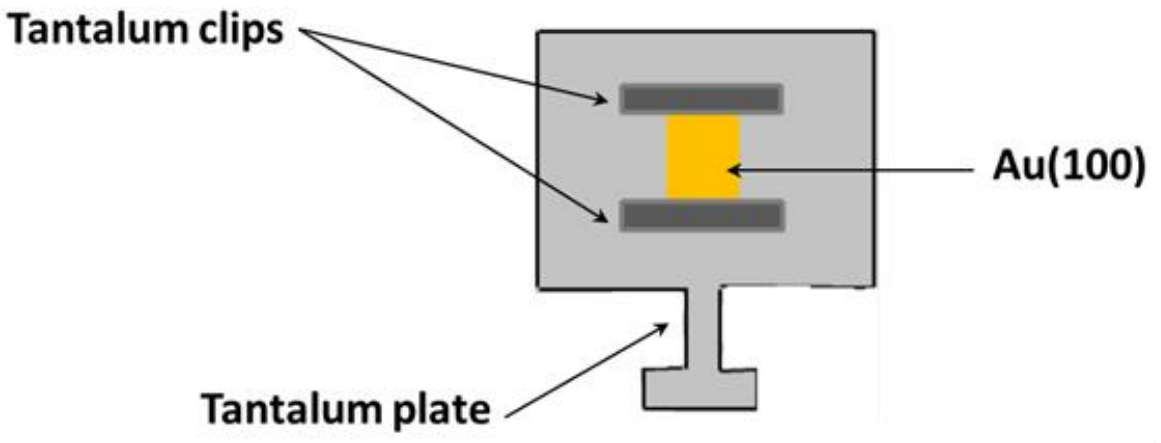

Figure 6.4: Schematic of a Au(100) crystal mounted onto a tantalum plate.

After mounting, the sample was placed into the load-lock of the SPECS NAP XPS equipment. Once at high vacuum, the sample was transferred to the main UHV chamber. The Au(100) crystal surface was cleaned by Ar ion sputtering cycles (sputter for 900 s, sputter again for another 1800 s followed by annealing 20 mins via e-beam heating at ∼1000 K, and sputter again for 30 min). Initially, a wide kinetic energy range XPS spectrum was recorded to verify that the sample was clean. While no oxygen was found on the surface after this cleaning procedure, a fair bit of carbon was still present (not shown). After further cleaning, the UHV chamber was left to pump down to a base pressure $\sim 10^{-9}$ Torr and the sample was transferred to the NAP cell, and the gate between the cell section and the UHV chamber was closed. XP spectra were recorded with NO flowing into the cell at 1 mbar and varying substrate temperatures. However, we failed to detect any NO adsorbed on Au(100) even at a base temperature of 220 K after the substrate had been prepared by sputtering and annealing, hence XP spectra for O 1s and N 1s at 220 K and 266 K were all recorded on a only sputtered gold substrate. The binding energies of the photoelectron spectra were calibrated to the bulk Au 4f 7/2 peak at 84 eV. All spectra were normalised the baseline intensity, background subtraction has performed and spectra were fitted with an appropriate number of Gaussian functions using CasaXPS.[173]

6.4 Results

After exposure of Au(100) to NO at 1 mbar at room temperature, N 1s and O 1s spectra were recorded as a function of temperature and pressure allowing for the characterisation of nitrogen and oxygen surface species adsorbed on Au(100).

The N 1s spectrum Fig. 6.5 a) shows two peaks at binding energies of 406.1 eV and 407.5 eV with the latter less intense then the former. These peaks are attributed to gaseous NO molecules, and in agreement with the results obtained by Ye *et al.* [174, 175]

In the O 1s spectrum, Fig. 6.5 b), twin peaks appear at 531.3 and 532.8 eV, and one at 538.8 eV. The twin peaks can be attributed to residual CO adsorbed on the surface.[169] The peak at 538.8 eV is due to the oxygen atom in gas-phase NO.

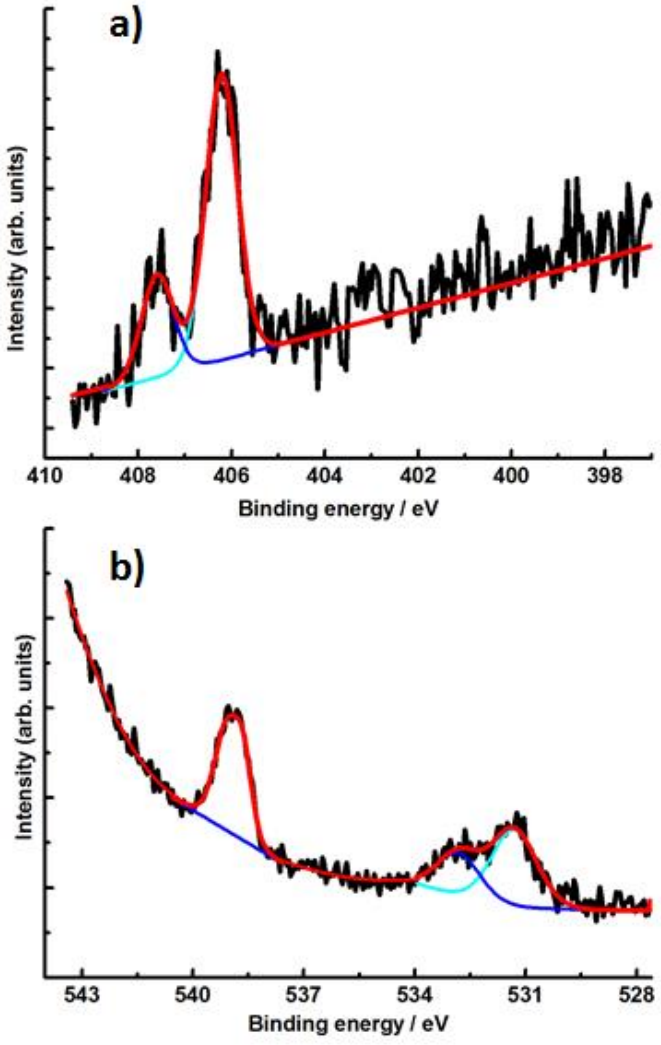

Figure 6.5: (a) N 1s and (b) O 1s X-ray photoelectron spectra during exposure of Au(100) to NO at 1 mbar pressure and 298 K. The black line is the recorded XP spectrum, while the red line is a fit, deconvoluted into the purple and turquoise contributions.

The above results show clearly that NO does not adsorb on Au(100) under these conditions of temperature and pressure.

Desorption in the S-VMI experiment was initiated at a low temperature of ∼178 K.[176] In the system used here, the lowest achievable temperature is 220 K, which is ∼50 K degrees higher than that reached in the 3D-VMI instrument.

Only gaseous NO was observed in the recorded spectrum at 220 with the ***sputtered and annealed*** (atomically flat) surface (not shown here). No peaks of N 1s and O 1s at ∼400 eV and ∼531 eV which indicate adsorbed NO species were found. Hence we studied NO adsorption on a ***sputtered and non-annealed*** gold surface with the knowledge that sputtering leaves some defects of lower coordination, hence being more reactive for NO adsorption at relatively higher temperatures. The surface was sputtered for 30 min after the cleaning procedure mentioned earlier followed by exposure to NO under the same condition at 298 K on the gold surface. It is worthwhile mentioning here that Baumer and his group performed temperature-programmed desorption and infrared adsorption spectroscopy of CO/Au and found for the ***sputtered*** Au(111) surface a large number of rough pits and mound morphology.[177] In annealing experiments, they observed the loss of these sites which coincides with the loss of CO adsorption capacity. The binding energy significantly depends on the order of coordination. The same was mentioned in previous studies which demonstrated that the presence of defects on Au(111) surface can affect adsorption of NO, while an annealed Au(111) does not exhibit any activity towards NO adsorption. [96] Fig. 6.6 shows the N 1s and O 1s XPS core level spectra of nitric oxide adsorbed on Au(100) at 1 mbar NO pressure and 220 K on ***sputtered and non-annealed*** surface.

The N 1s spectrum (Fig. 6.6 a) shows three distinct peaks at 398.8, 401.9 and 405.8 eV, and a peak at 407.1 eV appearing as a shoulder of the 405.8 eV peak. The peaks at 405.8 and 407.1 eV are signs as gaseous NO peaks as mentioned earlier in Fig. 6.5 (no obvious shifts were observed in gaseous NO), the two new peaks at 398.8 and 401.9 eV point to the presence of an adsorbed NO species on the ***sputtered*** gold surface. A large binding energy difference of 3.2 eV is found in N 1s for different molecular species i.e. 398.8 and 401.9 eV. This is in agreement with Rienks group, who reported the presence of three main features at 394.7, 398.1 and 401.3 eV in the N 1s spectrum recorded during the exposure of Pt(100) to NO at 200 K.[178]

Peaks appearing at 398.1 eV and 401.3 eV were attributed to two different NO molecularly adsorbed species on the surfaces, and this is in agreement with other studies on different surfaces. [179–181]

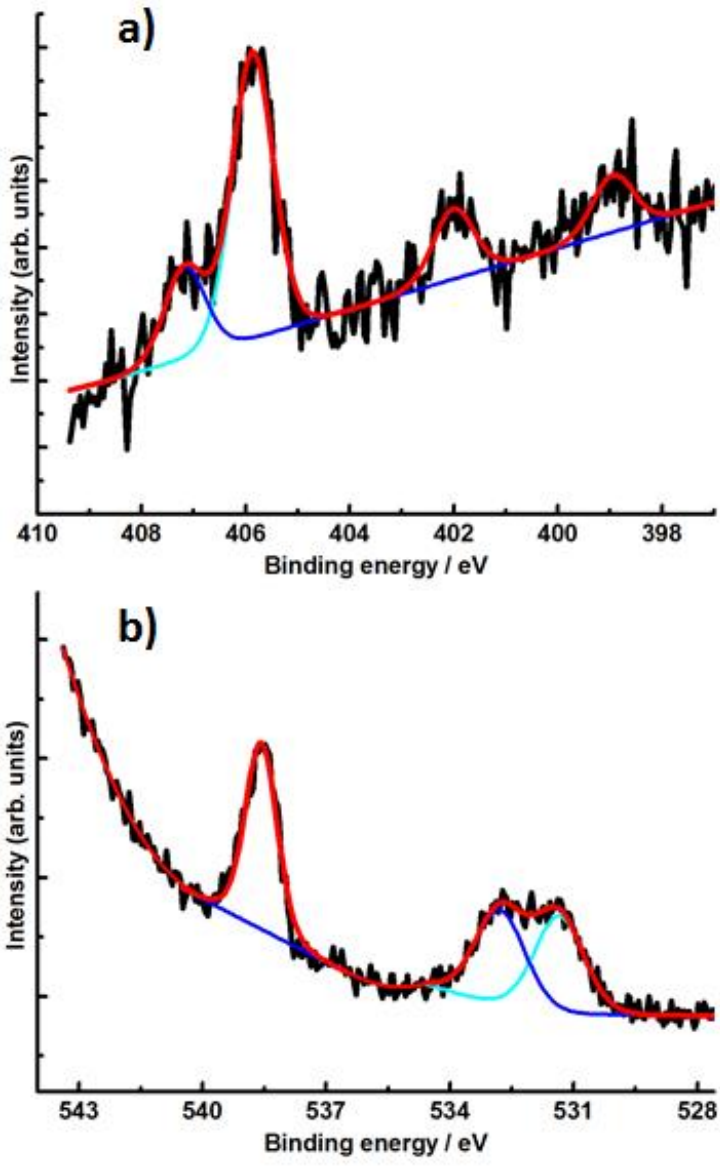

Figure 6.6: (a) N 1s and (b) O 1s XPS core-level spectra of NO adsorbed on sputtered gold surface taken at 220 K and 1 mbar NO pressure. The black line is the recorded XP spectrum, while the red line is a fit, cdeonvoluted into the purple and turquoise contribution.

The peak appearing at 394.7 eV which is not observed in this study was suggested by the authors to be due to atomic nitrogen because the temperature is just high enough to allow dissociation at specific sites. Further support of molecularly adsorbed NO comes from a study by Sugai *et al.* who observed a peak at 401.5 eV due to molecularly

adsorbed NO on Pt(100) and (310),[182] and a study by Kiskinova *et al.* who observed a N 1s peak at 400.7 eV due to molecularly adsorbed NO on Pt(111). [183] Large chemical shift at ∼4 to 6 eV were observed between the N ls spectra associated with the molecularly desorbed NO. Madey *et al.* reported large chemical shifts, as great as 8 eV, between the N ls spectra associated with weakly and strongly chemisorbed NO on a polycrystalline tungsten ribbon. Chemical shifts in both the N ls and O ls spectra suggest that NO is largely non-dissociatively chemisorbed at 100 K.[184]

All the observed peaks on the O 1s spectrum (Fig. 6.5 b) appeared again at 220 K at nearly same binding energies (Fig. 6.6 b). While the higher energy peak is due to gas-phase NO, the twin O 1s peaks show an increase in intensity and/or area under the curve when compared with that recorded at 298 K reflecting the contribution from the molecularly adsorbed NO at 220 K, with some contribution from residual CO. Similarly O 1s twins peaks were observed for NO adsorption on Ru(001) and CO adsorption on Pt(111) which were interpreted as being due to two molecular adsorption states. In both cases, adsorption of NO on an on-top site was associated with a higher binding energy of O 1s, and on bridge sites with a lower BE of the O 1s. It is not possible to elucidate the nature of adsorption sites further since the adsorption only occurred on a ***sputtered, non-annealed*** surface which is not atomically flat, and adsorption sites as on-top (ot), hollow (2f) are both defined. In general, XPS peaks in the energy regions above 532 eV and 399 eV for O and N, respectively, were found by several authors and attributed to molecularly adsorbed NO.[184, 185]

Crucially, the fact that a large shift of the N 1s binding energy is observed, while only a small O 1s difference is found, leads us to conclude that the orientation of the adsorbed nitric oxide is with the N-end facing the metal surface. The fact that NO is molecularly adsorbed in this study is further supported by the absence of N 1s peaks at around 399.4 eV or 402.7 eV mentioned earlier and reported to be arising from the dissociative adsorption of NO. Also, no feature at around 529.5 eV in the O 1s region characteristic of atomic O was observed.[186, 187] The difference between the binding energy of O 1s and N 1s in this study was found to be 132 eV which has been suggested that NO is bound linear to the surface from the N terminal with the Au-N-O angle around 180°, i.e. no appreciable tilting with respect to the surface normal. A difference of 128 eV was attributed to a bent form of NO. A bent form of NO where the

metal N-O angle is not 180° has been found in many nitorsyls. Bent metal-N-O form will bring the O atom closer to the metal surface and hence increase its interaction with it. The extent of interaction usually manifests itself in the extent of the shift in the binding energy of O 1s compared to that of O 1s in the gaseous phase. The greater the size of the bending angle, the closer the O atom to the metal surface and the greater the O 1s BE shift. The fact that no significant shift is observed for the O 1s BE in this study for the adsorbed NO when compared with that of the gaseous NO is a clear indication that NO alignment is perpendicular to the surface plane, or that the tilting angle is too small to cause an observable shift in the O 1s binding energy. After adsorption at 220 K and recording of the XPS spectra, the temperature of the surface was gradually raised to 266 K while keeping the NO flowing into the cell, and the spectra were recorded again and are shown in Fig. 6.7. Only peaks related to gaseous NO are observed. The two peaks associated with the two N surface desorption species have disappeared.

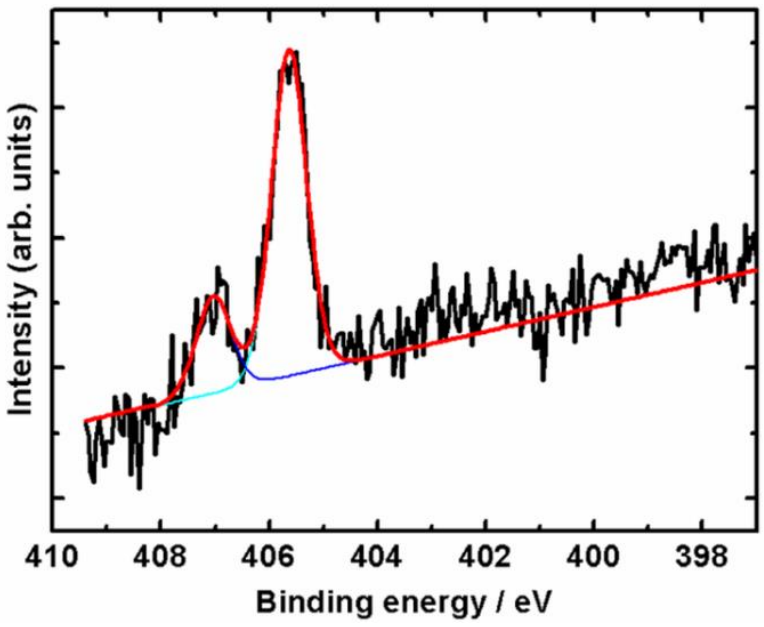

Figure 6.7: N 1s XPS core-level spectra during exposure of NO at 266 K and 1 mbar pressure.

6.5 Summary

The adsorption of NO on Au(100) under 1 mbar NO pressure was carried out at three different temperatures, room temperature, 220 K and 266 K. NO adsorbed species was recorded only at 220 K. NO was molecularly adsorbed with the N end facing the surface, and O pointing away from the surface.

Chapter 7

Density Functional Theory

The adsorption of NO on clean Au(100) has been studied using the DFT-slab approach as a supported material in order to interpret our experimental results and to shed light on the excitation mechanism. In this thesis work DFT used to determine the adsorption geometries and energies of NO of Au(100).

7.1 Introduction

DFT is the most popular computational method available in chemistry and condensed-matter physics, computational physics since the 90s. [188, 189] It is an ab-initio approximation to investigate the electronic structure of many-body systems, in particular atoms, molecules and the condensed phases. The development of DFT and the availability of faster computational resources have allowed the investigation of increasing size and complex systems.

The basic statements of DFT in briefly can be summarised in two points:

1. The basic idea is based on the Hohenberg and Kohn (HK) theorem [190] which replaces the many-body-wave-function ψ with the electron density.

   The total ground state energy E of the many-particle system can be described by the electron density and the sum of external fields $\nu(r)$, see eq. 7.1

   $$E = \int n(r)\, v(r) dr + \frac{1}{2} \iint \frac{n(r)\, n(\grave{r})}{r - \grave{r}} dr d(\grave{r}) + G[n] \tag{7.1}$$

   where: $v(r)$ is a unique function of state single particle density n(r), and G[n] is universal functional independent of $v(r)$

2. The mainstay of DFT is the Kohn-Sham (KS) theorem. [191] Here the stage where one maps the many particle problem onto a corresponding set of effective single parameters problems. The KS split the G[n] into two terms:[192]

$$G[n] \equiv T_s[n] + E_{xc}[n] \tag{7.2}$$

where: $T_s[n]$ is kintic energy of non-interacting electron gas with density n(r), and E_{xc} is the exchange and correlation of interacting electron gas with density n(r). In the DFT calculations, the KS questions will be solved rapidly by choosing a single particle density n(r), until self-consistency is reached, Fig. 7.1

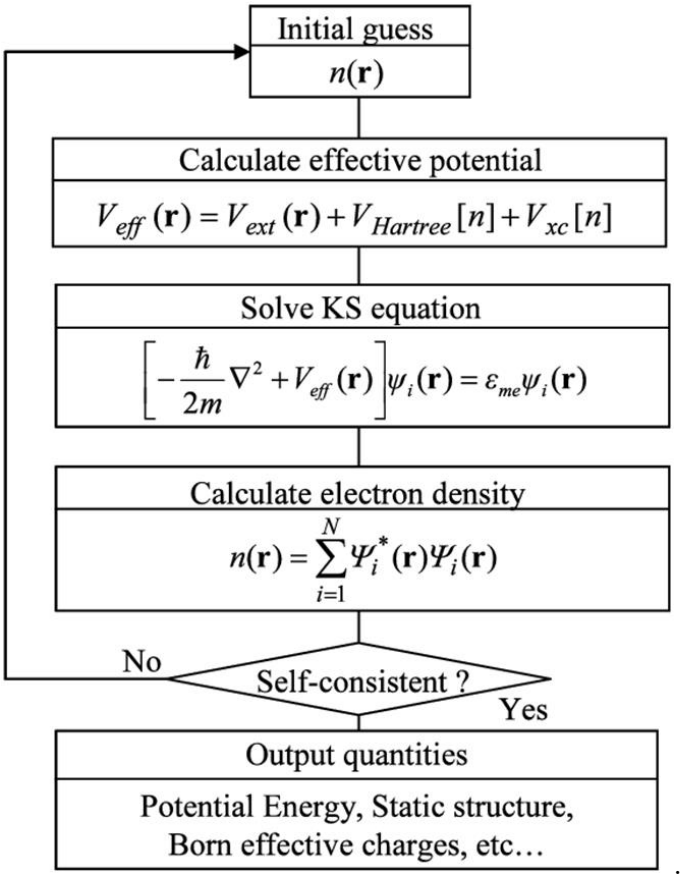

Figure 7.1: Flow chart of solving the Kohn-Sham equation. At first, an initial guess for the electron density is assumed, which is required for the calculation of $V_{eff}(r)$, the diagonalisation of the Kohn-Sham equations, and the subsequent evaluation of n(r) along with E_{Total}. As long as the convergence criterion is not fulfilled, the numerical procedure is continued with the last n(r) instead of the initial guess. When the criterion is satisfied, various output quantities are computed.

The total energy of the system is then given by

$$E = \sum_{n=1}^{\infty} \xi_i - \frac{1}{2} \iint \frac{n(r)\, n(\grave{r})}{r - \grave{r}} dr d(\grave{r}) + E_{XC}[n] - \int v_{xc}\, n(r)\, d(r) \tag{7.3}$$

as the energy cannot be calculated exactly but instead must be approximated. Three levels of approximations can be distinguished during the development of modern DFT since the mid-sixties:

- Local density approximations (LDA)

  The exchange and correlation energy is only a fraction of the density, which is a good approximation if the electron density varies slowly. The E_{xc} is given by

  $$E_{xc}[n] = \int n(r)\, \xi(n(r))\, d(r) \tag{7.4}$$

- Gradient expanded GE or generalised gradient functional GGA

  In this case the energy depends both on the electron density and the gradient of the electron density

  $$E_{xc}[n] = \int n(r), \nabla_n(n(r))\, d(r) \tag{7.5}$$

  However, the GGA fails when the electron density varies too fast.

Adsorption energies, adsorption sites, vibrational frequencies and the density of state were determined to interpret the 3D- SVMI results and to understand the desorption mechanisms which were presented in chapter 5. The core level calculation was obtained to explain the NAP-XPS results in chapter 6.

7.2 Computational Methodology

The calculations have been performed using the Cambridge serial total energy package (CASTEP), [192] which solve the Kohn-Sham equations in a plane-wave basis set employing three-dimensional periodic boundary condition.[193] The electron wave functions were expanded in plane wave basis set and the ionic cores were described by ultrasoft pseudopotentials. Electronic exchange and correlations are described in the generalised gradient approximation GGA, using the functional proposed by Perdew-Burke-Ernzerhof (PBE). For bulk FCC Au, a cut-off energy of up to 750 eV was utilized in all the calculations. Using the primitive fcc unit cell, we obtained a lattice constant

of bulk Au as 4.046 Å, which agrees well with the experimental finding (4.078 Å). In this work the Au(100) surfaces were modelled with 8 layers in slab mode, the vacuum region above the slabs is 20 Å. NO molecules were adsorbed on three sites of the slab. Only the top four layers were relaxed, whilst the remaining four layers had their movement constrained.

Previous work reported that the adsorption energy of CO does not depend on the number of Au layers if there are more than two layers.[194] NO was adsorbed on each of the three potential sites on the fcc Au(100) surface, i.e. on top(ot), bridge site (2f) and hollow site (4f) for representative cell geometries and degrees of coverage , see Fig. 7.2.

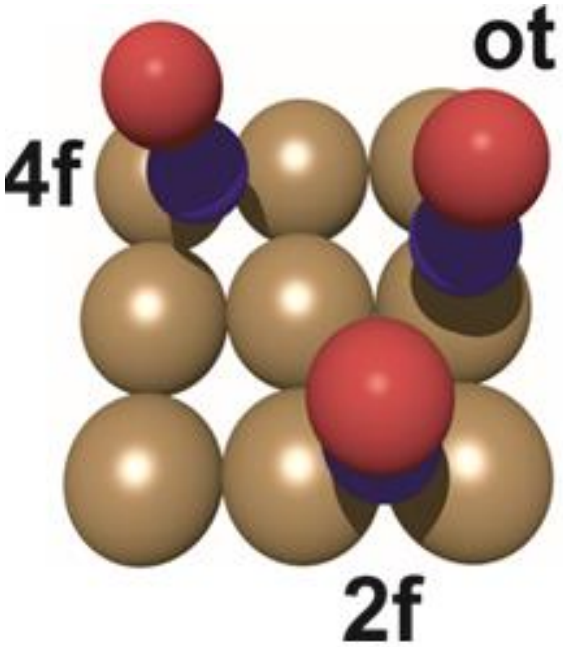

Figure 7.2: Potential adsorption sites for NO on the Au(100) surface in gold . ot = on-top, 2f = bridge site, 4f = hollow site. Oxygen in red, nitrogen in blue.

Using the relaxed geometry, the adsorption energy was computed for each case to find the most stable site. The adsorption energy, E_{ads} is given by

$$E_{ads} = \frac{1}{N}[E_{NO+slab} - (NE_{NO} + E_{slab})] \tag{7.6}$$

where: $E_{(N+slab)}$ is the total energy of the relaxed slab with NO adsorbed, N is the number of NO adsorbed per unit cell, E_{NO} is the ground state energy of a single NO molecule in a (10 x 10 x10 $\AA^3$) box , and E_{slab} is the total energy of the NO free slab. The relaxed geometries were carried forward into the frozen phonon calculations, to

compute vibrational frequencies of the surface adsorbed NO on high symmetry sites. The Au slab atoms had constrained motion, whilst the NO atoms were free to move. A finite displacement of 0.01 Å on N atoms was applied to compute the force constant matrix, which was then implemented in calculating the vibrational frequencies.

To further investigate the electronic properties of the gas-surface interaction, the spin-polarised projected density of states (PDOS) were calculated using the OPYADOS code for all structures of NO adsorbed on Au.

Theoretical simulations of core-level shifts (CLS) deduced from XPS are performed using Slater-Janak transition state approximation. The CLS is defined by the difference of binding energy between the interested and referenced atom. The binding energy of particular core level is defined by the difference of total energies of the ground E(n_i) and photo-excited (n_i - 1) systems, n_i is the number of electron in the core level i.

$$E_{CLS} = [(n_i - 1) - E(n_i)] - [E_{ref}(n_i - 1) - E_{ref}(n_i)]. \tag{7.7}$$

7.3 Results and Discussion

7.3.1 Adsorption Energy of Nitric Oxide on Au(100)

We have calculated the adsorption energies of NO molecules at the three main geometry sites of the Au(100) surface, namely on-top (ot), bridge site (2f) and hollow site (4f), as shown in Fig. 7.2, for representative coverage.

The variation in the adsorption energies could be related to the energy of adsorption on the different adsorption sites. See table 7.1, for the adsorption energy results.

Table 7.1: Adsorption energies of NO on Au(100) at ot, 2f and 4f sites at different coverages. The highlighted value indicated the most favourable site in our study.

Coverage	**Current work (eV)**		
	ot	**2f**	**4f**
100%	0.51	0.46	0.71
50%	0.78	0.82	0.70
25%	0.20	0.69	0.65

As presented in the table 7.1, for all but 100% coverage, the NO preferentially adsorbs on the bridge (2f) site with weak adsorption energies between 0.69 eV and 0.8 eV depending on coverage. This is roughly in agreement with previous calculations by

OlveraNeria *et al.* (0.53 eV) for NO on a single gold atom,[195] and by Niemantsverdriet and co-workers (0.57 eV) for adsorption on the bridge site (both studies used 25% covarage).[88] Thermal desorption experiments (0.59 eV) also agree with the above calculated adsorption energies.[176] Liu and co-workers computationally studied 25% coverage of NO on Au(100) and found an adsorption energy of 0.26 eV for the on-top (ot) site; we calculated an adsorption energy of 0.20 eV for the ot site, but as mentioned above also find an energetically more favourable conformation in the form of the 2f site.[89]

Fig. 7.3 presents all the adsorption energies at the different covarages and sites.

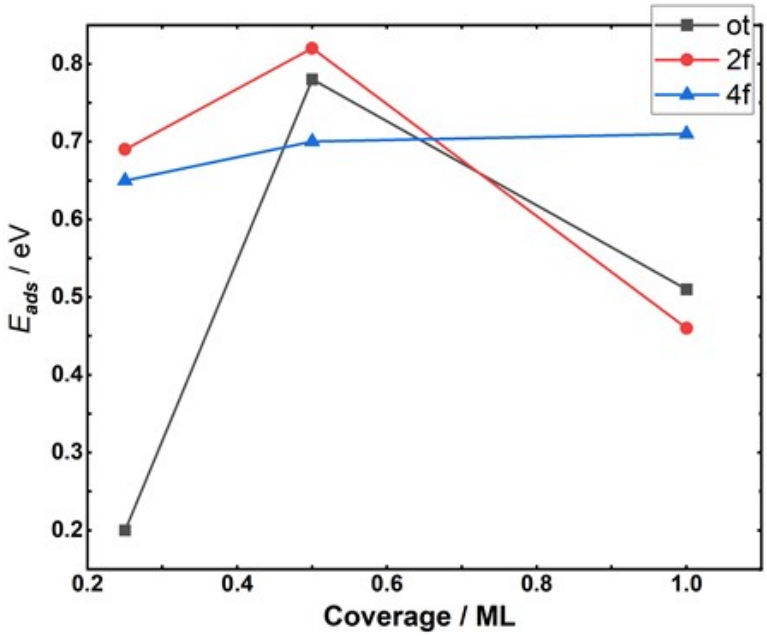

Figure 7.3: All calculated adsorption energy as function of coverage at 3 different adsorption sites: red line present bridge site(2f) at 25%, 50% and 100% coverage, black line present on-top (ot) at 25%, 50% and 100% coverage and blue line present hollow site (4f) at 25%, 50% and 100% coverage respectively.

On the 2f and 4f site (Fig. 7.4) the single electron in the two NO π^* orbitals (belonging to the nitrogen atom) can efficiently overlap with the orbitals on two neighbouring Au atoms at the surface between which the NO is located, resulting in an N–O bond aligned along the surface normal. We find this upright arrangement in fact for all sites and coverages apart from the on-top site for all 50% coverage case.

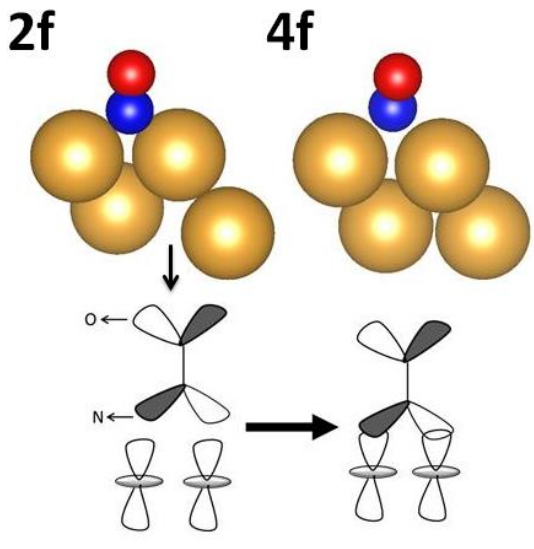

Figure 7.4: Adsorption of NO on the Au(100) surface on 2f and 4f sites for 50 % coverage, and the orbital interaction between the NO molecule and the surface Au atom on the hollow site

Fig. 7.5 where the overlap of the π^* orbital with the orbitals on a single Au atom causes the NO to tilt, which is in agreement with Wiu.[89] In contrast, Tratnik reported that in most cases NO adsorbs on a bridge site with N-O bond being perpendicular to the surface plane.[196]

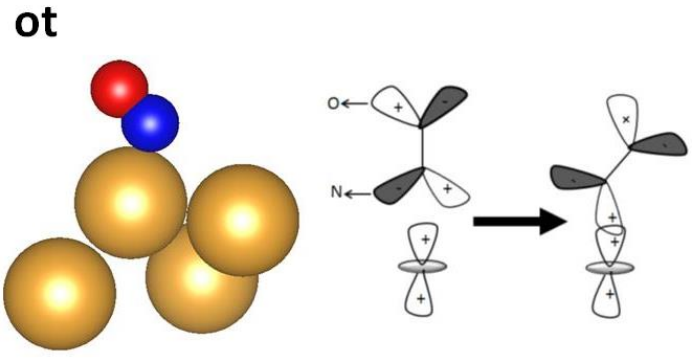

Figure 7.5: Adsorption for NO on the Au(100) surface, on the top site for 50 % coverage, and the orbital interaction between the NO molecule and the surface Au atom on the top site.

7.3.2 Vibrational Frequencies

Calculated vibrational frequencies of NO were found to be dependent on the coverage. This seems to be in agreement with the finding by li and Co-worker.[197] Vibrational frequencies of the adsorbed NO were calculated for the different coverages investigated, namely 100%, 50% and 25% together with the various adsorption sites. For 100% coverage, N-O stretch frequency of 1784, 1885 and 1726 cm^{-1} were found for 4f, ot and 2f sites respectively. Their values are 120 cm^{-1}, 19 cm^{-1} and 178 cm^{-1} smaller than the frequency of NO in gas phase (1904 cm^{-1}).[198] The results here indicate that the 2f site is more stable than the others. Similarly, for 50% coverage the 2f adsorption site with 1654 cm^{-1} was found to be more stable than ot (1755 cm^{-1}) and 4f (1730 cm^{-1}). For 25% coverage, calculation of the NO frequency indicates that the 4f adsorption site (1604 cm^{-1}) is more stable than 2f (1629 cm^{-1}) and ot (1755 cm^{-1}). The results obtained here indicate that the coverage plays an important role in deciding on identity of the most stable site for the adsorption of NO, see Table. 7.2

Table 7.2: Vibrational frequencies of NO on Au(100) at three sites ot, 2f and 4f at different coverages in order of the most favourable site.

Unit cell	**Site**	**V**	**eV**
100%	4f	1784.03 (-8%)	0.23
	ot	1885.05 (-3%)	0.23
	2f	1726.29 (-11%)	0.21
50%	2f	1654.21 (-15%)	0.20
	ot	1755.32 (-10%	0.21
	4f	1730.17 (-11%)	0.21
25%	2f	1629.42 (-16%)	0.20
	4f	1604.77 (-17%)	0.20
	ot	1755.24 (-10%)	0.22

7.3.3 Work Function

We have calculated the work functional of NO on Au(100) by using DFT to judge if there is change caused by the adsorption of NO on Au(100). The work function ϕ of a metal can be calculated directly using the formula:

$$\phi = V - E_F \tag{7.8}$$

where V and E_F are the electrostatic potential at the reference point outside the surface and the Fermi energy, respectively. Both the potential in the vacuum region (V) and the Fermi energy (E_F) are derived from the same calculation and the results summarised in Table 7.3.

Table 7.3: Work-function change, ϕ in eV, induced by NO adsorption on Au(100).

Adsorption sites	25% $\Delta\phi$	50% $\Delta\phi$	100% $\Delta\phi$
ot	-0.13	-0.06	-0.72
2f	-0.04	0.34	-0.12
4f	0.04	0.05	0.15

The work function for clean Au is ∼4.9 eV according to the calculation in this work. After NO adsorbes on the surface, the work function was in the range $4.2 - 5.26$ eV which is in agreement with the results obtained by Hansson group (5.10 eV)[199, 200] and the Fall group (5.53 eV)[201], which is in a good agreement with the experimental value (5.25 ± 0.31). [200] From the inspection of the table above, the positive ϕ is expected for NO adsorption on gold,[202] as the electronegativities of O and N atoms (which are 3.44 and 3.04) are significantly larger than that of Au atom which is 2.54. This is indeed found for NO in the hollow site for all coverages and bridge sites at 50%. However, it does not apply to the ot site for all coverages, and this is done to their different charge redistribution induced by adsorption.

It is interesting to note that in the case of 4f adsorption site and for all coverages investigated, there is an increase in the work function which is in contrast to the ot site for which a decrease in the work function is observed for the same coverage, see Fig. 7.6.

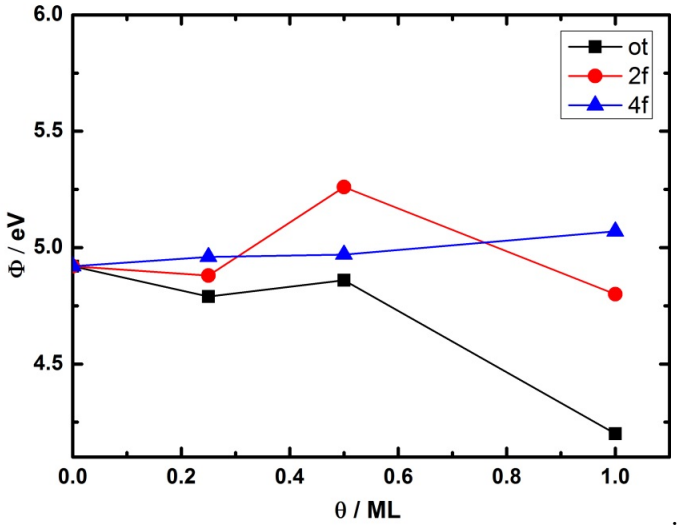

Figure 7.6: Work function of different sites on NO/Au(100) as a function of covarage.

According to Zeng *et al.*[203] an increase in the work function, i.e. a positive $\Delta\phi$, as observed in this study for the 4f site is expected if a net charge transfer from the substrate to the adsorbed NO occurs regardless of the adsorption site. It was suggested that a positive $\Delta\phi$ means an inward pointing surface dipole moment induced by adsorption. Following from this argument and for a top-site adsorption site, a net charge transfer from the adsorbed NO to the substrate could be envisaged in which the direction of the surface dipole moment is pointing outward to the vacuum.

7.3.4 Projected Density of State

Insights into the interaction between NO and Au surfaces can be obtained from the projected density of states (PDOS).

The PDOS have been calculated for clean Au(100), see Fig. 7.7. Mapped the partial density-of-states of the Au–NO complex around the Fermi energy separately for the Au atom and the NO molecule in search for a plausible non-thermal excitation mechanism, in case of 100% and 25% coverage. In the ot site for both investigated coverages, did not find any orbitals matching the desorption lasers energies, i.e. 3.5 and 4.6 eVdesorption laser respectively.

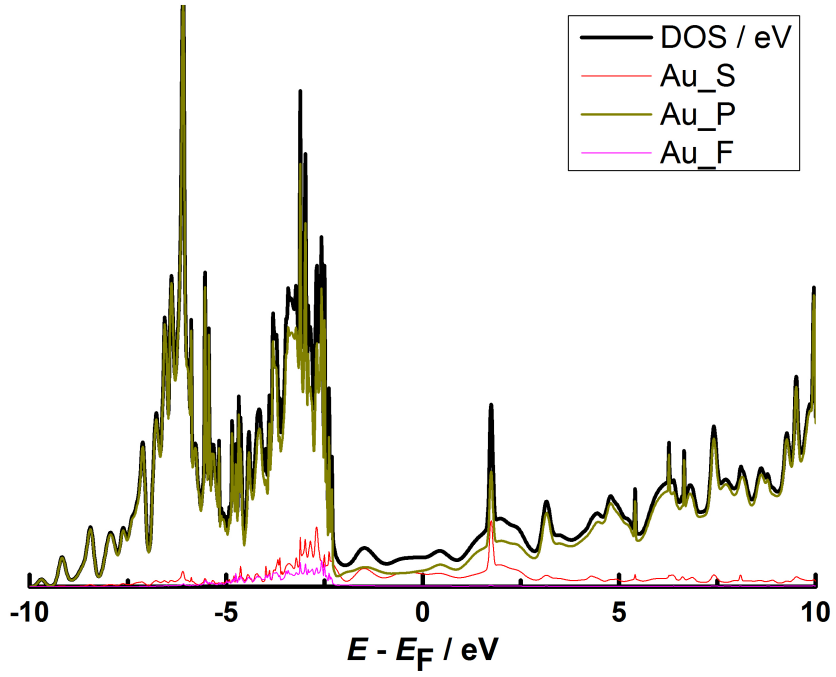

Figure 7.7: Projected density of state (PDOS) of clean Au(100) surface (s, p and f orbitals).

In Fig. 7.8, it appears that for the 2f site (as well as for the hollow 4f), some filled Au orbitals (belonging to p orbitals) at ∼3 eV below the Fermi energy and some unoccupied orbitals belonging to the nitrogen p orbitals of the NO around 0.5 eV above the Fermi energy exist witch is very close to the 355 nm desorption laser energy.

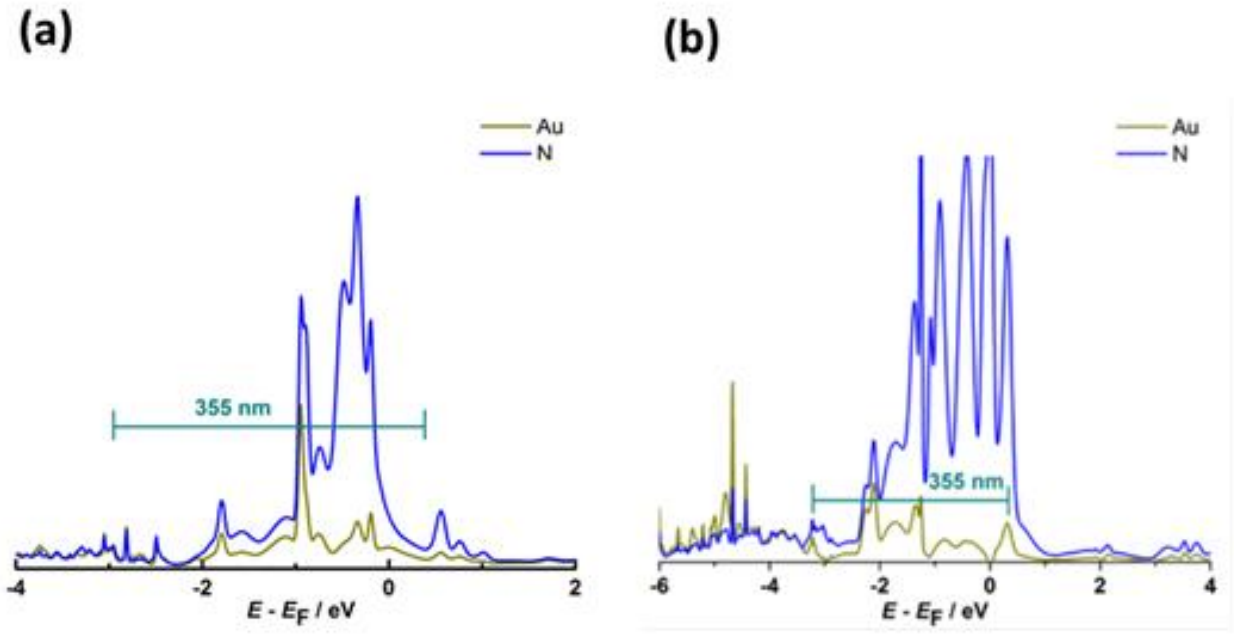

Figure 7.8: Projected density of state of adsorbed NO a) On bridge site (2f) for 25% showing unoccupied N orbital at 0.5 e V and an Au occupied orbital at 3 eV which match the 355 nm desorption laser, indicating the possibility for a non-thermal mechanism, b) On 2f site, for 100% covarage matches the 355 nm energy.

7.3.5 Core Level Shift

Electron core level shifts calculated for various electron removals from Au atoms and comparative spectrum possible for hole-free systems were obtained. Present the core level shift (CLS) results for the N 1s states of NO adsorption only on (2f) and (ot) site, as the bridge site is the energetically more favourable adsorption site based, while the on-top site is the other suggested site in the literature, and close in terms of adsorption energy. We calculated a larger CLS shift for the bridge site than the on-top site; these shifts are $\sim$ 1.5 eV and 0.9 eV of the N 1s peak towards lower binding energies for bridge and on-top sites, respectively. CLS-DFT results are complementary to the experimental results (NAP-XPS).

7.4 Summary

NO preferentially adsorbs on the bridge (2f) site with a weak adsorption energy of between 0.65 eV and 0.8 eV for 25% and 50%. In all adsorption configurations but not the ot, the N-O molecular axis is perpendicular to the surfaces. The results for the PDOS indicate that an electronic transition from Au to NO is a feasible explanation for a non-thermal-desorption mechanism..

Chapter 8

Conclusions and Future Work

8.1 Conclusions

The adsorption of nitric oxide onto Au(100) has been studied with the aim of obtain 3D velocity distrbuions to learn about the photodesorption mechansim, and to identify the type of adsorption. The investigations were performed by employing a combination of experimental techniques and theoretical calculations including 3D-surface velocity map imaging, near-ambient pressure x-ray photoelectron spectroscopy and density functional theory.

Thermal vs. non-thermal NO desorption mechanism

Desorption of NO from the Au(100) surface was concluded to be dominated by a non-thermal mechanism when a 355 nm desorption laser is used. This conclusion was based on 1) the observed narrow angular and speed distribution of the desorbed NO molecules, 2) the rotational temperature of NO being higher than the surface temperature, 3) the coupling between the translational and rotational energies that allows partitioning of energy during the adsorption process. In contrast, desorption of NO from the Au(100) at 266 nm was seen to be dominated by a thermal mechanism. This conclusion was reached by considering 1) the angular speed distribution of the desorbed NO which was wider that that observed for 355 nm desorption, 2) the rotational temperature of the desorbed NO was not far from that of the surface temperature 178 K.

Angularly resolved velocity distributions

The angular-resolved speed distribution of the photo-desorbed NO molecules from an Au(100) surface is directed along the surface normal and extremely narrow, with all NO molecules desorbing from the surface within a very narrow angular distribution with a polar angle of less than 20° relative to the surface normal.

Based on these experimental findings, it was concluded that NO is either adsorbed on-top of a gold atom or at another site of high symmetry like a 2f or a 4f site.

Rotational state distributions of the photo-desorbed NO molecules

The results obtained here indicated that the laser-desorbed NO molecules are rotationally cold. The rotational temperatures were around (206 ± 5 K), which - although close to the surface temperature - was considered fairly cold when the excess photon energy is taken into account. Rotationaly cold NO molecules point to the N-O axis lying a long the surface normal such that little torque is imported into the NO during the disorption process.

Near-ambient pressure X-ray photoelectron spctroscopy

Results here confirmed the molecular adsorption of NO molecules onto the sputtered non-annealed Au(100) at 220 K. At around 260 K, no NO adsorbed was seen which is in agreement with the results obtained from 3D-surface velocity map imaging. Adsorption was carried out on a sputtered non-annealed Au(100) surface as no features of any adsorbed NO were recorded on the annealed gold surface at the lowest temperature achieved on this system (220 K). Although the adsorption of NO was carried out on a sputtered Au(100) and strictly speaking one cannot talk about regular adsorption sites, nonetheless it was concluded here that the NO adsorption sites resemble bridge sites and on-top sites. Furthermore, results indicated that NO adsorbs with N facing the surface and O pointing away from the surface.

Density function theory

Calculation here were performed on three different adsorption sites on the ordered Au(100) surface. The most energetically favourable adsorption site was found to be the bridge (2f) site. Adsorption energies were found to be coverage dependent. It was argued that this is due to the efficient overlap of the NO π^* orbital with the orbitals of two neighbouring gold surface atoms. This leads to the N-O bond aligned along the surface normal. This NO orientation with respect to the surface is in agreement

with both the 3D-surface VMI results and the cold rotational state distributions of the desorbed NO molecules.

8.2 Future Work

The novelty of this work is that it demonstrates the capability of the 3D-VMI technique not only in elucidating the photodesorption dynamics of pre-adsorbed molecules on metal substrates, but also in revealing the adsorption site, orientation and alignment of adsorbates. It can be used to study the bond orientation and mapping. In order to map the dissociation dynamics across interfaces, the use of selectively- Halogenated SAMs is proposed, see Fig. 8.1.

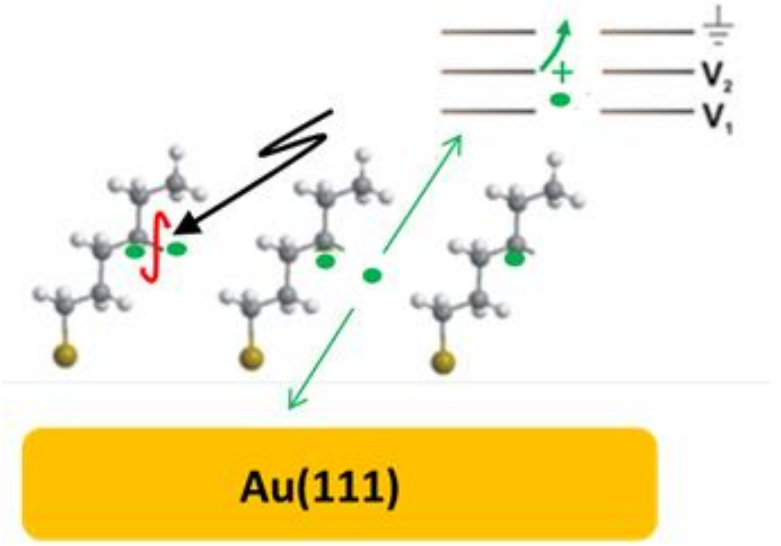

Figure 8.1: Dissociation of self assembled monolayers (SAMS)

This is similar to electron-stimulated desorption ion angular distribution studies (ESDIAD) by Madey, Yates, and co-workers.[4] By applying the axial recoil approximation, the atoms produced in the dissociation process will move outward along the direction of the bond that was broken, hence it will be possible to map the direction of the bond from the direction of travel of the fragments, which 3D-VMI can deliver.

Appendix A

Flux to Density Conversion

The TOF raw data for the NO desorbed from Au(100) does not represent the distribution. Hence has to be converted to extract the velocity distribution. Since the signal S(t) is proportional to the number density ρ(r,t) which is distribution in space, not in time, hence the S(t) refer to the TOF spectrum not the TOF distribution.
The recorded TOF signal, S(t)dt, was first converted to flux, I(t)dt:

$$I(t)\,dt = S(t)\,v(t)\,dt \tag{A.1}$$

The time domain data was then transformed to velocity space whilst retaining probability across each time and velocity component:

$$P(v)\,dv = I(t)\,dt = S(t)\,v(t)\,dt \tag{A.2}$$

$$P(v)\,|dv/dt| = S(t)\,v \tag{A.3}$$

The Jacobian matrix is given by:

$$|dv/dt| = l/t^2 = v^2/l \tag{A.4}$$

where: v is velocity and l the flight distance. The final transformation which use directly to convert the row TOF data to velocity distribution is described below:

$$P(v) = S(t)\,l/v \tag{A.5}$$

Appendix B

LIFBASE Fits

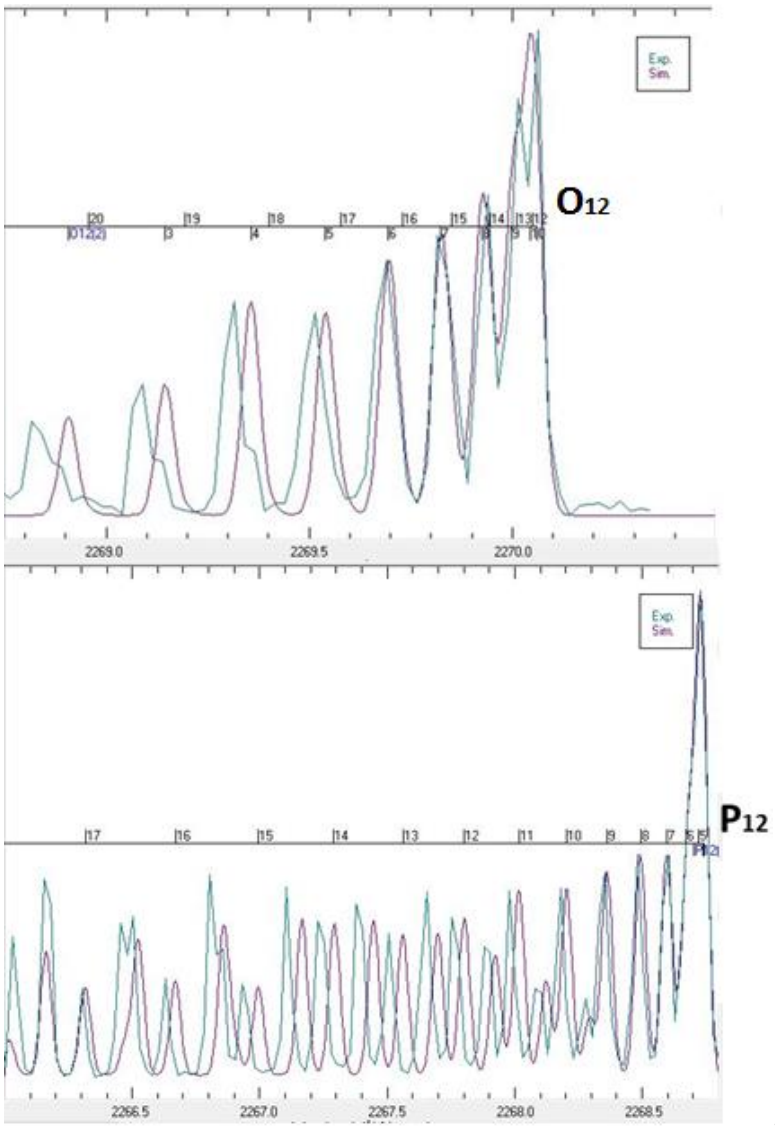

Figure B.1: Experimental data and LIFBASE fits for the O $_{12}$ and P_{12} branches for the GAS-Phase NO for Calibration.

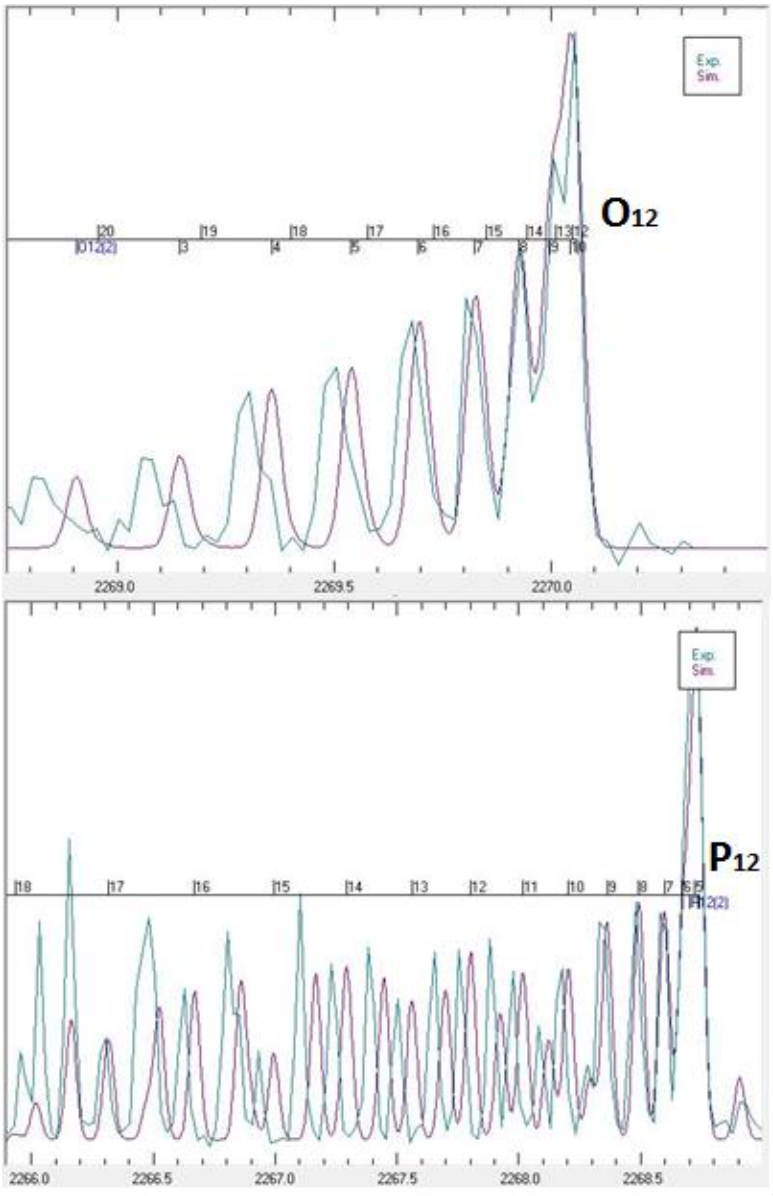

Figure B.2: Experimental data and LIFBASE fits for the O $_{12}$ and P_{12} branches at v_z=380 ms^{-1} and a desorption wavelength of 355 nm.

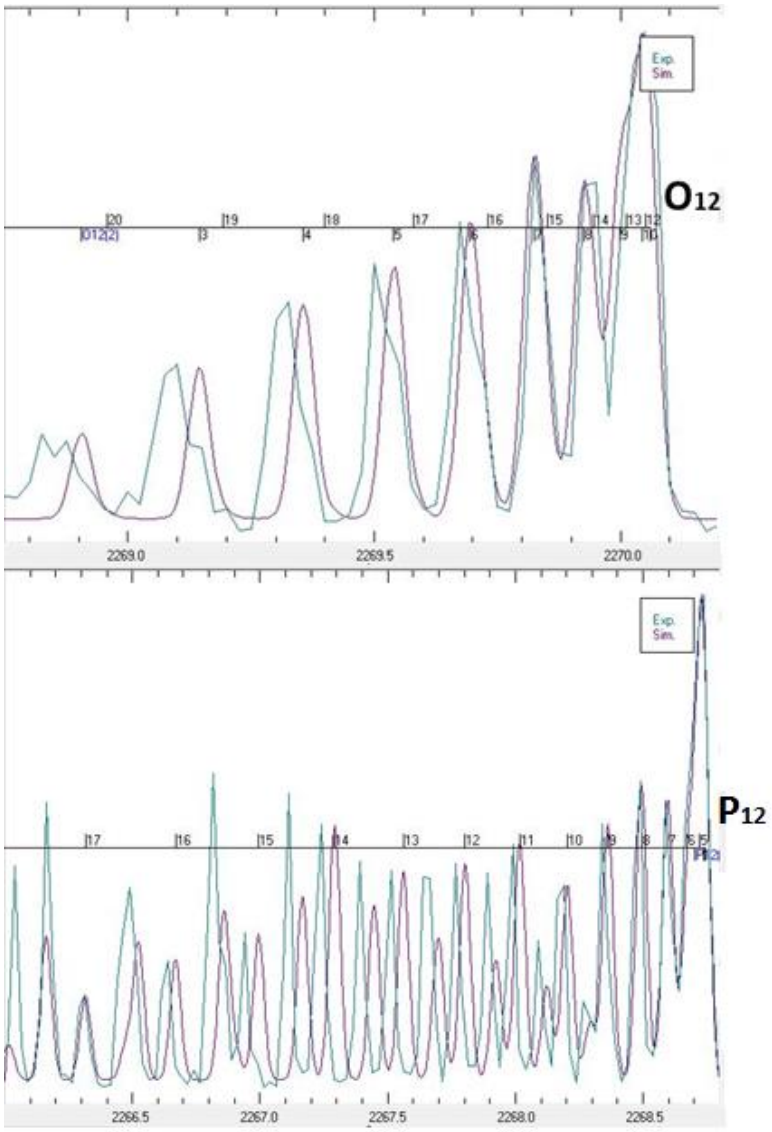

Figure B.3: Experimental data and LIFBASE fits for the O $_{12}$ and P_{12} branches at v_z=380 ms^{-1} and a desorption wavelength of 355 nm.

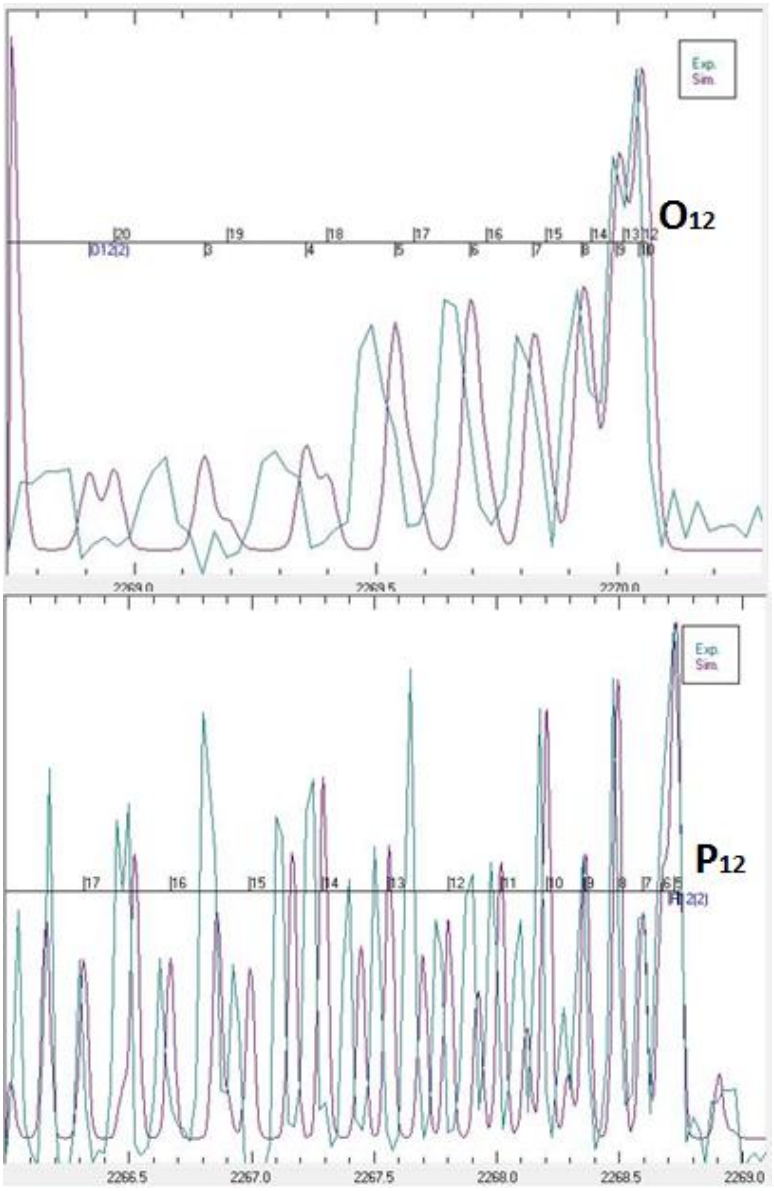

Figure B.4: Experimental data and LIFBASE fits for the O $_{12}$ and P_{12} branches at v_z=420 ms^{-1} and a desorption wavelength of 266 nm.

Appendix C

Paper1

Photodesorption of NO from Au(100) using 3D surface-velocity map imaging

Saada Abujarada, Huda AlSalem, Urslaan K. Chohan, Gemma L. Draper, and Sven P. K. Koehler

Citation: J. Chem. Phys. **145**, 184201 (2016); doi: 10.1063/1.4967248
View online: https://doi.org/10.1063/1.4967248
View Table of Contents: http://aip.scitation.org/toc/jcp/145/18
Published by the American Institute of Physics

Articles you may be interested in

Note: Velocity map imaging the scattering plane of gas surface collisions
Review of Scientific Instruments **87**, 106104 (2016); 10.1063/1.4965970

Ion and velocity map imaging for surface dynamics and kinetics
The Journal of Chemical Physics **147**, 013939 (2017); 10.1063/1.4983307

Validation of velocity map imaging conditions over larger areas
Review of Scientific Instruments **84**, 044101 (2013); 10.1063/1.4798646

Velocity map imaging of ions and electrons using electrostatic lenses: Application in photoelectron and photofragment ion imaging of molecular oxygen
Review of Scientific Instruments **68**, 3477 (1997); 10.1063/1.1148310

Substrate dependence of graphene reactivity towards hydrogenation
Applied Physics Letters **109**, 243103 (2016); 10.1063/1.4971385

Perspective: Advanced particle imaging
The Journal of Chemical Physics **147**, 013601 (2017); 10.1063/1.4983623

PHYSICS TODAY
WHITEPAPERS

ADVANCED LIGHT CURE ADHESIVES

Take a closer look at what these environmentally friendly adhesive systems can do

READ NOW

PRESENTED BY
MASTERBOND

THE JOURNAL OF CHEMICAL PHYSICS **145**, 184201 (2016)

Photodesorption of NO from Au(100) using 3D surface-velocity map imaging

Saada Abujarada,[1,2,a)] Huda AlSalem,[1,2,a)] Urslaan K. Chohan,[3,4] Gemma L. Draper,[1,2] and Sven P. K. Koehler[1,2,3,b)]
[1]*School of Chemistry, The University of Manchester, Manchester M13 9PL, United Kingdom*
[2]*Photon Science Institute, The University of Manchester, Manchester M13 9PL, United Kingdom*
[3]*Dalton Cumbrian Facility, The University of Manchester, Moor Row CA24 3HA, United Kingdom*
[4]*School of Materials, The University of Manchester, Manchester M13 9PL, United Kingdom*

(Received 13 September 2016; accepted 24 October 2016; published online 11 November 2016)

We measured the fully resolved 3-dimensional velocity distributions of nitric oxide photodesorbed from a gold single crystal. These experiments combine time-of-flight measurements and the velocity map imaging technique to yield velocity distributions resolved in three dimensions for a prototypical surface-adsorbate system. Nitric oxide adsorbed on Au(100) was photodesorbed using a 355 nm laser beam. The desorbed NO molecules were ionised in the gas-phase by resonance-enhanced multi-photon ionisation within a set of velocity map imaging optics. The NO molecules preferentially leave the surface along the surface normal with a very narrow angular distribution, indicating a non-thermal desorption process. *Published by AIP Publishing.* [http://dx.doi.org/10.1063/1.4967248]

I. INTRODUCTION

Studies of the detailed dynamics of chemical reactions frequently aim to record the product translational and/or internal energy distributions, both for gas-phase as well as for interfacial reactions, to learn about the energy re-distribution during the reaction and ultimately about the reaction mechanism. The photo-induced desorption of fragments from a single crystal presents a well-defined reaction system due to the well-known surface structure and photon energy. The photon energy may be preserved to some extent in the gas-phase fragments whose internal and translational energies can be probed after leaving the surface and can help to provide information about the dynamics of the desorption process.

A number of different experimental techniques have been employed in the past to study charged particle- and photon-induced desorption processes. Traditionally, one would use a time-of-flight (TOF) setup employing a mass-spectrometer that can be rotated around the fixed surface to acquire angularly resolved translational energy distributions.[1] However, this is time-consuming (and lacks the internal energy distribution), hence in order to record all fragments simultaneously in a single experiment, imaging methods have risen in popularity. Winograd and co-workers have reported the energy- and angular-resolved distributions of neutrals (EARNs) whose desorption was induced by ions, and they achieved an angular resolution of ~8°.[2,3] Similarly, ESDIADs (electron-stimulated desorption ion angular distributions) deliver angular distributions of ions desorbed from surfaces;[4] this method has successfully been employed for triangulation, i.e., it was in some cases possible to derive the orientations of molecular bonds at surfaces.[5]

State-resolved detection of neutrals typically involves the laser ionisation of neutral fragments, often performed in a resonance-enhanced multi-photon ionisation (REMPI) scheme. If a pump/desorption laser is employed to initiate an event at a surface, then the laser-detection of neutrals a few mm above the surface can deliver kinetic energy distributions of fragments. However, unless an elaborate optical detection geometry is used, such kinetic energy distributions lack any angular information. Menges *et al.* demonstrated an elegant example of sheet-focussing of the ionisation laser (with the sheet perpendicular to the surface) to record two-dimensional velocity distributions state-selectively. This was done for the model system of NO photodesorbed from NiO, for which they obtained a bimodal velocity distribution, with most of the kinetic energy release being directed along the surface normal.[6]

A number of groups have recently adopted ion imaging techniques, which are heavily employed in gas-phase reaction dynamics,[7] to the study of surface dynamics. Briefly, ion imaging techniques in the gas-phase may be used to study, e.g., photo-dissociation processes of small molecules; such molecules—seeded in a molecular beam—may be photo-dissociated and subsequently ionised within a set of ion optics which accelerate the ions down a TOF tube. Since the mass difference between the initially generated neutrals and the formed ions is negligible, the velocity of the neutrals expanding on a Newton sphere is preserved and can be re-constructed from the arrival position of the ions on a position-sensitive detector. Velocity-map imaging (VMI) was a technical improvement of ion imaging that ensured that the ions' arrival position is only a function of their velocity and not of the position where they were formed.[8] Velocity resolutions

[a)]S. Abujarada and H. AlSalem contributed equally to this work.
[b)]Author to whom correspondence should be addressed. Electronic mail: sven.koehler@manchester.ac.uk. Telephone: +44 161 306 4448.

of better than 1% have been achieved in some VMI spectrometers.[9–11]

It hence seemed a logical step to adopt the VMI technique for surface studies in order to derive high-resolution velocity distributions. Wodtke and co-workers were the first to apply the VMI technique to surface desorption processes by combining VMI with TOF measurements.[12] In the laser-induced desorption of neutral Br atoms from a KBr single crystal, the surface of the crystal was oriented parallel to the ion optics and the detector, and the surface normal to the crystal was aligned along the TOF tube. TOF information—and hence velocity distributions along the surface normal—was obtained by varying the delay between the desorption and the ionisation lasers, while VMI was used to derive the velocity distributions in the two dimensions parallel to the KBr surface. White and co-workers employed the surface-VMI technique to shed light onto the photodesorption of O_2 and photofragmentation of butanone adsorbed on TiO_2(110).[13,14] Nesbitt and co-workers also employed surface-VMI to study the molecular beam scattering of HCl from Au(100) single crystals;[15] most recently, they obtained 3D velocity information for HCl scattered from self-assembled monolayers by elegantly utilising the dc slicing technique to achieve a velocity resolution along the surface normal of around 11%.[16] In all of the above experiments, the surface normal was aligned along the TOF axis of the VMI spectrometer. In contrast, Harding *et al.* have recently demonstrated measurements of speed and angular distributions of N_2 scattered from a Au(111) single crystal whose surface normal lies in a plane parallel to the ion optics and detection plates.[17] Velocity distributions are in this case measured under spatial imaging conditions by varying the delay between the ionization laser pulse and extraction pulse to follow the movement of the scattered molecules away from the surface but parallel to the imaging detector.

The combination of TOF and VMI techniques can potentially produce fully resolved three-dimensional velocity distributions of neutral fragments from surfaces; if REMPI spectroscopy is applied, internal state distributions can be obtained as well, i.e., fully resolved internal and rotationally resolved translational energy distributions can be recorded, the "holy grail" of reaction dynamics. However, for surface desorption processes, one has to pay attention to the exact geometry of the detection system: If the fragments are produced at one small spot on the surface and detected within a small volume above the surface, then some fragments may be missed, and hence the angular distribution measured is determined by this optical geometry, and may not reflect the dynamics of the process. Wodtke and co-workers overcame that problem by desorbing fragments from a relatively large spot on the surface and ionising the neutral fragments within a small volume above the surface (referred to as *sheet-dot*), such that a relatively large polar angle of ~60° symmetric around the surface normal could be recorded.[12,18] We here present the first studies in which the more intuitive *dot-sheet* geometry is used to state-selectively record fully resolved three-dimensional velocity distributions over almost the full 2π sr; the experimental details and the advantages and disadvantages of this approach are discussed in more detail in Sec. II.

The test system investigated here is the photodesorption of NO from a Au(100) single crystal. Nitric oxide is a key intermediate in a range of industrially relevant processes, such as the reduction of higher oxidation state nitrogen compounds (nitrates and nitrites) to ammonium or ammonia compounds or laughing gas N_2O, as well as in the oxidation of ammonia.[19,20] On Pt surfaces, the exact pathway for ammonia reduction is still under dispute, not only regarding the intermediates but also the mechanism, with both Langmuir-Hinshelwood and Eley-Rideal mechanisms being suggested.[19,21,22]

As for gold substrates, NO is more strongly adsorbed to Au(100) than to Au(111).[23] There is an agreement that the nitrogen atoms face the gold surface, but there are conflicting reports as to whether the neutral NO binds to Au(100) on the bridge site, i.e., between two neighboring atoms (2f site)[24] or the on-top (ot) site;[25] it is also disputed whether the NO is in a bent geometry[25,26] or along the surface normal.[24] Temperature-programmed desorption experiments and density functional theory calculations agree that NO covalently binds to gold with an adsorption energy of ~57 kJ mol^{-1},[24] and adsorption at around ~170 K ensures sufficiently high coverages to induce a hex $\rightarrow (1 \times 1)$ phase transition.[27]

While the photodesorption of nitric oxide from Au(100) has not been studied to date, NO is an attractive candidate as it is experimentally straightforwardly detected using REMPI spectroscopy.

Buntin *et al.* as well as Chuang and co-workers studied the laser-desorption of NO from Pt(111). Depending on the excitation wavelength, both found a bimodal velocity distribution, the faster component of which was attributed to excitation followed by electron-transfer to the NO adsorbate.[28–30] The desorption of NO from a non-metal Si(111) surface, however, has been found to be due to electronic excitations of the covalent substrate bonds.[31] So *et al.* investigated the interaction between the laser radiation with NO adsorbed on GaAs(110) at 80 K over a range of wavelengths and found that the desorption and dissociation of NO molecules are induced by non-thermal processes. The authors concluded that the observed desorption and dissociation could be attributed to interactions of the adsorbed NO with photogenerated charge carriers.[32] Menges *et al.* reported results on the angular distribution of NO desorbing from NiO(111) after excitation with 193 nm laser light using an experimental setup capable of state-selectively obtaining the 2-dimensional velocity distribution of the desorbed neutrals in a single experiment.[6] Garcia *et al.* studied the photodissociation of NO adsorbed on Cu(110) using reflection-absorption infrared spectroscopy. The NO dimer was found to be photoactive in contrast to bridge-bonded NO which showed no photoactivity. NO dimers photodissociate by breaking the N–N bond, releasing one NO molecule to the gas phase, while the other NO remains adsorbed on the surface in the metastable atop position.[33]

We here reported the application of 3D surface-velocity map imaging to the 355 nm photodesorption of NO from Au(100) surfaces. Section II describes in detail how we achieved to record the velocity distributions in three dimensions independently through a combination of TOF and VMI measurements. The results are presented in Section III

and their analysis in Section IV, followed by a discussion of the non-thermal nature of the NO desorption process.

II. EXPERIMENTAL

The experimental setup was designed to measure the velocity distribution of NO molecules photodesorbed from a Au(100) surface in three dimensions independently using a combination of TOF and VMI methods; the gas-phase VMI setup has been described in detail previously.[34] In brief, the spectrometer consists of two chambers, namely a molecular beam chamber which is only in operation when calibration experiments are performed, and a chamber that contains the Au(100) single crystal and the VMI optics. This chamber is evacuated by a 1000 L s^{-1} turbomolecular pump to achieve ultra-high vacuum conditions (base pressure 5×10^{-10} Torr), backed by a mechanical pump. The VMI optics, described in more detail below, consist of twelve parallel plates of 10 cm diameter, the first of which, typically referred to as the repeller plate, features a 12 mm diameter central hole. A 10 mm diameter Au(100) crystal (1.5 mm thick) equipped with a K-type thermocouple is attached to a sample mount connected to a 3-axes/rotational manipulator which allows for heating and liquid nitrogen cooling, see Fig. 1.[35] While the 12 mm opening in the repeller plate can accommodate the Au crystal, the physical contact between the liquid nitrogen-cooled crystal and the room-temperature repeller plate heats up the crystal too quickly, and the crystal is hence set-back by 0.5 mm behind (i.e., further away from the laser) and parallel to the repeller plate. The surface normal of the gold crystal is aligned along the TOF tube (z axis) of the spectrometer, at the end of which a 40 mm diameter multi-channel plate detector (Burle Photonis) is located (time-of-flight path for mass-separation is 45 cm). The manipulator also holds a 10 mm diameter stainless-steel disc with a central 2 mm hole; this disc can be placed in position instead of the gold crystal and allows us to run gas-phase calibration experiments using the molecular beam under otherwise identical conditions without having to break the vacuum. Both the crystal and repeller plate are connected to separate power supplies held at the same voltage such that the field experienced by the fragments in vacuum at the point where they are ionised (between the repeller and the second plate) is homogenous, as proven by gas-phase calibration experiments.

The gold crystal is heated prior to experiments to 700 K and subsequently cooled to ~170 K. Nitric oxide (NO) gas is introduced into the chamber as background gas at a pressure of $\sim 5 \times 10^{-7}$ Torr for a few minutes, and the NO gas pressure is maintained at $\sim 5 \times 10^{-8}$ Torr during experiments to re-dose the surface, resulting in a sub-monolayer NO coverage.[6,27]

With the crystal in place, a frequency-tripled Nd:YAG laser (Quanta Ray DCR-11, $h\nu$ = 3.5 eV, pulse duration 7 ns) beam is directed through small holes in the VMI electrodes at the NO/Au(100) surface at an angle of 45°. The energy of 1.5 mJ and the repetition rate of 20 Hz result in a transient temperature increase of ~27 K at the surface of the crystal.[36] This increase does not cause *thermal* desorption of NO molecules as shown later. The laser pulse nonetheless causes desorption of NO molecules which can potentially fly in all directions in the hemisphere above the surface. Since we are interested in the 3D velocity distribution, we have to ensure the capture of *all* NO molecules desorbing under all possible angles by paying particular attention to the optical detection geometry. If one were to desorb fragments from a small spot on the surface and detect these fragments within a small volume above the surface, then the experiment is biased towards detecting only those fragments flying in a straight line from desorption spot on the surface to the detection volume. In order to detect all fragments, one can either increase the area which the desorption laser illuminates and detect the fragments within a small volume above the surface (*sheet-dot*);[12,37] alternatively, one can use a small desorption laser spot on the surface (here ~2 mm diameter) and employ a detection laser sheet that ionises the NO fragments in a rather large volume above the surface (*dot-sheet*), see Fig. 2. Here, we report the latter, more-intuitive method for the first time.

The NO molecules are ionised in a (1 + 1) REMPI scheme via the (0,0) A ← X transition; the third harmonic of a Continuum Powerlite 8020 Nd:YAG laser was used to pump a Radiant Dyes NarrowScan laser operating on Coumarin 460; the resulting output is frequency-doubled in a BBO (barium borate) crystal to yield ~200 μJ pulses at around 226 nm at 20 Hz. Employing the 8 mm diameter

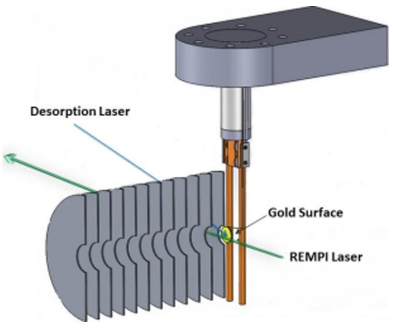

FIG. 1. Schematic of the 3D VMI setup showing the parallel alignment of the gold surface in relation to the ion optics.

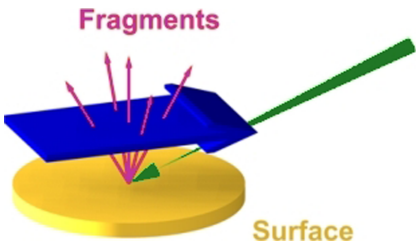

FIG. 2. Illustration of the dot-sheet conditions employed in this work. The photodesorption laser approaching from the right illuminates only a small area on the surface, while the probe laser forms a sheet above the surface to intersect as many desorbed molecules as possible.

output from this laser system, we use a cylindrical lens with a focal length of 28 cm to create such a laser sheet above the surface. This yields an effective Rayleigh length z_R for 1 + 1 REMPI detection (keeping in mind that the ionisation step is saturated and that the Rayleigh length for focusing with a cylindrical lens is defined by the beam dimension *in one direction* only doubling from waist to z_R) of more than 20 mm, hence effectively creating an 8 mm tall "curtain" above the surface through which the NO molecules have to fly. We note that we also translated the laser sheet up and down in front of the surface during measurements, but this did not affect the images, indicating that all NO radicals fly though the laser sheet. At a typical surface-to-laser distance of 3 mm, this allows us to detect all those NO molecules leaving the surface within a solid angle of 5.6 sr. As hinted above, the slightly more elaborate design of our ion optics consisting of twelve electrodes (yielding soft extraction conditions of around 50 V cm^{-1}) was chosen to increase the volume in which VMI conditions prevail, which we have previously established experimentally,[34] and we are hence confident that all NO molecules crossing the laser sheet are ionised and accelerated under true VMI conditions.

By varying the time delay between the desorption and the probe lasers, we record time-of-flight profiles, but crucially, since the probe laser beam is focussed using a cylindrical lens and hence forms a sheet above the surface, these TOF profiles can be converted into velocity distributions that deliver the velocity component along the surface normal (v_z) exclusively, i.e., not the overall speed.

An NO molecule desorbing from the surface straight along the surface normal ($v = v_z$) is detected by the REMPI laser after the same time delay as an NO molecule that leaves the surface with a certain angle and whose overall speed may be higher ($v > v_z$) as long as their velocity along z is the same; due to the "sheet"-shaped probe laser, converting these TOF profiles to velocity distributions hence delivers v_z. However, all particles ionised within this extended volume nonetheless adhere to velocity map imaging conditions as shown previously.[34] The ions are then accelerated down the time-of-flight tube (for mass separation) onto the position sensitive multi-channel plate (MCP) detector. This MCP detector is gated using a DEI PVX-4140 high voltage pulser in order to discriminate against ions other than NO^+. The ions' arrival positions are imaged onto a phosphor screen and captured by a synchronised CCD camera (FOculus FO124TB) before being transferred to a PC using a frame grabber (NI PCI-8254R). Custom-written LabVIEW software is used to accumulate and save the images, which are subsequently converted to velocity distributions. Since the gold surface and the detector are parallel to each other but perpendicular to the TOF axis of the spectrometer, the velocity distributions correspond to the remaining two velocity components v_x and v_y (where y is along the propagation direction of the REMPI laser and x is the vertical axis in the laboratory frame, see Fig. 1) for specific values of v_z.

In essence, by varying the time delay between the desorption and probe lasers in discrete steps, we are able to record velocity distributions along z (v_z), and for each time delay, we obtain the velocity distribution along x and y from the velocity map images.

III. RESULTS

Distributions of the NO velocity component flying along the z axis after 355 nm photodesorption were recorded by varying the delay time between the desorption and probe lasers; such a TOF profile for a surface-to-REMPI laser distance of 3 mm is shown in Fig. 3(a). Fig. 3(b) shows the velocity distribution v_z of NO molecules as an average of two runs; the time delays were now chosen to yield equally spaced velocity intervals. However, since the REMPI detection is sensitive to particle densities and since each time delay probes a subset of NO molecules over a time interval determined by the probe laser pulse width (~7 ns), we applied the appropriate density-to-flux conversion and Jacobian.[38] These experiments were repeated with a surface-to-REMPI laser distance of 2 mm in order to record a larger solid angle of desorbing NO molecules (not shown), but this yielded the same result within the error of the experiment. The S/N ratio at 2 mm was comparable to that at 3 mm, indicating that we detected all NO molecules in both cases, but the velocity resolution along z at 2 mm is slightly worse such that all results reported here are for a 3 mm surface-to-REMPI laser distance unless otherwise stated. The error in the velocity distribution along the z axis

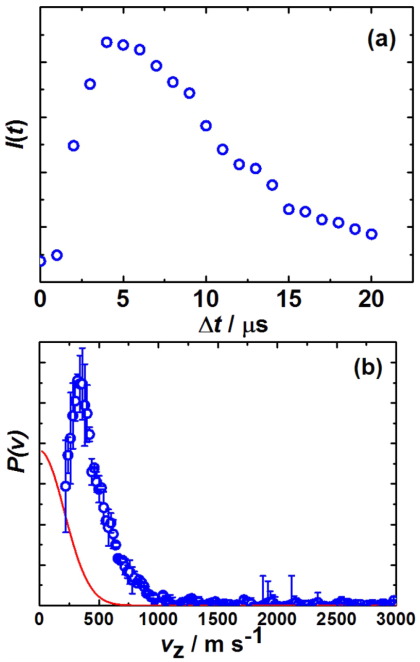

FIG. 3. (a) Raw time-of-flight data for NO photodesorbed from Au(100) at 355 nm. (b) v_z velocity distribution of photodesorbed NO after the density-to-flux conversion of the raw data (blue circles), errors represent average of two runs. A 1D Maxwell-Boltzmann distribution at the surface temperature is provided for comparison (red line).

is given by $\Delta l/l$, where Δl is the uncertainty of determining the exact distance between the surface and the probe laser; we estimate the error to be around 0.1 mm/3.0 mm = 3%. One major advantage of employing the TOF technique to acquire v_z with a well-defined laser-pump–laser-probe setup is the high velocity resolution obtained.

The remaining two velocity components v_x and v_y, which are parallel to the Au(100) surface, are derived from the velocity map images which are recorded at laser delay times corresponding to velocities v_z for which data points were recorded. These raw velocity map images, two of which are shown in Fig. 4, are recorded in density space and are subsequently converted to velocity space. Each raw image is composed of single images from approximately 20 000 laser shots. The center of these images corresponds to zero velocity in the x and y dimension, even though this center is shifted slightly with respect to the center of our CCD camera, an effect that we also observe to the same extent in our gas-phase experiments, and is due to the slight misalignment of the ion optics. The slight asymmetry we observe in some images is also likely due to either the misalignment of the ion optics or the round desorption laser illuminating an ellipsoidal area on the surface or the probe laser, which is focussed using a cylindrical lens and has a Gaussian intensity profile in the direction not affected by the focussing; the latter favours fragments desorbing along the surface normal over those flying up or down in the laboratory frame, but fragments seem to intersect the central part of the laser beam, keeping distortions at a modest level.

In order to obtain three-dimensional velocity distributions, the results from the TOF profiles and the VM images must be appropriately combined as described in Sec. IV.

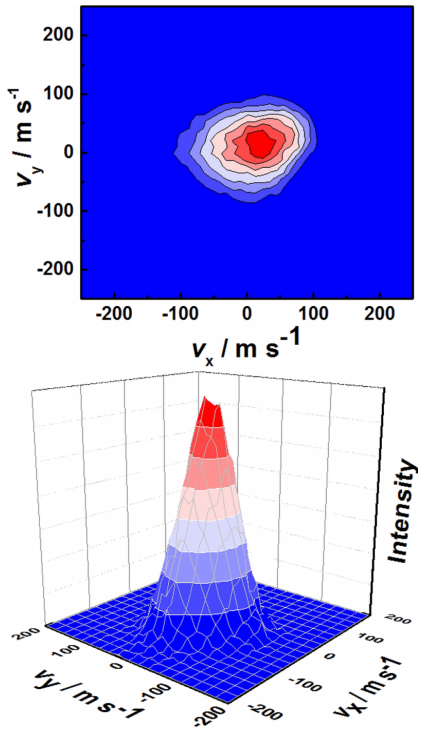

FIG. 4. Velocity map images of NO recorded at desorption-REMPI laser delay times corresponding to 420 m s^{-1} (top) and 560 m s^{-1} (bottom).

IV. DISCUSSION

Since the v_z distributions are strictly speaking 1D velocity distributions, they are compared in Fig. 3(b) with a 1D Maxwell-Boltzmann distribution at the temperature of the gold surface; however, the experimental v_z distribution of NO peaking at non-zero velocities is not well described by the 1D Maxwell-Boltzmann distribution, indicating a non-thermal desorption process. The experimental v_z distribution peaks at velocities just below 500 m s^{-1} and appears mono-modal.

Combining the TOF and VMI measurements results in 3D distributions which are cumbersome to visualize. Since the VM images appear roughly circular, i.e., there does not seem to be a preference for the NO molecules to fly along the [001] over the [010] direction, we azimuthally averaged the two velocity distributions parallel to the Au(100) surface to yield $v_{x/y}$. Fig. 5 shows a smoothed surface plot combining TOF data and VM images. It can be seen that while v_z is most intense at around 500 m s^{-1} and extends up to around 1000 m s^{-1}, $v_{x/y}$ almost completely vanishes at velocities higher than 200 m s^{-1}, illustrating that the desorption of NO molecules is confined to a rather narrow cone along the surface normal. To highlight this angular preference further, we created a polar contour plot of intensity as a function of both, overall speed and polar angle, see Fig. 6. The angular distribution is quite narrow throughout, always narrower than 25°, and it can be clearly seen that the NO molecules preferentially desorb along the surface normal. This is not unexpected, of course, as the flux of atoms or molecules leaving a surface typically peaks along the surface normal.[39,40] The smooth transition of the distributions from their peak along the surface normal to polar angles of only around 25° (i.e., without a sudden cutoff)

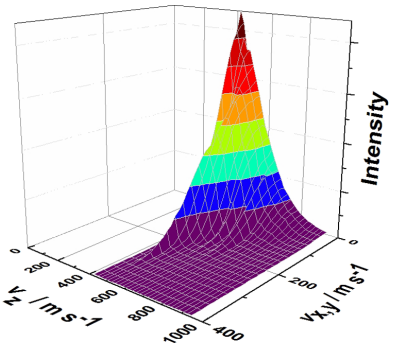

FIG. 5. Smoothed surface plot of the NO flux as a function of v_z (from TOF measurements) and the azimuthally averaged $v_{x/y}$ (from VM images) recorded at 3 mm surface-to-REMPI laser distances.

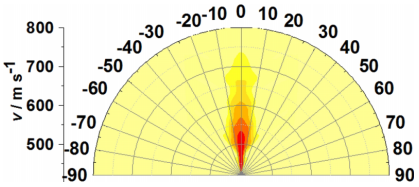

FIG. 6. Plot of the NO flux as a function of overall speed and angle after 355 nm photodesorption. Color scheme from red (most intense) to faint yellow (zero intensity). Note that the geometry of our 3D surface VMI setup allows NO molecules desorbing from the surface at angles of up to 53° to be detected.

also proves that we cover the full angular distribution which would theoretically, purely based on the detection geometry, and have allowed the detection of NO molecules up to polar angles of 53° (or even 63° for substrate-probe laser distances of 2 mm as used in some of the experiments here).

Fig. 7 shows the angular distribution of the NO molecules for selected overall speeds. Also shown are fits of these distributions to $\cos^n \theta$ functions, where a fitting parameter of $n = 1$ is typical for thermal desorption processes. The angular distributions for even the slowest NO molecules can only be fitted with $n > 1$, and it can also be seen that the angular distributions become narrower with increasing overall speed.

Fig. 8 shows the overall speed distribution of NO molecules independent of angle and compares it to a fitted 3D Maxwell-Boltzmann distribution at a temperature of 317 K. The lack of intensity below 400 m s^{-1} and the narrower distribution as compared to the Maxwell-Boltzmann fit are good indications that the overall speed distribution is not

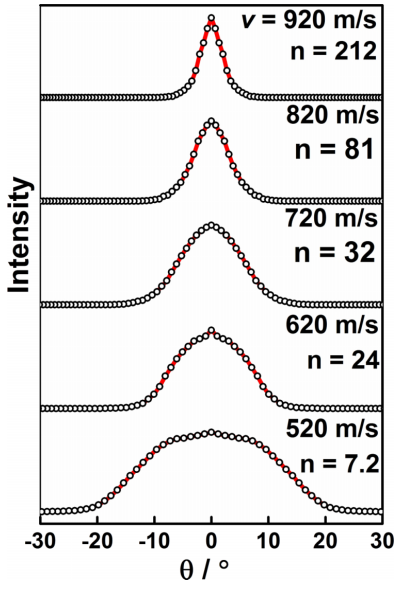

FIG. 7. Experimental angular distributions (circles) for selected speeds of photodesorbed NO molecules together with fits to a $\cos^n \theta$ distribution (red lines); plots are offset vertically for clarity.

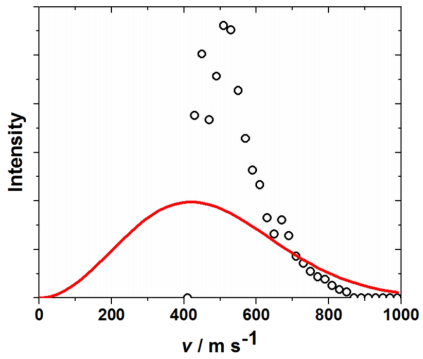

FIG. 8. Overall speed distribution of the desorbed NO molecules (obtained by appropriately combining v_z with v_x and v_y) and a Maxwell-Boltzmann best fit at a temperature of 317 K in red.

thermal. Fig. 9 shows the integrated (over all flight times) signal intensity of NO molecules desorbed from gold at various surface temperatures. It can be seen that a significant fraction of the NO molecules are still adsorbed to the surface even at and above the temperature reached during the laser pulse (~197 K), such that purely thermal desorption is unlikely to occur.

All the above results point to a non-thermal mechanism due to electronic excitation. This could either be a "hot" electron mechanism in which an electron from the conduction band is excited above the Fermi level (E_F); this is followed by tunnelling into an unoccupied state of the adsorbate forming a negative ionic state, from which the desorption of the neutrals occurs.[41,42] Fukutani *et al.* consider such a mechanism for the 193 nm photodesorption of NO from Pt(111).[30] Alternatively, the photon may cause excitation within the adsorbate molecule which—once in an excited state—undergoes desorption. For NO on Ni(111), Yates and co-workers argue that the interaction between the NO $2\pi^*$ antibonding orbital and the Ni d bands causes the occupied NO $2\pi^*$-d state and the unoccupied NO $2\pi^*$-d state to be below and above the Fermi level with an energy gap of ~3.7 eV, close to the excitation laser wavelength of 355 nm used in

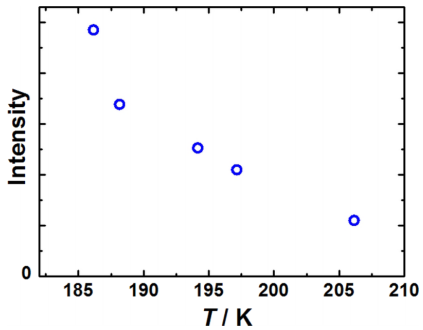

FIG. 9. Integrated signal intensity of NO desorbed from Au(100) as a function of temperature.

their experiments.[43] Rogozik *et al.* reported that these levels are expected to broaden and extend to near E_f as a result of the strong molecule/metal interaction.[44] It seems hence plausible that the desorption of NO from Au(100) observed in this work at 355 nm is also either due to excitation within the adsorbed NO itself or due to a substrate-mediated mechanism.

In order to shed more light onto the excitation mechanism of NO adsorbed on Au(100), we performed first principles quantum chemical calculations based on density-functional theory. We employed the Cambridge Serial Total Energy Package (CASTEP) which solves the Kohn-Sham equations with a plane wave basis set employing three-dimensional periodic boundary conditions,[45] similar to our previous work.[46] We used the Perdew–Burke–Ernzerhof (PBE) functional to approximate the exchange and correlation effects in the electronic properties.[47] For all but 100% coverage, we find that the NO preferentially adsorbs on the bridge (2f) site with a weak adsorption energy of between 0.65 eV and 0.8 eV depending on the coverage. This is roughly in agreement with previous calculations by Olvera-Neria *et al.* (0.53 eV) for NO on a single gold atom[26] and by Niemantsverdriet and co-workers (0.57 eV for adsorption on the bridge site).[24] Thermal desorption experiments (0.59 eV) also agree with the above calculated adsorption energies[27] but are in contrast to Liu and co-workers who computationally studied 25% coverage of NO on Au(100) and found an adsorption energy of 0.26 eV for the on-top (ot) site;[25] we note that we calculate an adsorption energy of 0.20 eV for the ot site, but—as mentioned above—also find an energetically more favourable conformation in the form of the 2f site. On the latter, the single electron in the two NO π^* orbitals (belonging to the nitrogen atom) can efficiently overlap with the orbitals on two neighbouring Au atoms at the surface between which the NO is located, resulting in an N–O bond aligned along the surface normal. We find this upright arrangement in fact for all sites and coverages apart from on-top cases, where the overlap of the π^* orbital with the orbitals on a single Au atom causes the NO to tilt.

We mapped the partial density-of-states of the Au–NO complex around the Fermi energy separately for the Au atom and the NO molecule in search for a plausible non-thermal excitation mechanism. It appears that for the 2f site (as well as for the hollow 4f, but not for the ot site), some filled Au orbitals (belonging to p orbitals) at ∼3 eV below the Fermi energy and some unoccupied orbitals belonging to the nitrogen p orbitals of the NO around 0.5 eV above the Fermi energy exist. Since this gap of ∼3.5 eV is roughly equivalent to our excitation laser wavelength of 355 nm, excitation from the substrate to the adsorbate is likely to be responsible for the non-thermal desorption of NO from Au(100).

V. CONCLUSIONS

In this paper, we have demonstrated the capability of a 3D surface VMI apparatus to study photodesorption processes. The combination of TOF and imaging methods negates the need for complex instrumentation employing rotatable mass-spectrometers for which data acquisition can be time-consuming. 3D surface VMI delivers fully resolved velocity distributions with high resolution if one ensures that all desorbing particles are detected and presents hence a faster method for surface reaction studies. The angularly resolved velocity distributions of NO photodesorbed from Au(100) indicate that a non-thermal mechanism is responsible for the NO desorption, and this seems likely to be induced by a substrate-mediated excitation.

Note added in proof. Since acceptance of this manuscript, Greaves and co-workers have presented scattering experiments of ammonia from dielectric PTFE surfaces with the surface placed within the ion optics and the surface normal aligned perpendicular to the spectrometer's axis using their 2D-VMI setup.[48]

ACKNOWLEDGMENTS

We thank the Dalton Cumbrian Facility program, funded in part by the Nuclear Decommissioning Authority. H.A.S. and S.A. thank the Saudi and Libyan government, respectively, for funding. We also thank Alisdair Macpherson for help with the Quanta Ray laser system.

[1]S. T. Ceyer and G. A. Somorjai, Ann. Rev. Phys. Chem. **28**, 477 (1977).
[2]P. H. Kobrin, G. A. Schick, J. P. Baxter, and N. Winograd, Rev. Sci. Instrum. **57**, 1354 (1986).
[3]S. W. Rosencrance, D. E. Riederer, R. Chatterjee, C. He, N. Winograd, and Z. Postawa, Nucl. Instrum. Meth. Phys. Res. B **101**, 137 (1995).
[4]J. J. Czyzewski, T. E. Madey, and J. T. Yates, Jr., Phys. Rev. Lett. **32**, 777 (1974).
[5]J.-G. Lee, J. Ahner, and J. T. Yates, Jr., J. Am. Chem. Soc. **124**, 2772 (2002).
[6]M. Menges, B. Baumeister, K. Al-Shamery, H.-J. Freund, C. Fischer, and P. Andresen, Surf. Sci. **316**, 103 (1994).
[7]D. W. Chandler and P. L. Houston, J. Chem. Phys. **87**, 1445 (1987).
[8]A. T. J. B. Eppink and D. H. Parker, Rev. Sci. Instrum. **68**, 3477 (1997).
[9]W. Li, S. D. Chambreau, S. A. Lahankar, and A. G. Suits, Rev. Sci. Instrum. **76**, 063106 (2005).
[10]G. Wu, W. Zhank, H. Pan, Q. Shuai, B. Jiang, D. Dai, and X. Yang, Rev. Sci. Instrum. **79**, 094104 (2008).
[11]J. J. Lin, J. Zhou, W. Shiu, and K. Liu, Rev. Sci. Instrum. **74**, 2495 (2003).
[12]S. P. K. Koehler, Y. Ji, D. J. Auerbach, and A. M. Wodtke, Phys. Chem. Chem. Phys. **11**, 7540 (2009).
[13]D. Sporleder, D. P. Wilson, and M. G. White, J. Phys. Chem. C **113**, 13180 (2009).
[14]M. D. Kershis, D. P. Wilson, M. G. White, J. J. John, A. Nomerotski, M. Brouard, J. W. L. Lee, C. Vallance, and R. Turchetta, J. Chem. Phys. **139**, 084202 (2013).
[15]J. R. Roscioli, D. J. Bell, D. J. Nelson, and D. J. Nesbitt, Phys. Chem. Chem. Phys. **14**, 4070 (2012).
[16]C. H. Hoffman and D. J. Nesbitt, J. Phys. Chem. C **120**, 16687 (2016).
[17]D. J. Harding, J. Neugebohren, D. J. Auerbach, T. N. Kitsopoulos, and A. M. Wodtke, J. Phys. Chem. A **119**, 12255 (2015).
[18]Y. Ji, S. P. K. Koehler, D. J. Auerbach, and A. M. Wodtke, J. Vac. Sci. Technol., A **28**, 807 (2010).
[19]S. Horold, K.-D. Vorlop, T. Tacke, and M. Sell, Catal. Today **17**, 21 (1993).
[20]V. Rosca, G. L. Beltramo, and M. T. M. Koper, Langmuir **21**, 1448 (2005).
[21]A. Cuesta and M. Escudero, Phys. Chem. Chem. Phys. **10**, 3628 (2008).
[22]A. Clayborne, H.-J. Chun, R. B. Rankin, and J. Greeley, Angew. Chem., Int. Ed. **54**, 8255 (2015).
[23]S. A. C. Carabineiro and B. E. Nieuwenhuys, Gold Bull. **42**, 288 (2009).
[24]A. Hussain, D. Curulla Ferré, J. Gracia, B. E. Nieuwenhuys, and J. W. Niemantsverdriet, Surf. Sci. **603**, 2734 (2009).
[25]Y. Wang, D. Zhang, and C. Liu, Sci. China Chem. **54**, 194 (2011).
[26]O. Olvera-Neria, V. Bertin, and E. Poulain, Int. J. Quantum Chem. **111**, 2054 (2011).
[27]E. D. L. Rienks, G. P. van Berkel, J. W. Bakker, and B. E. Nieuwenhuys, Surf. Sci. **571**, 187 (2004).
[28]S. A. Buntin, L. J. Richter, D. S. King, and R. R. Cavanagh, J. Chem. Phys. **91**, 6429 (1989).

[29]R. Schwarzwald, A. Mödl, and T. J. Chuang, Surf. Sci. **242**, 437 (1991).
[30]K. Fukutani, Y. Murata, R. Schwarzwald, and T. J. Chuang, Surf. Sci. **311**, 247 (1994).
[31]L. J. Richter, S. A. Buntin, D. S. King, and R. R. Cavanagh, in *Desorption Induced by Electronic Transitions DIET V*, Series in Surface Sciences (Springer, 1990), Vol. 31, pp. 227–232.
[32]S. K. So and W. Ho, Appl. Phys. A **47**, 213 (1988).
[33]N. Garcia Rey and H. Arnolds, J. Chem. Phys. **135**, 224708 (2011).
[34]M. Reid and S. P. K. Koehler, Rev. Sci. Instrum. **84**, 044101 (2013).
[35]J. Ahner, D. Mocuta, R. D. Ramsier, and J. T. Yates, Jr., J. Chem. Phys. **105**, 6553 (1996).
[36]J. H. Bechtel, J. Appl. Phys. **46**, 1585 (1975).
[37]D. A. Chestakov, S. M. Wu, G. R. Wu, D. H. Parker, A. T. J. B. Eppink, and T. N. Kitsopoulos, J. Phys. Chem. A **108**, 8100 (2004).
[38]I. Rahinov, R. Cooper, C. Yuan, X. Yang, D. J. Auerbach, and A. M. Wodtke, J. Chem. Phys. **129**, 214708 (2008).
[39]O. J. Maselli, J. R. Gascooke, W. D. Lawrance, and M. A. Buntine, Chem. Phys. Lett. **513**(1), (2011).
[40]G. Comsa and R. David, Surf. Sci. Rep. **5**, 145 (1985).
[41]P. R. Antoniewicz, Phys. Rev. B **21**, 3811 (1980).
[42]J. W. Gadzuk, L. J. Richter, S. A. Buntin, D. S. King, and R. R. Cavanagh, Surf. Sci. **235**, 317 (1990).
[43]J. Yoshinobu, X. Guo, and J. T. Yates, Jr., J. Chem. Phys. **92**, 7700 (1990).
[44]J. Rogozik, J. Kiippers, and V. Dose, Surf. Sci. **148**, L653 (1984).
[45]S. J. Clark, I. Matthew, D. Segall, C. J. Pickard, P. J. Hasnip, M. I. J. Probert, K. Refson, and M. C. Payne, Z. Kristallogr. Cryst. Mater. **220**, 567 (2005).
[46]U. K. Chohan, E. Jimenez-Melero, and S. P. K. Koehler, Appl. Surf. Sci. **387**, 385 (2016).
[47]J. P. Perdew, K. Burke, and M. Ernzerhof, Phys. Rev. Lett. **77**, 3865 (1996).
[48]D. J. Hadden, T. M. Messider, J. G. Leng, and S. J. Greaves, Rev. Sci. Instrum. **87**, 106104 (2016).

Appendix D

Paper2

THE JOURNAL OF PHYSICAL CHEMISTRY C

Article

pubs.acs.org/JPCC

Translational and Rotational Energy Distributions of NO Photodesorbed from Au(100)

Saada Abujarada,[†,‡] Christoph Flathmann,[†,‡,§] and Sven P. K. Koehler*[,‡,∥]

[†]School of Chemistry and [‡]Photon Science Institute, The University of Manchester, Manchester M13 9PL, United Kingdom

[§]IV. Physikalisches Institut, Georg-August-Universität Göttingen, Friedrich-Hund-Platz 1, 37077 Göttingen, Germany

[∥]School of Science and the Environment, Manchester Metropolitan University, Chester Street, Manchester M1 5GD, United Kingdom

ABSTRACT: We report velocity and internal state distributions of nitric oxide photodesorbed from an Au(100) single crystal using 355 and 266 nm photons. The velocity distributions were measured in all three dimensions independently using our novel 3D-velocity map imaging setup. Combined with the internal energy distributions we reveal two distinct desorption mechanisms for the photodesorption of NO from gold dependent on the photon wavelength. The 355 nm desorption is dominated by a nonthermal mechanism due to excitation of an electron from the gold substrate to the adsorbed NO; this leads to a superthermal and noticeably narrow velocity distribution and a rotational state distribution that positively correlates with the velocity distribution and can be described by a rotational temperature appreciably above the surface temperature. Desorption with 266 nm photons leads to a slower average speed and wider angular distribution and rotational temperatures not too far off the surface temperature. We conclude that in the absence of occupied orbitals in the substrate and unoccupied orbitals on the adsorbed NO separated by 4.7 eV, corresponding to 266 nm; the shorter wavelength desorption is dominated by a thermally activated mechanism.

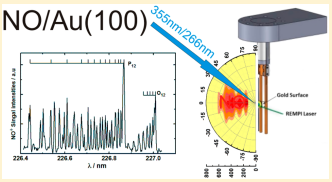

Downloaded via UNIV OF MANCHESTER on November 16, 2018 at 14:35:27 (UTC).
See https://pubs.acs.org/sharingguidelines for options on how to legitimately share published articles.

1. INTRODUCTION

Photon-induced chemical reactions including the desorption of small molecules such as NO, CO, or O_2 from solid surfaces have been a thriving area of research.[1−7] The aim of such investigations is typically to unravel and understand the basic processes that control the elementary steps, i.e., the mechanism and dynamics of adsorbate−substrate interactions during the desorption process. In this context, nitric oxide desorption from metal surfaces has been thoroughly investigated by many research groups using different experimental and theoretical methods.[8−11] NO has been the adsorbate of choice for many reasons, one of which is that NO is associated with many catalytic reactions in which it interacts with a surface.[12] Another reason is that NO molecules in the gas phase can easily be detected state selectively by, e.g., resonance-enhanced multiphoton ionization (REMPI) or laser-induced fluorescence (LIF) spectroscopy.

Some studies revealed the existence of two specific channels for NO desorption from various substrates, namely, a thermal and a nonthermal mechanism.[13] Thermal desorption is the result of complete energy equilibration before desorption occurs. Electronically excited intermediate states are short lived on metal surfaces where relaxation of exited states of adsorbed molecules is expected to be extremely rapid, with lifetimes of only a few femtoseconds; hence, fast and sensitive probes are required to monitor the dynamics of desorption (characterized by translational, vibrational, and rotational temperatures).[14,15] For nonthermal desorption, energy equilibration is incomplete at the time of desorption, and the internal and translational energy distribution of the desorbing molecule may provide clues regarding the desorption mechanism. The energy of the photon causing electronic excitation of the system is partitioned into translational and internal (vibrational and rotational) energy, as well as dissipation into the substrate. This partitioning is determined by the potential energy surface and the lifetime of the intermediate excited state as described by the Menzel−Gomer−Redhead (MGR)[16,17] and Antoniewicz[18] models. Therefore, measurements of the translational and internal energy distribution of the desorbed molecules can shed some light onto the desorption mechanism and the energy flow pathways during photodesorption.

King and co-workers reported thermal and nonthermal mechanisms of the laser-stimulated desorption of NO from Pt(111) at 1064, 532, and 355 nm; they deduced that the nonthermal desorption is hot carrier initiated due to excitation of the substrate at photon energies in the range from 1.17 to 3.5

Received: July 19, 2017
Revised: August 18, 2017
Published: August 23, 2017

ACS Publications © 2017 American Chemical Society

DOI: 10.1021/acs.jpcc.7b07116
J. Phys. Chem. C 2017, 121, 19922−19929

eV,[19,20] resulting in desorbed NO molecules exhibiting a non-Boltzmann rotational energy distribution. Fukutani et al. concluded that substrate excitation was responsible for the laser-induced NO desorption from Pt(001) for photon energies in the range between 3.5 and 6.4 eV;[21] the evidence provided was that translational and internal energy distributions were independent of the pump laser wavelength. In contrast to the work by King and co-workers, the rotational state distribution of desorbed NO from Pt(001) followed a Boltzmann distribution, with the two spin−orbit states in equilibrium with very similar rotational temperatures. The photon-stimulated desorption of NO from a Pt(111) surface at 80 K was investigated by Chuang and co-workers using REMPI spectroscopy.[22] Two distinctive desorption channels were identified on a nonannealed surface and a surface annealed to 220 K after NO adsorption at 80 K. The rotational energy distribution was found to follow a Boltzmann distribution for as-adsorbed Pt(111) and was non-Boltzmann on the annealed Pt(111) surface, with an inverted population of spin−orbit states, in agreement with the results reported by Buntin et al.[20]

Richter et al. studied the laser-induced desorption of NO from Si(111) at a surface temperature of 100 K[23] and found the desorption dynamics to be sensitive to the initial coverage with NO. The energy partitioning in the desorbed NO and the dependence of the energy partitioning on the desorption laser wavelength suggested that different photoreaction channels are in operation at low and high coverage; for low coverage, the resultant energy partitioning in the desorbed NO is such that translation and vibration carry most of the photon energy. The kinetic energy distributions were found to be non-Maxwellian, while the rotational state populations were adequately described by a Boltzmann distribution.

Mulugetaet et al. reported on the internal energy distributions of desorbed NO obtained by REMPI spectroscopy for Ag(111) and for Ag nanoparticles;[24] NO molecules were detected with hyperthermal velocities and with vibrational and rotational temperatures significantly higher than the sample temperature.

Recently, a number of groups began to exploit the advantages of the velocity map imaging (VMI) technique—so far predominantly used for gas-phase studies—for surface dynamics studies.[25−29] We previously reported on the use of a combination of time-of-flight (TOF) and VMI techniques for resolving 3-dimensional velocity distributions of NO photo-desorbed from a gold single crystal using 355 nm photons.[30] NO molecules were found to leave the surface preferentially along the surface normal with a very narrow angular and rather fast velocity distribution, indicating a nonthermal desorption process. This was attributed to the excitation of an electron from a filled p orbital on gold to an unoccupied p orbital on the nitrogen (of an adsorbed NO) around 3.5 eV higher in energy and close in energy to our excitation wavelength. In the present paper, we expand this work to include laser excitation with 266 nm photons and add the rotational state distribution for both excitation wavelengths, which allows us to compare and analyze results to identify any differences in the mechanism of the photodesorption of NO from Au(100).

2. EXPERIMENTAL METHODS

The experimental setup was designed to measure the velocity distribution of fragments photodesorbed from a surface in three dimensions independently using a combination of TOF and VMI methods as described in detail elsewhere.[31] In brief, the spectrometer consists of two chambers, namely, a molecular beam chamber which is only in operation when gas-phase calibration experiments are performed and a UHV chamber that contains the Au(100) single crystal and the VMI optics. This chamber is evacuated by a 1000 L s^{-1} turbomolecular pump backed up by a mechanical pump achieving a base pressure of 5×10^{-10} Torr. The Au(100) crystal (10 mm diameter, 1.5 mm thick, from Surface Preparation Laboratory) equipped with a K-type thermocouple is attached to a sample mount connected to a 3-axes/rotational manipulator which allows for heating and liquid nitrogen cooling. The VMI optics consist of 12 parallel plates of 10 cm diameter whose surface normals are aligned along the center axis of the TOF spectrometer. Twelve plates were employed in order to increase the volume in which VMI conditions prevail.[31] Prior to experiments, the gold single crystal is cleaned by heating to 700 K and subsequently cooled to ∼178 K. Pure NO gas is introduced into the chamber through a molecular beam valve at a background pressure of $\sim 5 \times 10^{-6}$ Torr for a few minutes to establish a submonolayer NO coverage. The valve was then adjusted to yield a background pressure of NO of 5×10^{-8} Torr; this suppressed the background signal sufficiently while allowing the surface to be redosed continuously during the experiment. Desorption of chemisorbed NO from the Au(100) crystal was initiated by a Nd:YAG laser (Quanta Ray DCR-11), which was either frequency tripled (3.5 eV) or quadrupled (4.7 eV) with a pulse duration of 7 ns at a repetition rate of 20 Hz and a pulse energy of ∼1.2 mJ. The beam was directed at the NO/Au(100) surface at an angle of 45°. The desorbed NO molecules may fly in all directions within the hemisphere above the surface. In order to obtain a complete 3D velocity distribution, the optical detection geometry design must ensure that all NO molecules flying off the surface at all possible angles are detected. We have done so by creating a small desorption laser spot on the surface (<1 mm in diameter) while detecting the NO molecules within a rather large volume in front of the surface such that a large fraction of the hemisphere above the surface is covered.[25,32] The desorbed NO molecules were detected state selectively by a 1 + 1 REMPI scheme via the A ← X (0,0) transition by employing a frequency-doubled Radiant Dyes NarrowScan laser, operating on Coumarin 460, pumped by a Continuum Powerlite 8020 Nd:YAG laser.[33] The resulting output is frequency doubled in a BBO (barium borate) crystal to yield ∼200 μJ pulses at around 226 nm at 20 Hz. A cylindrical lens of 28 cm focal length was used to focus the output of the laser system to create a laser sheet with an area of $\sim 20 \times 8$ mm^2 above the center of the surface. The REMPI laser beam path was adjusted using linear translation stages to pass in front of the surface with a surface-laser distance of 3 mm, giving a velocity resolution along the z axis of ∼3% (assuming we can adjust and reproduce the position to within 100 μm, hence $\Delta d/d \approx 3\%$) and allowing us to detect all those NO molecules leaving the surface within a solid angle of 5.6 sr. The elaborate design of the ion optics (by using 12 plates, resulting in a shallow electric field gradient and weak extraction conditions) allows all those NO molecules ionized by the laser to be accelerated under true VMI conditions.[31] We recorded TOF profiles by varying the time delay between the desorption and the probe laser; these profiles were converted into velocity distributions that deliver the velocity component along the surface normal (v_z) exclusively, i.e., *not* the overall speed of the desorbed molecules. NO^+ ions are accelerated down the time-of-flight tube (for mass separation) onto the

DOI: 10.1021/acs.jpcc.7b07116
J. Phys. Chem. C 2017, 121, 19922−19929

position-sensitive multichannel plate (MCP) detector, gated using a DEI PVX-4140 high-voltage pulser in order to discriminate against ions other than NO^+. The ions' arrival positions are imaged onto a phosphor screen and captured by a synchronized CCD camera (FOculus FO124TB). Custom-written LabVIEW software is used to accumulate and save the images, which are subsequently converted to velocity distributions. Since the gold surface and the detector are parallel to each other but perpendicular to the TOF axis of the spectrometer, the velocity distributions extracted from the VMI images correspond to the remaining two velocity components v_x and v_y parallel to the gold surface, where y is along the propagation direction of the REMPI laser, i.e., horizontal in the laboratory frame, and x is the vertical axis, for specific values of v_z.

Hence, we are able to record velocity distributions along z (v_z) by varying the time delay between the desorption and the probe laser in discrete steps, and for each time delay, we obtain the velocity distributions along x and y from the velocity map images. In order to record rotational state distributions, we fixed the delay time between the pump and the probe laser to correspond to specific velocities of the v_z distribution for both 355 and 266 nm desorption. The probe laser was scanned over an appropriate wavelength range in steps of 0.005 nm to obtain REMPI spectra for NO for a given v_z. To extract rotational state distributions of the desorbed NO molecules only, rotational spectra in the absence of the desorption laser were recorded, and background subtraction was carried out. We also applied a relative calibration scheme to avoid any factors that influence the sensitivity of different rotational lines to a different degree.[34] This was done by recording thermal NO spectra which yield a well-known Boltzmann distribution; the intensities of each rotational line of these thermal spectra were compared to the Boltzmann population of NO at 298 K to extract calibration factors which were used to convert the line intensities of the photodesorbed NO to rotational populations.

3. RESULTS AND DISCUSSION

Translational Energy. A time-of-flight (TOF) spectrum of NO following 266 nm photodesorption for a surface-to-REMPI laser distance of 3 mm is shown in Figure 1a. The probe laser wavelength was tuned to be resonant with the $Q_1(1)$ line of the (0,0) transition of NO. These TOF spectra only measure the velocity component of the NO molecules along the surface normal and were converted into a v_z distribution; Figure 1b shows the velocity distribution v_z of NO molecules as an average of three runs; the time delays in Figure 1a were chosen to yield equally spaced velocity intervals; a density-to-flux conversion was applied, as was the appropriate Jacobian.[35]

Figure 1b shows that the two 1D velocity distributions are shifted to higher velocities as compared to a 1D Maxwell–Boltzmann distribution at the surface temperature of 178 K, indicating a nonthermal desorption mechanism for both wavelengths investigated.[36,22] The 355 nm distribution can be described as bimodal, pointing toward two distinct desorption mechanisms, and most interestingly, the velocity distribution for the lower energy 355 nm desorption is shifted toward higher velocities compared to the 266 nm desorption.

We also note (not shown) that the absolute signal intensity is significantly weaker (~40%) for 266 nm desorption compared to 355 nm desorption for similar laser fluences, which may be indicative of one desorption channel not being available during

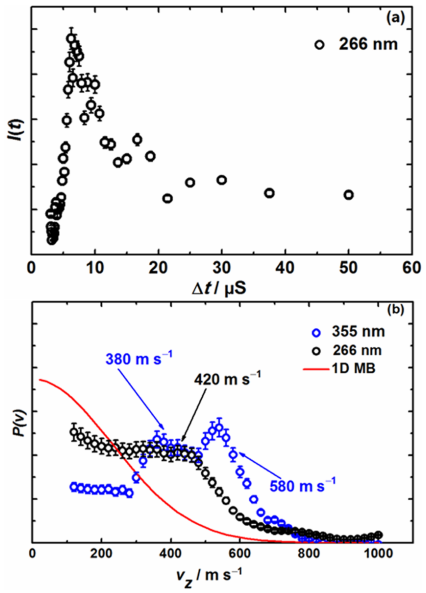

Figure 1. (a) Raw time-of-flight data for NO photodesorbed from Au(100) at 266 nm. (b) Normalized v_z velocity distribution of photodesorbed NO after density-to-flux conversion of the raw data at 266 (black circles) and 355 nm (blue circles). 1D Maxwell–Boltzmann distribution at the Au(100) surface temperature (178 K) is provided for comparison (red line). The three velocities indicated are those at which the rotational state distributions were measured.

266 nm desorption. The low signal obtained for the 266 nm desorption could also be due to the fact that the photon energy is very close to the work function of gold (5.3 eV),[37] raising the possibility of ionization of surface gold atoms forming a cationic surface, which is more active;[38] hence, the adsorbed NO will be more strongly held onto the surface.

The two velocity components v_x and v_y parallel to the Au(100) surface are extracted from the VM images which are recorded at laser delay times corresponding to velocities v_z for which images were recorded from 120 to 760 m s^{-1} in 20 m s^{-1} intervals. These raw velocity map images, two of which are shown in Figure 2, are recorded in density space and are subsequently converted to velocity space.

Each raw image is composed of 20 000 single images from equally many laser shots. The center of these images corresponds to zero velocity in the x and y dimensions, even though this center is shifted slightly with respect to the center of our CCD camera, an effect that we also observe to the same extent in our gas-phase experiments, and is due to the slight misalignment of the ion optics. This slight asymmetry obtained in some images has been also reported when using 355 nm laser.[25] This was suggested to be caused by a slight misalignment of the ion optics, by the round desorption laser illuminating an ellipsoidal area on the surface (due to its 45° angle of incidence), or by the probe laser, which is focused using a cylindrical lens and has a Gaussian intensity profile in the direction not affected by the focusing, leading to slightly different ionization efficiencies within the probe laser volume.

DOI: 10.1021/acs.jpcc.7b07116
J. Phys. Chem. C 2017, 121, 19922–19929

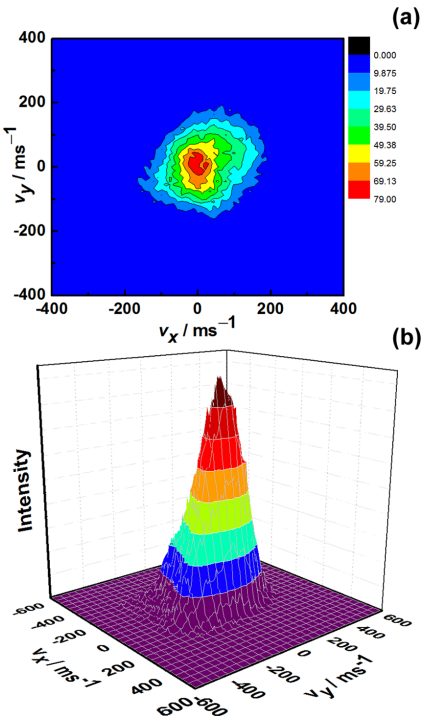

Figure 2. Velocity map images of NO recorded after 266 nm desorption at desorption-REMPI laser delay times corresponding to v_z = 360 (top) and 480 m s^{-1} (bottom).

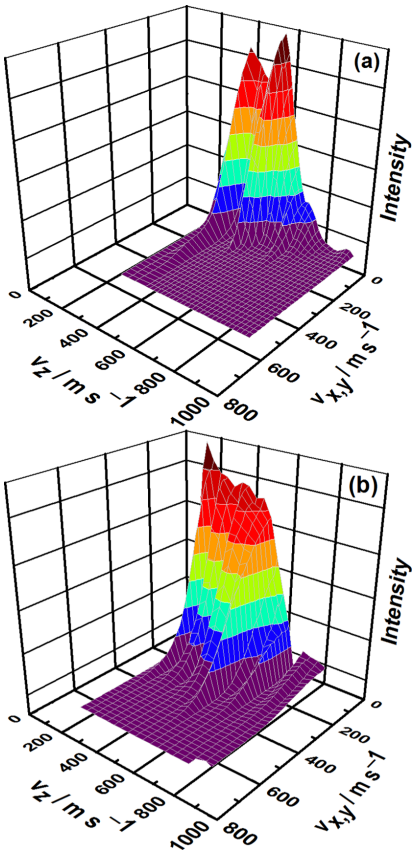

Figure 3. Smoothed surface plot of the NO flux desorbed using (a) 355 and (b) 266 nm photons as a function of v_z (from TOF measurements), and averaged parallel (to the gold surface) $v_{x/y}$ velocity components (from the VM images).

As observed when recording TOF profiles, the intensity of the images recorded after 266 nm desorption is weaker than for 355 nm desorption. An appropriate convolution of results obtained from the TOF profiles and the VM images produces 3-dimensional velocity distributions.

In order to display the intensity as a function of the velocity in three different dimensions, we chose a reduced representation by radially averaging over the two dimensions parallel to the gold surface yielding a combined $v_{x/y}$ distribution; the smoothed NO intensity as a function of $v_{x/y}$ and v_z is shown as a surface plot in Figure 3 for 266 and 355 nm desorption.

For 355 nm desorption, i.e., at photon energies considerably below the substrate's work function, v_z seems to peak at around 380 and 550 m s^{-1} but extends up to ~1000 m s^{-1}, with $v_{x/y}$ almost completely vanishing at velocities above 200 m s^{-1}, as seen in Figure 3a. However, when using 266 nm photons, i.e., energies just below the substrate's work function, the v_z velocity distribution seems to plateau between 120 and 420 m s^{-1} followed by a sharp decline with v_z vanishing at around 800 m s^{-1}, as seen in Figures 3b and 1b, while $v_{x/y}$ extends all the way to above 400 m s^{-1}. This faster-but-narrow (355 nm) vs slower-but-wide (266 nm) distribution is another indication that at least two distinct mechanisms may be in operation and is further highlighted below.

Figure 4 shows the angular distribution for 355 and 266 nm desorption as a function of the overall speed; the angular

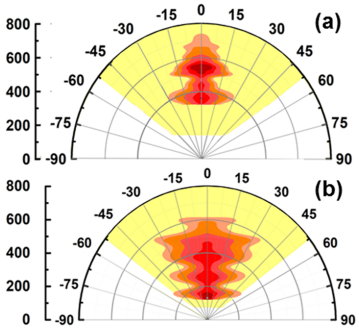

Figure 4. NO flux as a function of overall speed and angle after (a) 355 and (b) 266 nm photodesorption. Color scheme from red (most intense) to yellow (zero intensity); white areas indicate speed/angle combinations that could not be recorded.

DOI: 10.1021/acs.jpcc.7b07116
J. Phys. Chem. C 2017, 121, 19922−19929

distribution at 355 nm is rather narrow, i.e., the NO molecules preferentially desorb along the surface normal, while in the case of 266 nm desorption, the angular distribution is much wider.

The geometry of our 3D surface VMI setup allows much wider angular distributions to be detected than those measured here, up to 53°.

Figure 5 shows the angular distribution of the NO molecules for selected overall speeds for 266 nm desorption. Also shown

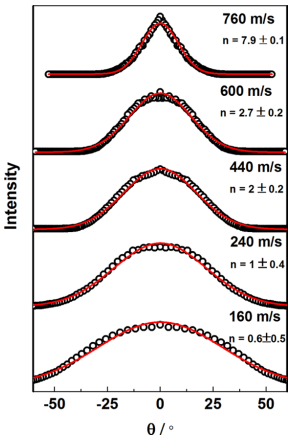

Figure 5. Angular distributions for selected speeds of desorbed NO molecules after 266 nm photodesorption together with fits to a $\cos^n \theta$ function.

are fits of these distributions to $\cos^n \theta$ functions, where a fitting parameter of $n = 1$ is typical for thermal desorption processes. As can be seen from Figure 5, at overall speeds of 240 m s^{-1} or lower, the angular distribution can be fitted resulting in $n \leq 1$, suggesting that a thermal desorption mechanism may be operating. However, for the higher speeds shown here, n is greater than 1, indicating a nonthermal desorption process. Fitting parameters for our data of the 355 nm desorption were significantly higher for the same respective speeds.[30]

Figure 6 shows the overall speed distribution of NO molecules after desorption with 266 and 355 nm photons averaged over all angles and compares it to a fitted 3D Maxwell–Boltzmann distribution at a (surface) temperature of 178 K. The figure shows that the overall speed distribution is fairly close to a thermal distribution for 266 nm desorption. This indicates that a thermal component at least contributes to the desorption mechanism, if not dominates it. This seems to be in agreement with the angular distributions, where a thermal desorption mechanism seems to be responsible for the slower NO molecules after 266 nm photodesorption, as indicated by the fitting parameter $n \leq 1$. In our previous work we have shown that NO desorption was induced predominantly by a nonthermal desorption mechanism at 355 nm.[26] We note that the temperature rise during laser irradiation is only ~27 K for 355 nm pulses, i.e., transient surface temperatures are ~205 K, but we also showed that NO still adsorbs to our substrate at those temperatures. The temperature jump for 266 nm irradiation is ~20 K (due to slightly lower laser fluences), and while the photon energy is higher than at 355 nm, the

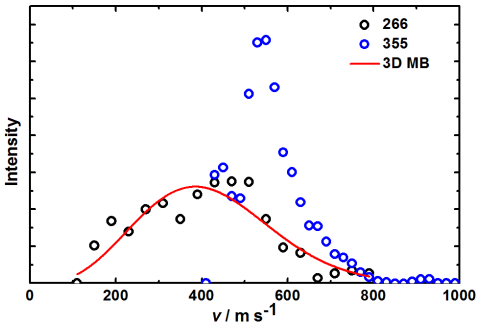

Figure 6. Overall speed distribution of the desorbed NO molecules after 266 (black circles) and 355 nm (blue circles) desorption, obtained by appropriately combining v_z with v_x and v_y, and a Maxwell–Boltzmann distribution corresponding to 178 K in red.

shorter wavelength photons seem to preferentially induce a thermal process.

For 266 nm desorption, all of the above results indicate that thermal and nonthermal desorption mechanisms are operating. This has also been suggested in the case of laser-induced desorption of NO molecules from a platinum foil[39] also from a Pt(111) surface,[18] from Ni(100)–O,[13] and from condensed films.[40]

Internal Energy. A rotationally resolved (1 + 1) REMPI spectrum of photodesorbed NO recorded on the $A^2\Sigma_{1/2} \leftarrow X^2\Pi_{3/2}$ (0,0) transition is shown in Figure 7; spectra were

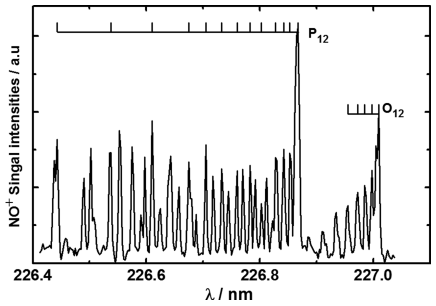

Figure 7. Typical (1 + 1) REMPI spectrum of NO desorbed from gold using 355 nm photons at time delays corresponding to NO molecules with v_z = 380 m s^{-1}.

recorded at fixed time delays Δt (i.e., at preselected velocities v_z along the surface normal) corresponding to the peak(s) in the velocity distribution, see Figure 1b; no vibrationally excited NO molecules were detected. As described in the Experimental Section, spectra of thermal NO were recorded to (a) perform background subtraction and (b) apply a relative calibration scheme to extract the rotational state distribution of the photodesorbed NO.

To simplify population analysis, we observed isolated lines from single branches, hence avoiding overlap, to obtain reliable rotational populations. Transitions originating from $N = 4–7$ and $N = 7–16$ of the O_{12} and P_{12} rotational branches of NO were chosen, respectively. After weighting the populations by

DOI: 10.1021/acs.jpcc.7b07116
J. Phys. Chem. C 2017, 121, 19922–19929

the degeneracy of the lower level, the energies of the rotational levels were calculated to yield Boltzmann plots,[41−43] shown in Figure 8 for various v_z velocities after 266 and 355 nm photodesorption. The contributions from the two spin−orbit states $^2X_{1/2}$ and $^2X_{3/2}$, which are energetically separated by about 124 cm^{-1},[40] result in similar rotational temperatures, indicating that rotational and spin−orbit excitations are in equilibrium. Since spin−orbit states are related to the axis around which rotation occurs, the results indicate that there is no preference for tumbling of the NO around a particular axis; this is expected for NO adsorbed along the surface normal on a symmetric Au(100) substrate.

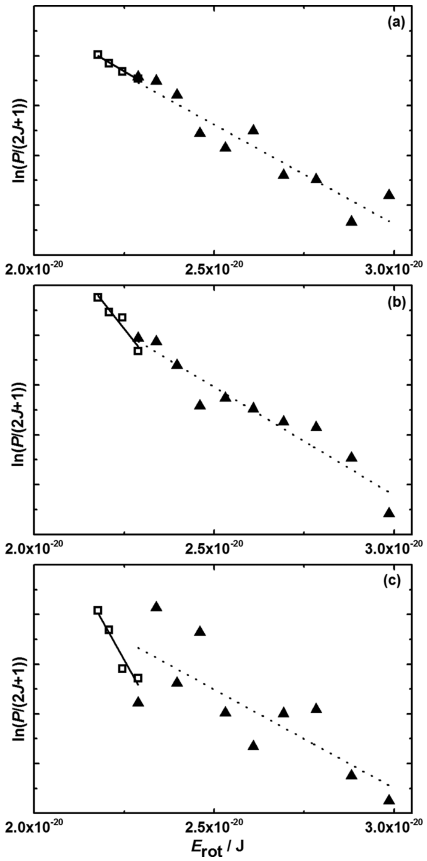

Figure 8. Rotational populations of NO molecules in $v' = 0$ desorbed from Au(100) at 178 K, extracted from the O_{12} (open squares) and P_{12} (closed triangles) branches; solid and dotted lines are linear best fits to evaluate the rotational temperature. Pump−laser wavelength and normal velocity were (a) 355 nm at v_z = 380 m s^{-1}, (b) 355 nm at 580 m s^{-1}, and (c) 266 nm at 420 m s^{-1}.

While there is no a priori reason for these nascent rotational state distributions of photodesorbed NO to be thermal, we nonetheless fitted the distributions to obtain rotational temperatures, thus simplifying comparison between different experimental conditions; the results are summarized in Table 1.

Table 1. Rotational Temperatures T_{rot} of Nascent NO Photodesorbed from an Au(100) Surface Using 355 and 266 nm Photons

	desorption laser wavelength		
	355 nm		266 nm
rotational branch	v_z = 380 m s^{-1}	v_z = 580 m s^{-1}	v_z = 420 m s^{-1}
O_{12}	(337 ± 12) K	(206 ± 5) K	(102 ± 1) K
P_{12}	(363 ± 4) K	(334 ± 4) K	(226 ± 5) K

Inspection of Table 1 reveals that the rotational temperatures for both O_{12} and P_{12} branches after 355 nm photodesorption are higher than the surface temperature at both v_z velocities measured, indicating a nonthermal desorption channel for NO. This is in agreement with the conclusions from our previous work based on the velocity distributions alone.[30] Furthermore, the rotational temperature in both O_{12} and P_{12} branches after 355 nm desorption is lower for the faster component, indicating a positive correlation, i.e., the translational and rotational energy are coupled and energy is partitioned during a common single step of the desorption process.

For the higher energy wavelength of 266 nm, the average rotational temperature of the O_{12} and P_{12} branches is lower than after 355 nm desorption and in the case of the O_{12} branch is even lower than the surface temperature. As noted earlier, the average translational energy after 266 nm desorption is also lower compared to 355 nm desorption. The rotational temperature of the O_{12} branch (102 K) suggests that rotational cooling may occur during desorption,[44] which is not unexpected for a thermal process based on the principle of detailed balance; NO molecules are likely to adsorb more readily onto a metal surface when they are rotationally cold (as rapidly rotating molecules would not spend sufficient time in the favorable head-on orientation for adsorption to occur); hence, the fraction of NO molecules thermally desorbing from the Au(100) surface after the laser-induced temperature jump may also be rotationally cold. This seems to agree with conclusions from the previous section, i.e., the presence of potentially two different mechanisms, or at least the contribution of a thermal mechanism to the 266 nm desorption. Theoretical calculations for very rapid laser-induced desorption (LID) processes have indicated a propensity toward near full translational accommodation in the desorbing molecules but less than full rotational accommodation,[45] similar to what we observe here. Cold rotational distributions are also expected as the NO is adsorbed on the bridge site of the Au(100) crystal along the surface normal with the N pointing toward the surface,[30] and little torque is hence imparted onto the NO during the desorption process.

The superthermal speed distribution of 355 nm desorption and the positive correlation between translational and rotational energy indicate that a nonthermal mechanism is in place; we attributed this to an electronic excitation of the surface and supported it by density functional theory calculations, the analysis of which showed that there are filled orbitals on the gold and unfilled orbitals on the adsorbed NO ∼3.5 eV apart, such that desorption may be mediated by an electronic transition from the metal to the adsorbate.[30] However, there may also be an underlying thermal mechanism in operation due

DOI: 10.1021/acs.jpcc.7b07116
J. Phys. Chem. C 2017, 121, 19922−19929

to the heating effect from the 355 nm laser. The weaker signal, and the absence of occupied (p orbitals of Au) and unoccupied p orbitals (on N) separated by 4.7 eV according to the density-of-states analysis of our DFT calculations,[30] indicates that a thermal mechanism may dominate the 266 nm desorption process.

For both desorption wavelengths, however, equivalent to 3.5 and 4.7 eV, we are certain that the vast majority of the photon energy goes into the substrate. Only between 0.6 and 0.8 eV are needed to desorb NO on the most stable bridge site from the Au(100) surface.[26] By (1) appropriately weighting the rotational state distributions and arriving at an average rotational energy of ∼0.1 eV, (2) calculating the average translational energy of the desorbed NO (∼0.04 eV), and (3) assuming an upper limit of vibrationally excited NO of 5% (resulting in an average vibrational energy of 0.01 eV), we conclude that more than 90% of the available photon energy goes into the substrate, in agreement with previous studies on related systems.[24,46]

■ CONCLUSION

Photodesorption of NO molecules preadsorbed on an Au(100) surface was investigated at 355 and 266 nm. Laser desorption of NO from Au(100) at 355 nm seems to *predominantly* occur through a nonthermal channel, likely involving an electronic excitation. However, when using 266 nm photons, our results show that a thermal mechanism is operating, which is caused by a jump of the surface temperature, the thermal energy associated with this being enough to cause desorption of NO molecules. Given the noticeable differences in yields, we believe that a thermal channel is also operating during 355 nm desorption but is overshadowed by the nonthermal mechanism, while the thermal mechanism contributes most of the intensity during 266 nm desorption.

We have shown the existence of these two channels for the desorption of NO from Au(100) at the two different photon energies of 266 and 355 nm using the detailed information available from our 3D-VMI experiments, rather than from TOF measurements alone, and we are confident that 3D-VMI from surfaces holds the potential to extract the detailed dynamics of many more interesting surface processes.

■ AUTHOR INFORMATION

Corresponding Author

*Phone: +44 161 247 1557. E-mail: s.koehler@mmu.ac.uk.

ORCID

Sven P. K. Koehler: 0000-0002-6303-6524

Notes

The authors declare no competing financial interest.

■ ACKNOWLEDGMENTS

S.A. thanks the Libyan government for funding, and C.F. was generously funded by an Erasmus+ scholarship. We also thank Alisdair Macpherson for help with the Quanta Ray laser system. The equipment was in part funded by the Nuclear Decommissioning Authority.

■ REFERENCES

(1) Zhou, X. L.; Zhu, X. Y.; White, J. M. Photochemistry at Adsorbate/Metal Interfaces. *Surf. Sci. Rep.* **1991**, *13*, 73−80.

(2) Zimmermann, F. M.; Ho, W. State Resolved Studies of Photochemical Dynamics at Surfaces. *Surf. Sci. Rep.* **1995**, *22*, 127−247.

(3) Menzel, D. Electronically Induced Surface Chemistry: Localised Bond Breaking Versus Delocalization. *Surf. Interface Anal.* **2006**, *38*, 1702−1711.

(4) Ho, W. Surface Photochemistry. *Surf. Sci.* **1994**, *299/300*, 996−1007.

(5) Zimmermann, F. M.; Ho, W. Velocity Distributions of Photochemically Desorbed Molecules. *J. Chem. Phys.* **1994**, *100*, 7700−7706.

(6) Olsen, T.; Gavnholt, J.; Schiøtz, J. Hot Electron Mediated Desorption Rates Calculated from Excited State Potential Energy Surfaces. *Phys. Rev. B: Condens. Matter Mater. Phys.* **2009**, *79*, 035403.

(7) Reimer, W.; Fink, Th.; Kuppers, J. Inverse Photoemission Spectroscopy of H, CO and NO Adsorbed at Ni(100) and Ni(111) Surfaces. *Surf. Sci.* **1988**, *193*, 259−270.

(8) Schwarzwald, R.; Mödi, A.; Chuang, T. J. Two Dimensional Imaging of Photodesorbed Species from Surface and the Desorption Dynamic. *Surf. Sci.* **1991**, *242*, 437−443.

(9) Heiz, U.; Xu, J.; Yates, J. T. Electron Stimulated Desorption of NO from Step Sites on Pt(112): The Role of Chemisorption Site Geometry on the Cross Section. *J. Chem. Phys.* **1994**, *100*, 3925−3929.

(10) Prybyla, J. A.; Heinz, T. F.; Misewich, J. A.; Loy, M. M. T.; Glownia, J. H. Desorption Induced by Femtosecond Laser Pulses. *Phys. Rev. Lett.* **1990**, *64*, 1537−1540.

(11) Saalfrank, P.; Boendgen, G.; Finger, K.; Pesce, L. Photodesorption of NO from a Metal Surface: Quantum Dynamical Implications of a Two-Mode Model. *Chem. Phys.* **2000**, *251*, 51−69.

(12) Rosca, V.; Beltramo, G. L.; Koper, M. T. M. Reduction of NO Adlayers on Pt(110) and Pt(111) in Acidic Media: Evidence for Adsorption Site-Specific Reduction. *Langmuir* **2005**, *21*, 1448−1456.

(13) Budde, F.; Hamza, A. V.; Ferm, P. M.; Ertl, G.; Weide, D.; Andresen, P.; Freund, H.-J. Photodesorption of NO from Ni(100)-O. *Phys. Rev. Lett.* **1988**, *60*, 1518−1521.

(14) Casassa, M. P.; Heilweil, E. J.; Stephenson, J. C.; Cavanagh, R. R. Time-Resolved Measurement of OH(v = 1) Vibrational Relaxation on SiO_2 Surfaces; Isotope and Temperature Dependence. *J. Chem. Phys.* **1986**, *84*, 2361−2364.

(15) Alivisatos, A. P.; Waldeck, D. H.; Harris, C. B. Neoclassical Behavior of Energy-Transfer from Molecules to Metal Surfaces: Biacetyl($^3np^*$)/Ag(111). *J. Chem. Phys.* **1985**, *82*, 541−547.

(16) Menzel, D.; Gomer, R. Desorption from Metal Surfaces by Low-Energy Electrons. *J. Chem. Phys.* **1964**, *41*, 3311−3328.

(17) Redhead, P. A. Interaction of Slow Electrons with Chemisorbed Oxygen. *Can. J. Phys.* **1964**, *42*, 886−905.

(18) Antoniewicz, P. R. Model for Electron- and Photon-Stimulated Desorption. *Phys. Rev. B: Condens. Matter Mater. Phys.* **1980**, *21*, 3811−3815.

(19) Buntin, S. A.; Richter, L. J.; Cavanagh, R. R.; King, D. S. Optically Driven Surface Reactions: Evidence for the Role of Hot Electrons. *Phys. Rev. Lett.* **1988**, *61*, 1321−1324.

(20) Buntin, S. A.; Richter, L. J.; King, D. S.; Cavanagh, R. R. State-Resolved Evidence for Hot Carrier Driven Surface Reactions: Laser-Induced Desorption of NO from Pt(111). *J. Chem. Phys.* **1989**, *91*, 6429−6446.

(21) Fukutani, K.; Peremans, A.; Mase, K.; Murata, Y. Photodesorption of NO from Pt(001) at λ=193, 248, and 352 nm. *Phys. Rev. B: Condens. Matter Mater. Phys.* **1993**, *47*, 4007−4010.

(22) Fukutani, K.; Murata, Y.; Schwarzwald, R.; Chuang, T. J. UV-Laser-Induced Desorption of NO from Pt(111). *Surf. Sci.* **1994**, *311*, 247−256.

(23) Richter, L. J.; Buntin, S. A.; King, D. S.; Cavanagh, R. R. State-Resolved Studies of the Laser-Induced Desorption of NO from Si(111) 7 × 7: Low Coverage Results. *J. Chem. Phys.* **1992**, *96*, 2324−2338.

(24) Mulugeta, D.; Watanabe, K.; Menzel, D.; Freund, H.-J. State-Resolved Investigation of the Photodesorption Dynamics of NO from

DOI: 10.1021/acs.jpcc.7b07116
J. Phys. Chem. C 2017, 121, 19922−19929

$(NO)_2$ on Ag Nanoparticles of Various Sizes in Comparison with Ag(111). *J. Chem. Phys.* **2011**, *134*, 164702.
(25) Koehler, S. P. K.; Ji, Y.; Auerbach, D. J.; Wodtke, A. M. Three-Dimensional Velocity Map Imaging of KBr Surface Photochemistry. *Phys. Chem. Chem. Phys.* **2009**, *11*, 7540−7544.
(26) Kershis, M. D.; Wilson, D. P.; White, M. G.; John, J. J.; Nomerotski, A.; Brouard, M.; Lee, J. W. L.; Vallance, C.; Turchetta, R. Exploring Surface Photoreaction Dynamics Using Pixel Imaging Mass Spectrometry (PImMS). *J. Chem. Phys.* **2013**, *139*, 084202.
(27) Hoffman, C. H.; Nesbitt, D. J. Quantum State Resolved 3D Velocity Map Imaging of Surface-Scattered Molecules: Incident Energy Effects in HCl + Self-Assembled Monolayer Collisions. *J. Phys. Chem. C* **2016**, *120*, 16687−16698.
(28) Hadden, D. J.; Messider, T. M.; Leng, J. G.; Greaves, S. J. Note: Velocity Map Imaging the Scattering Plane of Gas Surface Collisions. *Rev. Sci. Instrum.* **2016**, *87*, 106104.
(29) Harding, D. J.; Neugebohren, J.; Hahn, H.; Auerbach, D. J.; Kitsopoulos, T. N.; Wodtke, A. M. Ion and velocity map imaging for surface dynamics and kinetics. *J. Chem. Phys.* **2017**, *147*, 013939.
(30) Abujarada, S.; AlSalem, H.; Chohan, U. K.; Draper, G. L.; Koehler, S. P. K. Photodesorption of NO from Au(100) using 3D Surface-Velocity Map Imaging. *J. Chem. Phys.* **2016**, *145*, 184201.
(31) Reid, M.; Koehler, S. P. K. Validation of Velocity Map Imaging Conditions over Larger Areas. *Rev. Sci. Instrum.* **2013**, *84*, 044101.
(32) Chestakov, D. A.; Wu, S. M.; Wu, G. R.; Parker, D. H.; Eppink, A. T. J. B.; Kitsopoulos, T. N. Slicing Using a Conventional Velocity Map Imaging Setup: O_2, I_2, and I_2^+ Photodissociation. *J. Phys. Chem. A* **2004**, *108*, 8100−8105.
(33) Zacharias, H.; Schmiedl, R.; Welge, K. H. State Selective Step-Wise Photoionization of NO with Mass Spectrometric Ion Detection. *Appl. Phys.* **1980**, *21*, 127−133.
(34) Kohler, S. P. K.; Allan, M.; Kelso, H.; Henderson, D. A.; McKendrick, K. G. The Effects of Surface Temperature on the Gas-Liquid Interfacial Reaction Dynamics of $O(^3P)$+squalane. *J. Chem. Phys.* **2005**, *122*, 024712.
(35) Rahinov, I.; Cooper, R.; Yuan, C.; Yang, X.; Auerbach, D. J.; Wodtke, A. M. Efficient Vibrational and Translational Excitations of a Solid Metal Surface: State-to-State Time-of-Flight Measurements of HCl (v = 2, J = 1) Scattering from Au(111). *J. Chem. Phys.* **2008**, *129*, 214708.
(36) So, S. K.; Franchy, R.; Ho, W. Photodesorption of NO from Ag(111) and Cu(111). *J. Chem. Phys.* **1991**, *95*, 1385−1399.
(37) Sachtler, W. M. H.; Dorgelo, G. J. H.; Holscher, A. A. The Work Function of Gold. *Surf. Sci.* **1966**, *5*, 221−229.
(38) Wang, Y.; Zhang, D.; Liu, C. Theoretical Study of NO Adsorption on Gold Surfaces. *Sci. China: Chem.* **2011**, *54*, 194−199.
(39) Burgess, D. R., Jr.; Cavanagh, R. R.; King, J. D. S. Laser-Induced Desorption: Thermal and Nonthermal Pathways. *J. Chem. Phys.* **1988**, *88*, 6556−6569.
(40) Natzle, W. C.; Padowitz, D.; Sibener, S. J. Ultraviolet Laser Photodesorption of NO from Condensed Films: Translational and Internal Energy Distributions. *J. Chem. Phys.* **1988**, *88*, 7975−7994.
(41) Shaw, J. Nitric Oxide Fundamental. *J. Chem. Phys.* **1956**, *24*, 399−402.
(42) Gillette, R. H.; Eyster, E. H. The Fundamental Rotation-Vibration Band of Nitric Oxide. *Phys. Rev.* **1939**, *56*, 1113−1119.
(43) Herzberg, G. *The Spectra and Structures of Simple Free Radicals: An Introduction to Molecular Spectroscopy*; Dover: New York, 1971.
(44) Prybyla, J. A.; Heinz, T. F.; Misewich, J. A.; Loy, M. M. T. Direct Observation of Rotational Cooling Thermal Desorption: NO/Pd(111). *Surf. Sci.* **1990**, *230*, L173−L179.
(45) Holme, T. A.; Levine, R. D. Computational Studies of Rapid Laser Induced Desorption: a Microscopic Mechanism for Selectivity. *Surf. Sci.* **1989**, *216*, 587−614.
(46) Menges, M.; Baumeister, B.; Al-Shamery, K.; Freund, H.-J.; Fischer, C.; Andresen, P. Two-Dimensional State Resolved Imaging after UV-Laser Induced Desorption: NO/NiO(111). *Surf. Sci.* **1994**, *316*, 103−111.

DOI: 10.1021/acs.jpcc.7b07116
J. Phys. Chem. C 2017, 121, 19922−19929

Appendix E

Paper3

PCCP

PAPER

View Article Online
View Journal

Check for updates

Cite this: DOI: 10.1039/c9cp01963d

Adsorption site, orientation and alignment of NO adsorbed on Au(100) using 3D-velocity map imaging, X-ray photoelectron spectroscopy and density functional theory

Saada Abujarada,[ab] Alex S. Walton,[ab] Andrew G. Thomas,[bc] Urslaan K. Chohan[c] and Sven P. K. Koehler*[d]

Nitric oxide adsorption on a Au(100) single crystal has been investigated to identify the type of adsorption, the adsorption site, and the orientation and alignment of the adsorbed NO relative to the surface. This was done using a combination of 3D-surface velocity map imaging, near-ambient pressure X-ray photoelectron spectroscopy, and density functional theory. NO was observed to be molecularly adsorbed on gold at ~200 K. Very narrow angular distributions and cold rotational distributions of photodesorbed NO indicate that NO adsorbs on high-symmetry sites on the Au crystal, with the N–O bond axis close to the surface normal. Our density functional theory calculations show that NO preferentially adsorbs on the symmetric bridge (2f) site, which ensures efficient overlap of the NO π* orbital with the orbitals on the two neighbouring Au atoms, and with the N–O bond axis aligned along the surface normal, in agreement with our conclusions from the rotational state distributions. The combination of XPS, which reveals the orientation of NO on gold, with 3D-surface velocity map imaging and density functional theory thus allowed us to determine the adsorption site, orientation and alignment of nitric oxide adsorbed on Au(100).

Received 8th April 2019,
Accepted 6th May 2019

DOI: 10.1039/c9cp01963d

rsc.li/pccp

Open Access Article. Published on 07 May 2019. Downloaded on 5/20/2019 12:12:00 PM.
This article is licensed under a Creative Commons Attribution-NonCommercial 3.0 Unported Licence.

Introduction

Nitric oxide (NO) is a diatomic radical with one unpaired electron, which causes its notable reactivity.[1] It is known for its toxicity, has diverse physiological functions,[2] serves as a signalling molecule (neurotransmitter) in the nervous system,[3] and is also one of the gases contributing to acid rain. NO is a molecule of industrial importance, *e.g.* in the liquid-phase catalytic hydrogenation of nitric oxide or nitrate to hydroxylamine.[4,5] It is a key intermediate in many industrial processes, including the reduction of some nitrogen compounds such as nitrates and nitrites to ammonia or N_2O, and in the oxidation of ammonia.[6–8] The exact pathway for ammonia oxidation on metal surfaces is still under investigation, not only with regards to the intermediates formed but also the mechanism, with both Langmuir–Hinshelwood and Eley–Rideal mechanisms being suggested.[6,9,10]

NO_x is produced in fuel combustion engines, and its reduction to nitrogen by three-way-catalysts is crucial in reducing air pollution.[11] Catalytic convertors based on platinum group metals (PGMs) including platinum, rhodium and palladium play a crucial role in the clean-up of car emissions. Dispersed gold as nano-sized particles on transition metal oxides has demonstrated significant catalytic activity in the conversion of toxic car emissions including carbon monoxide, incompletely burnt hydrocarbons and nitrogen oxides.[12] The potential of using gold as a substitute of PGMs for car emission control is justified by its low-temperature activity and its thermal stability. Hence the interaction of NO_x with gold metal surfaces is of considerable importance. The complexity of the adsorption behaviour of NO on metal surfaces – due to the unpaired electron in the antibonding 2π* orbital – leads to various adsorbate species potentially being formed including NO itself, N, O, $(NO)_2$, N_2O, and NO_2. The coexistence of these species on some metal surfaces complicates the experimental characterisation and identification of individual chemical species.

Ueda and Haruta investigated the catalytic reduction of NO on a supported gold catalyst and concluded that N_2 and N_2O were the only products.[13] Thermal desorption spectroscopy (TDS) provided an estimate of the NO chemisorption strength on Au(100) of 57 ± 4 kJ mol^{-1}. Bukhtiyarov *et al.* investigated the adsorption of NO on gold particles deposited on an alumina film in the temperature range 300–500 K using *in situ* X-ray

[a] School of Chemistry, The University of Manchester, Oxford Road, Manchester, M13 9PL, UK
[b] Photon Science Institute, The University of Manchester, Oxford Road, Manchester, M13 9PL, UK
[c] School of Materials, The University of Manchester, Oxford Road, Manchester, M13 9PL, UK
[d] School of Science and the Environment, Manchester Metropolitan University, Chester Street, Manchester, M1 5GD, UK. E-mail: s.koehler@mmu.ac.uk

Open Access Article. Published on 07 May 2019. Downloaded on 5/20/2019 12:12:00 PM.
This article is licensed under a Creative Commons Attribution-NonCommercial 3.0 Unported Licence.

photoelectron spectroscopy (XPS).[14] Two nitrogen-containing adsorbed species were found to exist on the surface of gold particles. The first was identified as adsorbed nitrogen atoms characterised by a N 1s binding energy (BE) of 399.4 eV. The second species was identified as a surface complex with N_2O stoichiometry characterised by a BE of 402.7 eV and found to be thermally stable only in a narrow temperature range of 325–425 K. Identification of these species was aided by a separate experiment in which NO was adsorbed onto a stepped Au(533) crystal. The assignments of the recorded BEs seems to be in agreement with Vinod *et al.* who investigated the adsorption of NO on the (310) face of a gold single crystal in the temperature range of 80–220 K.[15]

Bukhtiyarov *et al.* employed XPS to investigate the decomposition of NO on flat Au(111) and stepped Au(310) and (533) surfaces at elevated NO pressures up to 7 Pa and temperature range between 300 and 500 K.[16] NO was found not to chemisorb on Au(111), however, dissociation of NO was observed on both Au(310) and (533) surfaces. The authors concluded that Au step-sites are responsible for adsorption and dissociation of NO. The study revealed that while NO dissociation on Au(310) exclusively forms N_{ads} on the surface whose coverage decreases with increasing surface temperature, NO dissociation on Au(533) initially forms N_2O_{ads} on the surface that is replaced by more stable N_{ads} at increasing NO exposure and/or surface temperature. Fajin *et al.* used density functional theory (DFT) to show that the presence of hydrogen was necessary for the dissociation of NO on the stepped Au(321) surface.[17] Employing XPS and TDS experiments, Vinod *et al.* observed the formation of N_2O and O_{ads} following adsorption of NO on a stepped Au(310) surface even at temperatures as low as 80 K.[15] A common theme amongst many of these studies is the importance of low coordinated Au atoms acting as active sites for adsorption.[18–22] Hussain *et al.* employed DFT to study NO adsorption on Au(111), (100), (110) and (310) surfaces, as well as on adatoms on Au(100).[23] The adsorption energy of the gaseous molecules was found to increase considerably with increasing coordinative unsaturation of the gold atoms. These results are consistent with the view that defects, steps and kinks on the surface determine the activity of gold catalysts. For low index surfaces, the bridge site is favoured, however top coordination is preferred at the stepped (310) surface. In all adsorption configurations, the N–O molecular axis is perpendicular to the surfaces except for Au(310).

Wu *et al.* investigated the low-temperature adsorption and decomposition of NO on low-coordinated Au(997) and Au(110)-1 × 2 surfaces employing TDS and XPS measurements as well as DFT calculations.[24] Although the lowest coordinated Au atoms on both surfaces are 7-coordinated, their surface chemistry towards NO adsorption and decomposition was found to be different. On both surfaces, $(NO)_2$ dimer species and not NO_{ads} were found to be the active surface species for the NO decomposition into O adatoms and N_2O. However, different types of $(NO)_2$ dimers were found to form depending on the Au surface structure. $(NO)_2$ dimer species adsorbed on the 7-coordinated ridge Au atoms on both surfaces decompose into O adatom and N_2O upon heating. This type of dimer dominates on Au(997). On the Au(110)-1 × 2 surface, another more abundant and less stable $(NO)_2$ dimer was found to easily decompose into O adatoms and N_2O during NO exposure at 105 K.

We have previously studied the dynamics of the laser-induced desorption of adsorbed NO from Au(100) surfaces using 3D-surface velocity map imaging (3D-surface VMI) which allowed us to capture all desorbed NO molecules from the gold surface within a sold angle of 5.6 sr. While this previous work focussed on the differentiation of two different desorption mechanisms, a direct and a thermal one depending on desorption wavelength, we here report on the use of 3D-surface VMI in combination with near-ambient pressure-XPS (NAP-XPS) and condensed-phase DFT simulations to ascertain the adsorption site, orientation and alignment of the adsorbed nitric oxide. 3D-VMI in particular delivers crucial information about the adsorption site of NO (through the narrow angular distribution of the desorbed NO) and the alignment of the N–O (through rotational state distributions), supported by the NAP-XPS and DFT results.

Methods

3D-surface velocity map imaging

The 3D-VMI apparatus has been described elsewhere;[25] here only brief description will be given. The spectrometer consists of two chambers, a molecular beam chamber and a UHV chamber that contains the Au(100) single crystal and the twelve plates VMI optics. A base pressure of 5×10^{-10} Torr is achieved using a 1000 L s^{-1} turbomolecular pump backed by a mechanical pump. A K-type thermocouple attached to the Au(100) crystal measures its temperature. The crystal is mounted on a 3-axes/rotational manipulator which allows for heating and liquid nitrogen cooling. Pure NO gas is introduced into the chamber for adsorption on the Au(100) crystal through a molecular beam valve at a background pressure of $\sim 5 \times 10^{-6}$ Torr. Desorption of NO from the Au(100) crystal is initiated by a frequency-tripled Nd:YAG laser (Quanta Ray DCR-11) with a pulse duration of 7 ns and a pulse energy of ~1.2 mJ. The beam was directed at the crystal surface at an angle of 45°. The desorbed NO molecules may fly in all directions within a hemisphere above the surface. The desorbed NO molecules are detected state selectively in a 1 + 1 resonance-enhanced multi-photon ionisation (REMPI) scheme *via* the A ← X (0,0) transition by employing a frequency-doubled Radiant Dyes NarrowScan laser, operating on Coumarin 460, pumped by a Continuum Powerlite 8020 Nd:YAG laser. NO^+ ions are accelerated down the time-of-flight tube (for mass separation) onto the position-sensitive multichannel plate (MCP) detector. The ions' arrival positions are imaged onto a phosphor screen and captured by a synchronized CCD camera (FO124TB). Time-of-flight spectra were recorded by varying the time delay between the desorption and the probe laser in discrete steps, and were converted into velocity distributions that provide the velocity component along the surface normal (v_z) only. For each time delay (and hence v_z), we recorded VM images which correspond to

Open Access Article. Published on 07 May 2019. Downloaded on 5/20/2019 12:12:00 PM.
This article is licensed under a Creative Commons Attribution-NonCommercial 3.0 Unported Licence.

the remaining two velocity components v_x and v_y parallel to the gold surface.

Near-ambient pressure X-ray photoelectron spectroscopy

The near-ambient pressure X-ray photoelectron spectroscopy (NAP-XPS) system employed in this work is equipped with a SPECS Focus 500 monochromatic Al Kα source (photon energy 1486.6 eV), which can be focused to a spot size of 300 μm. The analyser is a SPECS 150 mm Phoibos 150 NAP, fitted with a three-stage, differentially pumped electrostatic lens that allows working pressures up to 25 mbar. NAP-XPS measurements are performed in a specially designed cell which couples to the entrance cone of the analyser lens system. The Au(100) crystal surface was cleaned by Ar^+ ion sputtering cycles. The UHV chamber was left to pump down to a base pressure better than 10^{-9} Torr, after which the crystal was moved to the NAP-cell and the gate between the cell section and the UHV chamber was closed. XP spectra were recorded with NO flowing into the cell at 0.75 Torr and varying substrate temperatures. However, we failed to detect any NO adsorbed on Au(100) even at a base temperature of 220 K after the substrate had been prepared by sputtering and annealing, hence our XP spectra at 220 K and 266 K are all recorded on a sputtered-only gold substrate.

The binding energies of the photoelectron spectra were calibrated to the bulk Au $4f_{7/2}$ peak at 84 eV. All spectra were normalised using the baseline intensity and background subtraction and fitted with an appropriate number of Gaussian functions using CasaXPS.[26]

Condensed-phase density functional theory

We performed first principles quantum chemical calculations based on density-functional theory. We employed the Cambridge Serial Total Energy Package (CASTEP) which solves the Kohn–Sham equations with a plane wave basis set employing three-dimensional periodic boundary conditions.[27,28] The Perdew–Burke–Ernzerhof (PBE) version of the generalized gradient approximation (GGA) was used to represent the exchange and correlations, and on-the-fly ultrasoft pseudopotentials for Au, N and O. The Monkhorst–Pack (MP) algorithm was selected for k point sampling, and a cut-off energy of 750 eV was employed.

An eight-layer slab was employed to describe the (100) surface of a fcc gold single crystal. We used the BFGS algorithm to relax the positions of the Fe atoms in the top four layers, whilst the bottom four layers were constrained in position.

Adsorption energies were calculated *via* the relation

$$E_{ads} = E_{slab+NO} - (E_{slab} + E_{NO}) \quad (1)$$

where $E_{slab+NO}$ is the energy of the slab with NO adsorbed, E_{slab} is the energy of the NO-free slab, and E_{NO} is the ground state energy of a single NO molecule in a $10 \times 10 \times 10$ Å^3 box.

Most importantly for this work, core level shifts were calculated using the Slater–Janak transition state approximation,[29] which then allows convenient comparison with the NAP-XPS data.

Results and discussion

3D-VM images

Fig. 1 shows a raw velocity map image recorded for NO molecules which were photodesorbed from the surface with a speed along the surface normal (v_z) of 420 m s^{-1}. This and similar images were converted to velocity space and then deliver the velocity distribution in the two dimensions, v_x and v_y, which are parallel to the Au(100) surface. The raw image is composed of single images from 20 000 laser shots.

Recording similar images for a range of velocities along the surface normal (v_z) allows us to extract a complete velocity distribution with the velocity components in all three dimensions in space obtained independently. This can then be converted to an angularly-resolved speed distribution of NO after 355 nm photodesorption from Au(100), see Fig. 2. It can be clearly seen that the angular distribution is (1) along the surface normal, and (2) extremely narrow, with all NO molecules desorbing off the surface within a very narrow angular distribution with a polar angle relative to the surface normal of $<20^\circ$, and much narrower for most molecules. The results from these VMI experiments indicate that NO is either adsorbed on-top of a gold atom, or at another high symmetry site such as a 2f or 4f site; this is because repulsive forces between gold and the NO molecule during the desorption process from these high-symmetry sites are along the surface normal; for example, the repulsive forces parallel to the surface from the four Au atoms in case of adsorption on the 4f site cancel each other out, while forces along the surface normal are accumulative; equally, in case of on-top adsorption, the NO molecules fly along the Au–N bond and hence along the surface normal, yielding a narrow angular distributions;[30] adsorption at a non-symmetry site would on the other hand result in the angular distribution being tilted away from the surface normal due to non-cancelling

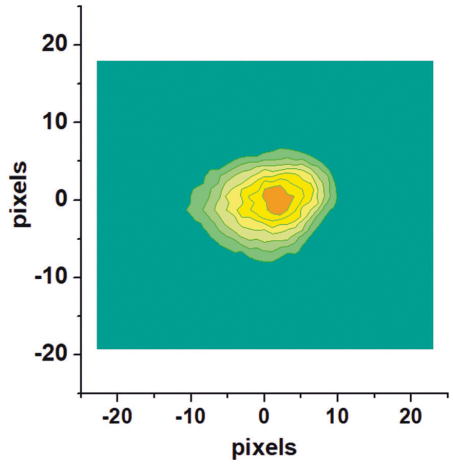

Fig. 1 Raw velocity map image for NO molecules photodesorbed from the Au(100) surface with a velocity along the surface normal, v_z, of 420 m s^{-1}.

Open Access Article. Published on 07 May 2019. Downloaded on 5/20/2019 12:12:00 PM.
This article is licensed under a Creative Commons Attribution-NonCommercial 3.0 Unported Licence.

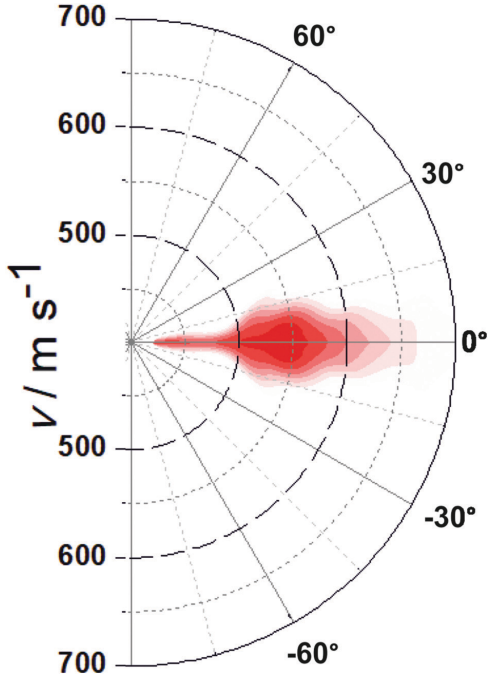

Fig. 2 Plot of the NO flux as a function of overall speed and angle after 355 nm photodesorption. Colour coding from dark red (most intense) to white (zero intensity).

lateral forces. This example shows the potential of 3D-VMI to learn about adsorption sites and surface structure through the measurement of angular distributions in laser desorption experiments.

Rotational state distributions

In order to record rotational state distributions, we fixed the delay time between the pump and the probe laser to correspond to the specific velocity of the v_z distribution of 560 m s^{-1}, which is the maximum in the velocity distribution. The probe laser was scanned over an appropriate wavelength range in steps of 0.005 nm to obtain REMPI spectra for NO. A rotationally resolved (1 + 1) REMPI spectrum of 355 nm photodesorbed NO recorded on the $A^2\Sigma_{1/2} \leftarrow X^2\Pi_{3/2}$ (0,0) transition is shown in Fig. 3. Rotational state distributions were extracted by comparison with thermal nitric oxide REMPI spectra, and rotational temperatures were fitted using Boltzmann plots. We want to stress that rotational distributions of laser-desorbed nitric oxide are not necessarily thermal ensembles, and rotational temperatures were merely fitted to obtain a single value for ease of interpretation. The rotational temperature based on analysis of a few isolated rotational lines of the O_{12} branch was found to be (206 ± 5) K. While slighter hotter than the surface temperature, this is surprisingly low considering the excess energy from the laser photon. We interpret this cold rotational temperature

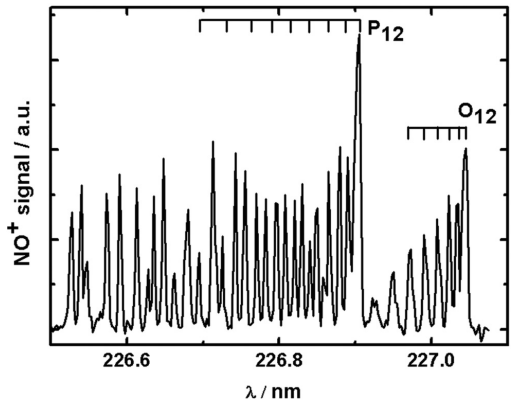

Fig. 3 Typical (1 + 1) REMPI spectrum of NO desorbed from gold using 355 nm photons at a time delay corresponding to NO molecules with v_z = 560 m s^{-1}.

to mean that the N–O bond is aligned along the surface normal. We concluded in the previous section that the repulsive forces between the gold surface and the N atom are along the surface normal. If the N–O bond was not along the surface normal (*i.e.* the angle between Au_{AS}–N–O, where Au_{AS} is the surface adsorption site, would deviate significantly from 180°), but the N would be repelled away from the surface along the normal, then this would impart a significant torque onto the NO molecule, causing it to tumble and rotate, which would lead to a much higher rotational temperature. A laser-desorbed N–O molecule which adsorbs with its molecular axis along the surface normal would on the other hand be rotationally cold, as in our case here.[31]

NAP-XPS results

XPS is considered by many as the standard for the identification of surface species, and one of the goals in this study was to support our conclusions from the 3D-VMI experiments using more established surface analysis techniques such as XPS. In particular, XPS would be able to reveal whether NO adsorbs molecularly or atomically on Au(100) under our conditions (backing-up the conclusions above from the detection of intact nitric oxide in the gas-phase), to reveal the alignment of NO (N–O parallel to the surface would shift the XPS peaks for N and O roughly equally, whereas N–O normal to the surface would shift the XPS peak of the atom closer to the surface more than the respective other atom, supporting our conclusions from the rotational distributions), and possibly to reveal the adsorption site.

Exposure of Au(100) to NO at 298 K

Fig. 4 shows XPS spectra recorded during 1 mbar NO exposure of the surface at room temperature. The N 1s spectrum (Fig. 4a) shows two peaks at binding energies of 406.1 eV and 407.5 eV, with the former being more intense. In accordance with the results obtained by Shimada *et al.* and Yu *et al.*, these peaks are attributed to gas-phase NO molecules.[32,33]

Open Access Article. Published on 07 May 2019. Downloaded on 5/20/2019 12:12:00 PM.
This article is licensed under a Creative Commons Attribution-NonCommercial 3.0 Unported Licence.

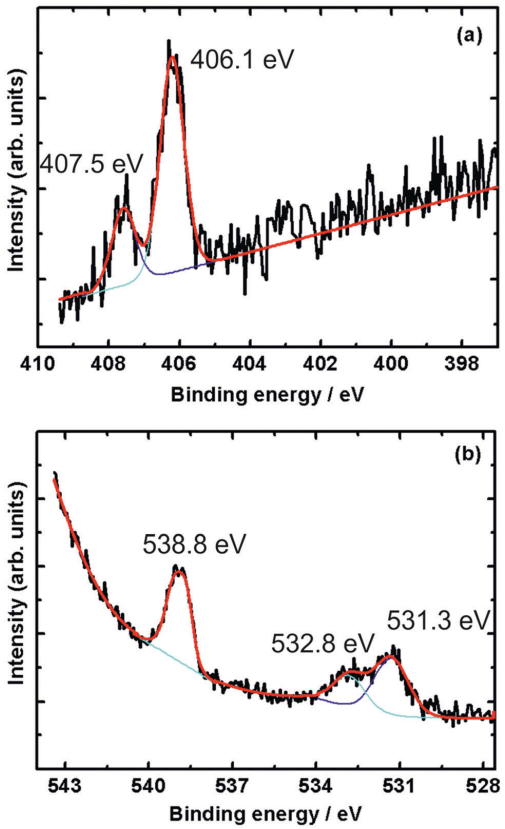

Fig. 4 (a) N 1s and (b) O 1s X-ray photoelectron spectra during exposure of Au(100) to NO at 1 mbar pressure and 298 K. The black line is the recorded XP spectrum, while the red line is a fit, deconvoluted into the purple and turquoise contributions.

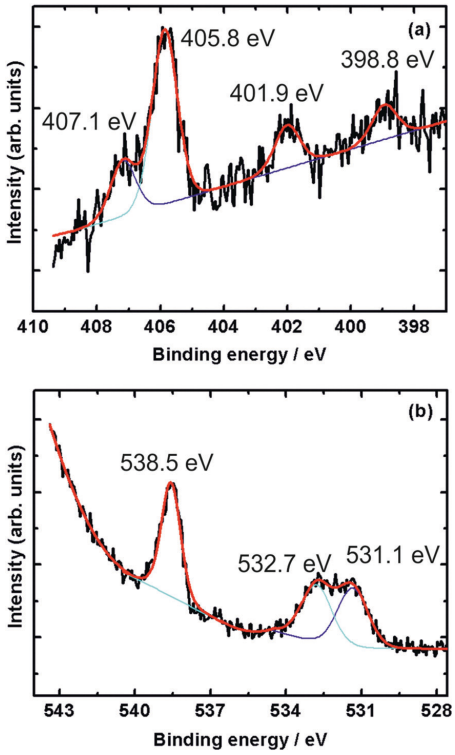

Fig. 5 (a) N 1s and (b) O 1s XPS core-level spectra of NO adsorbed on sputtered gold surface taken at 220 K and 1 mbar NO pressure. The black line is the recorded XP spectrum, while the red line is a fit, deconvoluted into the purple and turquoise contributions.

The O 1s spectrum shows three peaks at 531.3, 532.8 and 538.8 eV. While the peak at 538.8 eV is due to the oxygen atom in gas-phase NO, the twin peaks appearing at 531.3 and 532.8 eV can be attributed to residual CO adsorbed on the surface. The twin O 1s peaks appearing in this energy region were also reported in CO adsorption on Pt(111).[34,35] The above results show that NO does not adsorb on Au(100) under these conditions of temperature and pressure.

Adsorption at 220 K

As mentioned previously, XPS spectra recorded at 220 K for the ordered sputtered and annealed Au(100) surface show no adsorption of NO (data not shown, but spectra qualitatively similar to Fig. 4) as indicated by the absence of N 1s and O 1s peaks at ~400 eV and ~531 eV, respectively.[16] As in the case of room temperature measurements, only gas-phase NO peaks were observed.

We hence studied NO adsorption on a sputtered (but not annealed) gold surface. The surface was sputtered for 30 min followed by exposure to NO.

Fig. 5 shows the N 1s and O 1s XPS core level spectra of nitric oxide adsorbed on gold at 1 mbar NO pressure and 220 K, the lowest temperature reached in our NAP-spectrometer, but ~40 K higher than the base temperature in our 3D-VMI spectrometer (178 K).

The N 1s spectrum (Fig. 5a) shows three distinct peaks at 398.8, 401.9 and 405.8 eV, and another peak at 407.1 eV appearing as a shoulder of the 405.8 eV peak. The two peaks at 405.8 eV and 407.1 eV are due to gaseous NO, as shown in Fig. 4. The other two peaks at 398.8 eV and 401.9 eV point to the presence of adsorbed nitrogen species on the sputtered gold surface.

Rienks *et al.* reported three main peaks at 394.7, 398.1 and 401.3 eV in the N 1s region recorded during the exposure of Pt(100) to NO at 200 K.[36] The peak at 394.7 eV – not observed in the current study – was attributed to atomic nitrogen due to dissociation of adsorbed NO. The peaks at 398.1 eV and 401.3 eV, and hence close to those observed in the current study, were

Open Access Article. Published on 07 May 2019. Downloaded on 5/20/2019 12:12:00 PM.
This article is licensed under a Creative Commons Attribution-NonCommercial 3.0 Unported Licence.

attributed to two different molecularly adsorbed NO species on the surface. Further support of molecularly adsorbed NO comes from a study by Sugai *et al.* who observed a peak at 401.5 eV due to molecularly adsorbed NO on Pt(100) and (310),[37] and a study by Kiskinova *et al.* who observed a N 1s peak at 400.7 eV due to molecularly adsorbed NO on Pt(111).[38]

In case of dissociative adsorption, one might also expect a feature in the O 1s region just below 530 eV characteristic of atomic oxygen,[39,40] but this was not observed on our sputtered gold surface.

Instead, a peak at 538.5 eV and two partially overlapping peaks at 531.1 and 532.7 eV appear in the O 1s region of the spectrum, see Fig. 5b. All three peaks also appear in the room temperature spectra shown in Fig. 4, but in particular the latter two are now more intense. The higher binding energy peak is due to gas-phase NO, while the two peaks around 532 eV are likely due to molecularly adsorbed NO, possibly with some contribution from adsorbed residual CO. Kiskinova *et al.* assigned these two peaks in the case of NO adsorption on Pt(111) to bridge-bonded (lower BE, 530.6 eV) and on-top (higher BE, 532.5 eV) NO.[38] While we are working with a sputtered gold surface, we nonetheless conclude that we observe NO on adsorption sites that resemble bridge sites (398.1 eV in the N 1s spectrum and 531.1 eV in the O 1s spectrum) and on-top sites (401.3 eV in the N 1s spectrum and 532.7 eV in the O 1s spectrum). The fact that the difference in binding energy between the bridge and on-top site is greater in the N 1s region than it is for the oxygen indicates that N is facing the surface, in agreement with previous work for NO on Pt(100) and Pt(111).[36,38]

Adsorption at 266 K

After adsorption at 220 K and recording of the XPS spectra, the temperature of the surface was gradually raised to 266 K while keeping the NO flowing into the cell, and the spectra were recorded again, shown in Fig. 6. Once again only peaks related to gaseous NO are observed. The two peaks associated with the N surface species have disappeared. This shows that NO has desorbed from the surface at this temperature in agreement with our previous 3D-VMI results.[31]

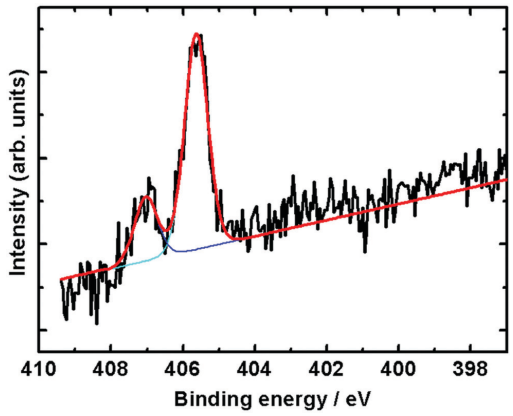

Fig. 6 N 1s XPS core-level spectra during exposure of NO at 266 K and 1 mbar pressure.

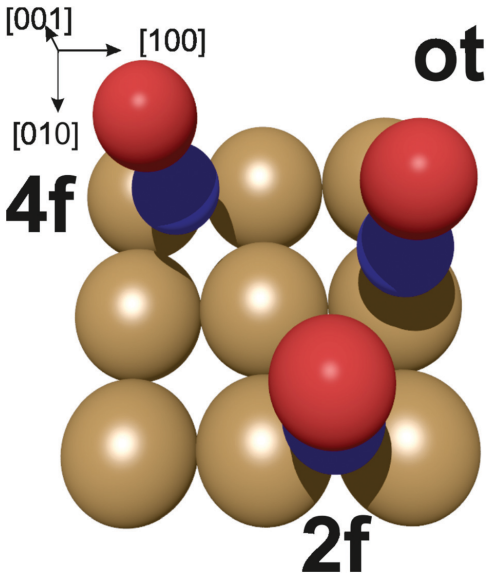

Fig. 7 Potential adsorption sites for NO on the Au(100) surface. ot = on-top, 2f = bridge site, 4f = hollow site. Oxygen in red, nitrogen in blue.

DFT results

Adsorption energies. We have studied three different adsorption sites on the ordered Au(100) surface, as indicated in Fig. 7, at NO coverages of 25%, 50%, and 100% with the aim of determining the most energetically favourable adsorption site and orientation of adsorbed NO. The results indicate that NO preferentially adsorbs on the bridge (2f) site, with an Au–N distance of 2.14 Å (such that the N atom is 1.43 Å above the surface), and a N–O distance of 1.18 Å. Adsorption energies vary between 0.65 eV and 0.8 eV depending on the coverage, and are roughly in agreement with those obtained by Olvera-Neria *et al.* (0.53 eV) for NO on a single gold atom,[41] and by Niemantsverdriet and co-workers (0.57 eV) for adsorption on the bridge site.[23] They are also in agreement with the adsorption energy obtained from TDS experiments (0.57 eV) by Rienks *et al.*[42] For the next-favourable on-top (ot) site, we calculated an adsorption energy of 0.26 eV, which is in agreement with that calculated by Liu and co-workers (0.26 eV) for a 25% NO coverage on Au(100).[43]

In the energetically more favourable 2f site, the single electron in the two NO π^* orbitals (belonging to the nitrogen atom) can efficiently overlap with the orbitals on two neighbouring Au atoms at the surface between which the NO is located, resulting in the N–O bond being aligned along the surface normal. In contrast, our calculations yield a small tilt angle of 0.2° of the N–O bond axis with respect to the surface normal in the case of the energetically slightly less-favourable

Open Access Article. Published on 07 May 2019. Downloaded on 5/20/2019 12:12:00 PM.
This article is licensed under a Creative Commons Attribution-NonCommercial 3.0 Unported Licence.

on-top adsorption. This is due to the overlap of the π^* orbital with the orbitals on a single Au atom. This tilting geometry of NO adsorbed on Au(111) was also calculated by Zhang *et al.*[44] In agreement with our 3D-surface VMI results, the cold rotational state distribution is due to the majority of the NO being aligned along the normal of the surface, with the slightly tilted NO at the on-top side not noticeably contributing to the low rotational excitation.

Core level shift calculations. We discuss the core level shift (CLS) results for the N 1s states of NO adsorption only on the bridge (2f) and on-top site, as the bridge site is the energetically more favourable adsorption site based on our DFT calculations, while the on-top site is the other suggested site in the literature, and close in terms of adsorption energy. We calculated a larger CL shift for the bridge site than the on-top site; these shifts are $\sim$1.5 eV and $\sim$0.9 eV of the N 1s peak towards lower binding energies for bridge and on-top sites, respectively. While the measured shifts are significantly larger ($\sim$4 to 6 eV), the greater CLS calculated for the 2f position compared to the on-top site agrees with our assignment in Fig. 5, *i.e.* a lower binding energy for the bridge site. The lack of quantitative agreement is most likely due to the difficulty of properly describing our system using density functional theory.[45]

Conclusions

In this paper, we have presented the results of NO adsorption on a Au(100) single crystal surface using 3D-VMI, NAP-XPS and condensed-phase DFT calculations. The combined results of those three different techniques point to a molecular adsorption of NO on the Au(100) surface at low temperatures. The VMI and DFT results show that NO adsorbs onto the gold surface from its N end with the O atom pointing away from the surface. The novelty of this work is that it demonstrates the capability of the 3D-VMI technique not only in elucidating the photodesorption dynamics of pre-adsorbed molecules on metal substrates, but also in revealing the adsorption site, orientation and alignment of adsorbates in a fashion not too dissimilar to early electron-stimulated desorption ion angular distribution studies (ESDIAD) by Madey, Yates, and co-workers.[46,47]

Conflicts of interest

There are no conflicts to declare.

Acknowledgements

S. A. is grateful to the Libyan government for funding. We also thank Rosemary Jones and Khadisha Zahrab for help in the interpretation of the photoelectron spectra.

Notes and references

1 G. Czapski, J. Holcman and B. H. J. Bielski, *J. Am. Chem. Soc.*, 1994, **116**, 11465–11469.
2 I. M. Goldstein, P. Ostwald and S. Roth, *Vision Res.*, 1996, **36**, 2979–2994.
3 J. V. Esplugues, *Br. J. Pharmacol.*, 2002, **135**, 1079–1095.
4 J. Ritz, H. Fuchs and H. G. Perryman, *Hydroxylamine. In Ulmann's Encyclopedia of Industrial Chemistry*, Wiley, Chichester, 6th edn, 2000.
5 C. G. M. van de Moesdijk, *The catalytic reduction of nitrate and nitric oxide to hydroxylamine: kinetics and mechanism*, PhD thesis, Eindhoven University of Technology, 1979.
6 S. Horold, K.-D. Vorlop, T. Tacke and M. Sell, *Catal. Today*, 1993, **17**, 21–30.
7 V. Rosca, G. L. Beltramo and M. T. M. Koper, *Langmuir*, 2005, **21**, 1448–1456.
8 N. I. ll'chenko and G. I. Golodets, *J. Catal.*, 1975, **39**, 57–72.
9 A. Cuesta and M. Escudero, *Phys. Chem. Chem. Phys.*, 2008, **10**, 3628–3634.
10 A. Clayborne, H.-J. Chun, R. B. Rankin and J. Greeley, *Angew. Chem., Int. Ed.*, 2015, **54**, 8255–8258.
11 B. E. Nieuwenhuys, *Adv. Catal.*, 1999, **44**, 259.
12 Y. Zhang, R. W. Cattrall, I. D. Mckelvie and S. D. Kolev, *Gold Bull.*, 2011, **44**, 145.
13 A. Ueda and M. Haruta, *Gold Bull.*, 1991, **32**, 3–11.
14 A. V. Bukhtiyarov, A. V. Nartova and R. I. Kvon, *Kinet. Catal.*, 2011, **52**, 756–760.
15 C. P. Vinod, J. W. H. Niemantsverdriet and B. E. Nieuwenhuys, *Appl. Catal., A*, 2005, **291**, 93–97.
16 A. V. Bukhtiyarov, R. I. Kvon, A. V. Nartova, I. P. Prosvirin and V. I. Bukhtiyarov, *Surf. Sci.*, 2012, **606**, 559–563.
17 J. L. C. Fajín, M. Natália, D. S. Cordeiro and J. R. B. Gomes, *J. Phys. Chem. C*, 2009, **113**, 8864–8877.
18 R. Zanella, S. Giorgio, C. H. Shin, C. R. Henry and C. Louis, *J. Catal.*, 2004, **222**, 357–367.
19 C. Lemire, R. Meyer, S. Shaikhutdinov and H.-J. Freund, *Surf. Sci.*, 2004, **552**, 27–34.
20 X. Deng, B. K. Min, A. Guloy and C. M. Friend, *J. Am. Chem. Soc.*, 2005, **127**, 9267–9270.
21 T. V. W. Janssens, A. Carlsson, A. Puig-Molina and B. S. Clausen, *J. Catal.*, 2006, **240**, 108–133.
22 T. V. W. Janssens, B. S. Clausena, B. Hvolbækb, H. Falsigc, C. H. Christensen, T. Bligaard and J. K. Nørskovb, *Top. Catal.*, 2007, **44**, 15–26.
23 A. Hussain, D. Curulla Ferré, J. Gracia, B. E. Nieuwenhuys and J. W. Niemantsverdriet, *Surf. Sci.*, 2009, **603**, 2734–2741.
24 Z. Wu, L. Xu, W. Zhang, Y. Mac, Q. Yuan, Y. Jin, J. Yang and W. Huang, *J. Catal.*, 2013, **304**, 112–122.
25 M. Reid and S. P. K. Koehler, *Rev. Sci. Instrum.*, 2013, **84**, 044101.
26 N. Fairley, *CasaXPS Manual 2.3.15 Introduction to XPS and AES*, Casa Software, 2009.
27 S. J. Clark, I. Matthew, D. Segall, C. J. Pickard, P. J. Hasnip, M. I. J. Probert, K. Refson and M. C. Payne, *Z. Kristallogr. – Cryst. Mater.*, 2005, **220**, 567–570.
28 U. K. Chohan, E. Jimenez-Melero and S. P. K. Koehler, *Appl. Surf. Sci.*, 2016, **387**, 385–392.
29 J. F. Janak, *Phys. Rev. B: Condens. Matter Mater. Phys.*, 1978, **18**, 7165.

Open Access Article. Published on 07 May 2019. Downloaded on 5/20/2019 12:12:00 PM.
This article is licensed under a Creative Commons Attribution-NonCommercial 3.0 Unported Licence.

30 S. Abujarada, H. AlSalem, U. K. Chohan, G. L. Draper and S. P. K. Koehler, *J. Chem. Phys.*, 2016, **145**, 184201.
31 S. Abujarada, C. Flathmann and S. P. K. Koehler, *J. Phys. Chem. C*, 2017, **121**, 19922–19929.
32 T. Shimada, B. S. Mun, I. F. Nakai, A. Banno, H. Abe, Y. Iwasawa, T. Ohta and H. Kondoh, *J. Phys. Chem. C*, 2010, **114**, 17030–17035.
33 S.-W. Yu, W. C. Stolte, R. Guillemin, G. Öhrwall, I. C. Tran, M. N. Piancastelli, R. Feng and D. W. Lindle, *J. Phys. B: At., Mol. Opt. Phys.*, 2004, **37**, 3583–3592.
34 P. N. Norton, J. W. Goodale and E. B. Selkirk, *Surf. Sci.*, 1979, **83**, 18.
35 M. Kiskinova, G. Pirug and H. P. Bonzel, *Surf. Sci.*, 1983, **133**, 321–343.
36 E. D. L. Rienks, J. W. Bakker, A. Baraldi, S. A. C. Carabineiro, S. Lizzit, C. J. Weststrate and B. E. Nieuwenhuys, *Surf. Sci.*, 2002, **516**, 109–117.
37 S. Sugai, K. Takeuchi, T. Ban, H. Miki, K. Kawasaki and T. Kioka, *Surf. Sci.*, 1993, **282**, 67–75.
38 M. Kiskinova, G. Pirug and H. P. Bonzel, *Surf. Sci.*, 1984, **136**, 285–295.
39 M. V. Ganduglia-Pirovano, M. Scheffler, A. Baraldi, S. Lizzit, G. Comelli, G. Paolucci and R. Rosei, *Phys. Rev. B: Condens. Matter Mater. Phys.*, 2001, **63**, 205415.
40 J. F. Zhu, M. Kinne, T. Fuhrmann, R. Denecke and H. P. Steinruck, *Surf. Sci.*, 2003, **529**, 384–396.
41 O. Olvera-Neria, V. Bertin and E. Poulain, *Int. J. Quantum Chem.*, 2011, **111**, 2054.
42 E. D. L. Rienks, G. P. van Berkel, J. W. Bakker and B. E. Nieuwenhuys, *Surf. Sci.*, 2004, **571**, 187–193.
43 Y. Wang, D. Zhang and C. Liu, *Sci. China: Chem.*, 2011, **54**, 194.
44 W. Zhang, Z. Li, Y. Luo and J. Yang, *J. Chem. Phys.*, 2008, **129**, 134708.
45 Z.-H. Zeng, J. L. F. Da Silva, H.-Q. Deng and W.-X. Li, *Phys. Rev. B: Condens. Matter Mater. Phys.*, 2009, **79**, 205413.
46 T. E. Madey and J. T. Yates Jr., *Surf. Sci.*, 1975, **49**, 465–496.
47 T. E. Madey and J. T. Yates Jr., *Surf. Sci.*, 1977, **63**, 203–231.

Bibliography

[1] S. Ceyer and A. G. Somorjai. Surface scattering. *J. Annu. Rev. Phys. Chem*, 28(1):477–499, 1977.

[2] P. H. Kobrin, G. A. Schick, J. P Baxter, and N. Winograd. Detector for measuring energy-and angle-resolved neutral-particle (EARN) distributions for material desorbed from bombarded surfaces. *J. Rev. Sci. Instr*, 57(7):1354–1362, 1986.

[3] SW. Rosencrance, DE. Riederer, R. Chatterjee, C. He, N. Winograd, and Z. Postawa. Quantitative determination of desorption time delays for ion bombarded {100} alkali halide single crystals. *Nucl. Instr. Meth. Phys. Res. B: Beam Interactions with Materials and Atoms*, 101(1-2):137–141, 1995.

[4] J. J Czyzewski, T. E Madey, and J. T. Yates Jr. Angular distributions of electron-stimulated-desorption ions: oxygen on W(100). *J. Phys. Rev. Lett.*, 32(14):777, 1974.

[5] J-G. Lee, J. Ahner, and J. T. Yates. The adsorption conformation of chemisorbed pyridine on the Cu(110) surface. *J. Chem. Phys*, 114(3):1414–1419, 2001.

[6] J. Ahner, D. Mocuta, and J. T. Yates. TOF-ESDIAD measurements of a coadsorbate system:CO on an oxidized Cu(110) surface. *J. Surf. Sci*, 390(1-3):126–131, 1997.

[7] M. Menges, B. Baumeister, K. Al-Shamery, H-J. Freund, C. Fischer, and P. Andresen. Two-dimensional state resolved imaging after UV-laser induced desorption: NO/NiO(111). *J. Surf. Sci*, 316(1-2):103–111, 1994.

[8] S .P .K. Koehler, J. Yuanyuan, D. J. Auerbach, and A. M. Wodtke. Three-dimensional velocity map imaging of KBr surface photochemistry. *J. Phys. Chem. Chem. Phys*, 11(35):7540–7544, 2009.

[9] D. Sporleder, D. P. Wilson, and M. G. White. Final state distributions of O_2 photodesorbed from TiO2(110). *J.Phys. Chem C*, 113(30):13180–13191, 2009.

[10] G. D. Billing. *Dynamics of Molecule Surface Interaction*. John Wiley & Sons, 2000.

[11] M. Brouard and C. Vallance. *Tutorials in molecular reaction dynamics*. Royal Society of Chemistry, 2015.

[12] R. D. Levine. *Molecular reaction dynamics*. Cambridge University Press, 2009.

[13] K. R. Jennings. *Fundamentals and applications of gas phase ion chemistry*, volume 521. Springer Science & Business Media, 1999.

[14] D. A. King and M. G. Wells. Molecular beam investigation of adsorption kinetics on bulk metal targets: Nitrogen on tungsten. *J. Sur. Sci*, 29(2):454–482, 1972.

[15] R. J. Cooper. *Molecular beam studies of energy transfer in molecule surface interactions*. PhD thesis, Niedersächsische Staats-und Universitätsbibliothek Göttingen, 2011.

[16] K. Christmann. *Introduction to surface physical chemistry*, volume 1. Springer Science & Business Media, 2013.

[17] P. Gundry and F. Tompkins. Chemisorption of gases on metals. *J. Q. Rev. Chem. Soc*, 14(3):257–291, 1960.

[18] D. W Readey. *Kinetics in materials science and engineering*. CRC Press, 2017.

[19] A. Auroux et al. Calorimetry and thermal methods in catalysis. 2013.

[20] J. Lennard. Processes of adsorption and diffusion on solid surfaces. *J. Trans. Faraday Soc.*, 28:333, 1932.

[21] S. LM. Schroeder and M. Gottfried. Temperature-programmed desorption (TPD) thermal desorption spectroscopy (TDS). *Userpage. Chemie. Fu-Berlin. De*, pages 1–22, 2002.

[22] C-C. Hwang and A. R Barron. Temperature-programmed desorption mass spectroscopy applied in surface chemistry.

[23] R. Plumlee and LP. Smith. Mass spectrometric study of solids I. preliminary study of sublimation characteristics of oxide cathode materials. *J. Appl Phys*, 21(8):811–819, 1950.

[24] T. E Madey and J.T. Yates Jr. Electron-stimulated desorption as a tool for studies of chemisorption: A review. *J. Vac. Sci. Technol*, 8(4):525–555, 1971.

[25] PA. Redhead. Interaction of slow electrons with chemisorbed oxygen. *Can J Phys*, 42(5):886–905, 1964.

[26] T. Klüner. Photodesorption of diatomic molecules from surfaces: A theoretical approach based on first principles. *J. Prog Surf Sci*, 85(5-8):279–345, 2010.

[27] RM. Nix. An introduction to surface chemistry: 5.6 temperature-programmed desorption. *School of Biological and Chemical Sciences, Queen Mary, University of London (6/8/2003). http://www. chem. qmul. ac. uk/surfaces/scc/scat5_6. htm*.

[28] T. E. Madey. Electron-and photon-stimulated desorption: probes of structure and bonding at surfaces. *Sci*, 234(4774):316–322, 1986.

[29] H. Massey. Collisions between atoms and molecules at ordinary temperatures. *J. Rep. Prog. Phys*, 12(1):248, 1949.

[30] H Tratnik. Electron stimulated desorption of condensed gases on cryogenic surfaces. Technical report, 2005.

[31] G. Ertl and J. Küppers. *Low energy electrons and surface chemistry*. 1985.

[32] D. Menzel and R. Gomer. Desorption from metal surfaces by low-energy electrons. *J. Chem Phys*, 41(11):3311–3328, 1964.

[33] P. R. Antoniewicz. Model for electron-and photon-stimulated desorption. *J. Phy. Rev B*, 21(9):3811, 1980.

[34] JD. Fan and Y. M. Malozovsky. Pauli exclusion principle. *J. Int J Mod Phys B*, 27(15):1362024, 2013.

[35] E. Illenberger and P. Swiderek. Editorial electron-driven molecular processes: A general introduction, 2005.

[36] A. Shiotari. *Reactivity of Nitric Oxide on Copper Surfaces: Elucidated by Direct Observation of Valence Orbitals*. Springer, 2017.

[37] M. Shelef. Nitric oxide: surface reactions and removal from auto exhaust. *J. Catal. Rev. Sci. Eng*, 11(1):1–40, 1975.

[38] SB. Roobol, WG. Onderwaater, MA. van Spronsen, F. Carla, O. Balmes, V. Navarro, S. Vendelbo, PJ. Kooyman, CF. Elkjær, and S. Helveg. In situ studies of NO reduction by H_2 over Pt using surface X-ray diffraction and transmission electron microscopy. *J. Phys. Chem. Chem. Phys*, 19(12):8485–8495, 2017.

[39] R. Hoffmann. Mml chen, m. elian, ar rossi, and dmp mingos. *Inorg. Chem*, 13:2666, 1974.

[40] W. A. Brown and D. A. King. NO chemisorption and reactions on metal surfaces: a new perspective, 2000.

[41] M. Gajdoš, A. Eichler, and Jürgen Hafner. CO adsorption on close-packed transition and noble metal surfaces: trends from ab initio calculations. *J. Phys-Condens. Mat*, 16(8):1141, 2004.

[42] G. C. Bond and D. T. Thompson. Gold-catalysed oxidation of carbon monoxide. *j. Gold. Bull*, 33(2):41–50, 2000.

[43] M. Haruta, N. Yamada, T. Kobayashi, and S. Iijima. Gold catalysts prepared by coprecipitation for low-temperature oxidation of hydrogen and of carbon monoxide. *J. Catal*, 115(2):301–309, 1989.

[44] D. Cunningham, W. Vogel, H. Kageyama, S. Tsubota, and M. Haruta. The relationship between the structure and activity of nanometer size gold when supported on $Mg(OH)_2$. *J. Catal*, 177(1):1–10, 1998.

[45] M. C. Raphulu. *Catalytic oxidation of carbon monoxide and methane with gold-based catalysts*. PhD thesis, 2006.

[46] M. Haruta. Preparation and environmental applications of supported gold catalysts. *Now Future*, 7:13–36, 1992.

[47] T. Hayashi, K. Tanaka, and M. Haruta. Selective vapor-phase epoxidation of propylene over au/TiO_2 catalysts in the presence of oxygen and hydrogen. *J.Catal*, 178(2):566–575, 1998.

[48] M. Haruta, BS. Uphade, S. Tsubota, and A. Miyamoto. Selective oxidation of propylene over gold deposited on titanium-based oxides. *J. Res Chem Intermediat*, 24(3):329–336, 1998.

[49] J. Jia, K. Haraki, J. N. Kondo, K. Domen, and K. Tamaru. Selective hydrogenation of acetylene over Au/Al2O3 catalyst. *J. Phys. Chem B*, 104(47):11153–11156, 2000.

[50] M. Okumura, T. Akita, and M. Haruta. Hydrogenation of 1, 3-butadiene and of crotonaldehyde over highly dispersed Au catalysts. *J. Catal today*, 74(3-4):265–269, 2002.

[51] H. A .and Anderson J. A. Bailie, J. E .and Abdullah, C. H. Rochester, N. V. Richardson, N. Hodge, J-Guo. Zhang, A. Burrows, C. J. Kiely, and G. J Hutchings. Hydrogenation of but-2-enal over supported Au/ZnO catalysts. *J. Phys. Chem. Chem. Phys*, 3(18):4113–4121, 2001.

[52] M. Haruta. Size-and support-dependency in the catalysis of gold. *J. Catal. today*, 36(1):153–166, 1997.

[53] H-S. Oh, JH. Yang, CK. Costello, YM. Wang, SR. Bare, HH. Kung, and MC. Kung. Selective catalytic oxidation of CO: effect of chloride on supported Au catalysts. *J. Catal*, 210(2):375–386, 2002.

[54] S. Ivanova, Véronique Pitchon, and C. Petit. Application of the direct exchange method in the preparation of gold catalysts supported on different oxide materials. *J. Mol. Catal A-Chem*, 256(1-2):278–283, 2006.

[55] A . K. Hashmi and G. J Hutchings. Gold catalysis. *J. Angew Chem Int Ed*, 45(47):7896–7936, 2006.

[56] A. Alshammari and V. N. Kalevaru. Supported gold nanoparticles as promising catalysts. In *Catalytic Application of Nano-Gold Catalysts*. IntechOpen, 2016.

[57] M. Haruta, T. Kobayashi, H. Sano, and N. Yamada. Novel gold catalysts for the oxidation of carbon monoxide at a temperature far below 0 C. *J. Chem. Lett*, 16(2):405–408, 1987.

[58] S. Tsubota, T. Nakamura, K. Tanaka, and M. Haruta. Effect of calcination temperature on the catalytic activity of Au colloids mechanically mixed with TiO_2 powder for CO oxidation. *J. Catal. lett*, 56(2-3):131–135, 1998.

[59] S. D. Gardner, G. B. Hoflund, B. T. Upchurch, D. R. Schryer, E. J Kielin, and J. Schryer. Comparison of the performance characteristics of Pt/SnOx and Au/MnOx catalysts for low-temperature CO oxidation. *J. Catal*, 129(1):114–120, 1991.

[60] S. Arrii, .F Morfin, AJ. Renouprez, and JL. Rousset. Oxidation of CO on gold supported catalysts prepared by laser vaporization: direct evidence of support contribution. *J. Am. Chem. Soc*, 126(4):1199–1205, 2004.

[61] A. Ueda, T. Oshima, and M. Haruta. Reduction of nitrogen monoxide with propene in the presence of oxygen and moisture over gold supported on metal oxides. *J. Appl. Catal B. Environ*, 12(2-3):81–93, 1997.

[62] S. D Lin, A. C Gluhoi, and B. E Nieuwenhuys. Ammonia oxidation over Au/MOx/γ-Al_2O_3—activity, selectivity and ftir measurements. *J. Catal Today*, 90(1-2):3–14, 2004.

[63] C. Portales, I. Carrizosa, Odriozola, et al. Gold supported CeO_2/Al_2O_3 catalysts for CO oxidation: influence of the ceria phase. *J. Catal. Lett*, 102(3-4):289–297, 2005.

[64] A. C. Gluhoi and B. E Bogdanchikova, N.and Nieuwenhuys. The effect of different types of additives on the catalytic activity of Au/Al_2O_3 in propene total oxidation: transition metal oxides and ceria. *J. Catal*, 229(1):154–162, 2005.

[65] A. Sanchez, S. Abbet, U. Heiz, W-D. Schneider, H. Häkkinen, RN. Barnett, and Uzi. Landman. When gold is not noble: nanoscale gold catalysts. *J.f Phys. Chem A*, 103(48):9573–9578, 1999.

[66] M. M Schubert, S. Hackenberg, A. C Van Veen, M. Muhler, V. Plzak, and R Jürgen Behm. CO oxidation over supported gold catalysts "inert" and "active" support materials and their role for the oxygen supply during reaction. *J. Catal*, 197(1):113–122, 2001.

[67] NA. Hodge, CJ. Kiely, R. Whyman, MRH. Siddiqui, GJ. Hutchings, QA. Pankhurst, FE. Wagner, RR. Rajaram, and SE. Golunski. Microstructural comparison of calcined and uncalcined gold/iron-oxide catalysts for low-temperature CO oxidation. *J. Catal. Today*, 72(1-2):133–144, 2002.

[68] J. Guzman and B. C Gates. Catalysis by supported gold: correlation between catalytic activity for CO oxidation and oxidation states of gold. *J. Am. Chem. Soc*, 126(9):2672–2673, 2004.

[69] J. Guzman and B. C Gates. Structure and reactivity of a mononuclear gold-complex catalyst supported on magnesium oxide. *J. Angew. Chem*, 115(6):714–717, 2003.

[70] B. Nkosi, M. D. Adams, N. J. Coville, and G. J. Hutchings. Hydrochlorination of acetylene using carbon-supported gold catalysts: A study of catalyst reactivation. *J. Catal*, 128(2):378–386, 1991.

[71] HH. Kung, MC. Kung, and CK. Costello. Supported Au catalysts for low temperature CO oxidation. *J. catal*, 216(1-2):425–432, 2003.

[72] CK Costello, MC Kung, H-S Oh, Y Wang, and HH Kung. Nature of the active site for co oxidation on highly active $Au/\gamma\text{-}Al_2O_3$. *J. Appl. CatalL A-Gen*, 232(1-2):159–168, 2002.

[73] S. Tsubota, D. Cunningham, Y. Bando, and M. Haruta. Co oxidation over gold supported on tio2. In *Studies in Surface Science and Catalysis*, volume 77, pages 325–328. Elsevier, 1993.

[74] K. Mitsuhara, H. Okumura, A. Visikovskiy, M. Takizawa, and Y. Kido. The source of the ti 3 d defect state in the band gap of rutile titania (110) surfaces. *J. Chem. Phys*, 136(12):124707, 2012.

[75] G. Mills, M. S. Gordon, and H. Metiu. The adsorption of molecular oxygen on neutral and negative Aun clusters (n= 2–5). *J. Chem. Phys. Lett*, 359(5-6):493–499, 2002.

[76] JY. Lee and J. Schwank. Infrared spectroscopic study of NO reduction by H_2 on supported gold catalysts. *J. Catal*, 102(1):207–215, 1986.

[77] Na. M Gupta and A. K Tripathi. The role of nanosized gold particles in adsorption and oxidation of carbon monoxide over Au/Fe_2O_3 catalyst. *J. Gold. Bull*, 34(4):120–128, 2001.

[78] A. Ueda and M. Haruta. Nitric oxide reduction with hydrogen, carbon monoxide, and hydrocarbons over gold catalysts. *J. Gold. Bull*, 32(1):3–11, 1999.

[79] S. Galvagno and G_ Parravano. Chemical reactivity of supported gold: Iv. reduction of NO by H_2. 1978.

[80] IW. Bassi, FW. Lytle, and G. Parravano. Chemical reactivity of supported gold: III. atomic binding and coordination of gold from X-ray absorption fine structure spectroscopy. 1976.

[81] L. Ilieva, G. Pantaleo, I. Ivanov, AM. Venezia, and D. Andreeva. Gold catalysts supported on CeO_2 and $CeO2–Al_2O_3$ for NOx reduction by CO. *J. Appl. Catal B-Environ*, 65(1-2):101–109, 2006.

[82] X. Wang, X. Wu, N. Maeda, and A. Baiker. Striking activity enhancement of gold supported on Al-Ti mixed oxide by promotion with ceria in the reduction of NO with CO. *J. Catal B-Environ*, 209:62–68, 2017.

[83] M. Ueda, A.and Haruta. Reduction of nitrogen monoxide with propene over Au/Al_2O_3 mixed mechanically with Mn_2O_3. *J. Appl Catal B-Environ*, 18(1-2):115–121, 1998.

[84] E. Seker and E. Gulari. Single step sol–gel made gold on alumina catalyst for selective reduction of nox under oxidizing conditions: effect of gold precursor and reaction conditions. *J. Appl Catal A: General*, 232(1-2):203–217, 2002.

[85] D. Niakolas, Ch. Andronikou, Ch. Papadopoulou, and H. Matralis. Influence of metal oxides on the catalytic behavior of au/al2o3 for the selective reduction of NOx by hydrocarbons. *J. Catal today*, 112(1-4):184–187, 2006.

[86] P. Miquel, P. Granger, N. Jagtap, S. Umbarkar, M. Dongare, and C. Dujardin. NO reduction under diesel exhaust conditions over Au/Al_2O_3 prepared by deposition-precipitation method. *J. Mol. Catal A-Chem*, 322(1-2):90–97, 2010.

[87] Y. Zhang, R. W. Cattrall, I. D. McKelvie, and S. D Kolev. Gold, an alternative to platinum group metals in automobile catalytic converters. *J. Gold Bull*, 44(3):145, 2011.

[88] A. Hussain, D. C. Ferré, J. Gracia, BE. Nieuwenhuys, and JW. Niemantsverdriet. Dft study of CO and NO adsorption on low index and stepped surfaces of gold. *J. Surf. Sci*, 603(17):2734–2741, 2009.

[89] Y. Wang, D. Zhang, and C. Liu. Theoretical study of NO adsorption on gold surfaces. *J. Sci. China Chem*, 54.

[90] AC. Carabineiro and B. E Nieuwenhuys. Adsorption of small molecules on gold single crystal surfaces. *J. Gold. Bull*, 42(4):288–301, 2009.

[91] ME. Bartram and B.E Koel. The molecular adsorption of NO_2 and the formation of N_2O_3 on au(111). *J. Surf. Sci*, 213(1):137–156, 1989.

[92] D Torres, S. González, K. M. Neyman, and F. Illas. Adsorption and oxidation of no on Au(111) surface: Density functional studies. *J. Chem. Phys. lett*, 422(4-6):412–416, 2006.

[93] C. D Zeinalipour-Yazdi, D. J Willock, A. Machado, K. Wilson, and A. F. Lee. Impact of co-adsorbed oxygen on crotonaldehyde adsorption over gold nanoclusters: a computational study. *J.Phys. Chem. Chem. Phys*, 16(23):11202–11210, 2014.

[94] D. Fedak and NA. Gjostein. On the anomalous surface structures of gold. *J. Surf. Sci*, 8(1-2):77–97, 1967.

[95] CP. Vinod, JW. Niemantsverdriet. Hans, and BE. Nieuwenhuys. Interaction of small molecules with Au(310): Decomposition of NO. *J. Appl Catal A-Gen*, 291(1-2):93–97, 2005.

[96] AV. Bukhtiyarov, RI. Kvon, AV. Nartova, IP. Prosvirin, and VI. Bukhtiyarov. In-situ XPS investigation of nitric oxide adsorption on (111),(310), and (533) gold single crystal faces. *J. Surf. Sci.*, 606(3-4):559–563, 2012.

[97] J. Fajin, M. Cordeiro, and José RB Gomes. The role of preadsorbed atomic hydrogen in the NO dissociation on a zigzag stepped gold surface: A DFT study. *J. Phys. Chem C*, 113(20):8864–8877, 2009.

[98] R. Zanella, S. Giorgio, C-Ho. Shin, C. R. Henry, and C. Louis. Characterization and reactivity in CO oxidation of gold nanoparticles supported on TiO_2 prepared by deposition-precipitation with NaOH and urea. *J. Catal*, 222(2):357–367, 2004.

[99] Ton VW. Janssens, Bj. S Clausen, Britt Hvolbæk, H. Falsig, C. H Christensen, T. Bligaard, and Jens K Nørskov. Insights into the reactivity of supported Au nanoparticles: combining theory and experiments. *j. Top. Catal*, 44(1-2):15, 2007.

[100] Z. Wu, L. Xu, W. Zhang, Y. Ma, Q. Yuan, Y. Jin, J. Yang, and W. Huang. Structure sensitivity of low-temperature NO decomposition on Au surfaces. *J. catal*, 304:112–122, 2013.

[101] Y. Tanimura, K. Yamashita, and Philip A Anfinrud. Femtochemistry. *J. Natl. Acad. Sci*, 96(16):8823–8824, 1999.

[102] L. R Khundkar and A. H. Zewail. Ultrafast molecular reaction dynamics in real-time: progress over a decade. *J. Annu. Rev. Phys. Chem*, 41(1):15–60, 1990.

[103] M. Gruebele and A. H Zewail. Ultrafast reaction dynamics. *Berichte der Bunsengesellschaft für physikalische Chemie*, 94(11):1210–1218, 1990.

[104] FJ. McClung and RW. Hellwarth. Giant optical pulsations from ruby. *J. Appl Phys*, 33(3):828–829, 1962.

[105] George Porter. Flash photolysis and some of its applications. *Science*, 160(3834):1299–1307, 1968.

[106] Denitsa Baykusheva and Hans Jakob Wörner. Chapter 4 - attosecond molecular dynamics and spectroscopy. In Roberto Marquardt and Martin Quack, editors, *Molecular Spectroscopy and Quantum Dynamics*, pages 113–161. Elsevier, 2021.

[107] M. Hollas, J. High resolution spectroscopy. *Wiley-Blackwell*, 1998.

[108] Gerhard Herzberg. Molecular spectra and molecular structure. vol. 1: Spectra of diatomic molecules. *New York: Van Nostrand Reinhold*, 1950.

[109] Friedrich Hund. Zur deutung einiger erscheinungen in den molekelspektren. *Zeitschrift für Physik*, 36(9):657–674, 1926.

[110] DC Jacobs, RJ Madix, and R No Zare. Reduction of 1+ 1 resonance enhanced mpi spectra to population distributions: Application to the no a $2\sigma+$–x 2π system. *The Journal of chemical physics*, 85(10):5469–5479, 1986.

[111] MJL De Lange, JJ Van Leuken, MMJE Drabbels, J Bulthuis, JG Snijders, and S Stolte. Direct spectroscopic determination of the degree of orientation of parity-selected no. *Chemical physics letters*, 294(4-5):332–338, 1998.

[112] WE. Stephens. A pulsed mass spectrometer with time disaersion. *J. Phys. Rev.*, 69:691, 1946.

[113] BA. Mamyrin, VI. Karataev, DV. Shmikk, and VA. Zagulin. The massreflect ron, a new non-magnetic time-of-flight mass spectrometer with high resolution. *Zh. Eksp. Teor. Fiz*, 64:82–89, 1973.

[114] WC. Wiley and Ii. H. McLaren. Time-of-flight mass spectrometer with improved resolution. *J. Rev. Sci. Instrum.*, 26(12):1150–1157, 1955.

[115] SB. Howarth, JH. Lippiatt, GB. Price, D .and Ward, and P. Myers. Development of a time-of-flight mass spectrometer to monitor fast gas reactions. *J. Mass. Spectrum. Ion. Phys*, 9(1):95–105, 1972.

[116] J. Solomon. Photodissociation as studied by photolysis mapping. *J. Chem. Phys*, 47(3):889–895, 1967.

[117] J. Solomon, C. Jonah, P. Chandra, and R. Bersohn. Photolysis mapping studies of aliphatic carbonyl compounds. *J. Chem. Phys*, 55(4):1908–1914, 1971.

[118] D. W Chandler and P. Houston. Two-dimensional imaging of state-selected photodissociation products detected by multiphoton ionization. *J. chem. phys*, 87(2):1445–1447, 1987.

[119] A. Eppink and D..H Parker. Velocity map imaging of ions and electrons using electrostatic lenses: Application in photoelectron and photofragment ion imaging of molecular oxygen. *Rev. Sci. Instrm*, 68(9):3477–3484, 1997.

[120] Heinrich Hertz. Ueber einen einfluss des ultravioletten lichtes auf die electrische entladung. *Annalen der Physik*, 267(8):983–1000, 1887.

[121] A. Einstein. On a heuristic point of view concerning the production and transformation of light. *Annalen der Physik*, pages 1–18, 1905.

[122] Roger Smart. X-ray photoelectron spectroscopy ray photoelectron spectroscopy. `http://www.physics.uwo.ca/~lgonchar/courses/p9826/Lecture7_XPS.pdf`, 2013 (accessed May 19, 2019.

[123] R. T. Haasch. X-ray photoelectron spectroscopy (XPS) and auger electron spectroscopy (AES). In *Practical Materials Characterization*, pages 93–132. Springer, 2014.

[124] DE. Starr, Z. Liu, M. Hävecker, A. Knop-Gericke, and H Bluhm. Investigation of solid/vapor interfaces using ambient pressure x-ray photoelectron spectroscopy. *J. Chem. Soc. Rev*, 42(13):5833–5857, 2013.

[125] M. D. Kershis, D. P. Wilson, M. G. White, J. J. John, A.i. Nomerotski, M. Brouard, J. WL. Lee, C. Vallance, and R. Turchetta. Exploring surface

photoreaction dynamics using pixel imaging mass spectrometry (PImMS). *J. Chem. Phys*, 139(8):084202, 2013.

[126] D. J Harding, J. Neugebohren, H. Hahn, DJ. Auerbach, TN. Kitsopoulos, and A. M. Wodtke. Ion and velocity map imaging for surface dynamics and kinetics. *J. Chem. Phys*, 147(1):013939, 2017.

[127] JR. Roscioli, DJ. Bell, DJ. Nelson, and DJ. Nesbitt. State-resolved velocity map imaging of surface-scattered molecular flux. *J. Phys. Chem. Chem. Phys*, 14(12):4070–4080, 2012.

[128] C. H Hoffman and D. J. Nesbitt. Quantum state resolved 3d velocity map imaging of surface-scattered molecules: Incident energy effects in HCl^+ self-assembled monolayer collisions. *J. Phys. Chem C*, 120(30):16687–16698, 2016.

[129] D. J Harding, J. Neugebohren, D. J Auerbach, TN. Kitsopoulos, and A.c M. Wodtke. Using ion imaging to measure velocity distributions in surface scattering experiments. *J. Phys. Chem A*, 119(50):12255–12262, 2015.

[130] AR. Bainbridge and WA. Bryan. Velocity map imaging of femtosecond laser induced photoelectron emission from metal nanotips. *New J. Phys*, 16(10):103031, 2014.

[131] H. Ye, S. Trippel, M. Di Fraia, A. Fallahi, O. D. Mücke, F. X. Kärtner, and J. Küpper. Velocity-map imaging for emittance characterization of multiphoton electron emission from a gold surface. *J. Phys. Rev. Appl*, 9(4):044018, 2018.

[132] J. J Lin, J Zhou, W Shiu, and K. Liu. Application of time-sliced ion velocity imaging to crossed molecular beam experiments. *J. Rev. sci. instr*, 74(4):2495–2500, 2003.

[133] M. Reid and S. P.K. Koehler. Validation of velocity map imaging conditions over larger areas. *Rev. Sci. Instr*, 84(4):044101, 2013.

[134] Mike Reid. *Velocity map imaging: from gases to surfaces.* The University of Manchester (United Kingdom), 2013.

[135] S. Manzhos and H-P. Loock. Photofragment image analysis using the onion-peeling algorithm. *J. Comput. Phys. Commun*, 154(1):76–87, 2003.

[136] I. Wilkinson, M. P de Miranda, and B. J Whitaker. Photodissociation of NO_2 in the $(2)(2)B_2$ state: The $(O_1(D_2))$ dissociation channel. *J. Chem. Phys*, 131(5):054308, 2009.

[137] JH. Bechtel. Heating of solid targets with laser pulses. *J. Appl. Phys*, 46(4):1585–1593, 1975.

[138] P. B. Johnson and R-W_ Christy. Optical constants of the noble metals. *Phys. Rev B*, 6(12):4370, 1972.

[139] CT. Rettner and DJ. Auerbach. Probing the dynamics of gas-surface interactions with high-energy molecular beams. *J. Comments At. Mol. Phys*, 20(3):153–69, 1987.

[140] J. A. Barker and D. J. Auerbach. Gas—surface interactions and dynamics; thermal energy atomic and molecular beam studies. *J. Surf. Sci. Reports*, 4(1-2):1–99, 1984.

[141] MC. Lin and G. Ertl. Laser probing of molecules desorbing and scattering from solid surfaces. *J. Annu. Rev. Phys. Chem*, 37(1):587–615, 1986.

[142] K. Fukutani, A. Peremans, K. Mase, and Y. Murata. Photo-stimulated desorption of NO from a Pt(001) surface. *J. Surf. Sci*, 283(1-3):158–168, 1993.

[143] K. Mase, K. Fukutani, and Y. Murata. Adsorption state selectivity of ultraviolet–laser-stimulated desorption of no chemisorbed on Pt(001) at 80 K studied by (1+1)-resonance-enhanced multiphoton ionization. *J. Chem. Phys*, 96(7):5523–5528, 1992.

[144] S. A. Buntin, L. J. Richter, R. R. Cavanagh, and D. S. King. Optically driven surface reactions: Evidence for the role of hot electrons. *J. Phys. Rev. Lett*, 61(11):1321, 1988.

[145] SA. Buntin, LJ. Richter, DS. King, and RR. Cavanagh. State-resolved evidence for hot carrier driven surface reactions: Laser-induced desorption of NO from pt(111). *J. Chem. Phys*, 91(10):6429–6446, 1989.

[146] K. Fukutani, Y. Murata, R. Schwarzwald, and TJ. Chuang. UV-laser-induced desorption of NO from pt(111). *J. Surf. Sci*, 311(1-2):247–256, 1994.

[147] AR. Burns, EB. Stechel, and DR. Jennison. Rotational dynamics and electronic energy partitioning in the electron-stimulated desorption of NO from pt (111). *J. Vac. Sci. Technol A*, 6(3):895–898, 1988.

[148] D. Mulugeta, K. Watanabe, D. Menzel, and Hs-J. Freund. State-resolved investigation of the photodesorption dynamics of NO from $(NO)_2$ on Ag nanoparticles of various sizes in comparison with Ag(111). *J. chem. phys*, 134(16):164702, 2011.

[149] L. J. Richter, S. A. Buntin, D. S. King, and R. R. Cavanagh. State-resolved studies of the laser-induced desorption of NO from Si(111) 7× 7: Low coverage results. *J. Chem. Phys*, 96(3):2324–2338, 1992.

[150] F. Budde, AV. Hamza, PM. Ferm, G. Ertl, D. Weide, P. Andresen, and H-J. Freund. Photodesorption of NO from Ni(100)-O. *J. Phys. Rev. Lett*, 60(15):1518, 1988.

[151] SK. So and W. Ho. Photon-induced reactions of No adsorbed on GaAs(110). *J. Appl. Phys A*, 47(3):213–217, 1988.

[152] I. Rahinov, R. Cooper, C. Yuan, X. Yang, D. J Auerbach, and A. M. Wodtke. Efficient vibrational and translational excitations of a solid metal surface: State-to-state time-of-flight measurements of HCl (v= 2, J= 1) scattering from Au(111). *J. Chem. Phys*, 129(21):214708, 2008.

[153] Th. Mull, B. Baumeister, M. Menges, H-J. Freund, D. Weide, C. Fischer, and P. Andresen. Bimodal velocity distributions after ultraviolet-laser-induced desorption of NO from oxide surfaces. experiments and results of model calculations. *J. Chem. Phys*, 96(9):7108–7116, 1992.

[154] Paul A Anderson. Work function of gold. *Physical Review*, 115(3):553, 1959.

[155] AR. Burns. Quantum-resolved angular distributions of neutral products in electron-stimulated processes: desorption of CO from pt(111). *J. Surf sci*, 280(3):349–358, 1993.

[156] WC. Natzle, D. Padowitz, and SJ. Sibener. Ultraviolet laser photodesorption of NO from condensed films: Translational and internal energy distributions. *J. Chem. Phys*, 88(12):7975–7994, 1988.

[157] RH. Gillette and E. H. Eyster. The fundamental rotation-vibration band of Nitric Oxide. *J. Phys. Rev*, 56(11):1113, 1939.

[158] A. Peremans, K. Fukutani, K. Mase, and Y. Murata. UV photodesorption of CO from Pt(001) at 193 nm investigated by state-selective detection. *J. Surf. Sci*, 283(1-3):189–194, 1993.

[159] E. Hasselbrink, S. Jakubith, S. Nettesheim, M. Wolf, A. Cassuto, and G. Ertl. Cross sections and NO product state distributions resulting from substrate mediated photodissociation of no2 adsorbed on Pd(111). *J. Chem. Phys*, 92(5):3154–3169, 1990.

[160] D. Burgess Jr, R. Viswanathan, I. Hussla, P. C. Stair, and E. Weitz. Pulsed laser induced thermal desorption of CO from copper surfaces. *J. Chem. Phys*, 79(10):5200–5202, 1983.

[161] R. R. Cavanagh and D. S. King. Rotational-and spin-state distributions: No thermally desorbed from Ru(001). *J. Phys. Rev. Lett*, 47(25):1829, 1981.

[162] D. A. Mantell, R. R. Cavanagh, and D. S. King. Internal states distributions of NO thermally desorbed from Pt(111): Dependence on coverage and co-adsorbed CO. *J. Chem. Phys*, 84(9):5131–5142, 1986.

[163] C. W Muhlhausen, L. R. Williams, and J. C. Tully. Dynamics of gas-surface interactions: scattering and desorption ofNO from Ag(111) and Pt(111). *J. Chem. Phys*, 83(5):2594–2606, 1985.

[164] TA. Holme and RD. Levine. Computational studies of rapid laser induced desorption: a microscopic mechanism for selectivity. *J. Surf. Sci*, 216(3):587–614, 1989.

[165] G. E. Moore. Dissociation of adsorbed CO by slow electrons. *J. Appl. Phys*, 32(7):1241–1251, 1961.

[166] M. Nishijima and F. M. Propst. Kinetics of electron impact desorption of ions and neutrals from polycrystalline tungsten. *J. Vac. Sci. Technol*, 7(3):420–428, 1970.

[167] Z. Ying and W. Ho. Photogenerated-charge-carrier-induced surface reaction: NO on Si(111) 7× 7. *J. Phys. Rev. Lett*, 60(1):57, 1988.

[168] AV. Bukhtiyarov, AV. Nartova, and RI. Kvon. Identification of nitrogen-containing species obtained by Nitric Oxide adsorption on the surface of model gold catalysts. *J. Kinet. Catal*, 52(5):756, 2011.

[169] T. Shimada, B. S. Mun, I. F Nakai, A. Banno, H. Abe, Y. Iwasawa, T. Ohta, and H. Kondoh. Irreversible change in the NO adsorption state on Pt(111) under high pressure studied by AP-XPS, NEXAFS, and STM. *J. Phys. Chem C*, 114(40):17030–17035, 2010.

[170] R. Toyoshima, M. Yoshida, Y. Monya, K. Suzuki, K. Amemiya, K. Mase, B. S. Mun, and H. Kondoh. Photoelectron spectroscopic study of CO and NO adsorption on Pd(100) surface under ambient pressure conditions. *J. Surf. Sci*, 615:33–40, 2013.

[171] M. Salmeron and Robert Schlögl. Ambient pressure photoelectron spectroscopy: A new tool for surface science and nanotechnology. *J. Surf. Sci. Reports*, 63(4):169–199, 2008.

[172] Roger Smart. Specs phoibos 150 NAP near ambient pressure hemispherical energy analyzer brochure. `http://www.specs.de/cms/upload/PDFs/SPECSProspekte/201011PHOIBOS150NAPproductbrochurefinalweb.pdf`, 2010 (accessed May 23, 2019.

[173] N. Fairley. *CasaXPS Manual 2.3. 15: Introduction to XPS and AES*. Casa Software, 2009.

[174] SW. Yu, W. C. Stolte, R. Guillemin, G. Öhrwall, IC. Tran, R. Piancastelli, M. N.and Feng, and DW. Lindle. Photofragmentation study of core-excited NO. *J. Phys B-AT Mol. Opt*, 37(18):3583, 2004.

[175] K. Hosaka, J. Adachi, M. Takahashi, and A. Yagishita. N 1s photoionization cross sections of Nitric Oxide molecules in the shape resonance region. *J. Phys B-AT Mol. Opt*, 36(23):4617, 2003.

[176] EDL. Rienks, GP. Van Berkel, JW. Bakker, and BE. Nieuwenhuys. Lifting of the Au(100) surface reconstruction by NO chemisorption. *J. Surf. Sci.*, 571(1-3):187–193, 2004.

[177] W. Yim, T. Nowitzki, Ma. Necke, H. Schnars, P. Nickut, J. Biener, M. M. Biener, V. Zielasek, K. Al-Shamery, and T.and others Klüner. Universal phenomena of CO adsorption on gold surfaces with low-coordinated sites. *J. Phys Chem C*, 111(1):445–451, 2007.

[178] EDL. Rienks, JW. Bakker, A. Baraldi, SAC. Carabineiro, S. Lizzit, CJ. Weststrate, and BE. Nieuwenhuys. Interaction of Nitric Oxide with Pt(100). a fast X-ray photoelectron spectroscopy study. *J. Surf. Sci*, 516(1-2):109–117, 2002.

[179] E. Umbach, S. Kulkarni, P. Feulner, and D. Menzel. A multimethod study of the adsorption of NO on Ru(001): I. XPS, UPS and XAES measurements. *J. Surf. Sci.*, 88(1):65–94, 1979.

[180] P. D. Schulze, D. L. Utley, and R. L. Hance. Chemisorption of NO on re studied by XPS. *J. Surf. Sci. Lett*, 102(1):L9–L13, 1981.

[181] MJ. Breitschafter, E. Umbach, and D. Menzel. An electron spectroscopic investigation of the adsorption of NO on Ni(111). *J. Surf. Sci*, 109(2):493–511, 1981.

[182] S. Sugai, K. Takeuchi, T. Ban, H. Miki, K. Kawasaki, and T Kioka. Adsorption and dissociation of NO on pt(100) and (310) studied by AES, UPS and XPS. *J. Surf. Sci*, 282(1-2):67–75, 1993.

[183] M. Kiskinova, G. Pirug, and HP. Bonzel. Coadsorption of potassium and CO on Pt(111). *J. Surf. sci*, 133(2-3):321–343, 1983.

[184] T. E. Madey, J. T. Yates Jr, and Nils. E. Erickson. X-ray photoelectron spectroscopic study of the adsorption of N_2 and NO on tungsten. *J. Surf. Sci*, 43(2):526–544, 1974.

[185] CR. Brundle. XPS and UPS studies of the interaction of nitrogen-containing molecules with nickel: The use of binding energy patterns and relative intensities to diagnose surface species. *J. Vac. Sci. Technol*, 13(1):301–309, 1976.

[186] JF. Zhu, M. Kinne, T. Fuhrmann, R. Denecke, and H-P Steinrück. In situ high-resolution XPS studies on adsorption of NO on pt(111). *J. Surf. Sci*, 529(3):384–396, 2003.

[187] M. Ganduglia-Pirovano, M. Scheffler, A. Baraldi, S. Lizzit, G. Comelli, G. Paolucci, and R. Rosei. Oxygen-induced Rh_3 d 5/2 surface core-level shifts on Rh(111). *J. Phys. Rev B*, 63(20):205415, 2001.

[188] E. Grossa, JF. Dobsonb, and M. Petersilkaa. Density functional theory of time-dependent phenomena. *J. Topics. Curr. Chem*, 181:81.

[189] Daniel Joubert. Density functionals: theory and applications. In *Lecture Notes in Physics, Berlin Springer Verlag*, volume 500, 1998.

[190] P. Hohenberg and Kohn W. PhysRev. 136b: 864: Kohn w and sham l j. *J. Phys Rev*, 140:1133, 1965.

[191] W. Kohn and L. J. Sham. Self-consistent equations including exchange and correlation effects. *J. Phys. rev*, 140(4A):A1133, 1965.

[192] S. J. Clark, M. D Segall, C. J. Pickard, P. J. Hasnip, M. IJ. Probert, K. Refson, and M. C. Payne. First principles methods using castep. *Zeitschrift für Kristallographie-Crystalline Materials*, 220(5/6):567–570, 2005.

[193] G Kresse and J Hafner. Norm-conserving and ultrasoft pseudopotentials for first-row and transition elements. *J. Phys.s: Condensed Matter*, 6(40):8245, 1994.

[194] M. Mavrikakis, P. Stoltze, and Jens Kehlet Nørskov. Making gold less noble. *J. Catal. Lett*, 64(2-4):101–106, 2000.

[195] O. Olvera-Neria, V. Bertin, and E. Poulain. The Nitric Oxide adsorption on gold neutral, cation, and anion atoms: A comparative ab initio MRCI—MRPT2 studies. *Int. J. Quantum. Chem*, 111(9):2054–2063, 2011.

[196] H. Tratnik, N. Hilleret, and H. Störi. The desorption of condensed noble gases and gas mixtures from cryogenic surfaces. *J. Vac*, 81(6):731–737, 2007.

[197] Z-H. Zeng, J. LF. Da Silva, H-Q. Deng, and W-X. Li. Density functional theory study of the energetics, electronic structure, and core-level shifts of NO adsorption on the Pt(111) surface. *J. Phys. Rev B*, 79(20):205413, 2009.

[198] R. Burch, JP. Breen, and FC. Meunier. A review of the selective reduction of NOx with hydrocarbons under lean-burn conditions with non-zeolitic oxide and platinum group metal catalysts. *J. Appl Catal B-Environ*, 39(4):283–303, 2002.

[199] N. E. Singh-Miller and N. Marzari. Surface energies, work functions, and surface relaxations of low-index metallic surfaces from first principles. *J. Phys. Rev B*, 80(23):235407, 2009.

[200] GV. Hansson and SA Flodström. Photoemission study of the bulk and surface electronic structure of single crystals of gold. *J. Phys Rev B*, 18(4):1572, 1978.

[201] CJ. Fall, N. Binggeli, and A. Baldereschi. Work-function anisotropy in noble metals: Contributions from d states and effects of the surface atomic structure. *J. Phys. Rev. B*, 61(12):8489, 2000.

[202] AL. Allred. Electronegativity values from thermochemical data. *J. Inorg. Nucl. Chem*, 17(3-4):215–221, 1961.

[203] Z-H. Zeng, J. LF. Da Silva, and W-X. Li. Theory of nitride oxide adsorption on transition metal (111) surfaces: a first-principles investigation. *J. Phys. Chem. Chem. Phys*, 12(10):2459–2470, 2010.